EXPERIMENTAL EVIDENCE FOR BLUE AND RED-SHIFTED HYDROGEN BOND: A MATRIX ISOLATION INFRARED SPECTROSCOPY AND AB INITIO STUDIES

By

R. GOPI

Enrolment No: CHEM 02 2012 04 008

Indira Gandhi Centre for Atomic Research, Kalpakkam

A thesis submitted to the

Board of Studies in Chemical Sciences

In partial fulfillment of requirements

For the Degree of

DOCTOR OF PHILOSOPHY

of

HOMI BHABHA NATIONAL INSTITUTE

July, 2017

Homi Bhabha National Institute

Recommendations of the Viva Voce Board

As members of the Viva Voce Board, we certify that we have read the dissertation prepared by **R. Gopi** entitled "**Experimental Evidence for Blue and Red-shifted Hydrogen Bond: A Matrix Isolation Infrared Spectroscopy and ab Initio Studies"** and recommend that it may be accepted as fulfilling the dissertation requirement for the Degree of Doctor of Philosophy.

_____ **Date:**

Chairman- Prof. M. Joseph

_____ **Date:**

Convener- Dr. K. Sundararajan

_____ **Date:**

Examiner- Dr. Bhalamurugan Sivaraman

_____ **Date:**

Member 1- Dr. T. R. Ravindran

_____ **Date:**

Member 2- Prof. B.S. Panigrahi

Final approval and acceptance of this dissertation is contingent upon the candidate's submission of the final copies of the dissertation to HBNI.

I hereby certify that I have read this dissertation prepared under my direction and recommend that it may be accepted as fulfilling the dissertation requirement.

Date:

Place: **Guide**

STATEMENT BY AUTHOR

This dissertation has been submitted in partial fulfillment of requirements for an advanced degree at Homi Bhabha National Institute (HBNI) and is deposited in the Library to be made available to borrowers under rules of the HBNI.

Brief quotations from this dissertation are allowable without special permission, provided that accurate acknowledgement of source is made. Requests for permission for extended quotation from or reproduction of this manuscript in whole or in part may be granted by the Competent Authority of HBNI when in his or her judgment the proposed use of the material is in the interests of scholarship. In all other instances, however, permission must be obtained from the author.

R. Gopi

DECLARATION

I, hereby declare that the investigation presented in the thesis has been carried out by me. The work is original and has not been submitted earlier as a whole or in part for a degree/diploma at this or any other Institution / University.

R. Gopi

List of Publications arising from the thesis

1) "Experimental Evidence for Blue-Shifted Hydrogen Bonding in Fluoroform-Hydrogen Chloride Complex: A Matrix Isolation Infrared and *ab initio* Study" **R. Gopi**, N. Ramanathan, K. Sundararajan, J. Phys. Chem. A, 2014, 118, 5529-5539.

2) "Hydrogen-bonded complexes of acetylene and acetonitrile: A matrix isolation infrared and computational study" **R. Gopi,** N. Ramanathan, K. Sundararajan, J. Mol. Struct. 2015, 1083, 364-373.

3) "Acetonitrile-Water Hydrogen-Bonded Interaction: Matrix-Isolation Infrared and *ab initio* Computation" **R. Gopi**, N. Ramanathan, K. Sundararajan, J. Mol. Struct. 2015, 1094, 118-129.

4) "Blue-shift of the C-H stretching vibration in CHF_3-H_2O complex: Matrix isolation infrared spectroscopy and *ab initio* computations" **R. Gopi**, N. Ramanathan, K. Sundararajan, Chem. Phys. 2016, 476, 36-45.

5) "Probing C-H···N interaction in acetylene-benzonitrile complex using matrix isolation infrared spectroscopy and DFT computations" **R. Gopi**, N. Ramanathan, K. Sundararajan, Chem. Phys. 2017, 487, 67-74.

6) "Experimental evidence for the blue-shifted hydrogen-bonded complexes of CHF_3 with π-systems" **R. Gopi**, N. Ramanathan, K. Sundararajan, Spectrochim. Acta Part A, 181, 2017, 137-147.

7) "Benzonitrile-Water Hydrogen-Bonded Interaction: A Matrix Isolation Infrared and *ab initio* Computation" **R. Gopi**, N. Ramanathan, K. Sundararajan (manuscript under preparation).

Oral Presentations:

1) **R. Gopi,** N. Ramanathan, K. Sundararajan, Acetonitrile-Water and Benzonitrile-Water Hydrogen-bonded Interaction: A Matrix Isolation Infrared and ab initio Computation, 12th Discussion Meeting on Spectroscopy and Dynamics of Molecules and Clusters, Nainital, Feb 19-22, 2014.

2) **R. Gopi,** N. Ramanathan, K. Sundararajan, "Study of blue shifting hydrogen bond in Fluoroform with Lewis bases (HCl, H_2O, and C_6H_6): A Matrix isolation infrared and *ab initio* studies" XXIth International Conference on "Horizons in Hydrogen Bond Research – H-Bond 2015" held at **University of Wroclaw, Poland**, September 13-18, 2015.

Poster Presentations:

1) N. Ramanathan, **R. Gopi,** K. Sundararajan, Acetylene-Acetonitrile complexes: Matrix isolation infrared and *ab initio* studies, Poster presentation, The Fourth Asian Spectroscopy Conference, Singapore, December 5-18, 2013.

2) **R. Gopi,** N. Ramanathan, K. Sundararajan, Experimental Evidence for Blue Shifted Hydrogen Bonding in Fluoroform (CHF_3)-Hydrogen Chloride (HCl) Complex: A Matrix Isolation Infrared and *ab initio* Studies, Poster presentation, 11th Discussion Meeting on Spectroscopy and Dynamics of Molecules and Clusters, Puri, India, February 20-23, 2014.

3) **R. Gopi,** N. Ramanathan, K. Sundararajan, Experimental Evidence for Blue-Shifted Hydrogen Bonding in Fluoroform-Water Complex: Matrix Isolation Infrared and *ab initio* Study, Poster presentation, 11th Discussion Meeting on Spectroscopy and Dynamics of Molecules and Clusters, Puri, India, February 20-23, 2014.

4) **R. Gopi,** N. Ramanathan, K. Sundararajan, 1:1 Hydrogen-bonded complexes of Acetylene-Benzonitrile: A Matrix Isolation and Computational Study, Poster presentation, Recent Trends on

Spectroscopy (RTS-2014), Chennai, IIT, India, June 20- 21, 2014.

5) **R. Gopi,** **N**. Ramanathan, K. Sundararajan, "Study of blue shifting hydrogen bond in Fluoroform with Lewis bases (HCl, H_2O, and C_6H_6): A Matrix isolation infrared and *ab initio* studies" XXIth International Conference on "Horizons in Hydrogen Bond Research – HBond 2015" held at University of Wroclaw, Poland, *S*eptember 13-18, 2015.

Other Publications (not included in the thesis):

1) "Ortho-Para Converter for Producing Para hydrogen Gas for Matrix Isolation Spectroscopy" K.Sundararajan, K.Sankaran , N.Ramanthan and **R. Gopi**, J. Mol. Struct. 2016, 1117, 181-191.

2) "Conformations of propargyl alcohol and its interaction with acetylene: A matrix isolation infrared and DFT computations" K. Sundararajan, **R. Gopi**, N. Ramanathan, J. Mol. Struct. 2016, 1121, 26-34.

3) "Photooxidation of Trimethyl Phosphite in Nitrogen, Oxygen, and *para*-Hydrogen Matrixes at Low Temperatures" N. Ramanathan, K. Sundararajan, **R. Gopi,** K Sankaran. J. Phys. Chem. A, 2017, 121 (10), 2121-2120.

4) "Pyrrole Multimers and Pyrrole-Acetylene Hydrogen bonded Complexes Studied in N_2 and *para*-H_2 Matrixes using Matrix Isolation Infrared Technique and computations" Shubhra Sarkar, **R. Gopi**, N. Ramanathan, K. Sundararajan, J. Mol. Struct. 2017, 1149, 387-403.

Poster Presentations:

1) S. Sarkar, **R. Gopi,** N. Ramanathan, K.Sundararajan, "Pyrrole Multimers and Pyrrole-Acetylene Hydrogen bonded Complexes Studied in N_2 and *para*-H_2 Matrixes using Matrix Isolation Infrared Technique and computations" 6th International Conference on Perspectives in Vibrational Spectroscopy, Golden blossom imperial resorts, University of Lucknow, Lucknow, India, 5-8, November, 2016.

R. Gopi

ஊன் கொடுத்த தாய்க்கும்,

உயிர் கொடுத்த தந்தைக்கும்,

சமர்ப்பணம்...

DEDICATED

TO

MY PARENTS…

ACKNOWLEDGEMENTS

The realization of this Ph.D. thesis would not be possible without a kind support and help of a large number of people. And here I would like to thank each one of them.

First of all, I would like to express my sincere gratitude to my supervisor *Dr. K. Sundararajan*. Without his continuous support, understanding, tactful guidance and endless patience, this thesis would not have been possible. Passing on some of his impressive knowledge to me, he helped me to develop independent thinking and research skills. His straightforward approach to problems and his art of imparting knowledge and skills have been instructive and inspirational to me.

I sincerely express my thanks and regards to the doctoral committee members, *Prof. M. Joseph, Dr. T. R. Ravindran,* and *Prof. B. S. Panigrahi* for their valuable suggestions and evaluating my work at each step. Also, I would like to thank my former committee member *Dr. K. Nagarajan, Dr. K. V. G. Kutty and Dr. A. Bharathi* for their support.

My sincere thanks to the Dean of chemical sciences, *Dr. N. Sivaraman and former Deans Prof. S. Anthonysamy and Dr. V. Ganesan* for providing a warm and friendly environment in the Chemistry Group.

It is my duty to thank *former Directors IGCAR,* Dr. *P. R. Vasudeva Rao, and Dr. S.A.V. Satya Murty* and *present Director, A. K. Bhaduri,* for giving me the permission to work at the IGCAR and allowing me to stay at JRF enclave with excellent facilities during my research period. Also, I express my thanks to *Prof. U. Kamachi Mudali, Director, Materials Chemistry & Metal Fuel Chemistry Group, Prof. M. Joseph, Associate Director, Prof. V. Jayaraman, Head, Materials Chemistry Division* and *Prof. K. Sankaran, Head, Analytical Chemistry and Spectroscopy Section* for allowing me to use all the facilities available during my research tenure.

I am grateful for the financial support provided by the Department of Atomic Energy research fellowship scheme from Indira Gandhi Centre for Atomic Research, Kalpakkam.

Special mention goes to most enthusiastic persons in lab *Dr. N. Ramanathan* and *Prof. K. Sankaran*. On a day-to-day basis, I am thoroughly enjoyed my work with them and feeling proud to be associated. I have very fond memories of my time in the spectroscopy section.

I sincerely thank my senior lab-mates *Dr. S. Vijayalakshmi, Dr. Siuli, Mr. R. Sriram, Mrs. Usha Lakshmi, Mrs. Hemalatha, Mr. Shiva Kumar, Mrs. Annapoorani, Mrs. Uma Maheshwari, Mr. Sekar, and Mrs. Deivanayaki.* I would like to thank my comrades *Dr. Pavan kumar Narayanam, Dr. Satendra Kumar, Ms. Shubhra and Ms. Sruthi* for our interesting discussions and for the good times we spent together.

I wish to thank my best friend Dr. Siddarth and his family for helping me get through the difficult times and for all the emotional support, comraderie and scientific discussions.

I would like to thank all my friends for helping and supporting me unconditionally on this long and sometimes difficult journey and for being with me whenever I needed. I can’t list all the names here, but you are always on my mind. The memories and stories from the time we spent together would fill a book thicker than this one.

Last, but most importantly, I would like to express my heartful thanks to my wife, Sumathi, for her patience and love. She encouraged and inspired me every time, teaching to never give up no matter how tough the situation is.

R. Gopi,
Kalpakkam

CONTENTS

SYNOPSIS

Hydrogen bonds (H-bonds) are ubiquitous and one of the most abundant and important inter/intra molecular interactions in nature. They determine the structure, stability and function of chemical and biological systems. Well known examples of H-bonding include O-H···O, and N-H···O interactions. Due to this interaction, the O-H, and N-H stretching bands show large red shift, broadening of peaks, and an increase in infrared intensity; such spectral changes can thus be regarded as a signature of H-bond formation. On the contrary, the C-H bond also acts as proton donor and it is now well established that C-H···O and C-H···π type H-bonds are important in biological and molecular assemblies, in spite of their small binding energies. The hybridization of the carbon in the C-H type H-bonds dictates the strength of the interaction and the corresponding shift in the vibrational wavenumbers. The hydrogen attached to the carbon with 'sp' and 'sp^2' hybridization generally shows a red shift (decreasing wavenumber) in the C-H stretching wavenumber and the interaction energies are greater than the hydrogen attached to the 'sp^3' carbon, which predominantly shows a blue shift (increasing wavenumber). Complexes of haloforms with various Lewis bases (proton acceptors) have been observed spectroscopically in the gas phase, cryogenic liquids, and in solid inert gas matrixes and the vibrational wavenumber shift of the C-H stretching band are found to be dependent on the strength of the proton donor and acceptor.

In $CHCl_3$-fluorobenzene complex, the C-H bond length decreases with concomitant increase in the C-H stretching wavenumber of $CHCl_3$ (blue-shift) and associated decrease in the infrared intensity was observed and these H-bonds were named as "improper blue-shifting hydrogen bond". On the other hand, the $CHCl_3$-NH_3 shows a proper red-shifted H-bonded signature. The C-H type H-bond has been the subject of extensive theoretical studies, and its

spectral signature has been reproduced computationally. However, the underlying mechanisms still not fully understood.

The object of the thesis is to provide the experimental evidence, supported by computations, for the improper blue and proper red-shifted H-bonded complexes. Fluoroform (CHF_3) is a simple molecular model to observe blue-shifted H-bonding and several groups have performed computations on this system with various proton acceptors. Experimental evidence for the blue-shifted H-bonds for the CHF_3 system is sparse and in this thesis, I have studied the blue-shifted H-bonded complexes of CHF_3 with HCl, C_2H_2, H_2O and C_6H_6 using matrix isolation (MI) infrared spectroscopy. Furthermore, red-shifted H-bonds were also studied in the CH_3CN-C_2H_2, CH_3CN-H_2O, C_6H_5CN-C_2H_2, and C_6H_5CN-H_2O. The thesis highlights the experimental and computational studies on the blue and red-shifted complexes and different H-bonded properties such as geometrical parameters, interaction energies, electron densities, hyperconjugative delocalization energy, and calculated vibrational wavenumbers are critically analysed and compared with the experimental wavenumbers.

Chapter 1: Introduction

In this chapter, a concise introduction on blue- and red-shifted hydrogen bonds is presented. Furthermore, a detailed account on the experimental and theoretical studies on the blue- and red-shifted hydrogen bonds by various spectroscopic techniques pertaining to the systems studied in the thesis are discussed.

Chapter 2: Experimental Techniques

This chapter gives a comprehensive account of the experimental and computational methods employed in this thesis work. Matrix isolation infrared spectroscopy is a versatile technique to study the hydrogen-bonded interactions, conformations, reactive and transient intermediates etc. In this technique, the sample molecule of interest is mixed with large excess of inert gas (Ar, Kr, Ne and Xe) in a typical matrix to solute ratio of 1000:1 and

deposited at low temperatures (4 K-12 K). The main components of the matrix isolation technique are: two-stage closed cycle helium cryostat to achieve a low temperature, vacuum chamber, sample handling system, and FTIR spectrometer. In this chapter, the experimental procedures are briefly described.

Computations were carried out for the hydrogen-bonded complexes using Gaussian 09 suite of programs running on a Fujitsu workstation with Xeon processor. Geometry optimizations were performed at B3LYP and MP2 level of theory using 6-311++G(d,p) and aug-cc-pVDZ basis sets. Various properties like structural parameters, interaction energies, vibrational wavenumber and dipole moment were computed at the aforementioned level of theory and basis sets. The interaction energies were corrected separately for zero point energy (ZPE) and basis set superposition error (BSSE) using the procedure outlined by Boys and Bernadi. In order to understand the nature of the blue- and red-shifted H-bonds, Atoms-in-molecules (AIM) theory, Natural bond orbital (NBO) analysis and Energy Decomposition Analysis (EDA) were carried out.

Chapter 3: Blue-shifted hydrogen bonds

This chapter describes the experimental studies on CHF_3 with HCl, H_2O, C_2H_2 and C_6H_6. Experimentally a blue-shift of 6.7 cm^{-1} (CHF_3-HCl), 20.3 cm^{-1} (CHF_3-H_2O), 7.7 cm^{-1} (CHF_3-C_2H_2), and 32.3 cm^{-1} (CHF_3-C_6H_6) was observed in the C-H stretching mode of CHF_3 submolecule in these complexes in Ar matrix. This is for the first time, blue-shifting in the C-H stretching region of CHF_3 was reported for these complexes using matrix isolation infrared spectroscopy. Extensive computations were carried out to compare the experimental vibrational wavenumber and also to explain the genesis of the blue-shift in these complexes.

Chapter 4: Red-shifted hydrogen bonds

This chapter describes the experimental and computational results on the red-shifted hydrogen bond between nitriles (acetonitrile, CH_3CN and benzonitrile, C_6H_5CN) with C_2H_2

and H_2O. Experimentally, a red-shift of 46.8/54.0 and 48.3 cm^{-1} corresponding to 1:1 C_2H_2-CH_3CN and complex were observed in Ar and N_2 matrixes respectively. Computations indicated one minimum for the C_2H_2-CH_3CN with a C-H⋯N interaction. Computations were also performed for the higher complexes of C_2H_2 and CH_3CN. One minimum was found for the 1:2 C_2H_2-CH_3CN complex and two minima for the 2:1 C_2H_2-CH_3CN complexes at all levels of theory. Experimentally, a red shift of 60.3 and 55.0 cm^{-1} corresponding to 1:2 C_2H_2-CH_3CN complex was observed in Ar and N_2 matrixes respectively.

Computations indicated two minima corresponding to the C-H⋯N (global) and C-H⋯π (local) of 1:1 C_2H_2-C_6H_5CN complex, where C_2H_2 is the proton donor in both complexes. Experimentally, a red shift of 50.2 and 44.0 cm^{-1} was observed in Ar and N_2 matrixes for the 1:1 C-H⋯N C_2H_2-C_6H_5CN complex.

Computations showed two types of complexes formed between H_2O with CH_3CN and C_6H_5CN, a linear complex with C≡N⋯H-O interaction and a cyclic complex, in which the interactions are between the hydrogen (of nitriles) with oxygen of H_2O and hydrogen of H_2O with π-cloud of C≡N. Experimentally, a red-shift of 99.4 and 14.1 cm^{-1} in the $\upsilon_1$and υ_3 stretching region of H_2O and a blue-shift of 8.3 cm^{-1} in the C≡N stretching region of nitriles in Ar matrix were observed corresponding to CH_3CN-H_2O linear complex. For the 1:1 linear C_6H_5CN-H_2O complex, experimentally a red-shift of 66.3 and 24.2 cm^{-1} was observed in the $\upsilon_1$and υ_3 stretching region of H_2O and a blue shift of 10.3 cm^{-1} in the C≡N stretching region of nitriles in Ar matrix. Onsager self consistent reaction Field (SCRF) model was used to explain the effect of the matrixes on the complexes.

Chapter 5: Summary and Conclusion

This chapter summarizes the results presented in the thesis. Various computed results such as geometrical parameters, interaction energies, hyperconjugative interactions, second order perturbation energies, electron densities at the intermolecular bond critical point (BCP),

shift in the computed and experimental vibrational wave numbers are compared.

Among the blue-shifted complexes, the change in the C-H bond length correlates well with the corresponding experimental/computed blue-shift in the C-H stretching wavenumber of CHF_3 submolecule and for the red-shifted complexes the change in the C-H and O-H bond lengths of C_2H_2 and H_2O, respectively, correlates well with the experimental/computed shift in the C-H and O-H stretching wavenumbers. Interaction energies were found to increase in the order CHF_3-HCl< CHF_3-C_2H_2< CHF_3-H_2O< CHF_3-C_6H_6. Comparison of interaction energy and the experimental blue-shift in the C-H stretching mode of CHF_3 sub-molecule for the different complexes shows a linear correlation. Similarly, for the red-shifted complexes the interaction energy increases in the order C_2H_2-C_6H_5CN< C_2H_2-CH_3CN< H_2O-C_6H_5CN< H_2O-CH_3CN, which correlates well with the shift in the C-H, O-H and C≡N stretching wavenumbers.

Likewise, interaction energies show a good correlation with the shift in the experimental vibrational wavenumber, topological properties such as electron density $\rho(r_c)$ and Laplacian of electron density $\nabla^2\rho(r_c)$ of the blue- and red-shifted complexes investigated in this work. It is well known that topological parameters are quite useful in delineating H-bonding interactions. The interaction energy of the blue-shifted complexes increase in the order of CHF_3-HCl < CHF_3-C_2H_2 < CHF_3-H_2O < CHF_3-C_6H_6, which is consistent with the gas phase basicity of the proton acceptor. Similarly, the proton accepting ability of the red-shifted complexes was found in the order HCN < CH_3CN < C_6H_5CN with C_2H_2 and H_2O. Shift in the computational vibrational wavenumbers of the blue- and red-shifted complexes gives a linear correlation with experimental wavenumbers. NBO analysis showed that the electron population of the antibonding orbital σ*(C-H) of CHF_3 for the different complexes decreases in the order $\sigma^*(C\text{-}H)_{CHF3\text{-}HCl}$ > $\sigma^*(C\text{-}H)_{CHF_3\text{-}C_2H_2}$ > $\sigma^*(C\text{-}H)_{CHF_3\text{-}H_2O}$ > $\sigma^*(C\text{-}H)_{CHF_3\text{-}C_6H_6}$, which eventually leads to shortening of the C-H bond with the

concomitant blue-shift in the C-H stretching mode of CHF_3. Clearly, the subtle balance between different delocalization interactions in the complexes is responsible for the experimental observation of the blue-shift. The second order perturbation energy was found to decrease in the order CHF_3-C_6H_6 > CHF_3-H_2O > CHF_3-C_2H_2 > CHF_3-HCl, which is consistent with the corresponding experimental/computed blue-shift observed in these complexes. In the case of red-shifted complexes, the hyperconjuagative interaction between the donor and acceptor orbitals in the nitrile-acetylene complexes is increasing in the order HCN-C_2H_2 < C_6H_5CN-C_2H_2 < CH_3CN-C_2H_2, which correlates well with the corresponding red-shift in the C-H stretching vibrational wavenumber of C_2H_2 sub-molecule. A similar trend is observed for the O-H symmetric stretching vibrational wavenumber of H_2O submolecule in the nitrile-water complexes: HCN-H_2O< C_6H_5CN-H_2O< CH_3CN-H_2O. Energy decomposition analysis showed the electrostatic interaction contribution to the total bonding energy is significant for the red-shifted when compared to the blue-shifted complexes.

LIST OF FIGURES

LIST OF TABLES

LIST OF ABBREVIATIONS

AIM	Atoms-in-Molecules
ADF	Amsterdam Density Functional
AR	Analytical Reagent
B3LYP	Becke-3-Parameter-Lee-Yang-Parr functional
BCP	Bond Critical Point
BLYP	Becke-Lee-Yang-Parr functional
BSSE	Basis Set Superposition Error
CCSD(T)	Coupled-Cluster methods with Single-, Double- and Triple-excitation operators
CP	Counter poise
CT	Charge transfer
DFT	Density Functional Theory
2D	2Dimension
DTGS	Deuterated Triglycine Sulphate
EDA	Energy Decomposition Analysis
EDT	Electron Density Transfer
ESR	Electron Spin Resonance
HF	Hartree-Fock
IUPAC	International Union of Pure and Applied Chemistry
K	Kelvin degrees
kJ/mol	Kilojoules per mol
LIF	Laser Induced Fluorescence
MO	Molecular Orbital
MP2	Møller-Plesset second order perturbation
MCT	Mercury Cadmium Telluride
NAO	Natural Atomic Orbital
NBO	Natural Bond Orbital
NHO	Natural Hybrid Orbital
NLMO	Natural Localized Molecular Orbital
NMR	Nuclear Magnetic Resonance
***p*-H_2**	*Para*-Hydrogen
PCM	Polarizable Continuum Model
QST2	Quasi-Synchronous Transit method with two geometry input
QST3	Quasi-Synchronous Transit method with three geometry input
SCRF	Self Consistent Reaction Field
TS	Transition State
vdW	van der Waal
ZPE	Zero Point Energy

CHAPTER 1

INTRODUCTION

Hydrogen bonds are ubiquitous and one of the most interesting, abundant and important inter/intra molecular interactions in nature that influences a variety of chemical and biological processes [1]. The weak forces such as hydrogen bond and van der Waal's forces govern their mutual interaction between the atoms and alter the physical and chemical properties of the molecules. It is well documented that the hydrogen bonding interaction is important for the structure and function of biomolecules, such as protein folding, binding, and enzyme catalysis [1-4]. The hydrogen bonding interactions in nucleic acids play a crucial role in the double helical structure of DNA and RNA along with stacking interactions, facilitating molecular recognition via replication processes and protein synthesis [2-34]. Extensive theoretical methods have been used to derive information about the hydrogen bonding in DNA base pairing [5-9].

Hydrogen bonds are the most notable 'weak' interactions encountered in solid, liquid and gas phases. The simple definition of hydrogen bond is an attractive interaction between two molecular moieties in which at least one of them contains a hydrogen atom that is bonded to other structural moiety (X-H⋯A). In simple words, hydrogen bond is an attractive interaction between a hydrogen donor X-H and a hydrogen acceptor A. According to the classical definition, X and A atoms are electronegative (N, O, F, Cl, Br) which show a very high electrostatic interaction between H and A [10-13]. The electrostatic nature of hydrogen bond was first proposed by Linus Pauling, where the H atom is immersed in an electron cloud of A and the distance between H⋯A becomes shorter than the sum of van der Waals radii of H and A [10]. The electrostatic nature of hydrogen bonds is observed in N-H⋯O, O-H⋯O and O-H⋯N type of interaction [10] and it is explained on the basis of natural bond

orbital (NBO) analysis, where there is a transfer of lone of pair of electron from non-bonding orbital of A to the antibonding orbital of X-H, resulting in (n)A → σ*(X-H) charge transfer interaction [14]. The strength of the hydrogen-bonded interaction varies from -0.2 to -40 kcal/mol [15].

The historical perspective of hydrogen bonds is extensively described in several books and articles [10-13,16-20]. Furthermore, the definition of hydrogen bonding keeps changing over time starting from Werner, Pauling, Steiner and Saenger to Pimentel and McClellan [10,11,21,22].

Desiraju coined the definition of the hydrogen bond as ‘‘a conventional hydrogen bond may be represented as X-H⋯Y-Z, where the three dots denote the bond, which essentially is weaker compared to a permanent covalent bond. X-H represents the hydrogen bond donor. The acceptor may be an atom or an anion Y, or a fragment or a molecule Y-Z, where Y is bonded to Z. In specific cases X and Y can be the same with both X-H and Y-H bonds being equal. The acceptor is an electron-rich centre which can be a lone pair in Y or π-bonded pair in Y-Z”. Furthermore, the entire unit ‘X-H⋯Y-Z’ represents a hydrogen bond [23].

Finally, IUPAC task group modified the earlier definition of hydrogen bond and gave a new definition “The hydrogen bond is an attractive interaction between a hydrogen atom from a molecule or a molecular fragment X-H in which X is more electronegative than H, and an atom or a group of atoms in the same or a different molecule, in which there is evidence of bond formation” [24].

Hydrogen bonds are of two types a) Intermolecular hydrogen bonding, where the association is between two different species to form a complex and b) Intramolecular hydrogen bonding, where two or more groups within the same molecule are associated. The formation of intramolecular hydrogen bond depends on the favourable orientation of the

atoms in the same molecule.

G. A. Jeffrey classified the hydrogen bonding based on the values of enthalpies into strong, moderate and weak hydrogen bonds [12]. The strength of the strong hydrogen bonding interactions ranges from 15 to 40 kcal/mol. For the moderate and weak hydrogen bonds, the strength varies from 4-15 to 1-4 kcal/mol, respectively.

Strong and weak hydrogen-bonded interactions play a dominant role in the crystal engineering. Antigens are bound to antibodies through weak and non-covalent hydrogen bonded interactions [25]. Hydrogen bond is one of the main forces responsible for the spatial organization of supramolecular assembly [26,27]. The role of weak hydrogen-bonded interactions in various molecules and crystals has been discussed in great detail by Desiraju and Steiner [1].

There are several techniques such as infrared (IR), NMR [28], microwave [29], far infrared (FAR-IR) [30], terahertz [31], electronic [32], 2D-IR [33], mass detected IR [34], Raman [35], UV-IR and UV-UV double resonance spectroscopy [36,37] were used to study H-bonds [11]. Recently, ultra cold (T = 0.37-0.15 K) helium nano droplet, a new technique, has been employed to synthesize molecular complexes including hydrogen-bonded complexes [38].

Among several spectroscopic techniques that may be used to characterize the H-bonding, the most sensitive and widely used is the infrared (IR) spectroscopy [11,12]. The IR technique probes the shift in vibrational wavenumber of the hydrogen-bonded complex with respect to the monomer.

For the X-H⋯Y, the intermolecular vibrations mainly occur either in the X-H molecule or in the Y molecule that appears in the mid-IR region (400-4000 cm^{-1}), that constitute the hydrogen-bonded complex. The formation of H-bonds is often associated with the change in the infrared intensity (change in the electric dipole moment), which is due to

the relatively small displacement of electrons that accompanies an increase of the X-H distance in X-H···Y. Intermolecular vibrations due to H-bonds in X-H···Y that appear in the FAR-IR region (50-400 cm^{-1}) are due to the relative vibrations of the two parts X-H and Y. These bands disappear when these H-bonds gets disrupted and subsequently provide information about the nature of H-bonds [39].

Despite many advantages, the infrared method is not free from drawbacks. The effects of weak hydrogen bonds on vibrational spectra are not always as clear as for strong bonds and can be quite dissimilar for different kinds of weak hydrogen bond. Even for relatively simple systems, spectral complexity can prevent proper interpretation; this is the case in particular for systems exhibiting vibrational coupling. In consequence, the weak C-H donor types such as methyl ($-CH_3$), $=CH_2$ and phenyl (-Ph) are difficult to study with IR spectroscopic methods. With the help of high-resolution technique such as Matrix Isolation coupled with the infrared technique, it is possible to overcome the difficulty to study weak interaction.

Classical hydrogen bonding is characterized by an elongation of the X-H bond, a decrease of its stretching wavenumber and an associated increase in intensity of the spectral band [11,12,24]. The origin of the conventional hydrogen bonding (X-H···Y) is well understood and is explained by electron density transfer (EDT) from lone electron pairs of the proton acceptor Y to the σ*-antibonding orbital (hyperconjugation) of the X-H proton donor. The increase of electron density (ED) in the σ*-antibonding orbital is accompanied by a weakening of the bond, its elongation and a concomitant lowering of the X-H stretching frequency (red shift). According to Guerra et al. hyperconjugation of the s and p orbitals only marginally contributes to hydrogen bonding, which also holds true for weak hydrogen bonds containing X-H···F and C-H···Y motifs [40, 41]. For a long time, the red shift has

been considered as a “fingerprint” of hydrogen bonding and a correlation is made between red shift and stabilization of the hydrogen-bonded interaction.

In some systems, hydrogen bonding results in unusual blue shifting especially when hydrogen is connected to sp^3 and sp^2 hybridized carbon, as in $CHCl_3$/CHF_3/C_6H_6. In contrast to the bond lengthening and a red shift under normal circumstances, the C-H bond exhibits bond shortening and a blue shift. The first experimental proof for the blue-shifted hydrogen bonding was reported by Trudeau et al. [42-44]. Hobza et al. first coined the term “anti-H-bond” for the blue-shifted H-bond and confirmed the existence of the hydrogen bonding in the benzene dimer $(C_6H_6)_2$, C_6H_6-CH_4 and C_6H_6-$CHCl_3$ complexes using correlated *ab initio* computations [45-47]. Later, the “anti-H-bond” was renamed by the same group as “improper H-bond” or “blue-shifted hydrogen bond” and this term are now commonly used. Hobza et al. using double-resonance IR ion-depletion spectroscopy reported blue-shifted hydrogen bonding in $CHCl_3$-C_6H_5F complexes [47]. Riemann et al. found experimental evidence for the blue shift in the C_6H_5F-CHF_3 and other related complexes using IR-ion depletion spectroscopy [48,49]. Furthermore, the same group used a supersonic beam coupled with IR vibrational pre-dissociation spectroscopy confirmed the existence of blue-shift in the C-H stretching wavenumber of $CHCl_3$/CHF_3 complexes. Van der Veken and co-workers using IR spectroscopy studied the blue-shifted hydrogen bonding in $HCCl_{3-x}F_x$ complexes with different oxygen containing bases in cryo solutions [50-58]. Using matrix isolation IR spectroscopy, Ahokas et al. studied the blue-shifted hydrogen bonding in formyl fluoride dimers [59]. The first experimental proof for the intramolecular blue-shifted hydrogen bonding was reported by Matsuura et al. [60]. Using IR and Raman spectroscopy, Craig et al. observed a blue shift in the C-H stretching region of cis-3,4-difluorocyclobutene in the liquid phase [61].

CHF_3 is a simple molecular model to observe the blue-shifted hydrogen bonding and

several groups have performed computations on this system with various proton acceptors [62-77].

Paulsen and Barnes using matrix isolation technique examined the infrared and Raman spectra of trifluoromethane and trichloromethane mixed with water and ammonia in argon and nitrogen matrixes [78]. Formation of the CHF_3-H_2O complex was evidenced in the υ_1, υ_2 and υ_3 modes of H_2O submolecule but they could not observe a distinct blue-shifted feature in the C-H stretching region of CHF_3 submolecule in the complex. Moreover, in their work, computation on the CHF_3-H_2O complex was not reported to correlate with the experimental vibrational wavenumbers. The structure of the CHF_3-H_2O complex was well studied by several theoretical groups [63-71,79,80]. All these studies showed that the complex has a near linear geometry (∠C-H···O=~175º) with C-H···O interaction. Anharmonic vibrational wavenumber calculation performed at MP2/6-311++G(d,p) level of theory showed a blue shift 33 cm^{-1} in the C-H stretching wavenumber of the CHF_3-H_2O complex [63].

It is important to point out that the acceptor of the CH···π interaction is not only limited to an aromatic π system but also to other unsaturated functional groups, such as C≡C, C=C, and C=O etc [81]. During the last two decades, several experimental studies have been reported to support the existence of this non-covalent attraction [4]. Even though, C-H···π interaction appears similar to conventional O-H···π and N-H···π interactions, there are some striking differences. The stabilization energy of the C-H···π interaction is much smaller than the interactions involving electronegative oxygen and nitrogen atoms. Another significant difference is the shift of the C-H vibrational mode in the C-H···π complex (where the proton attached to the sp^3 hybridized carbon), which is towards higher vibrational wavenumber in comparison to usual red shift in O-H and N-H stretching vibrational modes. The hydrogen attached to a sp^3 carbon atom as well as to other elements such as Si, P, and N shows blue

shifting [82]. Oliveira et al. using QTAIM method analyzed the blue-shifted hydrogen bonds in the weakly bound complexes [83]. Several groups have performed experimental and theoretical studies on the C_6H_6-CH_4 (C-H···π) complex [84,85]. Herrebout and co-workers studied the H-π complexes of halothane with C_6H_6 and C_6D_6 using infrared and Raman spectra of liquefied krypton solutions [86]. They also examined C-X···π (X= Cl, Br, I or H) and C-H···π hydrogen bonding interaction of CF_3X with ethene and propene in liquid argon and weak C-H···π hydrogen bonded complexes of sevoflurane and benzene in liquid xenon [87,88]. Shirhatti and Wategaonkar experimentally identified the blue-shifted hydrogen bonding in a variety of complexes such as 3-methylindole-CHX_3, p-cresol-CHX_3 and p-cyano phenol-CHX_3 using IR-UV double resonance spectroscopy [89].

Lopez et al. studied the CHF_3-C_6H_6 complex by Fourier Transform Microwave Spectroscopy (FTMW). From the pure rotational spectra of the ^{12}C and ^{13}C-C_6H_6 species, they identified the structure of the CHF_3-C_6H_6 C-H···π complex [90].

Several theoretical groups have studied the structure of the CHF_3-C_6H_6 complex and found that it has a T-shaped geometry with the corresponding blue shift in the C-H vibrational mode of the CHF_3 submolecule in the complex [91-94]. Isenor et al. systematically studied the interaction of CH_4, CHF_3, $CHCl_3$, and $CHBr_3$ with C_6H_6 and C_6F_6 at the MP2/6-31G(d) and MP2/6-311++G(2d,p) levels of theory and found that in the CHF_3-C_6H_6 complex, the C-H stretching mode of CHF_3 is blue-shifted by ~28 cm^{-1} [95].

Sundararajan et al. studied the C-H···π interaction in $CHCl_3$-C_2H_2 and CHF_3-C_2H_2 systems using matrix isolation infrared spectroscopy and *ab initio* calculations [96,97]. Computations performed at MP2/aug-cc-pVDZ level of theory indicated two minima for the 1:1 CHF_3-C_2H_2 complex, with C-H···π complex being the global minimum, where CHF_3 is the proton donor. The second minimum corresponded to a relatively less exothermic C-H···F complex. Experimentally, the formation of 1:1 CHF_3-C_2H_2 C-H···π complex A was

identified from the shifts in the vibrational modes involving C_2H_2 submolecule in N_2 and Ar matrixes. However, the blue-shifted feature could not be observed in the C-H stretching region of CHF_3 submolecule for the C-H···π complex in both the matrixes.

Among the several explanations proposed for the blue shifting of vibrational wavenumbers, a few have gained considerable attention. Van der Veken, Hobza and co-workers suggested that the contraction of an X-H bond results in a blue shift when a transfer of lone pair of electron density occurs mainly to atoms linked to X rather than to the X-H σ* orbital (X-carbon) [50]. Based on the analysis of a number of complexes that resulted in blue shifting of the vibrational wavenumber, Hobza and co-workers provided an alternative explanation. The blue shift is observed in complexes where electron transfer occurs mainly to the non-participating part of the proton donation, thereby leading to the structural rearrangement of the proton donor resulting in the contraction of the C-H bond [65,75,76]. Alabugin et al. proposed a new theory for the C-H bond length change in the blue-shifted H-bonds based on re-hybridization. The hyper-conjugative interaction and re-hybridization act in opposite directions, the former being responsible for C-H bond elongation and the latter making the C-H bond shorten. This re-hybridization was found to be responsible for an increase in the %s character of the carbon atom in the complex [68]. Recently, Joseph and Jemmis provided an explanation for the blue- or red-shifted H bonds based on electron affinity of atoms involved in the hydrogen bonding [77].

Nitrile groups are used as IR probes in biomolecules. Furthermore, they are chemically stable and have relatively high extinction coefficients [98]. Acetonitrile, CH_3CN has a unique properties such as high dielectric constant and remarkable miscibility with a range of ionic and polar solvents [99], which makes CH_3CN as a solvent of choice for a variety of organic synthesis. CH_3CN is a simple organic nitrile detected in the gas phase in interstellar clouds [100]. CH_3CN is also used as a mobile phase in HPLC and LC-MS.

CH_3CN has been extensively used in synthetic organic chemistry and enormous literature on this area has been reported. Earlier, Freedman and Nixon investigated the infrared spectra of CH_3CN in solid argon matrix [101]. Later, Kim and Kim re-investigated the vibrational spectra of CH_3CN using Fourier transform infrared spectra and made precise assignments of monomers, dimers and higher multimers of CH_3CN [102]. Givan and Loewenschuss studied the Raman spectrum of CH_3CN using matrix isolation spectroscopy [103]. Coussan et al. studied the CH_3OH-CH_3CN complexes trapped in Ar and N_2 matrixes. On photolysis, they observed both hydrogen-bonded homo and hetero aggregates of methanol in these matrixes. Further, these aggregates are reported to be better formed in an Ar than in N_2 matrix [104]. Kryachko and Nguyen theoretically studied the hydrogen-bonded complexes of phenol and CH_3CN [105]. The computational results were corroborated with the experiments [106-109]. From the computations, they predicted that phenol and CH_3CN form 1:1 σ- and π-type complexes, where the former is more stable than the latter. The π-type structure becomes more stable when one more acetonitrile molecule interacts with 1:1 phenol-CH_3CN complex. Phillips et al. studied the vibrational spectra of CH_3CN-BF_3 complexes in solid argon [110]. Later, Shimizu et al. studied the matrix effects on the vibrational spectra of the CH_3CN-BF_3 complex in solid matrixes of Ar, N_2, and Xe [111].

Ahm and Lee computationally studied the σ- and π-type hydrogen-bonded complexes of acetonitrile-water clusters. They found at MP2/6-31+G(d,p) level of theory the π-type complex is slightly lower in ZPE corrected energy by 0.11 kcal/mol while the σ-type complex is lower in energy by 0.09 kcal/mol at MP2 level of theory using aug-cc-pVDZ and 6-31G+(d,p) basis sets [112].

Mixtures of CH_3CN and water are popular solvents and have been studied extensively both experimentally and theoretically [113-118]. Rutkowski et al. studied the formation of 1:1 complexes between acetylene and trimethylamine in liquefied krypton

solvent. They observed red shift in the C-H mode of C_2H_2 submolecule and blue shift in the CN stretching mode of trimethylamine submolecule in the complex. The experimental frequencies were corroborated with MP2/6-311++G(2d,2p) level of theory [119]. Domagala and Gabrowski performed *ab initio* computations on the hydrogen-bonded complexes between hydrogen cyanide HCN···HF and acetylene C_2H_2···HF using B3LYP and MP2 levels of theory with 6-311++G(d,p) basis set. They found that π-electrons of acetylene act as a proton accepting centers and the C_2H_2···HF complex forms a T-shaped structure whereas in the HCN···HF complex, the nitrogen atom in the hydrogen cyanide molecule acts as a proton acceptor centre but not π-electrons [120]. Ault et al. reported photochemical reaction of CH_3CN with $CrCl_2O_2$ and $OVCl_3$ and the product was trapped in an Ar matrix. The formation of 1:1 complex was identified using UV/Vis spectroscopy. When the matrix was irradiated with light of λ>300 nm, new features in the infrared spectra was observed and assigned for $ONCCH_3$ complexes of CH_3CN n-oxide with $CrCl_2O$ and VCl_3, respectively. Identification of these species was supported by extensive isotopic labelling (^2H and ^{15}N), and computations performed at B3LYP/6-311++G(d,2p) level of theory [121]. Suzuki et al. studied the 1:1 hydrogen-bonded complexes of CH_3CN with BF_3 in Ar, N_2 and Xe matrixes. The experimental observed shift agreed well the calculation performed at B3LYP/6-311++G(d,p) level of theory [122]. Samet et al. studied the C-H···N hydrogen-bonded complexes of pentachlorocyclopropane (PCCP) with the bases acetonitrile, ammonia, monomethyl amine and dimethyl amine isolated in argon matrixes at 10 K. Both IR spectroscopy and DFT computations supported the formation of 1:1 complexes between PCCP with different bases which were evidenced by the shift in the vibrational modes of PCCP and base submolecule [123].

Allamandola et al. studied 16 nitriles and related compounds in Ar and H_2O matrixes. The strong C≡N stretching vibrations of these compounds are probed using vibrational

spectroscopy in matrixes. The absorption band of these nitriles in Ar and H_2O matrixes are then used to facilitate the search for these features observed by Infrared Space Observatory (ISO) [124]. Several groups studied the C-H⋯N interactions both by experimental and theoretical methods [125-128]. Recently, Zins and Krim studied the formation of 1:1 complex between CH_3CN and formic acid (HCOOH) in neon matrix. The formation of the 1:1 complex is evidenced in the modes corresponding to the HCOOH and CH_3CN submolecules. *Ab initio* computations performed at MP2 level of theory using 6-31++G(d,p) and aug-cc-pVTZ basis sets gave one minima corresponding to the 1:1 and 2:1 complex and two minima for the 1:2 complex. Experimentally, they also observed 2:1 and 1:2 CH_3CN-HCOOH complexes in Ne matrix. Furthermore, they have photolysed the Ne matrix using VUV photons. The photochemical reaction induces the formation cyanomethanoic acid [129].

Interaction of CH_3CN with H_2O was studied extensively by many theoretical groups. Ajay Chaudhari and Shyi-Long Lee using DFT/6-31+G(d) level of theory studied the interaction of CH_3CN with one, two, and three water molecules. For the 1:1 CH_3CN-H_2O complex, it was found that the cyclic structure is less stable than open structure [130].

Canuto et al. performed *ab initio* computations on the CH_3CN⋯H_2O complex to obtain the structure, vibrational frequencies, Rayleigh and Raman activities including light scattering depolarization and binding energies. All the theoretical models showed shortening of the CN distance, leading to a blue shift of around ~15 cm^{-1} in the CN stretching mode. In the Raman spectrum, the depolarization due to the intense CN stretching vibration was increased by 20% after the hydrogen bond formation. Further, there was a large red shift of 75 cm^{-1} observed in the OH mode of water, which leads to an intensification of the Raman scattering activity [131].

Imre Bako et al. investigated the structure of CH_3CN-H_2O mixture using *ab initio*

computations, molecular dynamics and X-ray Diffraction techniques. Computations showed two types of complexes; a) Hydrogen-bonded complex between the nitrogen of CH_3CN and hydrogen of H_2O b) CH_3CN and H_2O molecules are in side-by-side anti dipole arrangement. Both the complexes were minima on the potential energy surface, which have nearly the same interaction energy. They also confirmed the formation of micro heterogeneity in the CH_3CN-H_2O system [132].

Masaaki Tabata et al. studied the liquid structure of CH_3CN-H_2O using X-ray Diffraction and Infrared technique. They observed due to the dipole-dipole interaction between water and CH_3CN-H_2O, CH_3CN completely miscible with water at all concentration ratios. Furthermore, they found that CH_3CN-H_2O and water clusters co-exist, as micro heterogeneity occurs in CH_3CN-H_2O mixtures [133].

Chaban studied the interaction of three nitrile molecules, cynamide (H_2N-C≡N), CH_3CN and amino acetonitrile (H_2N-CH_2-C≡N) with water molecules using second-order Møller-Plesset perturbation theory with triple-ξ basis sets. For the CH_3CN-H_2O system, *ab initio* computations identified two equilibrium geometries. The lowest energy complex was the one where the hydrogen of water molecule is bound to the C≡N end of the nitrile molecule through hydrogen bond and the second complex has two weak hydrogen bonds between CH_3CN and H_2O [134].

Spectroscopic studies of weak complexes isolated at low temperatures have provided a wealth of information on the structures and dynamics, which paved way to understand the macroscopic phenomena.

Benzonitrile (C_6H_5CN) is a prototypical system for an aromatic molecule with a cyano group, which forms a key element in many bio-molecular systems [135,136]. C_6H_5CN has a high dielectric constant (ε =26.0), and it is miscible with a range of ionic and polar solvents [99]. C_6H_5CN is widely used as a precursor and considered to be a useful solvent in

organic synthesis. In view of its wide uses in chemistry, the spectroscopic studies on C_6H_5CN are extensive. C_2H_2 and C_6H_5CN are used as a starting material for the preparation of pyrimidines and pyridines [137].

Green and Harrison studied the infrared and Raman spectra of C_6H_5CN in the vapor phase and assigned its vibrational features [138,139]. Jakobsen reported the infrared and Raman spectra of isotopically substituted liquid C_6H_5CN-d_5 and subsequently assigned its vibrational features [140]. Hoops and Ault studied the photochemical reactions of chlorobenzene, α,α,α-trifluoro toluene, benzonitrile and nitrobenzene with $CrCl_2O_2$. The matrix isolation infrared technique and theoretical calculations were used to identify the photoproducts. Photo-irradiation resulted in oxygen atom transfer, the formation of complexes between the corresponding cyclic ketone derivatives and $CrCl_2O_2$. In C_6H_5CN, on irradiation, the C-H group gets activated and insertion of oxygen atom into the C-H group resulted in the formation of cyanophenol and the interaction of the cyanophenol with $CrCl_2O_2$ was observed [141].

Several groups have studied the C-H⋯N interactions both by experimental and theoretical methods [125,126,142,143]. Weak hydrogen-bonded complexes of C_2H_2 with CHF_3, $CHCl_3$, C_2H_4, C_6H_6, C_6H_5OH, CH_3CN, C_5H_5N, and CH_3OH were studied using matrix isolation infrared spectroscopy and *ab initio* methods [96,97,144-148].

Kobayashi et al. studied the van der Waals complexes of C_6H_5CN with Ar, Kr, N_2O, CHF_3, and H_2O using free jet Laser induced fluorescence (LIF) technique [149,150]. The LIF spectra showed a red shift for the complexes relative to that of C_6H_5CN monomer. For the C_6H_5CN-H_2O complex was predicted to be a planar structure in which the oxygen atom lies in the plane of the benzene ring. Two such locations are possible for the oxygen atom; collinear to the -C≡N bond or ortho to the C-H bond. The former is the hydrogen bonding between CN and H_2O and the latter is the interaction between electron deficient ortho-

hydrogen and electron rich oxygen atom. The cyclic structure is more preferred due to dipole–dipole interaction between C_6H_5CN and H_2O molecule. The results from rotational spectra concluded that the structure of the C_6H_5CN-H_2O complex is planar and has a ring like structure showing double hydrogen-bonded arrangement with a O-H bond length of 2.472 Å, and a N-H bond length of 2.660 Å [151,152]. Helm et al. investigated the structure of C_6H_5CN-H_2O complex with microwave and highly resolved optical spectroscopy. From the rotational constants, they assigned that the water molecule is bound sidewise and in-plane to the aromatic ring of the C_6H_5CN by two H-bonds: one a π-type H-bond to the CN group and other an σ-type H-bond to the CH group in ortho position [153]. Later, Melandri et al. performed free-jet absorption rotational technique and confirmed the C_6H_5CN-H_2O complex forms a ring like structure [154].

Mikami et al. studied the size selected clusters of C_6H_5CN-$(H_2O)_{n=1-3}$ and C_6H_5CN-$(CH_3OH)_{n=1-3}$ using time resolved Raman-UV double resonance combined with fluorescence detection [155-158]. Kryachko and Nguyen studied the hydrogen bonding interaction between C_6H_5CN-H_2O and C_6H_5CN-$(H_2O)_2$ complexes using hybrid B3LYP density functional in conjunction with 6-311G(d,p) and aug-cc-pVDZ basis sets. Computations gave two most stable and nearly iso-energetic complexes; the ring conformer $[BZCN\text{-}w_1]_1$ and the linear one $[BZCN\text{-}w_1]_2$. They have discussed the mechanism of the large-amplitude dynamics of the water moiety around the C_6H_5CN-H_2O potential energy minima and compared the computed results with the experiments conducted by Mikami's group and gave evidences for the formation of the $[BZCN\text{-}w_1]_1$ ring complex [159]. Borst et al. studied the 1:1 complexes of C_6H_5CN with H_2O, NH_3, CH_3OH, CH_3CN, and C_6H_5CN dimer using high-resolution fluorescence excitation spectra in the gas phase [160].

Several theoretical groups have performed calculations on the C_6H_5CN-H_2O system and found that the C_6H_5CN and H_2O form iso-energetic cyclic and linear type complexes.

Gas phase experiments coupled with fluorescence and IR-UV double resonance technique revealed the formation of the cyclic complex. It should be mentioned that matrix isolation infrared technique offers a unique advantage of trapping and studying the iso-energetic complexes. For example in C_2H_2-CH_3OH [148] and C_2H_2-C_6H_5OH [146] system both the C-H⋯O and O-H⋯π complexes were experimentally observed.

1.1 Scope of the thesis

The main objective of this thesis is to study the blue-shifted hydrogen bonding in CHF_3-HCl, CHF_3-H_2O, CHF_3-C_6H_6, and CHF_3-C_2H_2 complexes and the red-shifted hydrogen bonding in CH_3CN-C_2H_2, CH_3CN-H_2O, C_6H_5CN-C_2H_2, and C_6H_5CN-H_2O systems.

Experimentally, the blue-shift in the C-H stretching region of the CHF_3 submolecule in HCl, H_2O, C_6H_6 and C_2H_2 complexes and the red-shifted feature in the H_2O and C_2H_2 submolecule in CH_3CN and C_6H_5CN complexes were discerned using matrix isolation infrared spectroscopy. The experimental observations were compared with the *ab initio* computations carried out for these complexes at B3LYP and MP2 levels of theory using 6-311++G(d,p) and aug-cc-pVDZ basis sets. Atoms in Molecules (AIM), Natural Bond Orbital (NBO) and Energy Decomposition (EDA) analyses for the blue- and red-shifted complexes were carried out to understand the nature of the interaction in these complexes.

CHAPTER 2

EXPERIMENTAL AND COMPUTATIONAL METHODOLOGY

This chapter is intended to provide an overview of the experimental and computational methods employed in this thesis work.

2.1 Experimental method

2.1.1 Matrix isolation infrared spectroscopy

Matrix isolation (MI) is a technique where the molecules of interest are trapped in solid inert gas matrixes at high dilution. This technique was initially developed by G. C. Pimentel in the mid-1950s for the study of free radicals [161]. Matrix isolation infrared spectroscopy can be used to study the hydrogen-bonded interactions, conformations in molecules, reactive and transient intermediates etc. In this technique the sample molecules is mixed with large excess of inert gas (Ar, Kr, Ne or Xe) in a typical solute to matrix ratio of 1:1000 and deposited at low temperatures (4K/12K). The trapped species in the transparent solid matrix are probed by a variety of techniques such as infrared (IR), fluorescence, electron spin resonance (ESR) etc. and among these methods, the most popular one is infrared technique. A comprehensive account of matrix isolation technique is available in several books and in the literature [162-166].

The advantages of using the MI technique are sharp peaks with smaller line width when compared with the solid, liquid and gaseous spectra. The reduction in line width is due to the isolation of the molecules in rare gas matrixes, which prevents the intermolecular interactions between the molecules. Furthermore, the low temperature and rare gas cage ceases the rotational motion of the molecules, eliminate Doppler and collision broadening and it ensures only the lowest ro-vibronic levels of the molecule being populated. A few of the studies where MI technique has been employed are described below:

• Matrix interactions -The interaction of matrix with the guest molecules are probed to gain a complete understanding of the matrix environment.

• Vapor species studies - Samples are heated under vacuum thermally (pyrolysis), the vapor species produced is then co-condensed with a matrix gas and deposited at low temperature. The species are then characterized.

• Characterization of radical and novel species -Production of radicals by laser ablation process (focusing of a high-power laser onto a sample) and the radicals thus generated are deposited along with the matrix gas and probed by a variety of spectroscopic techniques. Electron gun is also used to produce radicals.

• Reactions in matrixes-Reaction between the trapped species are brought about by selectively exciting the species using a particular wavelength of light or by broad band photolysis (light energy). In some case the reaction between the species is facilitated by annealing the matrix (thermal energy). The reacted species are probed spectroscopically.

Apart from these studies, the matrix isolation infrared spectroscopy is used to study conformations, weak interactions such as hydrogen and halogen bonding interactions.

2.1.2 Matrix gases

The matrix gas used in the MI technique should have important properties: a) It should be chemically inert b) It must be easily available with high purity and it should be transparent in the wavelength region of interest c) It should have sufficient vapor pressure at room temperature and able to form rigid matrix at low temperature and prevent diffusion of guest molecules. Rare gases such as Ne, Ar, Kr, Xe and diatomic gases N_2 meet the above criteria and hence are commonly used as matrix gases. Recently, *p*-H_2 gas has emerged as a promising matrix material for use in MI technique [167-169].

Eventhough the matrix gases are considered to be inert, in reality, these gases do interact with the guest molecules in a variety of ways and perturbs the spectrum of the

trapped species. These perturbations are manifested in the spectrum as multiple peaks, shifts in the peak absorption and broadening of peaks. Detailed account of the matrix effects is discussed in various articles [170-174]. In an extreme case, the matrix molecules even react with the guest molecules to form stable species (Laser ablation technique).

Matrix shifts otherwise known as wavenumber shifts from the gas phase value is the most common and readily identified matrix effects. These shifts arise due to electrostatic, inductive, repulsive and dispersion interactions of the guest molecules with the matrix atoms/molecules. In case of inert gas matrixes, dispersive and repulsive interactions are the major contributors for the wavenumber shifts.

Site splitting of the infrared features or multiple site effects arise due to the trapping of guest molecules with distinctly different matrix environment. If the multiple trapping sites are not resolved then it will lead to the broadening of the spectrum. In some cases, though not always, the multiple site split features may vanish on annealing at elevated temperatures, as the guest molecules transform from an unstable to stable site. The multiple site effects can be clearly delineated by performing the MI experiments in different matrixes.

2.1.3 Matrix isolation set-up

A detailed account of the experimental methodologies of MI technique is given in several textbooks [162-166]. Only the important aspects of the technique are presented in this thesis. The main components of the matrix isolation technique are 1) a two-stage closed cycle helium cryostat to produce low temperature (12K/4K) 2) Vacuum chamber 3) Sample handling system 4) FTIR spectrometer to record the spectra of the matrix isolated species.

2.1.3.1 Cryostat

MI experiments were performed using two different closed cycle helium compressor cooled cryostats; RD210 Model (Leybold AG) and RDK-408D2 Model (Sumitomo Heavy Industries Ltd.). The Leybold and Sumitomo cryostat can attain a temperature of ~12 K and

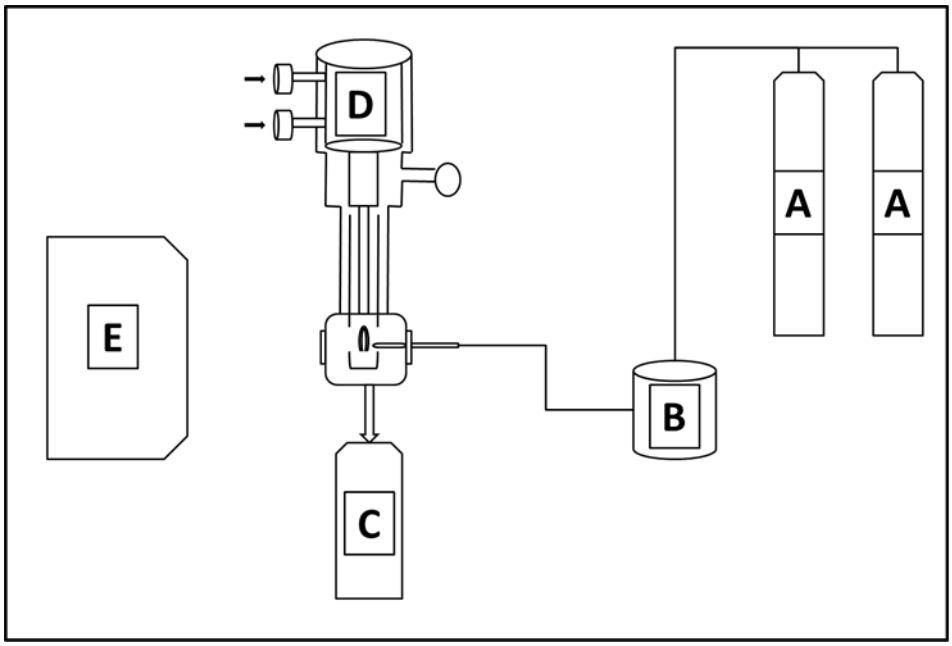

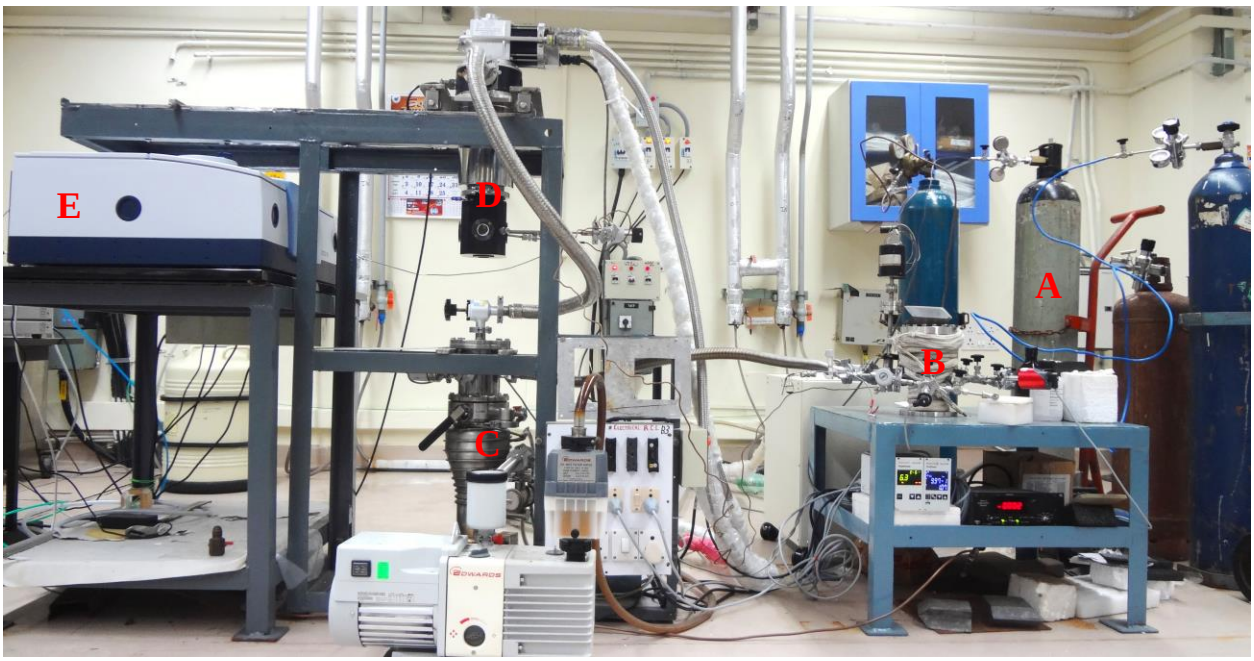

Figure 2.1: Schematic diagram and photograph showing the matrix isolation (MI) set up.

A) Inert gas cylinder B) Mixing chamber C) Diffusion pump D) Cryostat E) FTIR spectrometer

~4 K, respectively. Both the cryostat work on the principle of the Gifford-McMahon cycle and the cooling is achieved by the continuous compression and expansion of helium gas in an enclosed space. Helium is first compressed to a pressure of about 20 bars and the heat due to compression is removed by circulating cold water. The helium is then delivered to the cold head, where it expands against a piston, and eventually cools the regenerator. The expanded helium is then returned to the compressor for the next cycle.

The temperature of the cold head was measured using silicon diode in RD210 Model (Leybold AG) and Cernox resistor in RDK-408D2 Model (Sumitomo Heavy Industries Ltd.) cryostat. A resistive heater is provided on the cold head to anneal the matrix to different temperatures.

2.1.3.2 Vacuum chamber

The entire cryostat unit along with the cold tip and mixing chamber are continuously pumped by a diffusion pump (Edwards, Diffstak MK2 with a pumping speed of 280 l/s) backed by a rotary pump. A vacuum of $< 10^{-6}$ torr is essential to avoid contamination and for the successful conduct of an MI experiment. The pressure in the vacuum chamber is measured using a cold cathode gauge (Pfeiffer vacuum, Model TPG 261).

Suitable pressure gauges model APR 265, G ¼", 5500 hPa (0-5000 torr) and CCR (0-100 torr) were used to prepare the gas mixture in the mixing chamber. In case of high volatile sample the vapor pressure of the liquid is controlled by keeping the sample bulb containing liquid in a temperature controlled alcohol bath. If the sample is a non-volatile liquid, the sample bulb with liquid is placed near to the cold tip and the vapours are allowed to deposit dynamically onto the cold tip along with the matrix gas.

2.1.3.3 Sample handling system

A variety of deposition methods are used to prepare the matrix isolated sample. In the single jet effusive nozzle method, the matrix gas and the sample(s) of interest are mixed to

the desired ratios in the mixing chamber and the gas mixture is then allowed to deposit onto a cold KBr substrate. The gas flow through this nozzle is controlled using a dosing valve. The gas mixture was deposited at a typical rate of ~ 3mmol/h and deposition lasted for about ~ 60-120 minutes.

In the twin and triple jet nozzle experiments, co-deposition of the sample(s) and the matrix gas is done by streaming them separately onto the substrate.

Once the sample and the matrix are deposited onto the cold substrate, the FTIR spectrum of the matrix-isolated sample is recorded. Soon after recording the spectrum, the matrix is warmed to different temperatures depending upon the nature of the matrix gas used. The matrix is kept at a particular temperature Ar(35K)/N_2(30K)/Ne(10K) for about ~15-20 minutes and then cooled back to 12K/4K and the spectrum is again recorded. This process is called annealing. During annealing the guest molecules undergoes diffusion through the matrix and interacts with other molecules to form complexes. It is also possible that the unstable multiple trapping sites are removed as a result of annealing.

Figure 2.2: Photograph showing various nozzles used for the deposition of the gas sample. A) Single jet B) Double jet C) Triple jet

2.1.3.4 Fourier transform infrared spectrometer

Infrared spectra of matrix isolated samples were recorded using BOMEM MB 100 FTIR spectrometer operated at a resolution of 1 cm^{-1} using Deuterated Triglycine Sulphate (DTGS) detector in the range 4000-400 cm^{-1} and typically 16 scans were co-added to obtain good signal to noise ratio.

Vibrational spectra of matrix isolated species were also recorded using Bruker Vertex 70 FTIR spectrometer, which is equipped with liquid nitrogen cooled Mercury Cadmium Telluride (MCT) detectors in the range of 4000-500 cm^{-1} with a resolution of 0.5 cm^{-1} and typically 32 scans were co-added to obtain a good signal-to-noise ratio.

2.2 Computational methods

Computational chemistry is a powerful tool to solve electronic structure, potential energy surfaces, reaction pathways, hydrogen bonding interactions etc [175,176]. Several quantum chemical methods are available in the literature to study the hydrogen bonding interactions [177]. Starting from primitive semi-empirical molecular orbital to high end coupled-cluster methods are used to investigate hydrogen bonding interactions. In this thesis work, *ab initio* computations were performed for the blue- and red-shifted hydrogen-bonded complexes using the Gaussian 09W [178] package running on a Fujitsu machine with Intel 2X XEON E5-2687W v2 processors, with 64 GB RAM. Molecular properties such as structures, stabilization energies and vibrational wavenumbers were calculated. Detailed treatments of *ab initio* calculations are given in various books [176,179-182]. Natural bond orbital (NBO 3.1) [183] and Atoms in molecule (AIM) package [184] were used to understand the nature of the interactions. Energy decomposition analysis (EDA) was performed using ADF 2016 package [185,186]. A brief discussion on these topics is given in the following sections.

2.2.1 Geometry optimization and wavenumber calculation

Geometry optimizations were carried out at B3LYP [187], Møller-Plesset second order perturbation (MP2) levels of theory [188] using 6-311++G(d,p) and aug-cc-pVDZ basis sets. The B3LYP uses the Becke three-parameter non-local exchange functional with non-local correlation of lee et al. [189]. It should be mentioned that B3LYP level of theory has been used by several theoretical groups to study the hydrogen-bonded interactions [190,191,192]. Monomer geometries were first optimized and without imposing any structural constraints, the geometry of the complexes was optimized. Various properties such as stabilization energies, vibrational wavenumbers and dipole moments were computed. Vibrational wavenumber calculations were performed at the same level of theory to ascertain that the optimized structure of the blue- and red-shifted complexes correspond to a minimum on the potential energy surface, by ensuring all the wavenumbers were positive and also to assign the observed vibrational wavenumbers in our matrix isolation infrared experiments. All the structures discussed in this thesis did indeed correspond to a minimum.

2.2.1.1 Scaling factors

It is important to point out that the computations are performed for isolated gas phase molecules without taking into consideration the effect of matrix and it is indeed difficult to incorporate the matrix effect for different vibrational modes in the computations. Furthermore, the levels of theory and the basis sets used for the calculation can give rise to such deviation between the calculated and observed vibrational wavenumber. The deviations between the experimental and calculated vibrational wavenumbers are attributed to matrix shifts as well as the possible deficiencies of the theoretical model used.

Scaling procedure for vibrational wavenumbers were applied to correct the deficiencies in the theoretical method, harmonic corrections and for the basis sets used to compute the optimized geometries. A uniform scaling, two different scaling factors [193] for

the higher and lower wavenumber and a mode by mode scaling procedures were used to scale the computed vibrational wavenumber.

Scaling factors were calculated for each vibrational mode of the monomers separately to correct these deviations. The computed wavenumbers for the different modes were scaled on a mode-by-mode basis, by comparing the computed wavenumbers for monomer, with the observed experimental wavenumbers, in a given matrix. These scaling factors were then used to scale the computed wavenumbers in the complexes. Since the experimental wavenumbers for monomer in Ar and N_2 matrixes were slightly different, the scaling factors were also correspondingly different [146-148]. Hence the raw (unscaled) vibrational wavenumbers computed for the blue- and red-shifted complexes, were scaled differently depending on the matrixes used. Applying scaling factor to the modes of the complexes allows one to reasonably predict the band positions of the blue- and red-shifted complexes.

2.2.2 Stabilization energy of complexes

The stabilization energy of the complex was computed using the method described below. The stabilization energy (ΔE) of a complex is given by

$$\Delta E = E_{AB} - (E_A + E_B) \qquad \ldots\ldots\ldots\ldots\ldots\ldots (1)$$

Where, E_A, E_B and E_{AB} represent the energies for the monomers A, B and complex AB respectively. The negative sign of ΔE indicates that the complex is more stable relative to the precursors. The stabilization energy of the complex corrected for zero point energy (ZPE) was also calculated. Stabilization energies thus derived from the calculated energies E_A, E_B and E_{AB} are associated with the error due to difference in number of basis functions for the complex with respect to monomers which is termed as basis set superposition error (BSSE) [194-198]. The commonly used method to correct for BSSE is by counterpoise (CP) correction proposed by Boys and Bernadi [194]. In this scheme, one calculates all quantities

(energies of monomer E_A, E_B and the complex E_{AB}) in the same basis set spanned by the functions of the complex AB and the difference in energies is obtained as follows.

$$\Delta E = E_{AB}(AB) - (E_A(AB) + E_B(AB)) \qquad \ldots\ldots\ldots\ldots\ldots\ldots (2)$$

Where, E_A (AB) = Energy of the monomer A using the basis set AB

E_B (AB) = Energy of the monomer B using the basis set AB

E_{AB} (AB) = Energy of the complex AB using the basis set AB

In our studies, the stabilization energies of the complex corrected for the BSSE have also been included. Corrections of energies for ZPE and BSSE simultaneously were not included as these values are known to overcorrect the stabilization values [199,200].

2.2.3 Atoms-in-molecules (AIM) methodology

Atoms-in-molecule (AIM) theory was first proposed by Bader and used extensively to study the nature of the chemical bond in terms of electron density topology [184,201]. In order to generate the electron density topology by AIMPAC package, the wavefunction corresponding to the optimized geometry of the complex or monomers are used as input. From the electron density plots, one obtains the (3,-1) bond critical point and the following properties at this BCP were examined: the electron density ($\rho(r_c)$), Laplacian of electron density ($\nabla^2\rho(r_c)$) and the ratio of the eigenvalues $|\lambda_1|/\lambda_3$. The number of bond critical points that can coexist in a system with finite number of atoms is given by the Poincaré-Hopf relationship.

$$n-b+r-c=1 \qquad \ldots\ldots\ldots\ldots\ldots\ldots (3)$$

Where n is the number of nuclei, b the number of bond critical point, r the number of ring critical point and c the number of cage critical point.

Bader and Essen have concluded that for the ‘‘shared’’ (i.e., covalent) interactions electron density at BCP is of the order $>10^{-1}$ a.u. [202]. Weak interactions are always associated with small values of $\rho(r_c)$ and $\nabla^2\rho(r_c) > 0$ [203]. The Laplacian of the electron

density ($\nabla^2\rho(r_C)$) is a measure of local concentrations of electron density, the positive value indicates the depletion of electron and the negative value shows the concentration of electron density at the BCP.

2.2.4 Natural bond orbital (NBO) analysis

NBO analysis was performed to understand the role of hyperconjugative interactions in the complexes stabilized through hydrogen-bonded interaction. The NBOs are one of a sequence of natural localized orbital sets that include "natural atomic orbitals" (NAO), "natural hybrid orbitals" (NHO), "natural bonding orbitals" (NBO) and "natural localized molecular orbitals" (NLMO). These natural localized sets are intermediate between basis atomic orbitals (AO) and molecular orbitals (MO):

Atomic orbital → NAO → NHO → **NBO** → NLMO → Molecular orbital

Natural (localized) orbitals are used in computational chemistry to calculate the distribution of electron density in atoms and in bonds between atoms. They have the "maximum-occupancy character" in localized 1-center and 2-center regions of the molecule. Natural bond orbitals (NBOs) include the highest possible percentage of the electron density, ideally close to 2.000, providing the most accurate possible “natural Lewis structure” of ψ. A high percentage of electron density (denoted %-ρ_L), often found to be >99% for common organic molecules, correspond with an accurate natural Lewis structure [204].

The concept of *natural orbitals* was first introduced by Per-Olov Löwdin in 1955, to describe the unique set of orthonormal 1-electron functions that are intrinsic to the *N*-electron wavefunction [205].

Each bonding NBO σ_{AB} (the donor) can be written in terms of two directed valence hybrids (NHOs) h_A, h_B on atoms A and B, with corresponding polarization coefficients c_A, c_B:

$$\sigma_{AB} = c_A\, h_A + c_B\, h_B \qquad \text{…….……. (4)}$$

The bonds vary smoothly from covalent ($c_A = c_B$) to ionic ($c_A >> c_B$) limit.

Each valence bonding NBO σ must be paired with a corresponding valence antibonding NBO σ* (the acceptor) to complete the span of the valence space:

$$\sigma_{AB}^* = c_A\, h_A - c_B\, h_B \qquad \text{…….……. (5)}$$

The bonding NBOs are of the "Lewis orbital"-type (occupation numbers near 2); antibonding NBOs are of the "non-Lewis orbital"-type (occupation numbers near 0). In an idealized Lewis structure, full Lewis orbitals (two electrons) are complemented by formally empty non-Lewis orbitals. Weak occupancies of the valence anti bonds signal irreducible departures from an idealized localized Lewis structure, which means true "delocalization effects".

In NBO analysis, the off–diagonal elements of the fock matrix in their NBO basis give the measure of delocalization effects. The second order perturbation energy (E_2) gives an estimate of the strength of these delocalization interactions.

2.2.5 Energy decomposition analysis (EDA)

Energy decomposition analysis was performed to clearly delineate the contribution of different energy components and the role of other dominant interactions [206], in the stabilization the blue- and red-shifted complexes. In the EDA methods, the total stabilization energy is defined as the difference between the energy of the complex and the energy of the monomers or fragments [207] and it is decomposed into electrostatic (E_{el}), exchange repulsion (E_{er}) , polarization (E_{pol}) and dispersion (E_{disp}) components.

$$E_{tot} = (E_{el}) + (E_{er}) + (E_{pol}) + (E_{disp}) \qquad \text{…..……. (6)}$$

The electrostatic energy term can be defined as the interaction between the static charge densities of each monomer within the complex. This term includes the attractive Coulomb interactions between nuclei of one monomer with the electrons of the other monomer, repulsive Coulomb interactions both between the nuclei of each monomer and

between the electrons of each monomer. The total electrostatic interaction is normally attractive. The Pauli term contains the exchange and repulsion energies, which are stabilizing and destabilizing respectively. The exchange interaction arises due to the antisymmetric nature of a wave function that allows electrons to exchange between monomers. The repulsion interaction originates largely from other types of 2-electron integral terms for monomer orbitals. The orbital delocalization term is always attractive. On the other hand, the dispersion term computed in this method is an attractive term, which arises due to electron correlation [206].

EDA calculations have been performed using B3LYP+D3-TZ2P level of theory for the optimized geometries of blue- and red-shifted hydrogen bond complexes using ADF 2016 package [186,208,209,210].

CHAPTER 3

BLUE SHIFTING HYDROGEN BOND

3.1 Blue shifting hydrogen bond

The hydrogen bond between X-H and Y, where X is a more electronegative atom or group than H and Y has a lone pair of electrons or π electrons, which makes X-H bond to elongate with the associated red shift and enhanced intensity in IR spectra. In contrast to conventional hydrogen bonds, blue-shifted hydrogen bonds are characterized by contraction of the X-H bond, and a concomitant blue shift and decrease in IR intensity. CHF_3 is a prototypical molecule to observe the blue-shifted hydrogen bonding and several groups have performed computational and experimental studies on this system with various proton acceptors [45-73].

This chapter gives the comprehensive account of the experimental and computations on the blue-shifted hydrogen bond between CHF_3 with HCl, H_2O, C_2H_2 and C_6H_6. Computations were performed at B3LYP and MP2 level of theory using 6-311++G(d,p) and aug-cc-pVDZ basis sets. AIM and NBO analyses were carried out for the complexes to understand the nature of the interaction in stabilizing the blue-shifted hydrogen bonds.

The systems studied are:

- Fluoroform-Hydrogen Chloride (CHF_3-HCl)
- Fluoroform-Water (CHF_3-H_2O)
- Fluoroform-Benzene (CHF_3-C_6H_6)
- Fluoroform-Acetylene (CHF_3-C_2H_2)

3.2 Interaction of fluoroform (CHF_3) with hydrogen chloride (HCl)

The aim of this work is to identify the 1:1 hydrogen-bonded complex of CHF_3 and HCl using matrix isolation infrared spectroscopy and *ab initio* computations. Using B3LYP and MP2 levels of theory with 6-311++G(d,p) and aug-cc-pVDZ basis sets, the structures of the CHF_3-HCl complexes and their energies were computed. The experimental vibrational wavenumber of the complex was corroborated with the computed wavenumbers.

3.2.1 Experimental details

CHF_3 (Air products, USA, Electronic Grade) were used as such, without further purification. HCl gas was prepared by mixing AR grade H_2SO_4 and HCl solutions, in a vacuum bulb attached to a burette. Prior to mixing of the reagents, it was ensured that the vacuum bulb was evacuated to ~5 x 10^{-6} mbar. The HCl gas that was produced was trapped in a low temperature bath, which was maintained at a temperature of ~ -100° C. The experiments were performed by streaming CHF_3 and HCl separately through a twin-jet nozzle system and co-deposited along with the inert gas matrix. In this experiment CHF_3, was mixed with matrix gas, in the required ratio in the mixing chamber and the resultant mixture was allowed to stream through one nozzle and deposited onto the matrix, with the flow being adjusted by a fine needle valve. Through a second nozzle and a needle valve, HCl gas was deposited. In these experiments, HCl in the reservoir was maintained at a temperature of ~ -80° C to control its concentration in the matrix. High purity Argon (INOX, 99.9995%) was used as a matrix gas. Typical matrix-to-sample ratios ranging from 1000:1 to 1000:2 for CHF_3 and 1000:1 to 1000:1.5 for HCl was used in the experiments. Infrared spectra of matrix isolated samples were recorded using BOMEM MB100 FTIR spectrometer. All the spectra shown in this report were those recorded after annealing the matrix.

Figure 3.1 shows the IR spectra of CHF_3 with and without HCl in an Ar matrix, spanning the region 3075-3025 cm^{-1}. In Ar matrix, the υ_1 C-H stretching mode of CHF_3 occurs at 3044.4 cm^{-1}. The feature observed at 3058.9 cm^{-1} is due to the aggregates of CHF_3,

which agree well with the reported literature value [78]. When CHF_3 and HCl were co-deposited in an Ar matrix, a new feature was observed in the C-H stretching region at 3051.1 cm^{-1}, and the intensity of the feature increased on annealing the matrix. Figure 3.2 shows the IR spectra over the region 1390-1360 cm^{-1}. The feature observed at 1376.1 cm^{-1} and a site split feature at 1374.2 cm^{-1} in the Ar matrix are assigned to the doubly degenerate υ_4 C-H bending mode of CHF_3. Co-deposition of CHF_3 and HCl in an Ar matrix and subsequent annealing produced new features at 1379.4 and 1371.8 cm^{-1}. Figure 3.3 shows the IR spectra spanning the region 1160-1110 cm^{-1}. The doubly degenerate υ_5 C-F stretching mode in CHF_3 appears as a doublet at 1148.0 and 1145.2 cm^{-1}, while the υ_2 C-F symmetric stretching mode is observed at 1136.0 cm^{-1} (fig. 3.3a). When CHF_3 and HCl were co-deposited, new features were observed at 1141.7, 1149.9 and 1110.0 cm^{-1}. The features observed at 1129.7 and 1122.4 cm^{-1} are due to aggregates of CHF_3 [78].

Figure 3.4 shows the IR spectral region 2960-2800 cm^{-1}, corresponding to the HCl vibrational stretching region. The HCl molecule shows rotational fine structure in an Ar matrix. The feature observed at 2887.7 cm^{-1} (R branch) is assigned to the HCl stretch in the monomer in Ar matrix. The features observed at 2869.4 and 2854.4 cm^{-1} (fig. 3.4a) correspond to the Q and P branches of HCl, respectively [211]. When CHF_3 and HCl were co-deposited and annealed, a new feature appeared at 2863.6 cm^{-1} (fig. 3.4b, c). The feature observed at 2816.8 cm^{-1} is due to HCl dimer in an Ar matrix [211]. The new feature appeared only when both CHF_3 and HCl were co-deposited and showed concentration dependence; hence, the feature is due to the CHF_3-HCl complex.

3.2.2 Computational

Ab initio computations on the CHF_3-HCl system yielded two minima corresponding to CHF_3-HCl complexes A and B. Figure 3.5 shows the structure for the CHF_3-HCl complexes A and B computed at MP2/aug-cc-pVDZ level of theory. Table 3.1 and 3.1a gives the selected structural parameters of both complexes A and B computed at B3LYP and MP2 levels of theory using aug-cc-pVDZ basis sets. For complex A, the primary interaction is

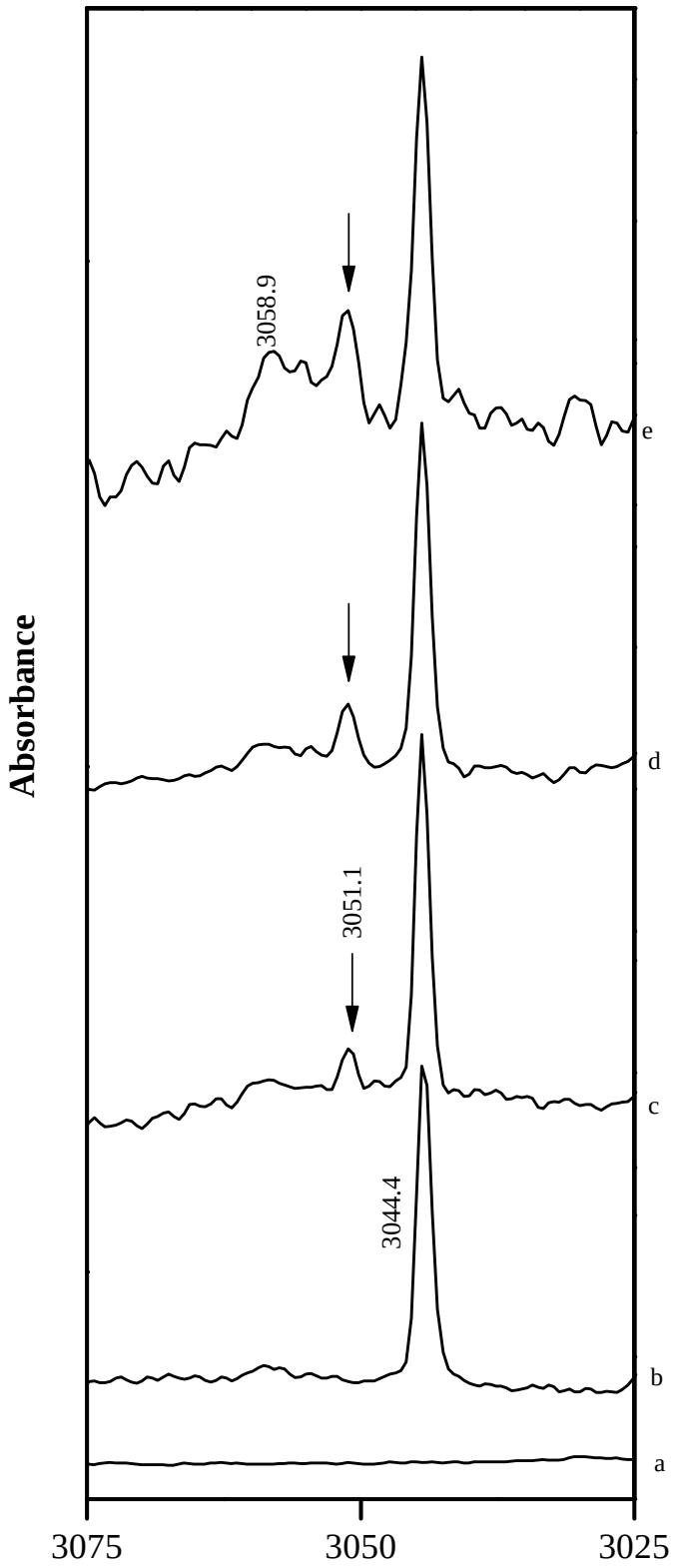

Figure 3.1: Matrix isolated infrared spectra of the CHF_3/HCl complex in an Ar matrix in the region 3075-3025 cm^{-1}. Spectra for various concentrations of CHF_3/HCl/Ar (a) 0/1/1000; (b) 2/0/1000; (c) 1/1/1000; (d) 2/1/1000; (e) 1/1.5/1000.

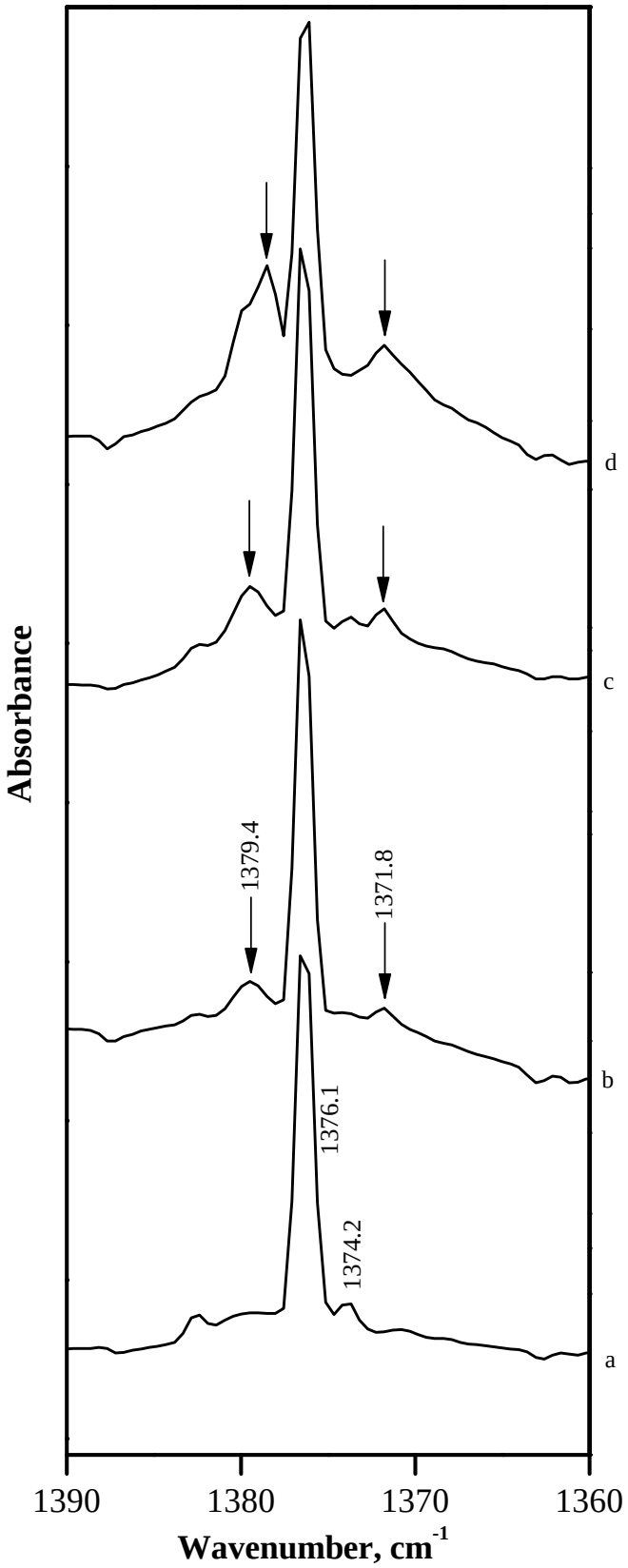

Figure 3.2: Matrix isolated infrared spectra of CHF_3/HCl complex in an Ar matrix covering the region 1390-1360 cm^{-1}. Spectra for various concentrations of CHF_3/HCl/Ar (a) 2/0/1000; (b) 1/1/1000; (c) 2/1/1000; (d) 1/1.5/1000.

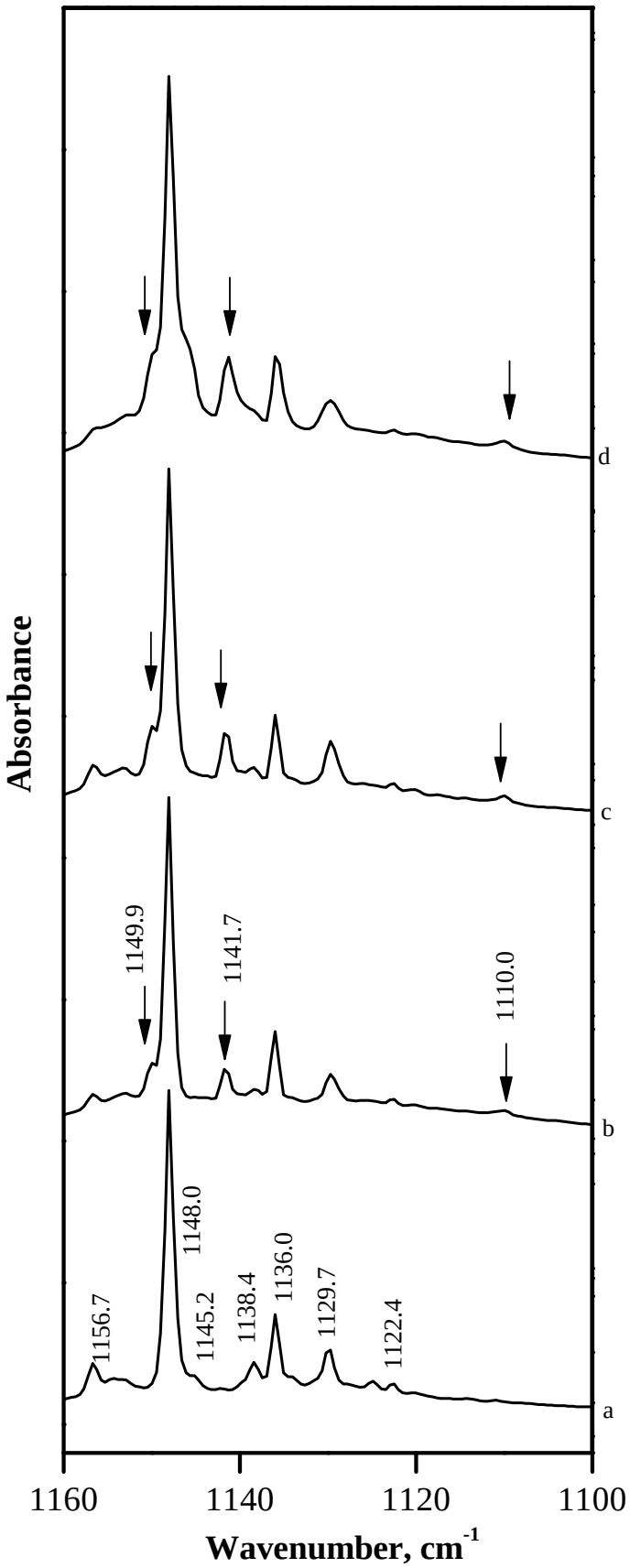

Figure 3.3: Matrix isolated infrared spectra of CHF_3/HCl complex in an Ar matrix covering the region 1160-1100 cm^{-1}. Spectra for various concentrations of CHF_3/HCl/Ar (a) 2/0/1000; (b) 1/1/1000; (c) 2/1/1000; (d) 1/1.5/1000.

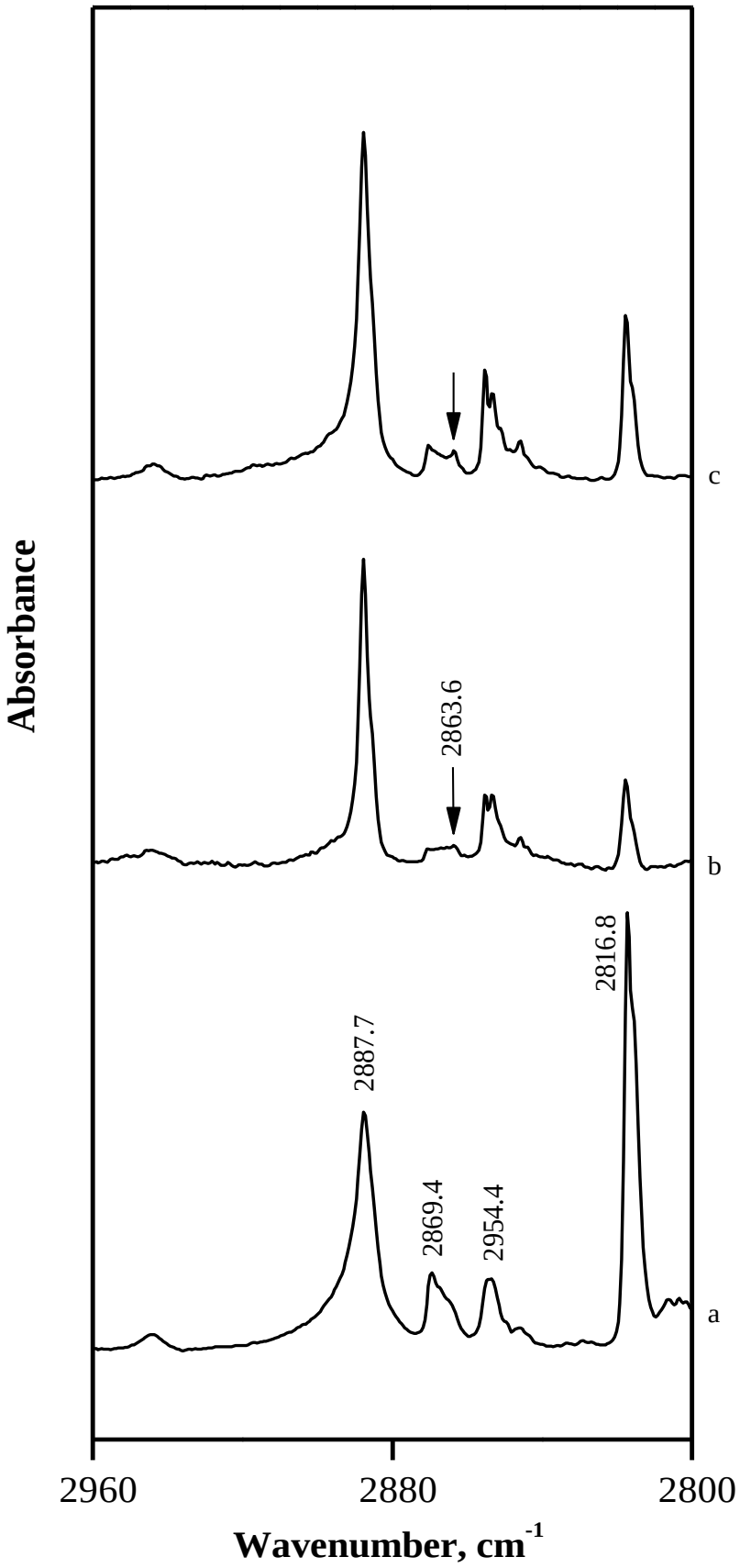

Figure 3.4: Matrix isolated infrared spectra of the CHF_3/HCl complex in an Ar matrix in the region 2960-2800 cm^{-1}. Spectra for various concentrations of HCl/CHF_3/Ar (a) 2/0/1000; (b) 1/1/1000; (c) 2/1/1000.

between fluorine F3 of CHF_3 and hydrogen H7 of HCl, and the bond distance is 2.349 Å at MP2 level of theory using aug-cc-pVDZ basis set. In addition, our calculation showed a weaker secondary interaction between hydrogen H2 of CHF_3 and Cl6 of HCl, and the bond distance is 2.958 Å, respectively at the aforementioned level of theory. Due to the presence of a secondary interaction, the HCl molecule shows a tilt toward CHF_3, and overall the complex is cyclic, with C_s symmetry. It should be mentioned that our results agree well with the structures reported by Ramasami and Thomas [212]. Unlike complex A, complex B is stabilized only by C-F⋯H interaction and is acyclic. The transition state structure connecting complexes A and B was calculated using the QST3 [213] method at B3LYP/aug-cc-pVDZ level of theory and found to be barrier less.

Table 3.2 gives the stabilization energies for the CHF_3-HCl complexes computed at B3LYP and MP2 levels of theory using the 6-311++G(d,p) and aug-cc-pVDZ basis sets. From the table, it is clear that the raw stabilization energies for complexes A and B are -1.2 and -1.0 kcal/mol at the B3LYP/aug-cc-pVDZ level of theory. Furthermore, calculation performed at the MP2/aug-cc-pVDZ revealed that complex B is ~0.5 kcal/mol higher in energy than complex A. Since, complex A is the global minimum structure at all levels of theory, we will henceforth compare the calculated vibrational wavenumber of this complex with the experimental wavenumber.

3.2.3 Vibrational assignments

The experimental vibrational wavenumbers of the CHF_3-HCl complex were compared with the calculated wavenumber using B3LYP and MP2 (Tables 3.3 and 3.3a) level of theories with aug-cc-pVDZ basis set. The mode-by-mode scaling factors were used to correct the deficiencies of the theoretical model, to correct the matrix shifts, and to predict the band positions for the CHF_3-HCl complexes.

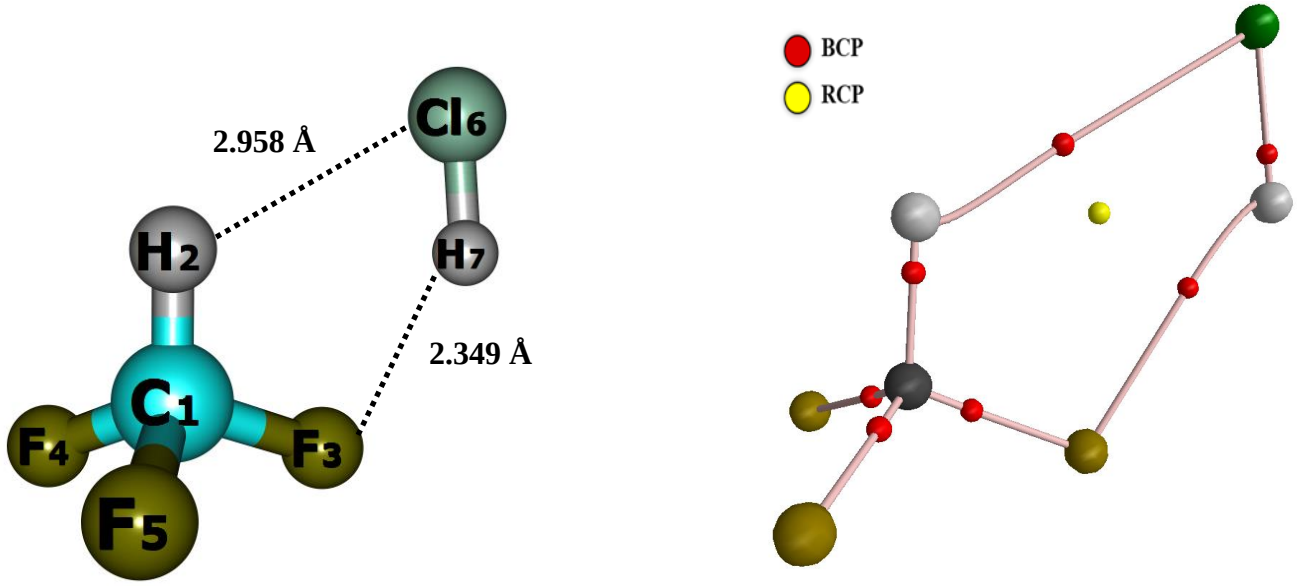

Complex A

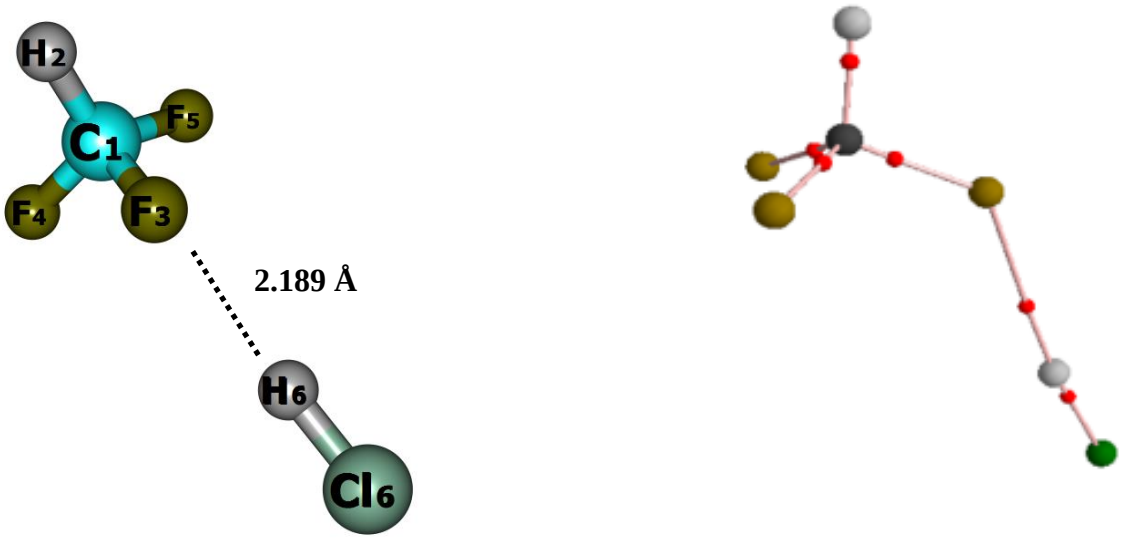

Complex B

Figure 3.5: Structures of CHF_3-HCl complexes A and B computed at MP2/aug-cc-pVDZ level of theory. Bond critical points (BCP) and ring critical point (RCP) are also shown in the figure.

Table 3.1: Selected structural parameters[a] for the CHF_3-HCl complexes A and B calculated at B3LYP/aug-cc-pVDZ level of theory.

Parameters	Complex-A	Complex-B	Monomer
C1-H2	1.096	1.096	1.097
C1-F3	1.358	1.359	1.349
C1-F4	1.346	1.345	1.349
C1-F5	1.346	1.345	1.349
F3-H7	2.438	2.281	---
H2-Cl6	3.178	---	---
H7-Cl6	1.297	1.297	1.295
∠H2-C1-F3	110.2	110.1	110.6
∠F3-H7-Cl6	131.6	172.1	---
tor∠H2-C1-F3-H7	-9.9	-168.8	---
tor∠C1-F3-H7-Cl6	4.6	161.4	---

Table 3.1a: Selected structural parameters[a] for the CHF_3-HCl complexes A and B calculated at MP2/aug-cc-pVDZ level of theory.

Parameters	Complex-A	Complex-B	Monomer
C1-H2	1.095	1.095	1.096
C1-F3	1.350	1.348	1.352
C1-F4	1.362	1.363	1.352
C1-F5	1.350	1.349	1.352
F3-H7	2.349	2.190	---
H2-Cl6	2.958	---	---
H7-Cl6	1.290	1.289	1.288
∠H2-C1-F3	110.2	110.1	110.6
∠F3-H7-Cl6	131.4	178.9	---
tor∠H2-C1-F3-H7	-7.9	-171.9	---
tor∠C1-F3-H7-Cl6	4.2	-105.1	---

[a]Bond lengths in Å, bond angles and dihedral angles in °.

Table 3.2: Raw[a]/ZPE-corrected/BSSE-corrected stabilization energies for the CHF_3-HCl complexes computed at the B3LYP and MP2 level of theory using 6-311++G(d,p) and aug-cc-pVDZ basis sets.

Complexes	Stabilization energy (ΔE)			
	B3LYP		MP2	
	6-311++G(d,p)	aug-cc-pVDZ	6-311++G(d,p)	aug-cc-pVDZ
A	-1.4/-0.7/-1.1	-1.2/-0.4/-1.0	-2.5/-1.9/-1.2	-2.5/-1.7/-1.7
B	-1.4/-0.8/-1.1	-1.0/-0.4/-0.9	-1.1/-1.4/-0.7	-2.1/-1.4/-1.3

All energies are in kcal/mol (see text for details).
[a]Raw stabilization energies refer to energies not corrected for either ZPE or BSSE.

Table 3.3: Computed unscaled (cm^{-1}), scaled vibrational wavenumbers (cm^{-1}), scaling factors and mode assignments computed at B3LYP/aug-cc-pVDZ level and comparison with experimental wavenumbers for the CHF_3-HCl complexes A and B in Ar matrix.

Computed/ unscaled (υ)	Ar matrix			Mode assignment
	Computed/ Scaled (υ)	Scaling factor	Exp (υ)	
CHF_3				
1111.1 (93)[a]	1136.0	1.0224	1136.0	υ_2 C-F sym. stretching mode in CHF_3(A)
1118.8 (303)	1148.0	1.0261	1148.0	υ_5 CF_3 def. mode in CHF_3(E)
1352.9 (35)	1376.1	1.0171	1376.1	υ_4 C-H bending mode in CHF_3(E)
3145.1 (24)	3044.4	0.9679	3044.4	υ_1 C-H stretching mode in CHF_3(A)
HCl				
2924.3 (38)	2887.5	0.9874	2887.5	H-Cl stretching mode
Complex-A				
1088.5 (219)	1112.9	1.0224	1110.0	C-F sym. stretching mode in complex-A
1118.1 (197) 1126.9 (285)	1147.2 1156.2	1.0261	1141.7 1149.9	CF_3 def. mode of CHF_3 in complex-A
1350.3 (23) 1358.2 (37)	1373.5 1381.4	1.0171	1371.8 1379.4	C-H bending mode of CHF_3 in complex-A
3155.8 (15)	3054.5	0.9679	3051.5	C-H stretching mode of CHF_3 complex-A
2908.5 (63)	2871.9	0.9874	2863.6	H-Cl stretching mode in complex-A
Complex-B				
1086.0 (291)	1110.3	1.0224	-[b]	C-F sym. stretching mode in complex-B
1120.1 (148) 1130.4 (289)	1149.3 1159.9	1.0261	-[b]	CF_3 def. mode of CHF_3 in complex-B
1346.4 (34) 1354.6 (35)	1369.4 1377.8	1.0171	-[b]	C-H bending mode of CHF_3 in complex-B
3155.4 (20)	3054.1	0.9679	-[b]	C-H stretching mode of CHF_3 in complex-B
2896.6 (138)	2860.1	0.9874	-[b]	H-Cl stretching mode in complex-B

[a]Computed infrared intensities (km/mol) are given in parentheses.
[b]Experimental features were not observed.

Table 3.3a: Computed unscaled (cm^{-1}), scaled vibrational wavenumbers (cm^{-1}), scaling factors and mode assignments computed at MP2/aug-cc-pVDZ level and comparison with experimental wavenumbers for the CHF_3-HCl complexes A and B in Ar matrix.

Computed/ unscaled (υ)	Ar matrix			Mode assignment
	Computed/ Scaled (υ)	Scaling factor	Exp (υ)	
CHF_3				
1118.6 (94)[a]	1136.0	1.0155	1136.0	υ_2 C-F sym. stretching mode in CHF_3(A)
1140.6 (299)	1148.0	1.0065	1148.0	υ_5 CF_3 def. mode in CHF_3(E)
1379.5 (39)	1376.1	0.9975	1376.1	υ_4 C-H bending mode in CHF_3(E)
3221.1 (21)	3044.4	0.9451	3044.4	υ_1 C-H stretching mode in CHF_3(A)
HCl				
3023.1 (43)	2887.5	0.9551	2887.5	H-Cl stretching mode
Complex-A				
1102.2 (157)	1119.3	1.0155	1110.0	C-F sym. stretching mode in complex-A
1132.8 (254) 1148.3 (280)	1140.1 1155.7	1.0065	1141.7 1149.9	CF_3 def. mode of CHF_3 in complex-A
1378.9 (23) 1385.4 (42)	1375.5 1381.9	0.9975	1371.8 1379.4	C-H bending mode of CHF_3 in complex-A
3231.2 (11)	3053.9	0.9451	3051.5	C-H stretching mode of CHF_3 complex-A
3001.2 (72)	2866.6	0.9551	2863.6	H-Cl stretching mode in complex-A
Complex-B				
1102.9 (231)	1119.9	1.0155	-[b]	C-F sym. stretching mode in complex-B
1133.8 (179) 1151.9 (279)	1141.2 1159.4	1.0065	-[b]	CF_3 def. mode of CHF_3 in complex-B
1372.9 (33) 1381.1 (39)	1369.5 1377.6	0.9975	-[b]	C-H bending mode of CHF_3 in complex-B
3229.9 (18)	3052.6	0.9451	-[b]	C-H stretching mode of CHF_3 in complex-B
3010.3 (154)	2875.3	0.9551	-[b]	H-Cl stretching mode in complex-B

[a]Computed infrared intensities (km/mol) are given in parentheses.
[b]Experimental features were not observed.

3.2.3.1 υ_1 C-H stretching mode of CHF_3

Ab initio computations together with AIM analysis indicated that both the primary and secondary interactions in complex A are responsible for a blue shift of ~10.1 cm^{-1}. The υ_1 C-H stretching mode of CHF_3 in complex A in an Ar matrix was observed at 3051.1 cm^{-1}, which amounts to a blue shift of 6.7 cm^{-1}. The experimental value agrees well with the scaled computed frequencies of complex A. It should be mentioned that even though the IR intensity of complex A is slightly reduced to 15 km/mol from that of 24 km/mol for the monomer (Table 3.3), we could still discern this feature clearly in the matrix.

3.2.3.2 υ_4 C-H bending mode of CHF_3

In Ar matrix, the C-H bending mode of CHF_3 is doubly degenerate. This mode splits in complex A and occurs at 1371.8 and 1379.4 cm^{-1}, yielding a red shift of 4.3 cm^{-1} and a blue shift of 3.3 cm^{-1}. The computation also showed the same trend, and the scaled computed values for this mode occur at 1373.5 (a red shift of 2.6 cm^{-1}) and 1381.4 cm^{-1} (a blue shift of 5.3 cm^{-1}), which compare well with the experimentally observed features.

3.2.3.3 υ_5 CF_3 deformation mode of CHF_3

In Ar matrix, the doubly degenerate υ_5 CF_3 deformation mode of monomeric CHF_3 is observed at 1148.0 cm^{-1}. On complex formation, this mode of the CHF_3 submolecule of complex A splits and is observed at 1149.9 and 1141.7 cm^{-1}, amounting to a blue shift of 1.9 cm^{-1} and a red shift of 6.3 cm^{-1}, respectively. Our computations indicated that the doubly degenerate for this mode occur at 1156.2 and 1147.2 cm^{-1}, yielding a red shift of 0.9 cm^{-1} and a blue shift of 8.2 cm^{-1}.

3.2.3.4 υ_2 C-F symmetric stretching mode of CHF_3

The scaled computed value for complex A was 1112.9 cm^{-1}, amounting to a red shift of 23.1 cm^{-1}, which corroborates well with the experimental value at 1110.0 cm^{-1}.

3.2.3.5 H-Cl stretch

Scaled computed wavenumber of complex A show a red shift of 15.6 cm^{-1} in the HCl submolecule, and experimentally, we discerned a new feature at 2863.6 cm^{-1}, with a red shift of 23.9 cm^{-1}.

3.2.4 Nature of the interaction: AIM analysis

To analyze the nature of the interaction in CHF_3-HCl complexes, the AIM theory was used. A (3,-1) bond critical point (BCP) was sought, using the optimized geometry of the CHF_3-HCl complexes A and B computed at the B3LYP/aug-cc-pVDZ basis sets. At the BCP for both complexes A and B, the values of ($\rho(r_c)$) were found to be of the order of 10^{-2} au, ($\nabla^2\rho\ (r_c)$) was positive, and $|\lambda 1|/\lambda 3 < 1$, as are typical of closed shell interaction. Table 3.4a gives the properties of the intermolecular (3,-1) BCP for complexes A and B. Two (3,-1) BCPs were located for complex A, one between hydrogen of CHF_3 and chlorine of HCl and another between fluorine of CHF_3 and hydrogen of HCl, confirming unambiguously the cyclic nature of the complex. The comparison of these two BCPs revealed that the electron density and Laplacian of the electron density ($\nabla^2\rho(r_c)$) for the BCP formed as a result of the C-F⋯H interaction is higher in magnitude than the former. This indicates that the C-F⋯H interaction is stronger than the C-H⋯Cl interaction in complex A. In the acyclic complex B, a BCP located between fluorine of CHF_3 and hydrogen of HCl confirms the existence of C-F⋯H interaction. BCPs corresponding to the C-H/C-F bonds of CHF_3 and the H-Cl bond of HCl in the complexes were evaluated to understand the effect of intramolecular interaction on the neighboring bonds in the submolecules. Table 3.4b-d gives the properties for these BCPs. In the same table the values for monomeric CHF_3 and HCl are given for comparison. In contrast to the BCPs produced due to the hydrogen bonding interaction, the BCPs of the neighboring bonds exhibit strong interactions. The high positive values of electron density and high negative values of Laplacian clearly confirmed the shared nature of the interactions

Table 3.4: Properties of (3,-1) bond critical points in CHF_3-HCl complexes computed at B3LYP/aug-cc-pVDZ level of theory.

(a) Intermolecular BCP's in CHF_3-HCl complexes

Complexes	**$\rho(r_C)$**	**$\nabla^2\rho(r_C)$**	**λ_1**	**λ_2**	**λ_3**	**$\lvert\lambda_1\rvert / \lambda_3$**
Complex-A	0.00400 0.00824	0.01185 0.03058	-0.00281 -0.00845	-0.00217 -0.00808	0.01806 0.04711	0.15559 0.17937
Complex-B	0.00956	0.03283	-0.01056	-0.01033	0.05372	0.19657

(b) Intramolecular BCP's corresponding to the C-H bond in CHF_3 and CHF_3-HCl complexes

Complexes	**$\rho(r_C)$**	**$\nabla^2\rho(r_C)$**	**λ_1**	**λ_2**	**λ_3**	**$\lvert\lambda_1\rvert / \lambda_3$**
CHF_3	0.29792	-1.25964	-0.82919	-0.82919	0.39874	2.07952
Complex-A	0.29895	-1.27683	-0.83817	-0.83778	0.39912	2.10000
Complex-B	0.29854	-1.26904	-0.83462	-0.83423	0.39981	2.08754

(c) Intramolecular BCP's corresponding to the C-F bond in CHF_3 and CHF_3-HCl complexes

Complexes	**$\rho(r_C)$**	**$\nabla^2\rho(r_C)$**	**λ_1**	**λ_2**	**λ_3**	**$\lvert\lambda_1\rvert / \lambda_3$**
CHF_3	0.26693	-0.34557	-0.59294	-0.51977	0.76714	0.77292
Complex-A	0.26025	-0.34335	-0.56804	-0.49449	0.71918	0.78984
Complex-B	0.25973	-0.34382	-0.56543	-0.49367	0.71528	0.79050

(d) Intramolecular BCP's corresponding to the H-Cl bond in CHF_3-HCl complexes

Complexes	**$\rho(r_C)$**	**$\nabla^2\rho(r_C)$**	**λ_1**	**λ_2**	**λ_3**	**$\lvert\lambda_1\rvert / \lambda_3$**
HCl	0.23894	-0.83645	-0.55311	-0.55311	0.26977	2.05030
Complex-A	0.23825	-0.84584	-0.55810	-0.55807	0.27033	2.06451
Complex-B	0.23808	-0.84105	-0.55705	-0.55704	0.27304	2.04018

in the neighbouring bonds of the submolecules of CHF_3-HCl complexes. The AIM analysis also revealed that the accumulated electron density $\rho(r_c)$ (Table 3.4b) in the C-H BCP of complexes A and B is slightly higher (~10^{-3} a.u.) than the monomer. This increased electron density may be responsible for shortening of the C-H bond in the complexes and the associated blue shift in the C-H stretching wavenumber. Conversely, the decrease in electron density with respect to the monomer on complex formation results in red shift of the C-F and H-Cl stretching frequency.

3.2.5 NBO analysis

The results of NBO analysis of CHF_3-HCl complexes A and B computed at B3LYP/aug-cc-pVDZ level of theory is shown in table 3.5. From the table it is clear that the electron occupancy of antibonding orbitals σ*(C1-H2), σ*(C1-F3), and n^3F3 (lone electron pair) of the CHF_3 submolecule and σ*(Cl6-H7) of the HCl submolecule increased relative to the CHF_3 and HCl monomers. Similarly, a reduction in electron occupancies is noticed for the n^3Cl6 non-bonding orbital and the σ(Cl6-H7) bonding orbital of the HCl submolecule and for the σ(C1-F3) bonding orbital of the CHF_3 submolecule in complex A with respect to the monomers. It should be noted from table 3.5 that there is a marginal increase in the occupancy of antibonding σ*(C1-H2) orbital of CHF_3 submolecule in complex A. NBO analysis revealed that complex A is mainly stabilized by charge-transfer interactions such as n^3Cl6→σ*(C1-H2) and n^3F3→σ*(Cl6-H7) making the complex cyclic. The second order perturbation E_2 energies for the delocalization were found to be ~0.7 kcal/mol. It is the n^3Cl6→σ*(C1-H2) transfer interaction that is responsible for C-H bond elongation. In addition to the delocalization of the lone pair, it also appeared that the stabilization arises from the bond pair acceptor orbital interaction such as σ(Cl6-H7)→σ*(C1-H2), σ(C1-H2)→ σ*(Cl6-H7), σ(C1-F3)→σ*(Cl6-H7), and σ(Cl6-H7)→σ*(C1-F3), whose magnitudes are smaller than lone pair-acceptor orbital interactions. Eventhough the magnitudes of these

Table 3.5: Electron occupancies of various natural bond orbitals (NBOs) of CHF_3-HCl complexes A and B computed at B3LYP/aug-cc-pVDZ level of theory along with the donor-acceptor delocalization interaction and delocalization energies (E_2).

NBO	Occupancy	Donor-acceptor delocalization interaction	Second order perturbation (E_2) energy (kcal/mol)
Complex-A			
Lone pair → Acceptor orbital interactions			
n^1Cl6	1.99930 (1.99968)[a]	n^3Cl6 → σ*(C1-H2) n^1Cl6 → σ*(C1-F3)	0.61 0.06
n^2Cl6	1.99782 (1.99787)[a]		
n^3Cl6	1.99535 (1.99787)[a]		
σ*(C1-H2)	0.05074 (0.05068)[b]		
σ*(C1-F3)	0.09104 (0.08706)[b]		
n^1F3	1.99262 (1.99275)[b]	n^1F3 → σ*(Cl6-H7) n^2F3 → σ*(Cl6-H7) n^3F3 → σ*(Cl6-H7)	0.14 <0.05 0.89
n^2F3	1.95468 (1.95434)[b]		
n^3F3	1.94419 (1.94039)[b]		
σ*(Cl6-H7)	0.00350 (0.00000)[a]		
Bond pair → Acceptor orbital interactions			
σ(Cl6-H7)	1.99945 (2.00000)[a]	σ(Cl6-H7) → σ*(C1-F3) σ(C1-F3) → σ*(Cl6-H7)	<0.05 <0.05
σ*(C1-F3)	0.09104 (0.08706)[b]		
σ(C1-F3)	1.99548 (1.99570)[b]		
σ*(Cl6-H7)	0.00350 (0.00000)[a]		
σ(C1-H2)	1.99087 (1.99094)[b]	σ(C1-H2) → σ*(Cl6-H7) σ(Cl6-H7) → σ*(C1-H2)	<0.05 0.11
σ*(Cl6-H7)	0.00350 (0.00000)[a]		
σ(Cl6-H7)	1.99945 (2.00000)[a]		
σ*(C1-H2)	0.05704 (0 .05068)[b]		
Complex-B			
Lone pair → Acceptor orbital interactions			
n^1Cl6	1.99934 (1.99968)[a]	n^3Cl6 → σ*(C1-H2) n^1Cl6 → σ*(C1-F3)	<0.05 0.06
n^2Cl6	1.99781 (1.99787)[a]		
n^3Cl6	1.99776 (1.99787)[a]		
σ*(C1-H2)	0.04973 (0.05068)[b]		
σ*(C1-F3)	0.09206 (0.08706)[b]		
n^1F3	1.99103 (1.99275)[b]	n^1F3 → σ*(Cl6-H7) n^2F3 → σ*(Cl6-H7) n^3F3 → σ*(Cl6-H7)	0.79 1.15 0.08
n^2F3	1.95449 (1.95434)[b]		
n^3F3	1.94479 (1.94039)[b]		
σ*(Cl6-H7)	0.00604 (0.00000)[a]		
Bond pair → Acceptor orbital interactions			
σ(Cl6-H7)	1.99982 (2.00000)[a]	σ(Cl6-H7) → σ*(C1-F3) σ(C1-F3) → σ*(Cl6-H7)	<0.05 0.05
σ*(C1-F3)	0.09206 (0.08706)[b]		
σ(C1-F3)	1.99508 (1.99570)[b]		
σ*(Cl6-H7)	0.00604 (0.00000)[a]		
σ(C1-H2)	1.99063 (1.99094)[b]	σ(C1-H2) → σ*(Cl6-H7) σ(Cl6-H7) → σ*(C1-H2)	<0.05 0.05
σ*(Cl6-H7)	0.00604 (0.00000)[a]		
σ(Cl6-H7)	1.99982 (2.00000)[a]		
σ*(C1-H2)	0.04973 (0.05068)[b]		

[a]Occupancy of monomeric HCl is given in parentheses; [b]Occupancy of monomeric CHF_3 is given in parentheses.

Table 3.6: Comparison of donor (n^2F3)-acceptor (σ^*(C1-H2)) delocalization interaction in CHF_3 monomer and in CHF_3-HCl complexes A and B.

Donor-acceptor delocalization interaction	Second order perturbation (E_2) energy (kcal/mol)		
	CHF_3	Complex-A	Complex-B
$n^2F3 \rightarrow \sigma^*$(C1-H2)	6.89	6.29	6.58
$n^2F4 \rightarrow \sigma^*$(C1-H2)	6.89	6.84	7.00
$n^2F5 \rightarrow \sigma^*$(C1-H2)	6.89	6.85	6.99

Table 3.7: Electron occupancies of various natural atomic orbitals (NAO) of CHF_3-HCl complexes computed at B3LYP/aug-cc-pVDZ level of theory along with %'s' and 'p' characters.

NAO	Occupancy	
	Complex-A	**Complex-B**
1s (H2)	0.84017 (0.85005)[a]	0.84478 (0.85005)
2s (C1)	0.89695 (0.89304)[a]	0.89521 (0.89304)
$2p_x$ (C1)	0.74849 (0.55904)[a]	0.76276 (0.55904)
$2p_y$ (C1)	0.55752 (0.55904)[a]	0.55807 (0.55904)
$2p_z$ (C1)	0.77547 (0.96184)[a]	0.75691 (0.96184)
2s (F3)	1.86089 (1.85792)[a]	1.86020 (1.85792)
$2p_x$ (F3)	1.89127 (1.93741)[a]	1.68206 (1.93741)
$2p_y$ (F3)	1.93062 (1.66002)[a]	1.93295 (1.66002)
$2p_z$ (F3)	1.69069 (1.09070)[a]	1.89822 (1.09070)
1s (H7)	0.69707 (0.70418)[b]	0.70019 (0.70418)
3s (Cl6)	1.89223 (1.89351)[b]	1.89026 (1.89351)
$3p_x$ (Cl6)	1.77450 (1.99546)[b]	1.42576 (1.99546)
$3p_y$ (Cl6)	1.98619 (1.99546)[b]	1.99304 (1.99546)
$3p_z$ (Cl6)	1.62755 (1.38795)[b]	1.97393 (1.38795)
% 's' character		
H2	99.82 (99.82)	99.82 (99.82)
C1	31.69 (31.34)	31.52 (31.34)
% 'p' character		
H2	0.18 (0.18)	0.18 (0.18)
C1	68.20 (68.54)	68.36 (68.54)

[a]Occupancy of monomeric CHF_3 is given in parentheses
[b]Occupancy of monomeric HCl is given in parentheses

interactions are smaller, they cannot be neglected. It is clear from table 3.5 that as a result of delocalization, the occupancies of all donor orbitals decreased with respect to the monomer, while there is an increase in the occupancy of acceptor orbitals except for the fluorine lone pair, n^3F3, whose occupancy is more than in the monomer even after its donation to the antibonding σ*(Cl6-H7) orbital by hyperconjugation. The reason for observing the increased occupancy is the delocalization of the lone pair on chlorine (n^3Cl6) and the bond pair of H-Cl (σ(Cl6-H7)) into the lone pairs of fluorine atom. In addition, electrons transfer to the σ*(C1-H2) acceptor orbital, and an increased electron density at the fluorine atoms leads to elongation of the C1-F3 bonds followed by a geometrical rearrangement of the CHF_3 submolecule that causes a contraction of the C-H bond. This observation is consistent with the prediction made by van der Veken and Hobza and co-workers [50].

In addition, the increase in C1-F3 bond length could also be attributed to (i) σ(Cl6-H7) → σ*(C1-F3) (*bond pair-acceptor orbital interaction*) and (ii) n^1Cl6 → σ*(C1-F3) (*remote delocalization*) charge-transfer interactions. The occupancy of n^1Cl6 and σ(Cl6-H7) donor orbitals was found to decrease with an increase in the occupancy of σ*(C1-F3) orbital with respect the CHF_3/HCl monomers, thereby supporting the partial electron delocalization interactions in the donor-acceptor orbitals discussed above. It is noteworthy to mention that the occupancy of '2s' valence orbital of carbon atom increased with respect to the CHF_3 monomer, and hence the '% s' character of carbon atom increased marginally (increase of the occupancy of the '2s' orbital of carbon also supports the increase of '%s' character as shown in table 3.7). This effect can also result in the decrease in the C-H bond length as suggested by Alabugin et al. [68] It can be summarized that the charge-transfer delocalization, such as n^3Cl6 ⟶ σ*(C1-H2), that contributes to the bond elongation is offset by other delocalization effects that increase the occupancy of the fluorine lone pairs. In addition, remote delocalization and *bond pair-acceptor orbital*

interaction elongate the C1-F3 bond while the C-H bond length gets contracted. Hence, there is a blue-shift in the C-H stretching frequency. It is needless to say that the charge-transfer interaction ($n^1F3 \rightarrow \sigma^*(Cl6\text{-}H7)$) is responsible for making the H-Cl stretch red-shifted.

The case of complex-B is interesting. Unlike the complex-A, in complex-B, there is no direct delocalization effect operating that can elongate the C-H bond. It is clear from table 3.5 that the principal delocalization interactions are charge-transfer interactions ($n^1F3 \rightarrow \sigma^*(Cl6\text{-}H7)$, $n^2F3 \rightarrow \sigma^*(Cl6\text{-}H7)$), bond pair-acceptor orbital interactions ($\sigma(Cl6\text{-}H7) \rightarrow \sigma^*(C1\text{-}F3)$), and remote delocalization interactions ($n^1Cl6 \rightarrow \sigma^*(C1\text{-}F3)$), which increase the C1-F3 bond length. Further, there is an increase in the '%s' character of the carbon atom. All the factors mentioned above are responsible for the contraction of C-H bond length that induces a blue-shift in the vibrational wavenumber (Tables 3.3 and 3.3a).

A comparison of the NBOs of monomer and complexes A and B revealed that the intramolecular hyperconjugation was impeded for the complex B. The $n^2F3 \rightarrow \sigma^*(C1\text{-}H2)$ donor-acceptor interaction, present in the CHF_3 monomer decreases because of the intermolecular hyperconjugative delocalization ($n^2F3 \rightarrow \sigma^*(Cl6\text{-}H7)$) in the complex formation (Table 3.5). It is clear from table 3.5 that the E_2 energy for $n^2F3 \rightarrow \sigma^*(C1\text{-}H2)$ delocalization in the complexes decreased by ~ 0.4 kcal/mol in comparison with the CHF_3 monomer. Nonetheless, $nCl6 \rightarrow \sigma^*(C1\text{-}H2)$ delocalization is responsible for the increase in the C-H bond length, the opposite effect of compression that is introduced because the lone pairs on fluorine are engaged in intermolecular hyperconjugation in complexes making them unavailable for intramolecular hyperconjugation, as should otherwise elongate the C-H bond. This interaction could be one of the reasons for only the marginal increase of the occupancy of $\sigma^*(C1\text{-}H2)$ orbital with respect to the monomer. As a corollary to the existing concepts based on charge-transfer interaction on blue-shifted H-bonding, we propose that *bond pair-acceptor orbital* charge-transfer delocalization and the role of intramolecular

hyperconjugation are also contributing factors for the blue-shifting of the vibrational frequencies. Therefore, it can be concluded that whether or not the delocalization interactions leading to C-H bond elongation are present, the other effects dominate and are responsible for C-H bond contraction.

3.3 Interaction of fluoroform (CHF_3) with water (H_2O)

As a result of hydrogen bonding in CHF_3-H_2O complex, *ab initio* computations exhibited a blue shift in the C-H stretching region of CHF_3 submolecule. In this work, we have investigated whether the blue shifting in CHF_3-H_2O complex can be experimentally discerned in Ar and Ne matrixes using matrix isolation infrared spectroscopy. The structure of the complex and the energies were computed at MP2 level of theory using a 6-311++G(d,p) and aug-cc-pVDZ basis sets.

3.3.1 Experimental details

CHF_3 (Air products, USA, Electronic Grade) was used as such without further purification. De-ionized water was purified by first chilling it to temperatures of ≈170 K, and then pumping on it to eliminate volatile impurities. High purity Argon (INOX, 99.9995%) and Neon (Chemtron, 99.995%) were used as matrix gases. A twin-jet nozzle system was used to co-deposit CHF_3 and H_2O by streaming them separately onto the cold substrate. A gas mixture of CHF_3 with Ar/Ne gas in the required ratio is prepared, in the mixing chamber, and this gas mixture was subsequently allowed to pass through the nozzle and deposited onto the KBr substrate through a fine needle valve. A temperature range of ~ -80 to -75 ºC kept for water in the bulb to control its concentration in the matrix and deposited through a second nozzle. The matrix to solute ratio varied between 1/0.5/1000 to 2/1/1000 for CHF_3/H_2O/Ar or CHF_3/H_2O/Ne. Infrared spectra of matrix isolated samples were recorded using Bruker Vertex 70 FTIR spectrometer. All the spectra shown in this report were those recorded after annealing the matrix. When CHF_3 with varying concentrations of H_2O was co-deposited and annealed, new features were produced in the υ_1 C-H stretching mode of CHF_3 at 3064.7 cm^{-1} in Ar matrix and the corresponding feature in Ne matrix was observed at 3066.1 cm^{-1} (fig. 3.6b-c block A and block B). Figure 3.6a (block A and B) shows the uncomplexed CHF_3 spectra in Ar and Ne matrixes. The feature observed at 3058.4 and 3064.4 cm^{-1} in Ar and Ne

matrixes, respectively is due to the aggregates of CHF_3 [78]. The site split features found at 1148.0/1145.5 cm^{-1} are due to the doubly degenerate υ_5 mode of CHF_3 in Ar matrix, and the corresponding peak was observed at 1151.1 cm^{-1} in Ne matrix (fig. 3.7a block A and block B). Co-deposition of CHF_3 and H_2O and subsequent annealing showed an increase in intensity of the doublet feature observed at 1138.3, 1135.6 cm^{-1} in Ar and at 1139.0 cm^{-1} in Ne matrix (fig. 3.7b-c block A and block B). Further, a new feature observed at 1146.0 cm^{-1} increase in intensity on annealing in Ne matrix. CHF_3 multimeric features were observed at 1138.3 and 1139.0 cm^{-1} in Ar and Ne matrixes, respectively [70]. The feature observed at 1135.6 and 1137.8 cm^{-1} is due to the υ_2 mode of CHF_3 in Ar and Ne matrixes, respectively (fig. 3.7a block A and block B). In the annealed matrix, a new feature in the υ_2 mode of CHF_3 submolecule appears at 1127.7 cm^{-1} and 1133.9 cm^{-1} in Ar and Ne matrixes, respectively. In the υ_2 mode, the CHF_3 aggregate feature is observed at 1129.6 cm^{-1} in Ar and 1126.0 cm^{-1} in Ne matrix [78]. Figure 3.8 shows the IR absorption spectrum in the υ_4 C-H bending region of CHF_3 in Ar matrix covering the region 1420-1350 cm^{-1}. The feature observed at 1376.2 cm^{-1} is due to the doubly degenerate υ_4 mode in an Ar matrix. Co-deposition and subsequent annealing of the precursors produced a new feature in the υ_4 mode of CHF_3 at 1387.6 cm^{-1}. In the υ_4 C-H bending region of CHF_3 submolecule in Ne matrix, new feature could not be observed. Figure 3.9 show the υ_3 anti-symmetric O-H stretching region of H_2O in Ar matrix covering the region 3800-3680 cm^{-1}. In Ar matrix, the three intense features for rotating H_2O molecule was observed at 3776.8 ($1_{01}\rightarrow2_{02}$), 3756.0($0_{00}\rightarrow1_{01}$), 3711.0 ($1_{01}\rightarrow0_{00}$) cm^{-1}. The proton acceptor and donor band for the H_2O dimer were found in Ar matrix at 3724.4 and 3699.3 cm^{-1}, respectively. The monomer and dimer features observed for the H_2O in Ar and Ne matrixes agreed well with the reported literature value [214,215]. When CHF_3 and H_2O were co-deposited and annealed, new feature was observed at 3727.8 cm^{-1} in Ar matrix. In the υ_3 anti-symmetric O-H stretching

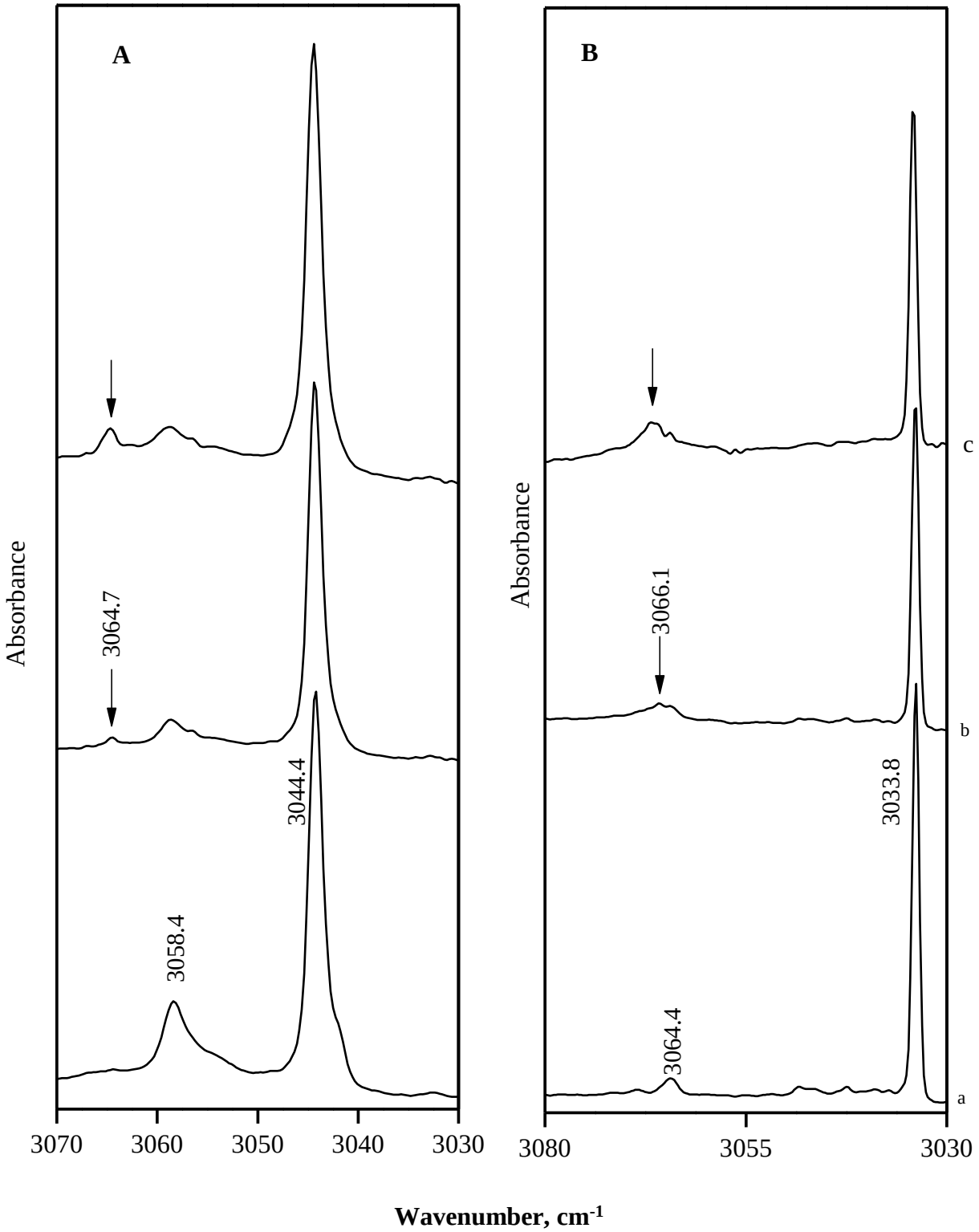

Figure 3.6: Matrix isolated infrared spectra of CHF_3/H_2O; block A in Ar matrix covering in the region 3070-3030 cm^{-1} and block B in Ne matrix covering the region 3080-3030 cm^{-1}. Spectra for various concentrations of CHF_3/H_2O/Ar or Ne (a) 2/0/1000; (b) 2/0.5/1000; (c) 2/1/1000. Block A and B correspond to 35 K and 9 K annealed spectra respectively.

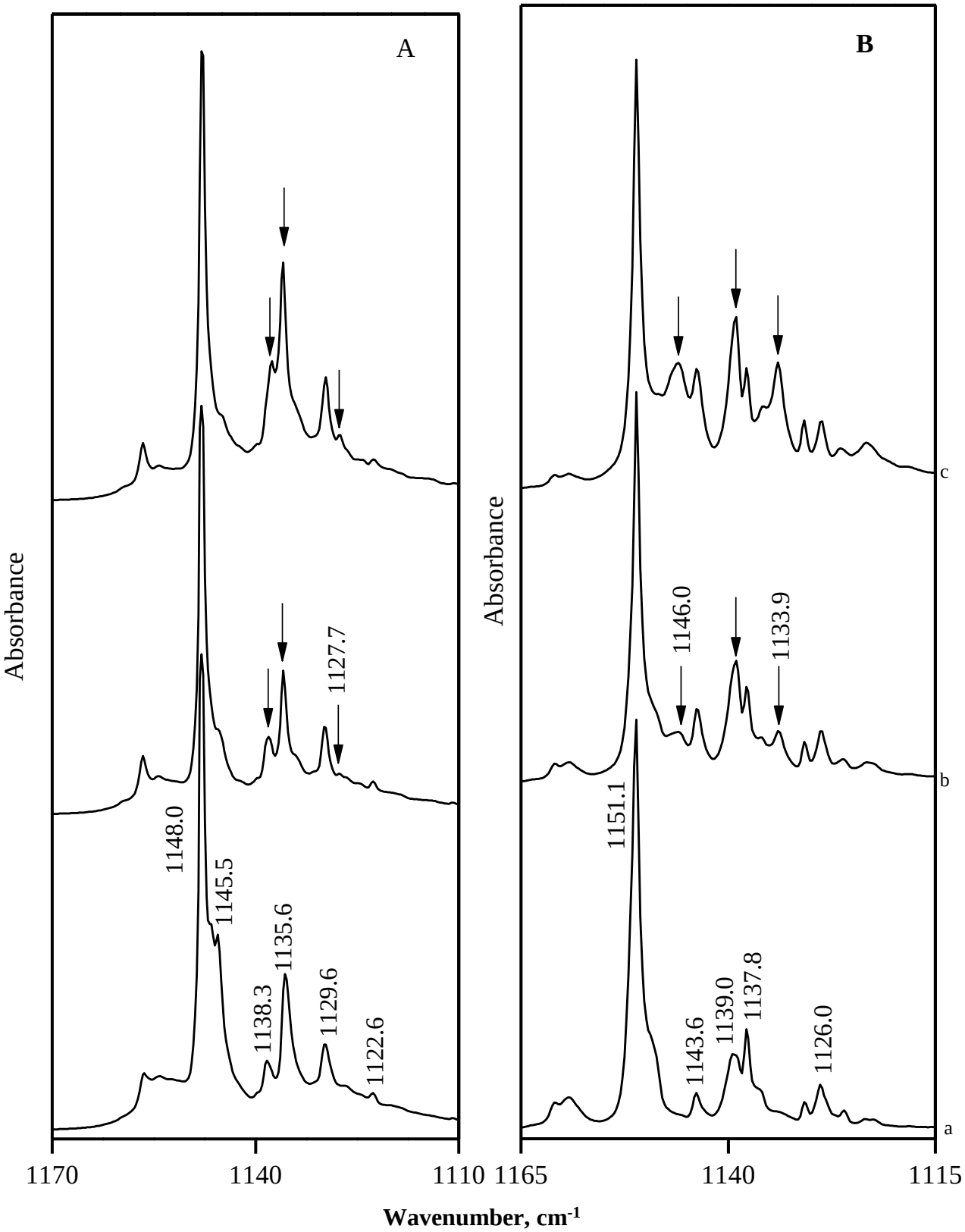

Figure 3.7: Matrix isolated infrared spectra of CHF_3/H_2O; block A in Ar matrix covering in the region 1170-1110 cm^{-1} and block B in Ne matrix covering the region 1165-1115 cm^{-1}. Spectra for various concentrations of CHF_3/H_2O/Ar or Ne (a) 2/0/1000; (b) 2/0.5/1000; (c) 2/1/1000. Block A and B correspond to 35 K and 9 K annealed spectra respectively.

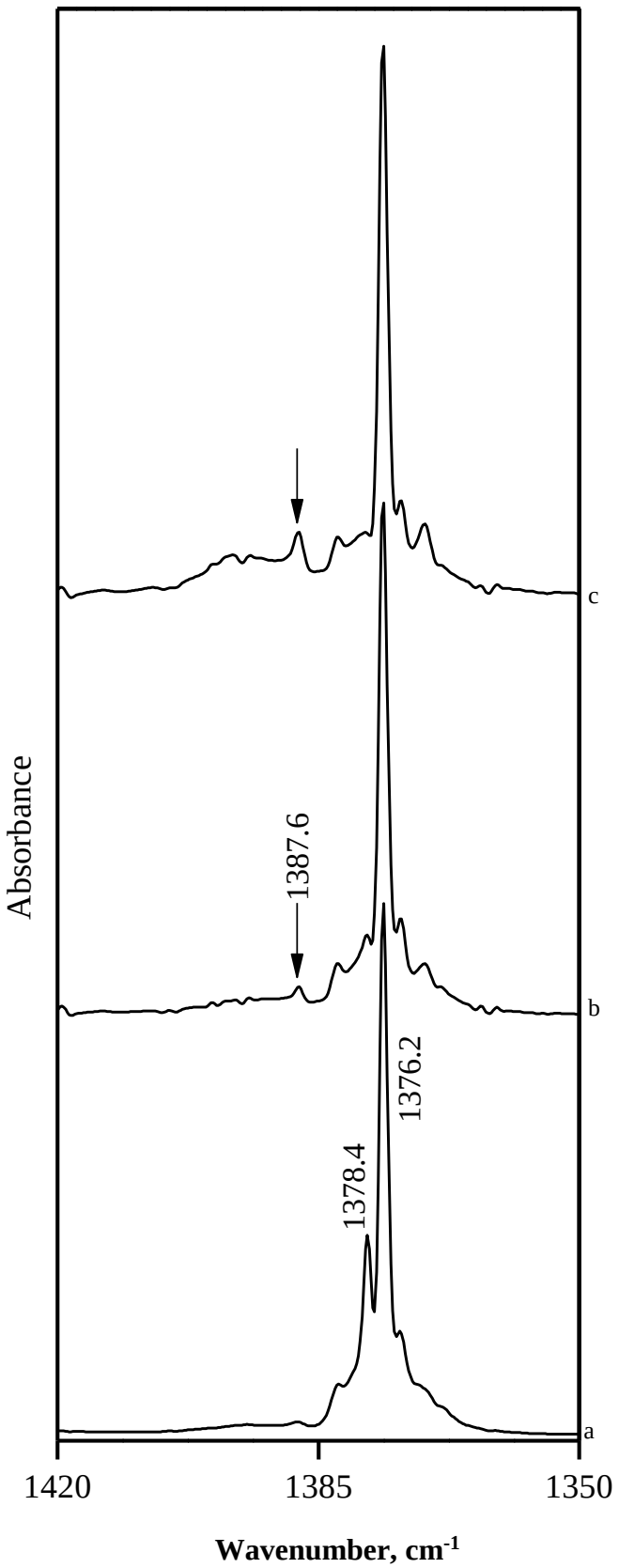

Figure 3.8: Matrix isolated infrared spectra of $CHF_3/H_2O/Ar$ covering in the region 1420-1350 cm^{-1}. Spectra for various concentrations of $CHF_3/H_2O/Ar$ (a) 2/0/1000; (b) 2/0.5/1000; (c) 2/1/1000. Spectra shown here were annealed at 35 K.

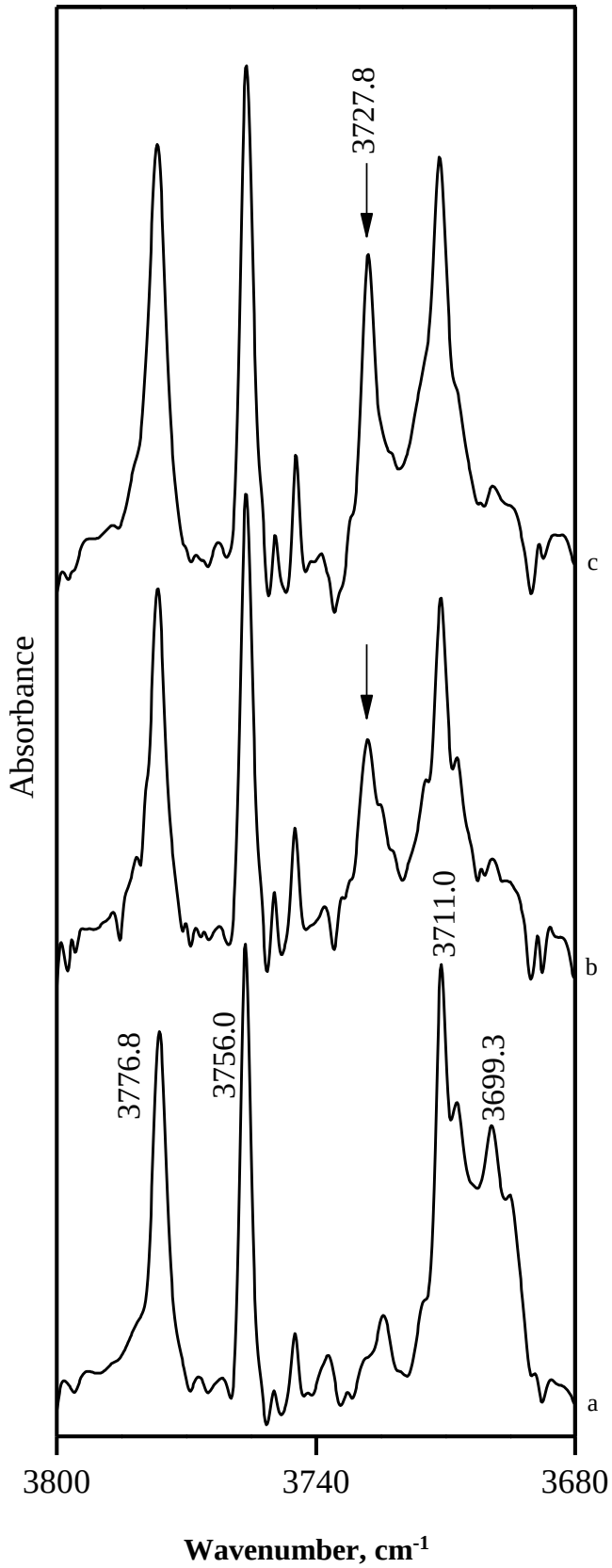

Figure 3.9: Matrix isolated infrared spectra of $CHF_3/H_2O/Ar$ covering the region 3800-3680 cm^{-1}. Spectra for various concentrations of $CHF_3/H_2O/Ar$ (a) 0/1/1000; (b)1/1/1000; (c) 2/1/1000. Spectra shown here were annealed at 35 K.

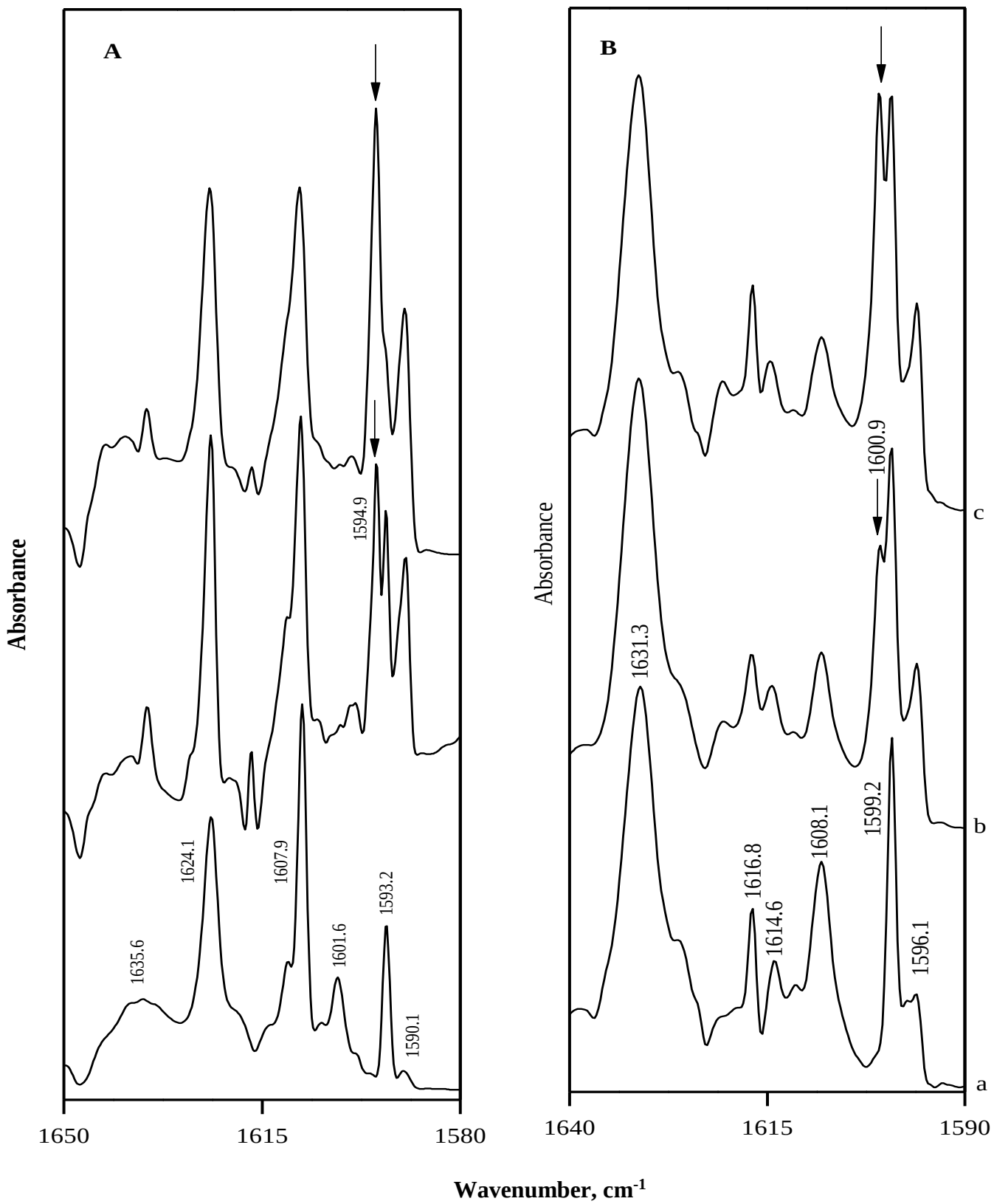

Figure 3.10: Matrix isolated infrared spectra of CHF_3/H_2O; block A in Ar matrix covering the region 1650-1580 cm^{-1} and block B in Ne matrix covering the region 1640-1590 cm^{-1}. Spectra for various concentrations of CHF_3/H_2O/Ar or Ne (a) 0/1/1000; (b) 1/1/1000; (c) 2/1/1000. Block A and B correspond to 35 K and 9 K annealed spectra respectively.

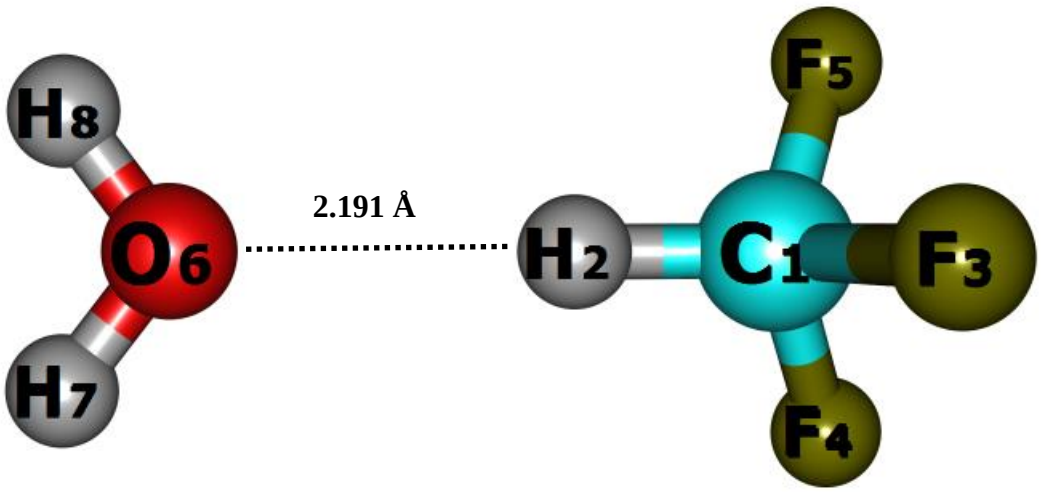

CHF_3-H_2O complex

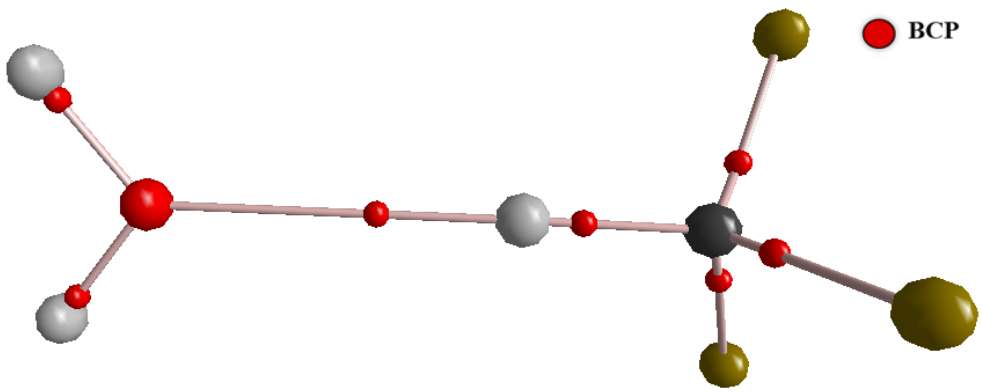

Figure 3.11: Structure of CHF_3-H_2O complex computed at MP2/aug-cc-pVDZ level of theory showing the bond critical point (BCP) between CHF_3 and H_2O.

region of H_2O submolecule in Ne matrix, new feature could not be discerned for the complex. Figure 3.10 block A (1650-1580 cm^{-1}) and block B (1640-1590 cm^{-1}) shows the O-H bending region of H_2O in Ar and Ne matrixes. The three most intense features observed at 1607.9 ($1_{01}\rightarrow1_{10}$), 1624.1 ($0_{00}\rightarrow1_{11}$), and 1635.6 ($1_{01}\rightarrow2_{12}$) cm^{-1} are due to rotating H_2O molecule in Ar matrix and the corresponding feature observed in Ne matrix at 1614.6, 1631.3 and 1649.9 cm^{-1} (not shown in the figure). The feature found at 1590.1 and 1596.1 cm^{-1} in Ar and Ne matrixes, respectively is due to the non-rotating monomer for the υ_2 bending mode of H_2O. The features observed at 1593.2, 1607.9 cm^{-1} in Ar matrix and 1599.2 and 1616.8 cm^{-1} are due to proton acceptor and proton donor of H_2O dimer, respectively [214,215]. Co-deposition of CHF_3 and H_2O and subsequent annealing the matrix, produced new feature at 1594.9 and 1600.9 cm^{-1} in Ar and Ne matrixes, respectively.

3.3.2 Computational

Calculations performed at the MP2 level of theory using 6-311++G(d,p) and aug-cc-pVDZ basis sets yielded *only* one minimum corresponded to a C-H⋯O interaction for the CHF_3-H_2O complex (fig. 3.11). For the complex, the primary interaction is between hydrogen H2 of fluoroform and oxygen O6 of water and the bond distance is 2.191 Å at MP2 level of theory with aug-cc-pVDZ basis set. Tables 3.8 and 3.8a gives the selected structural parameters for the complex at MP2 level of theory using 6-311++G(d,p) and aug-cc-pVDZ basis sets. The optimized structure of the complex performed at MP2/6-311++G(d,p) levels of theory agrees well with the earlier computational work on the CHF_3-H_2O system [63,64,67-68]. Table 3.9 gives the stabilization energies and tables 3.10 and 3.10a compare the experimental and computed vibrational wavenumbers computed at the aforementioned level of theory.

3.3.3 Vibrational assignments

The experimental vibrational wavenumber of the CHF_3-H_2O complex was compared

Table 3.8: Selected structural parameters[a] for the CHF_3-H_2O complex calculated at MP2/6-311++G(d,p) level of theory.

Parameters	Complex
C1-H2	1.085 (1.088)[b]
C1-F3	1.342 (1.338)
C1-F4	1.342 (1.338)
C1-F5	1.342 (1.338)
O6-H2	2.194
O6-H7	0.960 (0.959)
O6-H8	0.960 (0.959)
∠H2-C1-F3	110.9 (110.4)
∠F4-C1-F5	108.1 (108.5)
∠O6-H2-C1	176.6
∠H7-O6-H8	104.1 (103.5)
tor∠O6-H2-C1-F4	-35.0
tor∠C1-H2-O6-H7	62.2
tor∠C1-H2-O6-H8	-117.4

Table 3.8a: Selected structural parameters[a] for the CHF_3-H_2O complex calculated at MP2/aug-cc-pVDZ level of theory.

Parameters	Complex
C1-H2	1.094 (1.096)[b]
C1-F3	1.356 (1.352)
C1-F4	1.356 (1.352)
C1-F5	1.356 (1.352)
O6-H2	2.191
O6-H7	0.966 (0.966)
O6-H8	0.966 (0.966)
∠H2-C1-F3	111.1 (110.6)
∠F4-C1-F5	107.9 (108.3)
∠O6-H2-C1	176.8
∠H7-O6-H8	104.2 (103.9)
tor∠O6-H2-C1-F4	-65.4
tor∠C1-H2-O6-H7	93.9
tor∠C1-H2-O6-H8	-79.7

[a]Bond lengths in Å, bond angles and dihedral angles in °.
[b]Parameters of the monomers are given in parentheses.

Table 3.9: Raw[a]/ZPE-corrected/BSSE-corrected stabilization energies for the CHF_3-H_2O complex computed at the MP2 level of theory using the 6-311++G(d,p) and aug-cc-pVDZ basis set.

Complex	Stabilization Energy (ΔE)	
	MP2/6-311++G(d,p)	**MP2/aug-cc-pVDZ**
CHF_3-H_2O	-4.6/-3.6/-3.5	-4.2/-3.5/-3.3

All energies are in kcal/mol (see text for details).
[a]Raw stabilization energies refer to energies not corrected for either ZPE or BSSE.

Table 3.10: Comparison of computed wavenumbers (υ, cm^{-1}), experimental vibrational wavenumbers (υ, cm^{-1}), shift in the calculated ($\Delta\upsilon_{cal}$), and experimental vibrational wavenumbers ($\Delta\upsilon_{exp}$) in Ar and Ne matrixes computed at MP2/6-311++G(d,p) level of theory for the CHF_3-H_2O complex.

Computed/ unscaled	Computed $\Delta\upsilon^c_{cal}$	Ar			Ne		Mode assignment
		Exp[d]	$\Delta\upsilon^c_{exp}$	Exp[e]	Exp[d]	$\Delta\upsilon^c_{exp}$	
CHF_3							
1151.3(112)[a]	-	1135.6	-	1136.0	1137.8	-	υ_2 CF_3 sym. stretching mode in CHF_3(A)
1177.0 (335)	-	1148.0 1145.5	-	1148.0 1146.0	1151.1	-	υ_5 CF_3 def. stretching mode in CHF_3(E)
1425.7 (57)	-	1376.2	-	1376.0	1375.5	-	υ_4 C-H bending mode in CHF_3(E)
3223.1 (35)	-	3044.4	-	3043.0	3033.8	-	υ_1 C-H stretching mode in CHF_3(A)
H_2O							
1628.7 (57)	-	1590.1	-	1590.0	1595.6	-	υ_2 H-O-H bending of H_2O
3884.4 (13)	-	3637.9	-	3638.0	3665.6	-	υ_1 O-H symmetric of stretching of H_2O
4002.6 (62)	-	3732.9	-	3733.0	3761.1	-	υ_3 O-H anti-symmetric stretching of H_2O
CHF_3-H_2O Complex							
1141.7 (143)	-9.6	1127.7	-7.9	-[b]	1133.9	-3.1	υ_2 CF_3 sym. stretching mode in complex
1163.8 (343) 1163.1 (345)	-13.9 -13.2	1138.3 1135.6	-9.7 -12.4	-[b]	1146.0 1139.0	-5.1 -12.1	υ_5 CF_3 def. stretching mode of CHF_3 in complex
1448.1 (45) 1463.7 (41)	22.4 38.0	1387.6	11.4	1388.0 1392.0	-[b]	-	υ_4 C-H bending mode of CHF_3 in complex
3262.5 (1)	39.4	3064.7	20.3	-[b]	3066.1	32.3	υ_1 C-H stretching mode of CHF_3 in complex
1637.8 (71)	9.1	1594.9	4.8	1594.0	1600.9	5.3	υ_2 H-O-H bending mode of complex
3875.7 (17)	-8.7	-[b]	-	3634.0	-[b]	-	υ_1 O-H asymmetric stretching mode of
3994.6 (87)	-8.0	3727.8	-5.1	-[b]	-[b]	-	υ_3 O-H symmetric stretching mode of complex

[a]Computed infrared intensities (km/mol) are given in parentheses; [b]Experimental features were not observed; [c]$\Delta\upsilon = \upsilon_{complex} - \upsilon_{monomer}$; [d]This work; [e] Previous work Ref [78].

Table 3.10a: Comparison of computed wavenumbers (υ,cm^{-1}), experimental vibrational wavenumbers (υ, cm^{-1}), shift in the calculated ($\Delta\upsilon_{cal}$), and experimental vibrational wavenumbers ($\Delta\upsilon_{exp}$) in Ar and Ne matrixes computed at MP2/aug-cc-pVDZ level of theory for the CHF_3-H_2O complex.

Computed/ unscaled	Computed $\Delta\upsilon^c_{cal}$	Ar			Ne		Mode assignment
		Exp[d]	$\Delta\upsilon^c_{exp}$	Exp [e]	Exp[d]	$\Delta\upsilon^c_{exp}$	
CHF_3							
1118.6 (94)[a]	-	1135.6	-	1136.0	1137.8	-	υ_2 CF_3 sym. stretching mode in CHF_3(A)
1140.6 (299)	-	1148.0 1145.5	-	1148.0 1146.0	1151.1	-	υ_5 CF_3 def. stretching mode in CHF_3(E)
1379.6 (39)	-	1376.2	-	1376.0	1375.5	-	υ_4 C-H bending mode in CHF_3(E)
3221.1 (21)	-	3044.4	-	3043.0	3033.8	-	υ_1 C-H stretching mode in CHF_3(A)
H_2O							
1622.2 (67)	-	1590.1	-		1595.6	-	υ_2 H-O-H bending of H_2O
3803.4 (4)	-	3637.9	-	3638.0	3665.6	-	υ_1 O-H symmetric of stretching of H_2O
3937.7 (67)	-	3732.9	-	3733.0	3761.1	-	υ_3 O-H anti-symmetric stretching of H_2O
CHF_3-H_2O Complex							
1109.5 (129)	-9.1	1127.7	-7.9	-[b]	1133.9	-3.1	υ_2 CF_3 sym. stretching mode in complex
1126.9 (301) 1127.2 (303)	-13.7 -13.4	1138.3 1135.6	-9.7 -12.4	-[b]	1146.0 1139.0	-5.1 -12.1	υ_5 CF_3 def. stretching mode of CHF_3 in complex
1406.8 (35) 1417.1 (32)	27.2 37.5	1387.6	11.4	1388.0 1392.0	-[b]	-	υ_4 C-H bending mode of CHF_3 in complex
3250.3 (6)	29.2	3064.7	20.3	-[b]	3066.1	32.3	υ_1 C-H stretching mode of CHF_3 in complex
1626.9 (67)	4.7	1594.9	4.8	1594.0	1600.9	5.3	υ_2 H-O-H bending mode of complex
3800.9 (10)	-2.5	-[b]	-	3634.0	-[b]	-	υ_1 O-H asymmetric stretching mode of complex
3932.2 (83)	-5.5	3727.8	-5.1	-[b]	-[b]	-	υ_3O-H symmetric stretching mode of complex

[a]Computed infrared intensities (km/mol) are given in parentheses; [b]Experimental features were not observed; [c]$\Delta\upsilon = \upsilon_{complex} - \upsilon_{monomer}$; [d]This work; [e] Previous work Ref [78].

with the wavenumber calculated using MP2 level of theory with 6-311++G(d,p) and aug-cc-pVDZ basis sets (Tables 3.10 and 3.10a). The mode-by-mode scaling factors (Tables 3.10 and 3.10a) were used to correct the deficiencies of the theoretical model, to correct the matrix shifts, and to predict the band positions of the CHF_3-H_2O complex.

3.3.3.1 υ_1 C-H stretching mode of CHF_3

Co-deposition experiments in Ar and Ne matrixes produced new feature at 3064.7 and 3066.1 cm^{-1}, respectively, which amounts to a blue shift of 20.3 and 32.3 cm^{-1}. The experimental shift agrees well with the computed shift of 39.4 cm^{-1}. This agreement between the experimental and computed shift is a clear evidence that the CHF_3-H_2O complex is of C-H···O type as shown in figure 3.11. At all levels of theory, the υ_1 C-H stretching mode of CHF_3 submolecule in the complex showed a blue shift but the magnitude of the shift varied. The wavenumber difference between the experimental and the calculated value in Ar matrix is large (~19 cm^{-1}) when compared to Ne matrix (~7 cm^{-1}) could be attributed to the strength of interaction of Ar and Ne matrixes on the complex. The experimental shift reveals that Ar being more polarizable interacts strongly with the complex than Ne. When compared to Ne, Ar introduces a larger C-H bond elongation in the complex through its polarizability and subsequently the blue shift observed in the υ_1 C-H stretching mode of complex is less in the matrix. The blue-shifted feature is discerned clearly in both the matrixes even though the IR intensity reduced from 35 km/mol in the monomer to 1 km/mol in the CHF_3-H_2O complex (Tables 3.10 and 3.10a). It is also possible that the matrixes do play a significant role in enhancing the intensity of the complex.

3.3.3.2 υ_4 C-H bending mode of CHF_3

Computations showed on complex formation, the doubly degenerate C-H bending mode splits and occurs at 1448.1 and 1463.7 cm^{-1}, a blue shift of 22.4 and 38.0 cm^{-1}. Experimentally, only one feature was observed in an Ar matrix at 1387.6 cm^{-1}, yielding a blue shift of 11.4 cm^{-1}. The observed experimental shift of 11.4 cm^{-1} matches well with the computed shift of 22.4 cm^{-1}. In Ne matrix, new feature could not be discerned in this mode.

Non-observance of experimental vibrational feature in a particular mode depends upon factors such as infrared intensity of vibrational wavenumber of the complex and the shift of the vibrational feature due to the matrix effects. It is seldom possible that the perturbed mode may fall exactly on monomer absorption feature. Furthermore, the intensity and the vibrational shift in the complex is also matrix dependent. Due to the above reasons, the υ_4 C-H bending mode of CHF_3-H_2O complex is not clearly observed in Ne matrix.

3.3.3.3 υ_2 CF_3 symmetric stretching mode of CHF_3

In the co-deposition experiments, a new feature was observed at 1127.7 and 1133.9 cm^{-1} in Ar and Ne matrixes, a red shift of 7.9 and 3.1 cm^{-1}, which agree well with the computed shift of 9.6 cm^{-1}.

3.3.3.4 υ_5 deformation mode of CHF_3

The doubly degenerate mode gets split and computed to occur in the complex red shift by 13.9 and 13.2 cm^{-1} from the feature of the uncomplexed CHF_3 submolecule. Experimentally, features observed at 1138.3 and 1135.6 cm^{-1}, a red shift of 9.7 and 12.4 cm^{-1} in Ar matrix and 1146.0 and 1139.0 cm^{-1}, a red shift of 5.1 and 12.1 cm^{-1} in Ne matrix, which could be assigned to the CHF_3-H_2O complex based on its concentration dependence and its occurrence to the red of the υ_5 mode of the CHF_3 monomer. The features observed at 1138.3 and 1135.6 cm^{-1} are assigned to the higher aggregates in the υ_2 mode of CHF_3, respectively. As the concentration of H_2O was varied, the intensity of the features observed at 1138.3/1135.6 cm^{-1} and the relative ratio with the 1148.0 cm^{-1} feature increases. This observation clearly indicates the overlap of the complex feature with the features of CHF_3 aggregates. In Ne matrix, the complex feature appears at the same place (1139.0 cm^{-1}) where the multimeric absorption occurs.

3.3.3.5 H_2O anti-symmetric stretch (υ_3)

The experimental feature for this mode occurs at 3727.8 cm^{-1} in Ar matrix, which

amounts to a red shift of 5.1 cm^{-1} from the same mode of uncomplexed H_2O. This shift compares well with the computed shift of 8.0 cm^{-1} for this mode of CHF_3-H_2O complex. No new feature could be discerned in the υ_3 mode of H_2O in the Ne matrix.

3.3.3.6 H_2O bending (υ_2)

The υ_2 mode of the H_2O submolecule in the CHF_3-H_2O complex was observed at 1594.9 and 1600.9 cm^{-1}, which amounts to a blue shift of 4.8 and 5.3 cm^{-1} in Ar and Ne matrixes, respectively from the feature of the uncomplexed H_2O. This experimental shift compares well with the computed shift of 9.1 cm^{-1} for the CHF_3-H_2O complex.

3.3.4 Nature of the interaction: AIM analysis

AIM theory was used to analyze the nature of the interaction in CHF_3-H_2O complex [216]. A (3,1) bond critical point (BCP) located between the hydrogen of CHF_3 and oxygen of H_2O for the complex. Table 3.11 gives the properties of the intermolecular (3,-1) BCP for CHF_3-H_2O complex computed at MP2/6-311++G(d,p) level of theory. As can be seen from the table that the magnitude of $\rho(r_c)$ and $\nabla^2\rho(r_c)$ at the BCP for the complex is the order of 10^{-2} a.u. The small values of $\rho(r_c)$ and small positive values for $\nabla^2\rho(r_c)$ are indicative of the weak nature of the interaction of the closed shell type. Table 3.11(b), (c) and (d) gives the properties for the BCP's on the neighbouring bonds corresponding to the C-H/C-F bond of CHF_3 and O-H bond of H_2O in the CHF_3 and H_2O submolecules. In order to compare, BCP values for monomeric CHF_3 and H_2O are also given in the same table. BCP's of the neighboring bonds show high positive values of $\rho(r_c)$ and high negative Eigen values of electron density, which is characteristic of shared covalent interaction.

A closer look at the BCP of C-H bond in the complex and the monomer revealed that the electron density $\rho(r_c)$ is slightly higher (10^{-3}a.u.) in the complex (Table 3.11b) than the monomer, which is responsible for shortening of the C-H bond in the complex and the concomitant blue shift in the C-H stretching wavenumber. The C-F and O-H BCP's showed

a decrease in the electron density $\rho(r_c)$ in the complex, which resulted in the red shift of the stretching wavenumber (Table 3.11c and d).

3.3.5 NBO analysis

NBO analysis of CHF_3-H_2O complex computed at MP2/6-311++G(d,p) level of theory. A closer look at the table 3.12 reveals there is an increase in the electron occupancy of antibonding orbitals σ*(C1-H2) of CHF_3 submolecule and σ*(O6-H7) and σ*(O6-H8) of H_2O submolecule relative to CHF_3 and H_2O monomers. Further, in the non-bonding orbitals n^1O6, n^2O6 and σ(O6-H7) bonding orbital of H_2O submolecule a reduction in electron occupancies was noticed. From the table 3.12, the second order perturbation E_2 energies for the n^2O6→σ*(C1-H2) delocalization interaction was found to be ~3.95 kcal/mol and this interaction is mainly responsible for the stabilization of the complex. Due to this delocalization interaction, one would except the C-H bond to elongate and associated red shift in the C-H stretching wavenumber of CHF_3 submolecule. On the contrary, we have observed the C-H bond contraction with a concomitant blue shift. The probable reason for this observation is explained in the following section.

As can be seen from the table 3.13, as a result of delocalization, there is a marginal increase in the fluorine lone pairs, whose occupancy is more than the monomer whereas the occupancies of all donor orbitals decreased with respect to the monomer. This increase in the electron density on the fluorine atoms leads to elongation of the C-F bond followed by a geometrical rearrangement of the CHF_3 submolecule that causes a contraction of the C-H bond. The C-F bond length in the complex increases (~0.0039 Å) relative to the monomer. Table 3.13 shows the Mulliken atomic charges of different atoms in complex relative to the monomer. The positive sign indicates the loss of charge and the negative sign indicates the gain of charge. From the table, it is clear that the atomic charges on the carbon atoms were found to decrease by ~ 0.180e whereas the charges on the fluorine atoms were found to

increase by ~0.026e. The increase in the charges on the fluorine atoms is responsible for the elongation of the C-F bond in the complex, which leads to shortening of the C-H bond and a corresponding blue shift in the C-H stretching vibrational wavenumber. As suggested by Alabugin et al. [68] we also found the %s character of carbon in the CHF_3-H_2O complex increased marginally high to the monomer, which could make the C-H bond to contract. It can be surmised that the other delocalization interaction mentioned above dominate when compared to the charge transfer delocalization $n^2O6 \rightarrow \sigma^*(C1\text{-}H2)$, which causes the C-F bond to elongate and in turn shorten the C-H bond and hence a blue shift in the C-H stretching wavenumber. In the O-H stretch of H_2O submolecule red shift with respect to H_2O monomer was observed for the complex, mainly due to the charge-transfer interaction ($\sigma(C1\text{-}H2) \rightarrow \sigma^*(O6\text{-}H7)$). Table 3.14 shows the intramolecular hyperconjugation interaction between donor (n^2F3) and acceptor ($\sigma^*C1\text{-}H2$)) in CHF_3 monomer and CHF_3-H_2O complex computed at MP2/6-311++G(d,p) level of theory. From the table, the E_2 energy for $n^2F3 \rightarrow \sigma^*(C1\text{-}H2)$ delocalization in the complex decreased by 1 kcal/mol relative to the CHF_3 monomer. This decrease in the energy for the complex clearly shows that the lone pair on fluorine is involved in the intramolecular hyperconjugation making the C-H bond contract rather than for intermolecular hyperconjugation, which otherwise makes the C-H bond to elongate. This intramolecular hyperconjugation may be responsible for the marginal increase in the occupancy of $\sigma^*(C1\text{-}H2)$ orbital with respect to the monomer.

Table 3.11: Properties of (3,-1) bond critical points in CHF_3-H_2O complexes computed at MP2/6-311++G(d,p) level of theory.

(a) Intermolecular BCP's in CHF_3-H_2O complex

Complex	**$\rho(r_C)$**	**$\nabla^2\rho(r_C)$**	**λ_1**	**λ_2**	**λ_3**	**$\lvert\lambda_1\rvert / \lambda_3$**
CHF_3-H_2O	-0.01382	0.01466	-0.01741	0.08817	0.08817	0.19745

(b) Intramolecular BCP's corresponding to the C-H bond in CHF_3 and CHF_3-H_2O complex

	$\rho(r_C)$	**$\nabla^2\rho(r_C)$**	**λ_1**	**λ_2**	**λ_3**	**$\lvert\lambda_1\rvert / \lambda_3$**
CHF_3	0.28976	0.304591	-0.87723	-0.877236	0.59543	1.47327
CHF_3-H_2O	0.30131	0.30872	-0.91155	-0.91143	0.61771	1.47569

(c) Intramolecular BCP's corresponding to the C-F bond in CHF_3 and CHF_3- H_2O complex

	$\rho(r_C)$	**$\nabla^2\rho(r_C)$**	**λ_1**	**λ_2**	**λ_3**	**$\lvert\lambda_1\rvert / \lambda_3$**
CHF_3	0.03349	0.273892	-0.63095	-0.55683	1.05379	0.59874
CHF_3-H_2O	0.03064	0.26996	-0.61839	-0.53659	1.03239	0.59898

(d) Intramolecular BCP's corresponding to the O-H bonds in CHF_3- H_2O complex

	$\rho(r_C)$	**$\nabla^2\rho(r_C)$**	**λ_1**	**λ_2**	**λ_3**	**$\lvert\lambda_1\rvert / \lambda_3$**
H_2O	0.62874	0.36440	-1.80389	-1.75947	1.04839	1.72062
CHF_3-H_2O	0.62912	0.36191	-1.80982	-1.76620	1.05952	1.70814

Table 3.12: Electron occupancies of various natural bond orbitals (NBO) of CHF_3-H_2O complex computed at MP2/6-311++G(d,p) level of theory along with donor-acceptor delocalization interaction and delocalization energies (E_2) are also shown.

NBO	Occupancy	Donor-acceptor delocalization interaction	Second order perturbation (E_2) energy (kcal/mol)
Lone pair → Acceptor orbital interactions			
n^2 O6 n^1O6	1.99688(1.99747)[a] 1.99340(1.99664)[a]	n^2 O6 → σ*(C1-H2)	3.95
Bond pair → Acceptor orbital interactions			
σ*(O6-H7)	0.00025(0.00000)[a]	σ(C1-H2) → σ*(O6-H7) σ(C1-H2) → σ*(O6-H8) σ(O6-H8) → σ*(C1-H2) σ(O6-H7) → σ*(C1-H2)	0.15 0.16 0.05 0.05
σ*(O6-H8)	0.00026(0.00000)[a]		
σ(C1-H2)	1.99442(1.99433)[b]		
σ(O6-H8)	1.99903(1.99925)[a]		
σ*(C1-H2)	0.03677(0.03921)[b]		
Lone pair occupancies			
LP (1) F 3 LP (2) F 3 LP (3) F 3	1.99423(1.99394)[b] 1.96949(1.96728)[b] 1.95914(1.95803)[b]		
LP (1) F 4 LP (2) F 4 LP (3) F 4	1.99425(1.99394)[b] 1.96957(1.96728)[b] 1.95928(1.95803)[b]		
LP (1) F 5 LP (2) F 5 LP (3) F 5	1.99424(1.99394)[b] 1.96954(1.96728)[b] 1.95923(1.95803)[b]		

[a]Occupancy of monomeric H_2O is given in parentheses.
[b]Occupancy of monomeric CHF_3 is given in parentheses.

Table 3.13: Mulliken atomic charges (e) and changes of atomic charges on the atoms of CHF_3 and CHF_3-H_2O complex and %s and p character computed at MP2/6-311++G(d,p) level of theory.

	C1	H2	F3	F4	F5	Δq(C1)	Δq(H2)	Δq(F3)	Δq(F4)	Δq(F5)
CHF_3	1.757	-0.164	-0.531	-0.531	-0.531	-	-	-	-	-
complex	1.937	-0.270	-0.555	-0.557	-0.557	0.180	-0.106	-0.024	-0.026	-0.026

Atom	CHF_3-H_2O
% s Character	
C1	31.56% (30.25%)[a]
H2	99.83% (99.86%)[a]
% p Character	
C1	68.23% (69.55%)[a]
H2	0.17% (0.14%)[a]

[a]Monomeric CHF_3 is given in parentheses.

Table 3.14: Comparison of donor (n^2F3)-acceptor (σ*(C1-H2)) delocalization interaction in CHF_3 monomer and in CHF_3-H_2O complex computed at MP2/6-311++G(d,p) level of theory.

Donor-acceptor delocalization interaction	Second order perturbation (E_2) energy (kcal/mol)	
	CHF_3	CHF_3-H_2O
$n^2F3 \rightarrow \sigma^*(C1\text{-}H2)$	9.12	7.94
$n^2F4 \rightarrow \sigma^*(C1\text{-}H2)$	9.12	7.88
$n^2F5 \rightarrow \sigma^*(C1\text{-}H2)$	9.12	7.90

3.4 Interaction of fluoroform (CHF_3) with benzene (C_6H_6) and acetylene (C_2H_2)

Blue-shifted hydrogen-bonded complexes of fluoroform (CHF_3) with benzene (C_6H_6) and acetylene (C_2H_2) have been investigated using matrix isolation infrared spectroscopy and *ab initio* computations.

3.4.1 Experimental details

CHF_3 (Air products, USA, Electronic Grade), liquid benzene (Analytical grade, purity: > 99%) and acetylene gas (commercial grade, Asiatic Oxygen Limited, India) were used as such without further purification. High purity Argon (INOX, 99.9995%) was used as a matrix gas. The required ratio of the gas mixture was obtained by mixing the CHF_3 and C_6H_6 or C_2H_2 with Ar and the gas mixture was allowed to pass through a single jet nozzle and deposited onto the KBr substrate. The concentration was varied in the range between 2/2/1000 to 2/4/1000 for $CHF_3/C_6H_6/Ar$ and 2/0.5/1000 to 2/1/1000 for $CHF_3/C_2H_2/Ar$. Infrared spectra of matrix isolated sample were recorded using Bruker Vertex 70 FTIR spectrometer.

3.4.2 Computations on the CHF_3-C_6H_6 and CHF_3-C_2H_2 complexes

As mentioned in the introduction chapter several theoretical groups have studied the blue-shifted C-H⋯π CHF_3-C_6H_6 hydrogen-bonded interaction [63,64,67,68]. *Ab initio* computation performed at MP2/aug-cc-pVDZ level of theory gave one minimum, which agreed well with the earlier computed results. Figure 3.12 shows the structure of the CHF_3-C_6H_6 dimer computed at MP2/aug-cc-pVDZ level of theory. For the CHF_3-C_6H_6 adduct, the bond distance between the hydrogen of CHF_3 and the carbons of C_6H_6 are ~ 2.609 Å. Furthermore, the bond angles between the C2-H1 of CHF_3 and the carbons of C_6H_6 are ~147.0° making a perfect T-shaped geometry with $C_{3\upsilon}$ symmetry. For the complex B stabilized by H⋯F interaction, the bond distances calculated between F3⋯H13, F5⋯H13 and F4⋯H16 were 2.820, 2.817 and 2.620 Å, respectively. The structural parameters of the

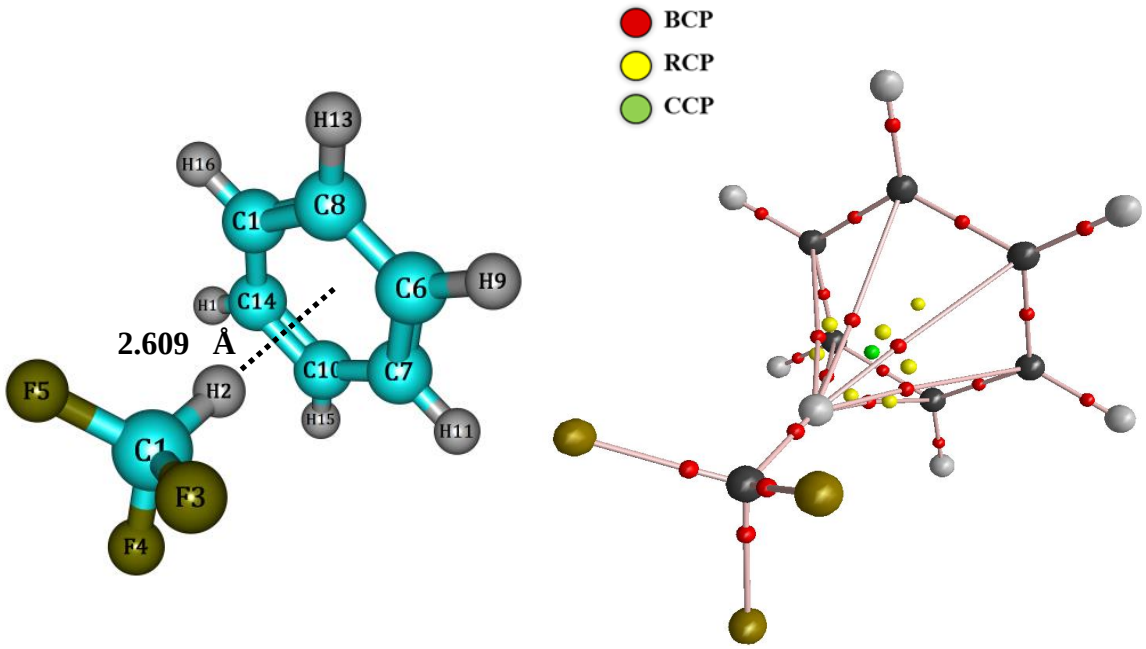

CHF_3-C_6H_6 Complex A

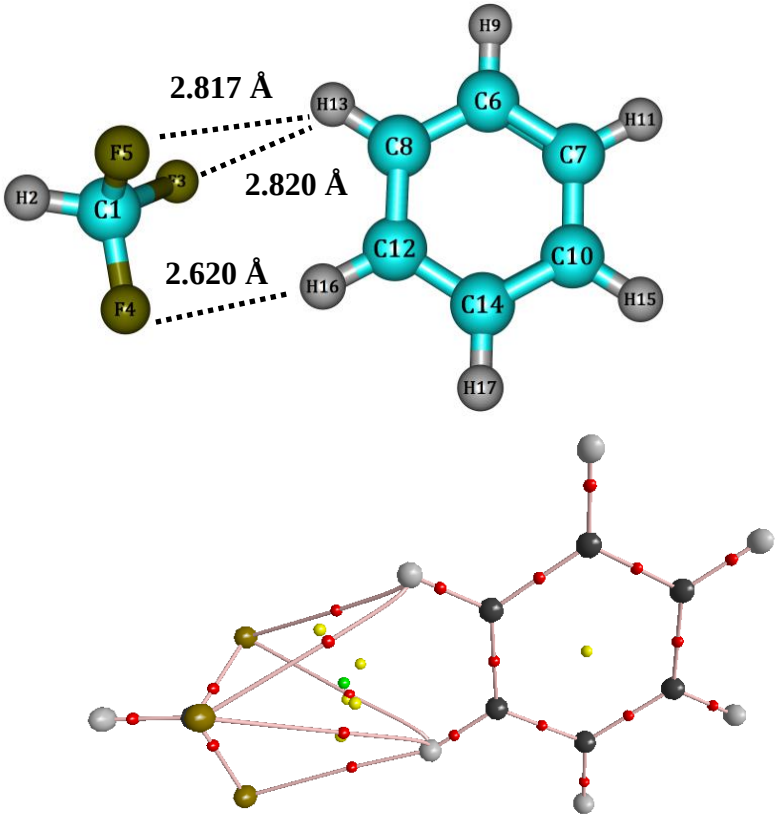

CHF_3-C_6H_6 Complex B

Figure 3.12: Structure of CHF_3-C_6H_6 hydrogen bonded complexes computed at MP2/aug-cc-pVDZ level of theory. Structures showing the bond critical points (BCP), ring critical point (RCP) and cage critical point (CCP) obtained from topological AIM analysis are also shown in the figure.

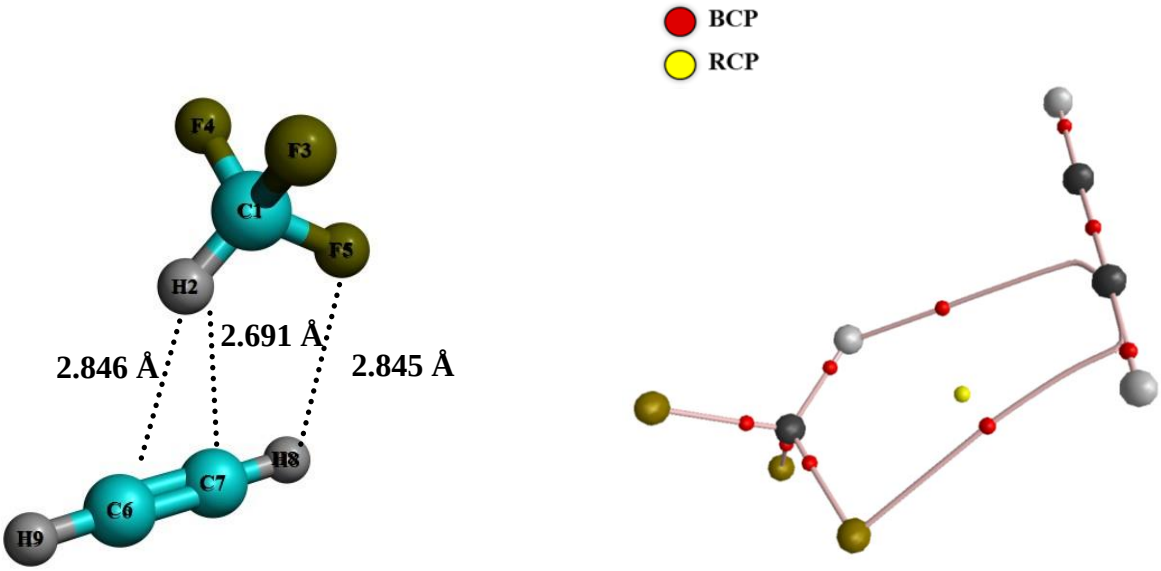

CHF_3-C_2H_2 Complex A

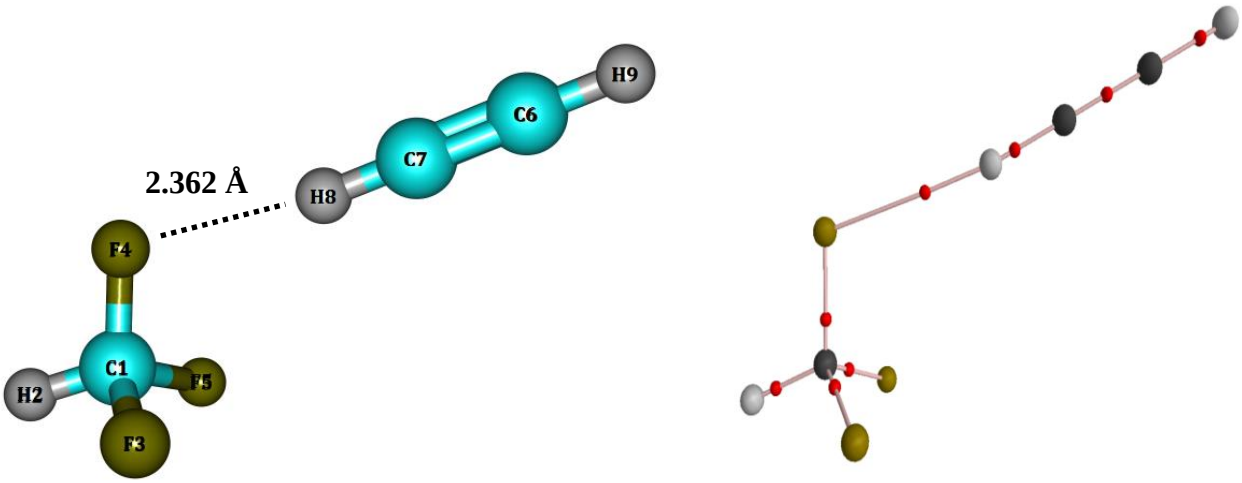

CHF_3-C_2H_2 Complex B

Figure 3.12a: Structure of CHF_3-C_2H_2 hydrogen bonded complexes A and B computed at MP2/aug-cc-pVDZ level of theory. Structure showing the bond critical points (BCP) and ring critical point (RCP) obtained from topological AIM analysis.

CHF_3-C_6H_6 complexes A and B computed at MP2/aug-cc-pVDZ level of theory is given in table 3.15.

For the CHF_3-C_2H_2 system computations showed two types of complexes, H⋯π (A) and n-σ (B), respectively, where the former complex is more stable than the latter. Figure 3.12a shows the structures of CHF_3-C_2H_2 complexes A and B. The stabilization energies (Raw, ZPE and BSSE corrected) for the CHF_3-C_6H_6 and CHF_3-C_2H_2 complexes computed at the MP2 and B3LYP levels of theory using 6-311++G(d,p) and MP2/aug-cc-pVDZ basis sets are given in table 3.16. From the table, it is clear that at all levels of theory with different basis sets CHF_3-C_6H_6 complex is more stable than the CHF_3-C_2H_2 complexes. Notably, the trends in the energies are found to be qualitatively similar for these complexes. At all levels of theory and basis set, the nature of the global and local minima was not altered. The deviation in the numerical values of stabilization energies arises due to the different basis sets and the methods used for computing the structure of the CHF_3-C_6H_6 and CHF_3-C_2H_2 complexes. Tables 3.17 and 3.17a gives the comparison of the experimental vibrational wavenumbers of the CHF_3-C_6H_6 and CHF_3-C_2H_2 complexes A and B with the wavenumbers calculated using the MP2/aug-cc-pVDZ level of theory. The deviation between the experimental and calculated wavenumbers is attributed to matrix shifts as well as to the deficiencies of the theoretical model. Since, at all levels of theory, for both CHF_3-C_6H_6 and CHF_3-C_2H_2 complexes, the one stabilized by C-H⋯π interaction is the global minimum and this structure is considered for vibrational assignments whereas the complex B (local minimum) does not assume any experimental significance. Anharmonic calculations were performed at MP2/aug-cc-pVDZ method using second order theory (VPT2) for the CHF_3-C_6H_6 and CHF_3-C_2H_2 complexes to compare with the harmonic vibrational wavenumber and the infrared intensities.

3.4.3 Results and discussion

Figure 3.13 block A and B shows the infrared spectra covering the region 3090-3040 cm^{-1}, which corresponds to the υ_1 C-H stretching region of CHF_3. In Ar matrix, the CHF_3 monomer absorption was observed at 3044.4 cm^{-1}. The feature observed at 3058.3 cm^{-1} is assigned to the aggregates of CHF_3, which agrees well with the reported literature value [78]. The features observed at 3046.8 and 3079.1 cm^{-1} are due to the C-H stretching mode (υ_2) of C_6H_6 in Ar matrix. (fig. 3.13b block A). When the concentrations of CHF_3 and C_6H_6/C_2H_2 were varied and annealed a new feature was observed in the C-H stretching region at 3076.7 cm^{-1} (fig. 3.13c-d block A) and 3052.1 cm^{-1} (fig. 3.13b-c block B), a blue shift of 32.3 and 7.7 cm^{-1} from the feature of uncomplexed CHF_3 submolecule, respectively. The experimental shifts agree well with the computed blue shift of 52.2 cm^{-1} and 18.2 cm^{-1} for the CHF_3-C_6H_6 and CHF_3-C_2H_2 complex A. This agreement between the experimental and computed shift is a clear evidence that the CHF_3-C_6H_6 and CHF_3-C_2H_2 adduct is of C-H⋯π type as shown in figure 3.12. The blue-shifted feature is discerned clearly in Ar matrix even though the IR intensity is reduced from 27 km/mol in the monomer to 0 km/mol for the CHF_3-C_6H_6 and 7 km/mol for the CHF_3-C_2H_2 adduct. This observation clearly shows that Ar matrix do play a significant role in enhancing the intensity of the blue-shifted feature in the complexes. Computations were also performed for the CHF_3-C_6H_6 and CHF_3-C_2H_2 complexes using the anharmonic approximation with MP2/aug-cc-pVDZ level of theory. The change in the infrared intensity and the vibrational wavenumber between anharmonic and harmonic calculations was found to be negligible. Further, the experimental blue shift of CHF_3-C_6H_6 complex (32.3 cm^{-1}) is more than that of CHF_3-C_2H_2 (7.7 cm^{-1}) keeping in trend with the larger basicity of C_6H_6 due to the delocalized π-electron cloud.

Figure 3.14 (block A and B) shows the infrared spectra of υ_4 C-H bending mode of CHF_3 over the region 1400-1350 cm^{-1}. The multiple site-split features observed at 1382.8,

1376.5, 1373.7 and 1370.8 cm^{-1} in Ar matrix are due to the doubly degenerate υ_4 C-H bending mode of CHF_3. Co-deposition and concentration variation with subsequent annealing of the precursors (C_6H_6 or C_2H_2) along with CHF_3 produced a new feature at 1371.7 cm^{-1} (fig. 3.14b-c, block A) and 1384.2 cm^{-1}(fig. 3.14b-c, block B), a red shift of 3.4 cm^{-1} and a blue shift of 8.9 cm^{-1}, respectively from the bare CHF_3 absorption. Computations showed that the υ_4 doubly degenerate mode occurs at 1372.7 cm^{-1} for the CHF_3-C_6H_6 dimer, a red shift of 6.9 cm^{-1}, which agrees well with the experimental shift of 3.4 cm^{-1}. For the CHF_3-C_2H_2 C-H⋯π adduct, computations showed the υ_4 doubly degenerate C-H bending mode of CHF_3 submolecule splits and occur at 1381.7 and 1389.0 cm^{-1}, a blue shift of 2.1 and 9.4 cm^{-1}. Experimentally, only one feature was observed at 1384.2 cm^{-1}, with a blue shift of 9.1 cm^{-1}, which agrees well with the computed shift of 9.4 cm^{-1} for the C-H⋯π complex A. The other blue-shifted feature (2.1 cm^{-1}) could not be observed as this feature probably overlaps with the feature of bare CHF_3 absorption.

Figure 3.15 blocks A and B corresponds to the υ_5 C-F stretching and υ_2 C-F symmetric stretching mode of CHF_3 covering the region 1155-1125 cm^{-1}. The doubly degenerate υ_5 mode occurs as a site split doublet at 1148.0 and 1145.5 cm^{-1}, while the υ_2 mode of CHF_3 was observed at 1135.9 cm^{-1} in Ar matrix. As the concentration of C_6H_6 was varied, the intensity of the feature observed at 1139.8 cm^{-1} increase in intensity. The experimental red shift of 7.0 cm^{-1} agrees well with the computed shift of 12.7 cm^{-1} from the uncomplexed CHF_3 absorption for the CHF_3-C_6H_6 complex in this mode.

Computations showed that the doubly degenerate υ_5 mode split and occurs at 1137.9 and 1131.1 cm^{-1} for the CHF_3-C_2H_2 C-H⋯π adduct. While the experimental feature observed at 1142.4 cm^{-1} (4.4 cm^{-1}) can be correlated with the computed feature at 1131.1 cm^{-1} (9.5 cm^{-1}), the other feature computed to occur at 1137.9 cm^{-1} (2.5 cm^{-1}) could not be observed as this feature might overlap with the site split feature of bare CHF_3.

Table 3.15: Selected structural parameters[a] for the CHF_3-C_6H_6 hydrogen-bonded complexes A and B computed at MP2/aug-cc-pVDZ level of theory.

Parameters	Complex-A	Complex-B
H2-C6	2.611	---
H2-C7	2.610	---
H2-C8	2.611	---
H2-C10	2.610	---
H2-C12	2.611	---
H2-C14	2.610	---
F3-H13	---	2.820
F3-H16	---	3.022
F5-H13	---	2.817
F5-H16	---	3.020
F4-H16	---	2.620
C8-H13	---	1.093
C12-H16	---	1.093
C1-H2	1.093 (1.096)[b]	1.096 (1.096)[b]
C1-F3	1.356 (1.352)	1.352 (1.352)
C1-F4	1.356 (1.352)	1.353 (1.352)
C1-F5	1.356 (1.352)	1.352 (1.352)
C-H bond $_{(benzene)}$	1.094 (1.094)	---
C-C bond $_{(benzene)}$	1.409 (1.408)	---
∠ C2- H1-C6	147.2	---
∠C1-F3-H13	---	100.2
∠C1-F5-H13	---	100.3
∠C1-F4-H16	---	95.8
∠ C2- H1-C7	147.5	---
∠ C2- H1-C8	147.0	---
∠ C2- H1-C10	147.7	---
∠ C2- H1-C12	147.1	---
∠ C2- H1-C14	147.4	---
∠F4-H16-C12	---	158.8
∠H2-C1-F3	111.0 (110.6)	---
Symmetry	$C_{3\upsilon}$	C_1

[a]Bond lengths in Å, bond angles and dihedral angles in °.
[b]Parameters of the monomers are given in brackets.

Table 3.16: Raw[a]/ZPE-corrected/BSSE-corrected stabilization energies for the CHF_3-C_6H_6 and CHF_3-C_2H_2 complexes computed at and MP2 level of theory using the 6-311++G(d,p) and aug-cc-pVDZ basis set and B3LYP level of theory using the 6-311++G(d,p) basis set.

Complexes	Stabilization Energy (ΔE)		
	MP2/6-311++G(d,p)	**MP2/aug-cc-pVDZ**	**B3LYP/6-311++G(d,p)**
CHF_3-C_6H_6 A	-5.8/-5.8/-3.0	-7.3/-6.4/-3.8	-2.1/-1.8/-1.7
CHF_3-C_6H_6 B	-2.5/-2.1/-0.4	-1.7/-1.4 /-0.8	-0.4/ -0.2/ -0.1
CHF_3-C_2H_2 A[b]	-2.4/-2.0/-1.4	-2.9/-2.5/-1.8	-1.3/-0.9/-1.2
CHF_3-C_2H_2 B[b]	-1.3/-0.6/-0.6	-1.8/-1.2/-0.6	-0.7/-0.4/-0.5

All energies are in kcal/mol (see text for details).
[a]Raw stabilization energies refer to energies not corrected for either ZPE or BSSE.
[b]Values taken from ref [97].

Table 3.17: Comparison of computed wavenumbers (υ, cm^{-1}), experimental wavenumbers (cm^{-1}), shift in the computed wavenumbers ($\Delta\upsilon_{cal}$)[b], and experimental vibrational wavenumbers ($\Delta\upsilon_{exp}$)[b] for the CHF_3-C_6H_6 and CHF_3-C_2H_2 complex A in Ar matrix computed at MP2/aug-cc-pVDZ level of theory.

Monomers		CHF_3-C_6H_6 Complex A				CHF_3-C_2H_2 Complex A				Mode assignment
Computed	Experiment	Computed		Experiment		Computed		Experiment		
		Complex	$\Delta\upsilon_{cal}$	Complex	$\Delta\upsilon_{exp}$	Complex	$\Delta\upsilon_{cal}$	Complex	$\Delta\upsilon_{exp}$	
1118.6 (94)[a]	1135.9	1111.4 (161)	-7.2	1131.6	-4.3	1113.0 (105)	-5.6	1132.5	-3.4	υ_2 CF_3 sym. stretching mode of CHF_3
1140.6 (300)	1148.0 1145.5	1127.9 (216)	-12.7	1139.8	-7.0[d]	1137.9 (281) 1131.1 (296)	-2.7 -9.5	1142.4	-4.4[d]	υ_5 CF_3 def. stretching mode of CHF_3
1379.6 (40)	1376.5 1373.7	1372.7 (40)	-6.9	1371.7	-3.4[d]	1381.7 (25) 1389.0 (42)	2.1 9.4	1384.2	9.1[d]	υ_4 C-H bending mode of CHF_3
3221.1 (21)	3044.4	3273.3 (0)	52.2	3076.7	32.3	3239.3 (7)	18.2	3052.1	7.7	υ_1 C-H stretching mode of CHF_3
C_6H_6 region										
678.2 (116)	675.0	691.0 (123)	12.8	683.2	8.2	-	-	-	-	υ_4 stretching mode of C_6H_6
C_2H_2 region										
702.9 (95)	736.9	-	-	-	-	707.1 (86) 714.4 (113)	4.2 11.5	741.8[c] 744.6[c]	4.9 7.7	υ_5 C–H bending mode of C_2H_2
3431.8 (93)	3288.9	-	-	-	-	3423.9 (105)	-7.9	3282.6[c]	6.3	υ_3 C–H assym. str. mode of C_2H_2

[a]Computed infrared intensities (km/mol) are given in parentheses

[b]$(\Delta\upsilon)_{cal/exp} = \upsilon_{complex} - \upsilon_{monomer}$

[c]Experimental vibrational wavenumbers taken from ref [97]

[d]Average doublet experimental wavenumbers of the monomer were taken to compute the experimental shift in the complexes ($\Delta\upsilon_{exp}$)

Table 3.17a: Comparison of computed wavenumbers (υ,cm^{-1}), experimental wavenumbers (υ, cm^{-1}), shift in the computed wavenumbers ($\Delta\upsilon_{cal}$)^b, and experimental vibrational wavenumbers ($\Delta\upsilon_{exp}$)^b for the CHF_3-C_6H_6 and CHF_3-C_2H_2 complex B in Ar matrix computed at MP2/aug-cc-pVDZ level of theory.

Monomers		CHF_3-C_6H_6 Complex B				CHF_3-C_2H_2 Complex B				Mode assignment
Computed	Experiment	Computed		Experiment		Computed		Experiment		
		Complex	$\Delta\upsilon_{cal}$	Complex	$\Delta\upsilon_{exp}$	Complex	$\Delta\upsilon_{cal}$	Complex	$\Delta\upsilon_{exp}$	
1118.6 (94)[a]	1135.9	1117.5 (127)	-1.1	-[c]	-	1115.1 (166)	-3.5	-[c]	-	υ_2 CF_3 sym. stretching mode of CHF_3
1140.6 (300)	1148.0 1145.5	1137.1 (216) 1140.4 (260)	-3.5 -0.2	-[c]	-	1133.8 (239) 1146.0 (283)	-6.8 5.4	-[c]	-	υ_5 CF_3 def. stretching mode of CHF_3
1379.6 (40)	1376.5 1373.7	1381.2 (27) 1381.6 (30)	1.6 2.0	-[c]	-	1376.6 (35) 1380.7 (37)	-3.0 1.1	-[c]	-	υ_4 C-H bending mode of CHF_3
3221.1 (21)	3044.4	3224.1 (33)	3.0	-[c]	-	3227.5 (22)	6.4	-[c]	-	υ_1 C-H stretching mode of CHF_3
C_6H_6 region										
678.2 (116)	675.0	680.8 (102)	2.6	-[c]	-	-	-	-	-	υ_4 stretching mode of C_6H_6
C_2H_2 region										
702.9 (95)	736.9	-	-	-[c]	-	731.4 (77) 733.8 (76)	28.5 30.9	-[c]	-	υ_5 C–H bending mode of C_2H_2
3431.8 (93)	3288.9	-	-	-[c]	-	3432.7 (144)	0.9	-[c]	-	υ_3 C–H assym. str. mode of C_2H_2

[a]Computed infrared intensities (km/mol) are given in parentheses

[b]$(\Delta\upsilon)_{cal/exp} = \upsilon_{complex} - \upsilon_{monomer}$

[c]Experimentally features were not observed.

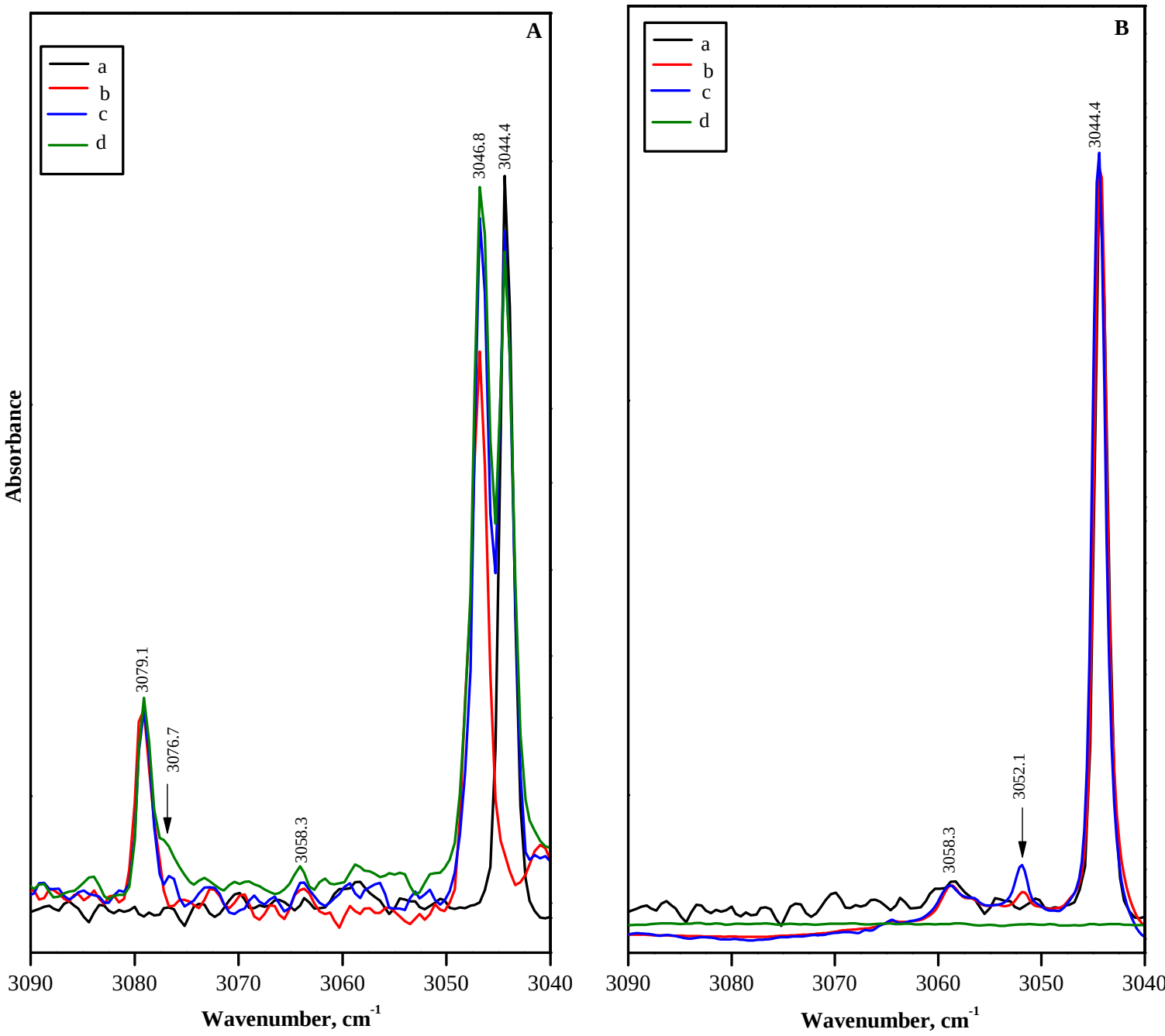

Figure 3.13: Infrared spectra covering the region 3090-3040 cm^{-1} in Ar matrix. Matrix isolation spectra for various concentrations of CHF_3/C_6H_6 /Ar in block A (a) 2/0/1000; (b) 0/4/1000; (c) 2/2/1000;(d) 2/4/1000. For CHF_3/C_2H_2/Ar in block B (a) 2/0/1000; (b) 2/0.5/1000; (c) 2/1/1000; (d) 0/1/1000.

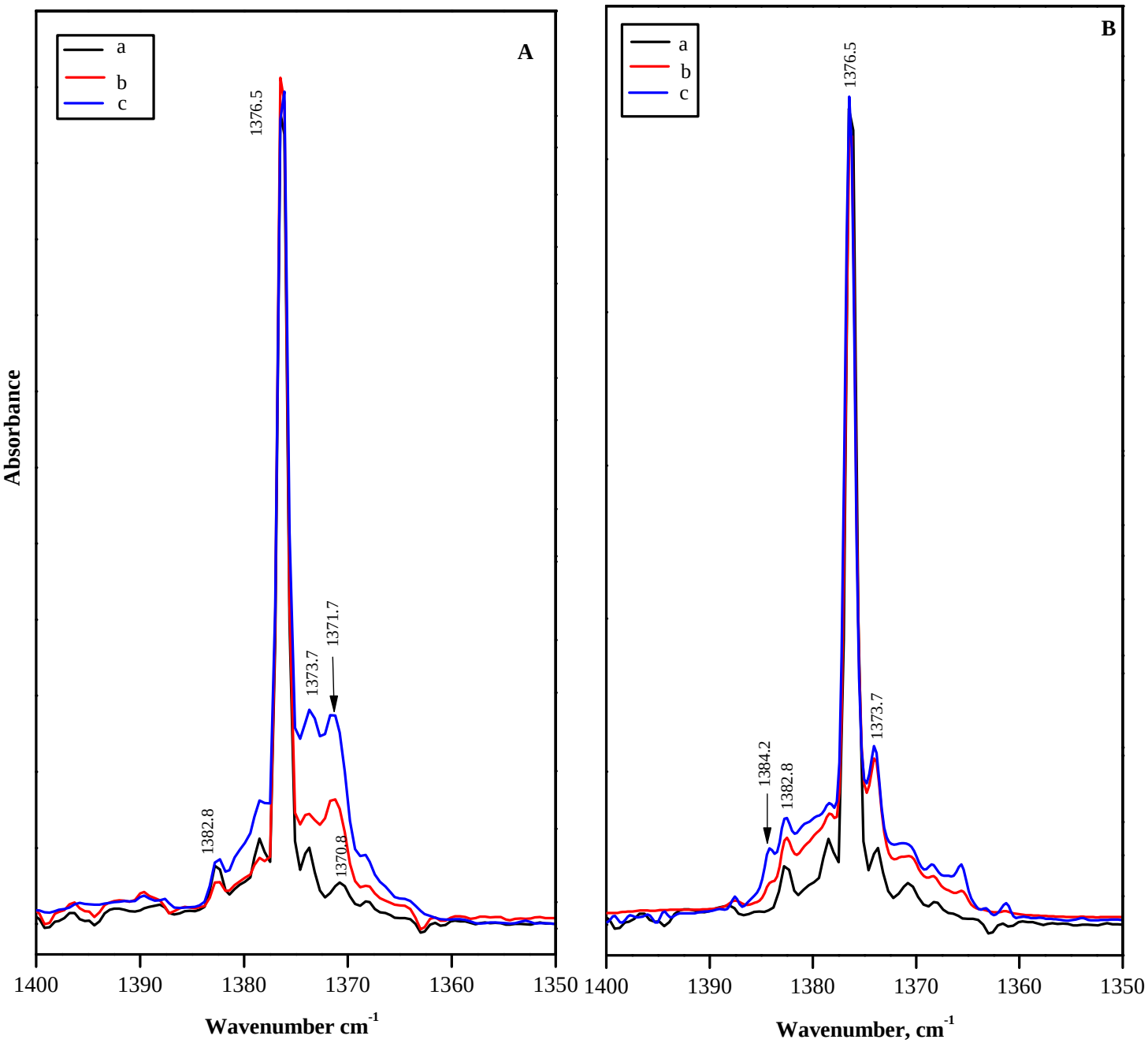

Figure 3.14: Infrared spectra covering the region 1400-1350 cm^{-1} in Ar matrix. Matrix isolation spectra for various concentrations of CHF_3/C_6H_6 /Ar in block A (a) 2/0/1000; (b) 2/2/1000; (c) 2/4/1000. For CHF_3/C_2H_2 /Ar in block B (a) 2/0/1000; (b) 2/0.5/1000; (c) 2/1/1000.

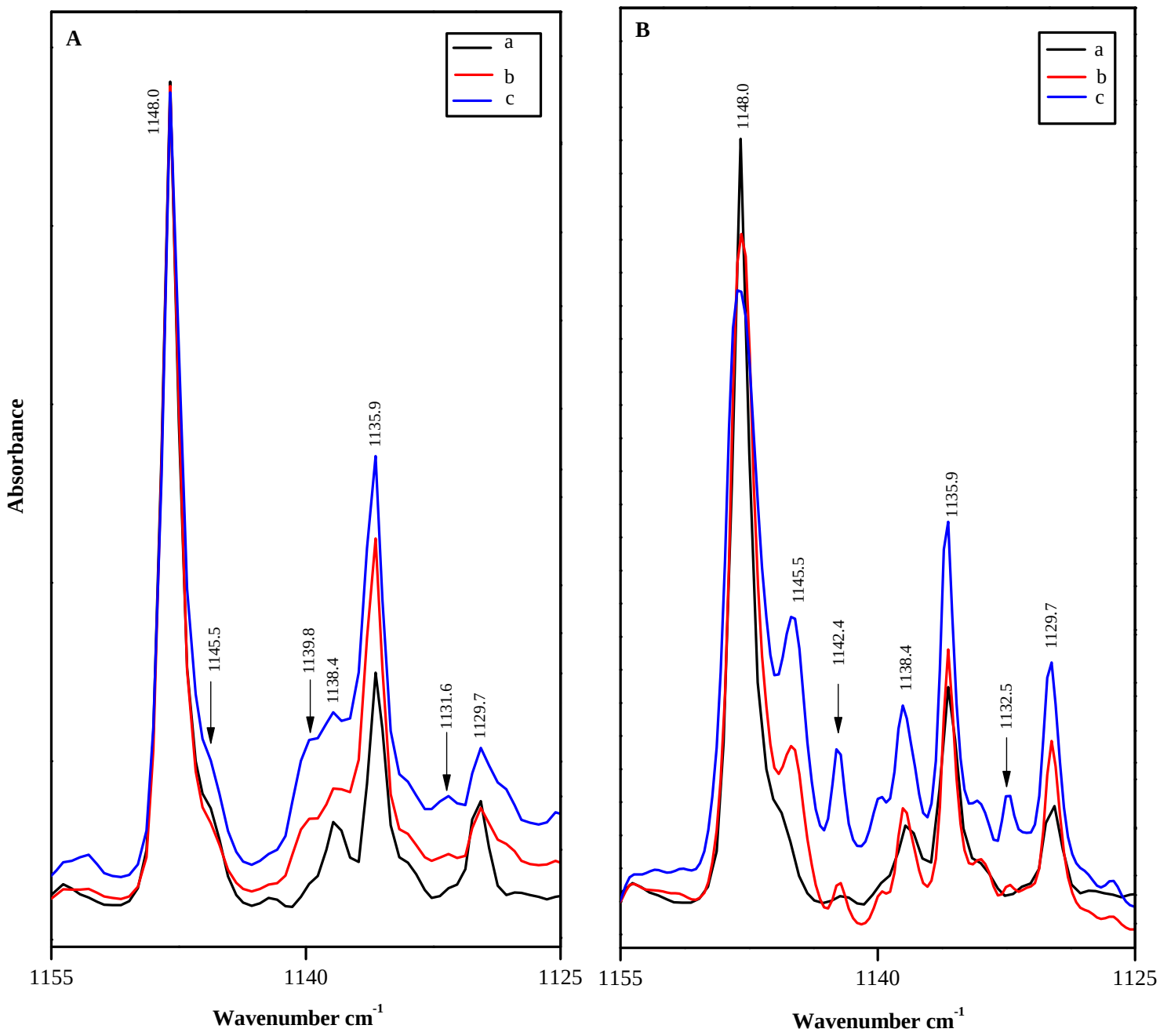

Figure 3.15: Infrared spectra spanning the region 1155-1125 cm^{-1} in Ar matrix. Matrix isolation spectra for various concentrations of $CHF_3/C_6H_6/Ar$ in block A (a) 2/0/1000; (b) 2/2/1000; (c) 2/4/1000. For CHF_3/C_2H_2 /Ar in block B (a) 2/0/1000; (b) 2/0.5/1000; (c) 2/1/1000.

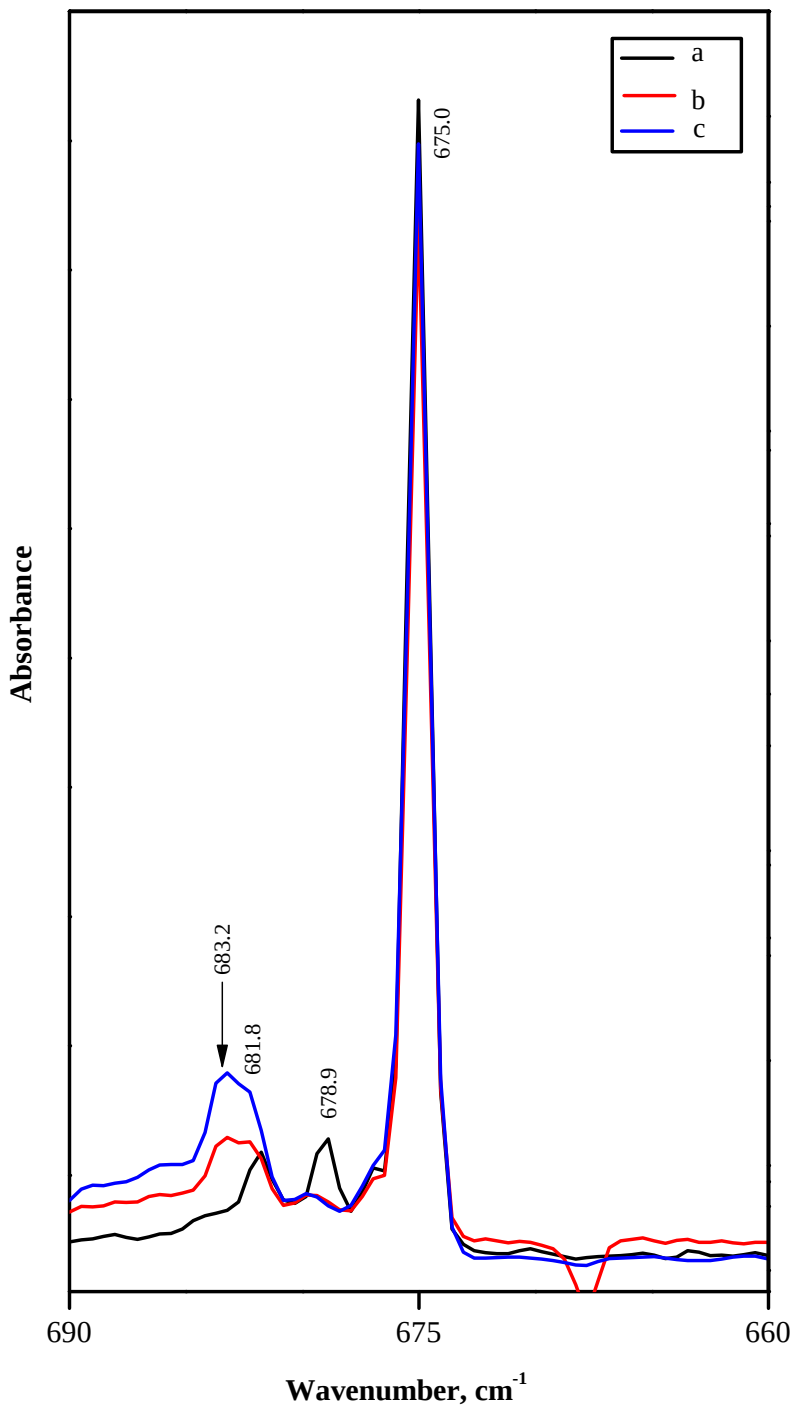

Figure 3.16: Infrared spectra spanning the region 690-660 cm^{-1} in Ar matrix. Matrix isolation spectra for various concentrations of CHF_3/C_6H_6 /Ar (a) 0/4/1000; (b) 1/4/1000; (c) 2/4/1000.

In the υ_2 mode of CHF_3 submolecule, a new feature was observed at 1131.6 cm^{-1} in the $CHF_3/C_6H_6/Ar$ experiments, a red shift of 4.3 cm^{-1}, which agrees well with the computed feature at 1111.4 cm^{-1}, a shift of 7.2 cm^{-1} for the CHF_3-C_6H_6 adduct. For the $CHF_3/C_2H_2/Ar$ experiments, a new feature observed at 1132.5 cm^{-1}, a red shift of 3.4 cm^{-1} compare well with the computed shift of 5.6 cm^{-1} from the bare CHF_3 submolecule of the CHF_3-C_2H_2 C-H···π adduct. The vibrational features of CHF_3 aggregates appear in the υ_5 and υ_2 mode at 1135.9/1138.4 cm^{-1} and 1129.7 cm^{-1} in Ar matrix.

Figure 3.16 shows the υ_4 C-H stretching mode of C_6H_6 in the region 690-660 cm^{-1}. The feature observed at 675.0 cm^{-1} is due to the C_6H_6 monomer in Ar matrix. The features observed at 681.8 and 678.9 cm^{-1} are assigned to the multimers of C_6H_6 in Ar matrix. Varying the concentrations of CHF_3 in Ar matrix, a new feature was observed at 683.2 cm^{-1} (fig. 3.16b-c). Computation showed that on complex formation the υ_4 mode occur at 691.0 cm^{-1}, a blue shift of 12.8 cm^{-1}, which agrees well with the experimental shift of 4.3 cm^{-1}.

The experimental evidence for the observation of 1:1 CHF_3-C_2H_2 C-H···π complex A in the υ_3 and υ_5 mode of C_2H_2 submolecule in Ar matrix are reported elsewhere [97]. Hence, for comparison, table 3.17 give the assignments of the vibrational wavenumbers in these modes.

3.4.4 Nature of the interaction: AIM analysis

Computations showed the CHF_3-C_6H_6 complex forms a T-shaped structure where the bond distance of hydrogen in CHF_3 is equidistant from all the carbons of C_6H_6. AIM analysis gave six (3,-1) intermolecular bond critical point (BCP), six (3, +1) intermolecular ring critical point (RCP) and one (3, +3) cage critical point (CCP) for the CHF_3-C_6H_6 complex and two (3,-1) intermolecular bond critical points between the hydrogen and fluorine of CHF_3 with the π cloud and hydrogen of C_2H_2 for the CHF_3-C_2H_2 C-H···π cyclic complex as shown in figures. 3.12 and 3.12a. Table 3.18 gives the properties of the intermolecular and

intramolecular (3,-1) bond critical point in the monomer and for the CHF_3-C_6H_6 and CHF_3-C_2H_2 C-H···π complexes computed at MP2/aug-cc-pVDZ level of theory. From the table it is clear that the magnitude of $\rho(r_C)$ and $\nabla^2\rho(r_C)$ at the BCP for the adduct is of the order of 10^{-2} a.u., which is indicative of the weak nature of the interaction of closed shell type.

It is also observed from the table that the magnitude of electron density $\rho(r_C)$ is slightly higher at the BCP of C-H bond of the CHF_3 in the CHF_3-C_6H_6 and CHF_3-C_2H_2 complexes than the monomer. This increase in the electron density at the C-H BCP of CHF_3 submolecule with respect to CHF_3 monomer in the complex could be the reason for the shortening of the C-H bond and the corresponding blue shift in the C-H stretching wavenumber. Between the two complexes, electron density $\rho(r_C)$ at the C-H BCP of CHF_3 submolecule is higher in the CHF_3-C_6H_6 than the CHF_3-C_2H_2 complex, which eventually induces a larger blue shift in the former complex than the latter and is consistent with the experimental shift in the C-H stretching mode of CHF_3 submolecule in the complexes. Table 3.18 (b-g) gives the properties for the intramolecular BCPs on the C-F bonds of CHF_3, C-H, C=C bonds of C_6H_6 in the complex and C-H, C≡C bonds of C_2H_2 in the complex. BCP values of the monomeric CHF_3, C_6H_6 and C_2H_2 are also given in the same table. The high positive values of $\rho(r_C)$ and high negative values of $\nabla^2\rho(r_C)$, which is characteristic of shared covalent interaction.

3.4.5 NBO analysis

Table 3.19 and 3.20 show the results of the NBO analysis of CHF_3-C_6H_6 and CHF_3-C_2H_2 C-H···π complexes computed at the MP2/aug-cc-pVDZ level of theory. It is evident from the table that there is a decrease in the electron occupancy of the π orbitals of the carbons (C6-C8, C7-C10 and C12-C14) of the C_6H_6 submolecule in the complex relative to the monomer. The magnitude of the decrease in the electron occupancy is larger in the π orbital than π* orbitals C_6H_6 submolecule in the complex, clearly showing the π orbital

Table 3.18: Properties of (3,-1) bond critical points in CHF_3-C_6H_6 and CHF_3-C_2H_2 hydrogen-bonded complexes (complex A) computed at MP2/aug-cc-pVDZ level of theory.

Complex	$\rho(r_C)$	$\nabla^2\rho(r_C)$	λ_1	λ_2	λ_3	$\lvert\lambda_1\rvert / \lambda_3$
(a) Intermolecular BCP in blue shifting hydrogen bond						
CHF_3-C_6H_6	0.00991	0.03290	-0.00645	-0.00033	0.03968	0.16255
CHF_3-C_2H_2	0.00800	0.02346	-0.00633	-0.00493	0.03472	0.18231
CHF_3-C_2H_2	0.00461	0.02174	-0.00374	-0.00189	0.02739	0.13655
(b) Intramolecular C-H bond BCPs corresponding H bond donor (CHF_3)						
CHF_3	0.29810	-1.26436	-0.82016	0.82016	0.37597	2.18145
CHF_3-C_6H_6	0.30109	-1.30400	-0.84389	-0.84389	0.38377	2.19895
CHF_3-C_2H_2	0.29992	-1.29187	-0.83509	-0.83463	0.37784	2.21017
(c) Intramolecular C-F bond BCPs corresponding H bond donor (CHF_3)						
CHF_3	0.26021	-0.29502	-0.57131	-0.49775	0.77404	0.73809
CHF_3-C_6H_6	0.25749	-0.28395	-0.56384	-0.48307	0.76296	0.73902
CHF_3-C_2H_2	0.25661	-0.28685	-0.55872	-0.48061	0.75249	0.74249
CHF_3-C_2H_2	0.25953	-0.28874	-0.57065	-0.49320	0.77511	0.73621
(d) Intramolecular BCPs corresponding to the C-H bond in C_6H_6 and CHF_3-C_6H_6 complex						
C_6H_6	0.27302	-0.99709	-0.68409	-0.67425	0.36125	1.89367
CHF_3-C_6H_6	0.27376	-1.00700	-0.68918	-0.67936	0.36156	1.90612
(e) Intramolecular BCPs corresponding to the C-C bond in C_6H_6 and CHF_3-C_6H_6 complex						
C_6H_6	0.29546	-0.69820	-0.58492	-0.48774	0.37446	1.56203
CHF_3-C_6H_6	0.29487	-0.69638	-0.58265	-0.48617	0.37245	1.56437
(f) Intramolecular BCPs corresponding to the C-H bond in C_2H_2 and CHF_3-C_2H_2 complex						
C_2H_2	0.27608	-1.10639	-0.71727	-0.71727	0.32815	-2.18580
CHF_3-C_2H_2	0.27603	-1.11486	-0.72218	-0.72216	0.32949	-2.19181
(g) Intramolecular BCPs corresponding to the C≡C bond in C_6H_6 and CHF_3-C_6H_6 complex						
C_2H_2	0.37002	-0.85987	-0.54463	-0.54464	0.22941	-2.37404
CHF_3-C_2H_2	0.36997	-0.86114	-0.54639	-0.54555	0.23080	-2.36737

Table 3.19: Electron occupancies of various NBOs of C-H···π blue-shifted hydrogen bond of CHF_3-C_6H_6 and CHF_3-C_2H_2 complexes computed at MP2/aug-cc-pVDZ level of theory.

CHF_3-C_6H_6		**CHF_3-C_2H_2**	
C_6H_6		**C_2H_2**	
NBO	**Occupancy (e)**	**NBO**	**Occupancy (e)**
π (C6-C8)	1.66212 (1.66397)[a]	σ(1) (C6-C7)	1.99945 (1.99980)[b]
π(C7-C10)	1.66220 (1.66397)	π (2) (C6-C7)	1.99200 (1.99980)
π (C12-C14)	1.66214 (1.66397)	π (3) (C6-C7)	1.99546 (1.99224)
π*(C6-C8)	0.33224 (0.33237)	σ (C6-H9)	1.99102 (1.99137)
π* (C7-C10)	0.33236 (0.33237)	σ (C7-H8)	1.99082 (1.99137)
π*(C12-C14)	0.33227 (0.33237)	σ* (1) (C6-C7)	0.00003 (0.00000)
		π* (2) (C6-C7)	0.00900 (0.00000)
		π* (3) (C6-C7)	0.00090 (0.00911)
		σ* (C6-H9)	0.00527 (0.00521)
		σ* (C7-H8)	0.00525 (0.00521)
CHF_3			
σ (C1-H2)	1.99188 (1.99004)[c]	σ (C1-H2)	1.99026 (1.99004)
σ*(C1-H2)	0.03612 (0.03720)	σ* (C1-H2)	0.03774 (0.03720)
σ(C1-F3) σ(C1-F4) σ(C1-F5)	1.99440 (1.99505) 1.99440 (1.99505) 1.99440 (1.99505)	σ(C1-F3) σ(C1-F4) σ(C1-F5)	1.99493 (1.99505) 1.99494 (1.99505) 1.99492 (1.99505)
σ*(C1-F3) σ*(C1-F4) σ*(C1-F5)	0.06036(0.06125) 0.06037(0.06126) 0.06036(0.06126)	σ*(C1-F3) σ*(C1-F4) σ*(C1-F5)	0.06024(0.06125) 0.06023(0.06126) 0.0616(0.06126)
LP (1) F 3 LP (2) F 3 LP (3) F 3	1.99273(1.99281) 1.97003(1.96786) 1.95833(1.95740)	LP (1) F 3 LP (2) F 3 LP (3) F 3	1.99283 (1.99281) 1.96873 (1.96786) 1.95746 (1.95740)
LP (1) F 4 LP (2) F 4 LP (3) F 4	1.99273(1.99281) 1.97004(1.96786) 1.95831(1.95740)	LP (1) F 4 LP (2) F 4 LP (3) F 4	1.99283(1.99281) 1.96872(1.96786) 1.95746(1.95740)
LP (1) F 5 LP (2) F 5 LP (3) F 5	1.99273(1.99281) 1.97003(1.96786) 1.95831(1.95741)	LP (1) F 5 LP (2) F 5 LP (3) F 5	1.99290(1.99281) 1.96856(1.96786) 1.95881(1.95741)

[a]Occupancy of monomeric C_6H_6 is given in parentheses.
[b]Occupancy of monomeric C_2H_2 is given in parentheses.
[c]Occupancy of monomeric CHF_3 is given in parentheses.

Table 3.20: Natural bond orbitals (NBO) analysis of CHF_3-C_6H_6 and CHF_3-C_2H_2 complexes computed at MP2/aug-cc-pVDZ level of theory along with donor-acceptor delocalization interaction and delocalization energies (E_2).

CHF_3-C_6H_6			CHF_3-C_2H_2		
Donor orbital	**Acceptor orbital**	**Second order perturbation (E_2) energy (kcal/mol)**	**Donor orbital**	**Acceptor orbital**	**Second order perturbation (E_2) energy (kcal/mol)**
σ (C6-C7)	σ* (C1-H2)	0.17	π (3) (C6-C7)	σ* (C1-H2)	2.17
σ (C6-C8)	σ* (C1-H2)	0.18	π (3) (C6-C7)	σ* (C1-F3)	0.05
π(C6-C8)	σ* (C1-H2)	1.37	π (3) (C6-C7)	σ* (C1-F4)	0.05
π(C6-C8)	σ* (C1-F4)	0.11	σ (C6-H9)	σ* (C1-H2)	0.08
σ (C6-C9)	σ* (C1-H2)	0.08	σ (C7-H8)	σ* (C1-H2)	0.19
σ (C7-C10)	σ* (C1-H2)	0.18			
π (C7-C10)	σ* (C1-H2)	1.39	σ (C1-H2)	π* (3) (C6-C7)	0.07
π (C7-C10)	σ* (C1-F5)	0.10	LP F5	π* (2) (C6-C7)	0.06
σ (C7-C11)	σ* (C1-H2)	0.08	LP F5	π* (3) (C6-C7)	0.14
σ (C8-C12)	σ* (C1-H2)	0.17	LP F5	σ* (C7-H8)	0.08
σ (C8-C13)	σ* (C1-H2)	0.08			
σ (C10-C14)	σ* (C1-H2)	0.17			
σ (C10-C15)	σ* (C1-H2)	0.08			
σ (C12-C14)	σ* (C1-H2)	0.18			
π (C12-C14)	σ* (C1-H2)	1.38			
π (C12-C14)	σ* (C1-F3)	0.10			
σ (C12-C16)	σ* (C1-H2)	0.08			
σ (C14-C17)	σ* (C1-H2)	0.08			

participation in forming the complex. A similar trend was observed in the CHF_3-C_2H_2 complex A where the π orbital electron occupancy of carbons (C6-C7) of C_2H_2 submolecule decreases in the complex relative to the monomer. Furthermore, the electron occupancy increases in the bonding orbital σ(C1-H2) and found to decrease in the antibonding orbital σ*(C1-H2) of CHF_3 submolecule in both the complexes. The second order perturbative delocalization E_2 energies show that the dominant charge transfer interaction for the CHF_3-C_6H_6 and CHF_3-C_2H_2 C-H⋯π complexes is from the π electron donor (C_6H_6/C_2H_2) to the σ*(C1-H2) of CHF_3. The cumulative delocalization energies for this interaction were found to be 4.14 and 2.17 kcal/mol, respectively (Table 3.20). Though the magnitude of interaction energies are smaller, additionally, the charge transfer also occurs from the π → σ*(C-F), σ → σ*(C-H) and lone pair⋯π interactions in both the complexes. As a result of the lone pair⋯π remote delocalization interaction, there is a marginal increase in the electron occupancy in the fluorine lone pairs in the complex than in the monomer (Table 3.19), which leads to elongation of the C-F bond followed by structural rearrangement of the CHF_3 submolecule that causes the contraction of the C-H bond. Similar trend was observed in the CHF_3-HCl complex in the previous work. From the table, it is clear that the magnitude of electron occupancy in the fluorine lone pair in the CHF_3-C_6H_6 is larger than in the CHF_3-C_2H_2 complex, which is responsible for the larger blue shift in the former complex than the latter.

3.5 Conclusions

For the first time using matrix isolation infrared spectroscopy and *ab initio* computations, we have reported the formation of C-H⋯Cl, C-H⋯O and C-H⋯π blue-shifted hydrogen-bonded complexes between CHF_3 with Lewis bases like HCl, H_2O, C_6H_6 and C_2H_2. Experimentally, a blue shift of 6.7, 20.3, 32.3, and 7.3 cm^{-1} was observed in the C-H stretching mode of CHF_3 submolecule for the CHF_3-HCl, CHF_3-H_2O, CHF_3-C_6H_6, CHF_3-C_2H_2 complexes. The observed experimental vibrational wavenumber correlates well

with the computations performed at the MP2/aug-cc-pVDZ level of theory. NBO analysis showed that the hyperconjugative charge-transfer interaction operates in all the complexes. Cumulative effects such as lone pair-acceptor orbital/bond pair-acceptor orbital, remote delocalization, re-hybridization and intramolecular hyperconjugation on complex formation are the contributing factors for the decrease in the C-H bond length and the observed blue shift of the C-H stretching frequency of CHF_3-HCl, CHF_3-H_2O, CHF_3-C_6H_6, CHF_3-C_2H_2 complexes. AIM analysis showed that the magnitude of electron density $\rho(r_C)$ is slightly higher at the BCP of C-H bond of CHF_3 in the CHF_3-HCl, CHF_3-H_2O, CHF_3-C_6H_6, CHF_3-C_2H_2 complexes than in the monomer. Clearly, this increase in the electron density at the C-H BCP of CHF_3 submolecule with respect to CHF_3 monomer in the complexes is responsible for the shortening of the C-H bond and corresponding blue shift in the C-H stretching wavenumber.

CHAPTER 4

RED SHIFTING HYDROGEN BOND

4.1 Red shifting hydrogen bond

Hydrogen bond (H-bond) is a non-covalent, attractive interaction between a proton donor X-H and a proton acceptor Y in the same or in a different molecule: X-H⋯Y, where X= N, O, F and Y is either an electronegative region or a region of electron excess. In classical H-bonding, there is a shortening of X⋯Y distance, if X-H is hydrogen-bonded to Y. The distance between X⋯Y is less than the sum of the van der Waals radii of the two atoms X and Y. hydrogen bonding interactions lead to increase in the X-H bond distance and a concomitant red shift is observed in the X-H stretching vibrational wavenumber.

In this chapter, an interaction of CH_3CN and C_6H_5CN with water (H_2O) and acetylene (C_2H_2) is studied to probe the red-shifting as a result of hydrogen bond. The systems studied are:

- Acetonitrile-Acetylene (CH_3CN-C_2H_2)
- Acetonitrile-Water (CH_3CN-H_2O)
- Benzonitrile-Acetylene (C_6H_5CN-C_2H_2)
- Benzonitrile-Water (C_6H_5CN-H_2O)

4.2 Interaction of acetonitrile (CH_3CN) with acetylene (C_2H_2) interaction

CH_3CN has two electron rich sites, lone pairs on nitrogen and C≡N triple bond, which can form either a σ- or π-type hydrogen bond or both. C_2H_2 acts as a proton donor as the hydrogen attached to the 'sp' carbon atom is sufficiently acidic. Alternatively, C_2H_2 can also play the role of a proton acceptor through its π-cloud. It is interesting to study the interaction between the C_2H_2 and CH_3CN and to see the competing ability of CH_3CN and C_2H_2 as proton donors and acceptors. The aim of this work is to explore the possibility of forming 1:1 complexes between C_2H_2 and CH_3CN in Ar and N_2 matrixes and to correlate with the computational results. The formation of higher CH_3CN-C_2H_2 complexes was also explored both computationally and experimentally.

4.2.1 Experimental details

C_2H_2 (Commercial Grade, Asiatic Oxygen Limited, India) and CH_3CN (Merck, HPLC grade 99.8%) were used as such, without further purification. Ar (INOX, 99.9995%) and N_2 (INOX, 99.995%) are used as matrix gases, in which C_2H_2 was pre-mixed to obtain the desired matrix-to-sample ratios. The C_2H_2/matrix gas mixture and CH_3CN were then deposited using double jet nozzle onto a KBr substrate maintained at 12 K. We used typical matrix-to-sample ratios ranging from 1000:0.1 to 1000:0.2 for C_2H_2 and 1000:1 to 1000:2.5 for CH_3CN. Infrared spectra of matrix isolated samples were recorded using BOMEM MB100 FTIR spectrometer.

Figure 4.1 (3320-3220 cm^{-1}) and figure 4.2 block A (3270-3200 cm^{-1}) and block B (830-760 cm^{-1}) shows the pre-annealed (soon after deposition) spectra of C_2H_2 with and without CH_3CN in an Ar and N_2 matrixes. Figure 4.3 block A (3275-3215 cm^{-1}) and block B (800-750 cm^{-1}), figure 4.4 block A (3270-3200 cm^{-1}) and block B (830-760 cm^{-1}) show the IR spectra obtained after the matrixes were annealed at 35 K (Ar) and 30 K (N_2), respectively. In the Ar matrix, C_2H_2 shows two strong absorptions at 3288.9 and 3302.9 cm^{-1}

(fig.4.1a), which have been assigned to components of a Fermi diad involving the$\upsilon_3$mode and a combination band (υ_2+υ_4+υ_5) [217] while the doubly degenerate υ_5 mode of C_2H_2 occurs as a single sharp peak at 736.8 cm^{-1} in an Ar matrix (not shown in figure), whereas the same mode appears as a doublet at 742.0 and 742.7 cm^{-1} in N_2 matrix (not shown in figure) [148]. When C_2H_2 and CH_3CN were co-deposited, new features were observed in the pre-annealed matrix at 3242.1, 3234.9 cm^{-1} in Ar (fig. 4.1b-d) and at 3234.3, 3227.6 cm^{-1} in N_2 matrix (fig. 4.2b-d, block A). On annealing, the feature observed in the as-deposited spectrum at 3234.9 cm^{-1} in Ar and 3234.3 and 3227.6 cm^{-1} in N_2 matrix increases in intensity.

Further, a new feature starts appearing at 3228.6 cm^{-1} in an Ar matrix, whereas the intensity of the feature observed at 3242.1 cm^{-1} (Ar) in the as-deposited spectra decreases (fig. 4.3b-d, fig. 4.4b-d, block A). In the υ_5 bending region of C_2H_2 in Ar matrix, only on annealing, new features were observed at 780.6, 783.0 cm^{-1} (fig. 4.3c-d, block B) whereas in N_2 matrix, new features observed at 773.9 and 778.7 cm^{-1} (fig. 4.4b-d, block B) in the pre-annealed spectra increases in intensity. It may be noted that the feature observed at 3262.8 and 3258.0 cm^{-1}in Ar and N_2 matrixes are due to the C_2H_2 dimer [148]. Since, water is an inevitable impurity the feature due to C_2H_2-H_2O complex was observed at 3240.2, 785.5 cm^{-1}in Ar and as site split doublets at 3218.5, 3225.2, 785.9, 795.1 and 798.0 cm^{-1} in N_2 matrix [148].

Figure 4.5 shows the infrared spectra of CH_3CN isolated in Ar and N_2 matrixes. The region spanned in this figure is between 2275-2245 cm^{-1} (block A and block B). The features observed at 2258.0 and 2257.5 cm^{-1} are due to υ_5 symmetric CN stretching mode of CH_3CN in Ar and N_2 matrixes, respectively. The features observed at 2256.1 and 2254.1 cm^{-1} are due to acetonitrile dimer $(CH_3CN)_2$ in Ar and N_2 matrixes, which agree well with the literature value [101,124]. When C_2H_2 and CH_3CN were co-deposited and the matrix then annealed,

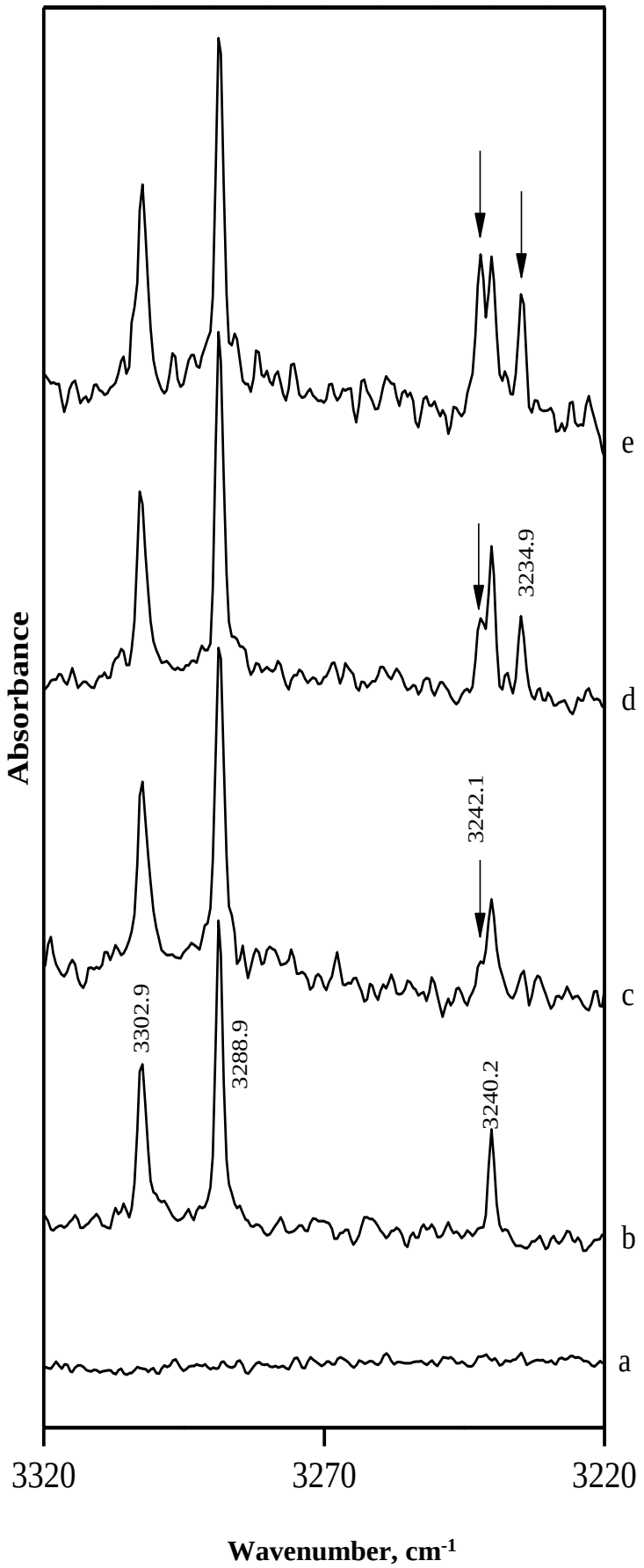

Figure 4.1: As deposited spectra of C_2H_2-CH_3CN complex in Ar matrix spanning the region 3320-3220 cm^{-1}. Matrix isolation spectra for various concentrations of $C_2H_2/CH_3CN/Ar$ (a) 0/2.5/1000; (b) 0.2/0/1000; (c) 0.1/1.5/1000; (d) 0.2/1.5/1000; (e) 0.1/2.5/1000. Spectra shown here were recorded at 12 K.

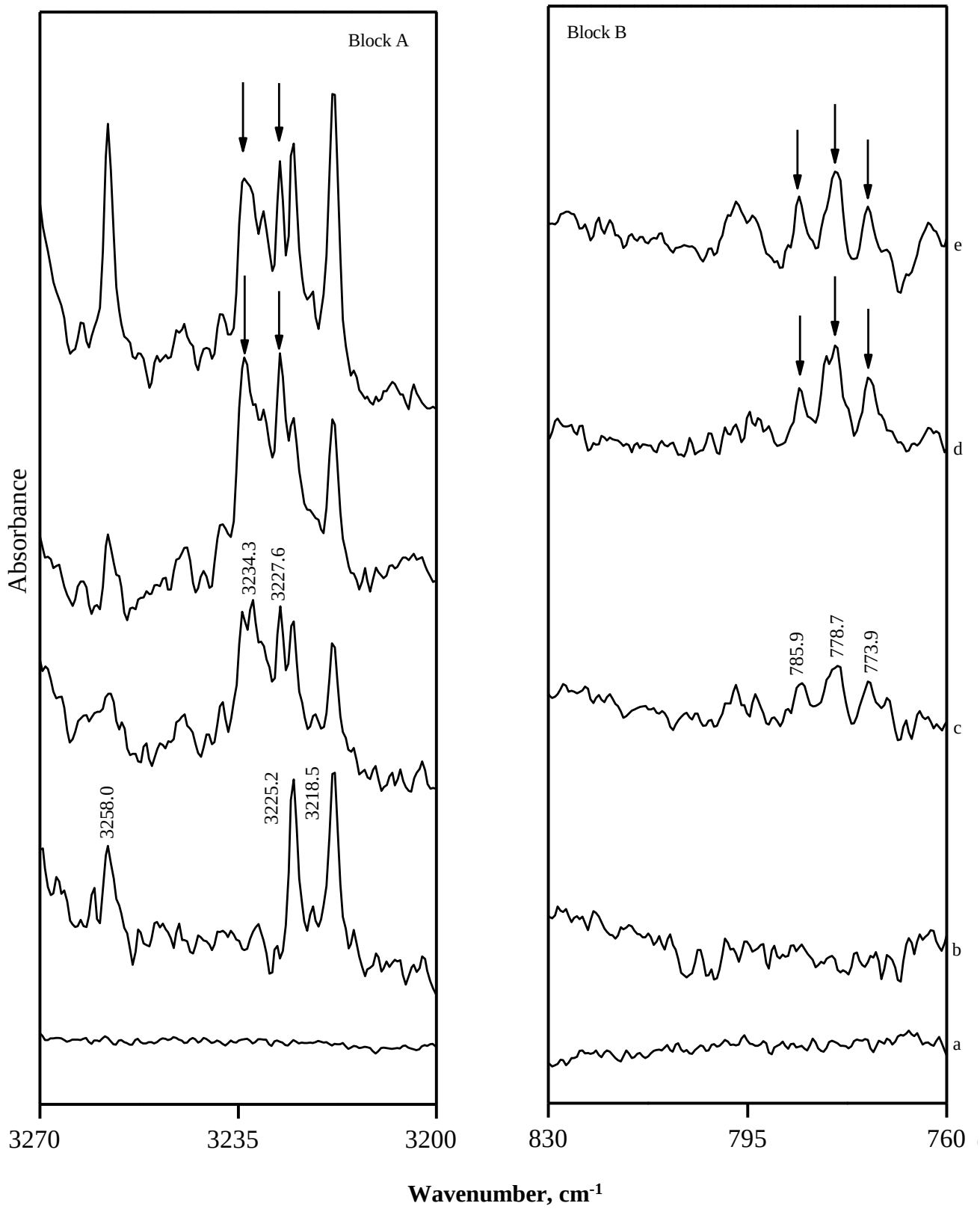

Figure 4.2: As deposited spectra of C_2H_2-CH_3CN complex in N_2 matrix spanning the region 3270-3200 (block A) and 830-760 (block B) cm^{-1}. Matrix isolation spectra for various concentrations of $C_2H_2/CH_3CN/N_2$ (a) 0/2.5/1000 (b) 0.25/0/1000; (c) 0.25/1.5/1000; (d) 0.25/2.5/1000; (e) 0.5/1.5/1000. Spectra shown here were recorded at 12 K.

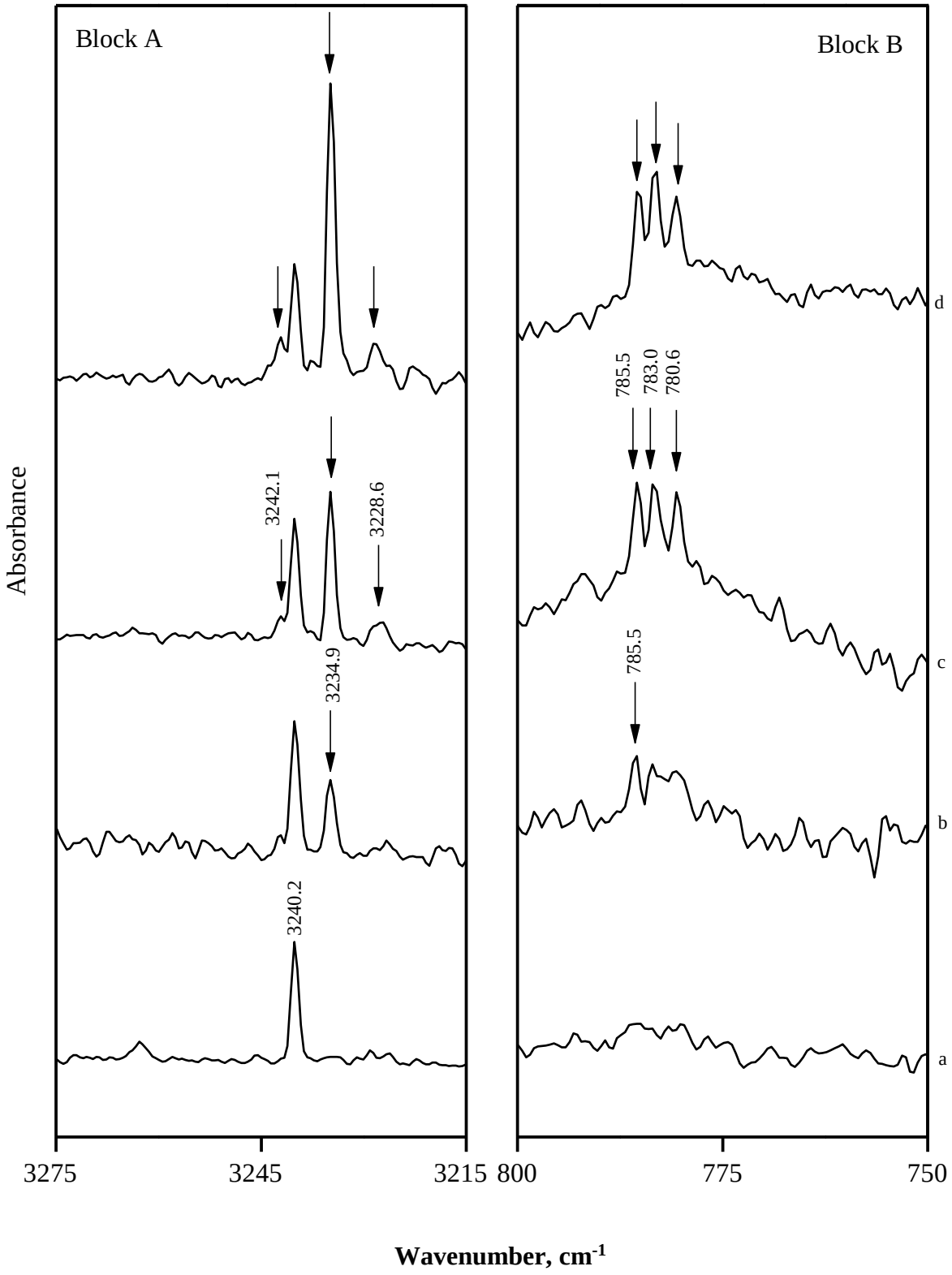

Figure 4.3: Spectra of C_2H_2-CH_3CN complex in Ar matrix spanning the region 3275-3215 cm^{-1} (block A) and 800-750 cm^{-1} (block B). Matrix isolation spectra for various concentrations of $C_2H_2/CH_3CN/Ar$. (a) 0.2/0/1000; (b) 0.1/1.5/1000; (c) 0.2/1.5/1000; (d) 0.1/2.5/1000. Spectra shown here were recorded after annealing the matrix at 35 K.

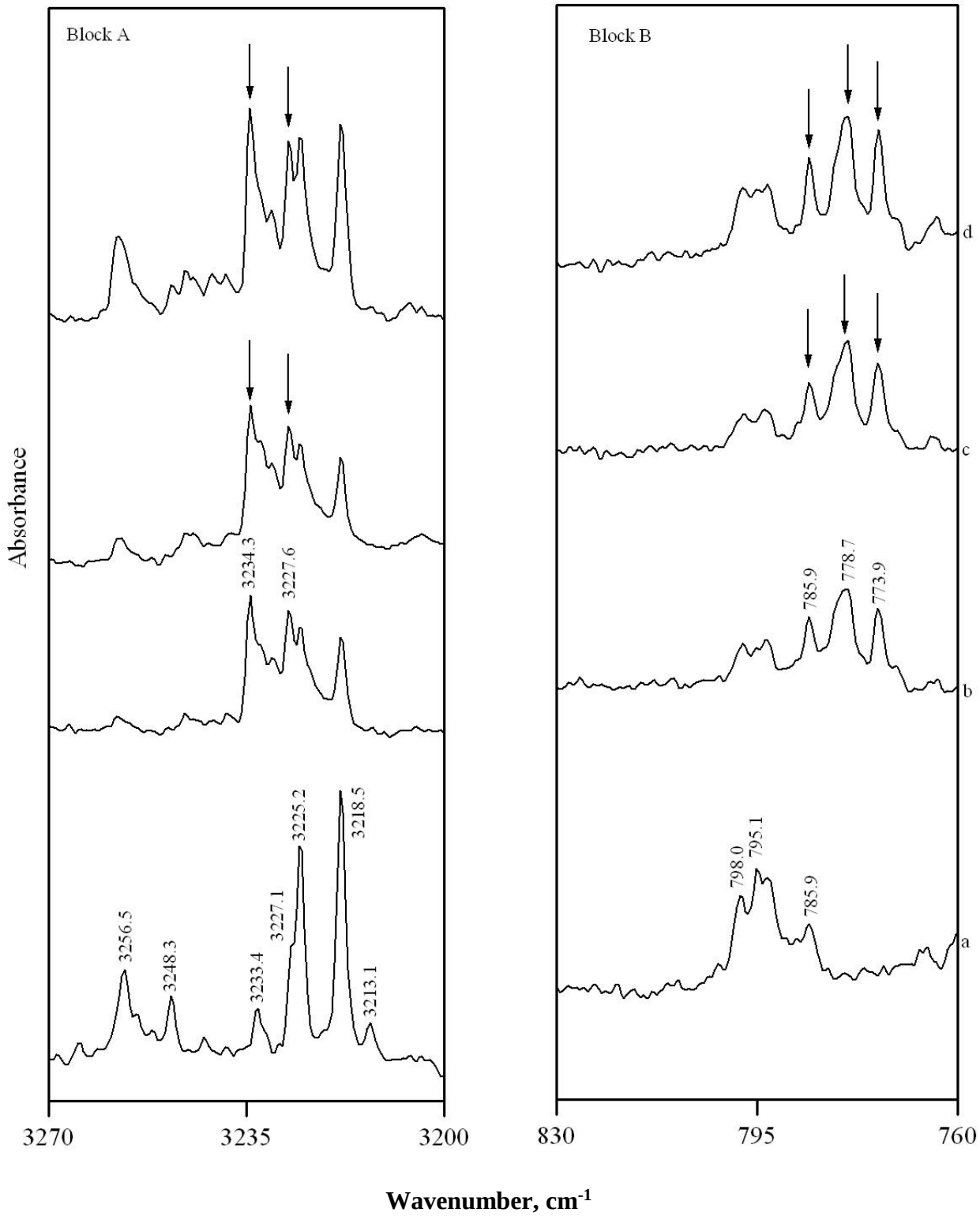

Figure 4.4: Spectra of C_2H_2/CH_3CN complex in N_2 matrix spanning the region 3270-3200 (block A) and 830-760 (block B) cm^{-1}. Matrix isolation spectra for various concentrations of $C_2H_2/CH_3CN/N_2$ (a) 0.25/0/1000; (b) 0.25/1.5/1000; (c) 0.25/2.5/1000; (d) 0.5/1.5/1000. Spectra shown here were recorded after annealing the matrix at 30 K.

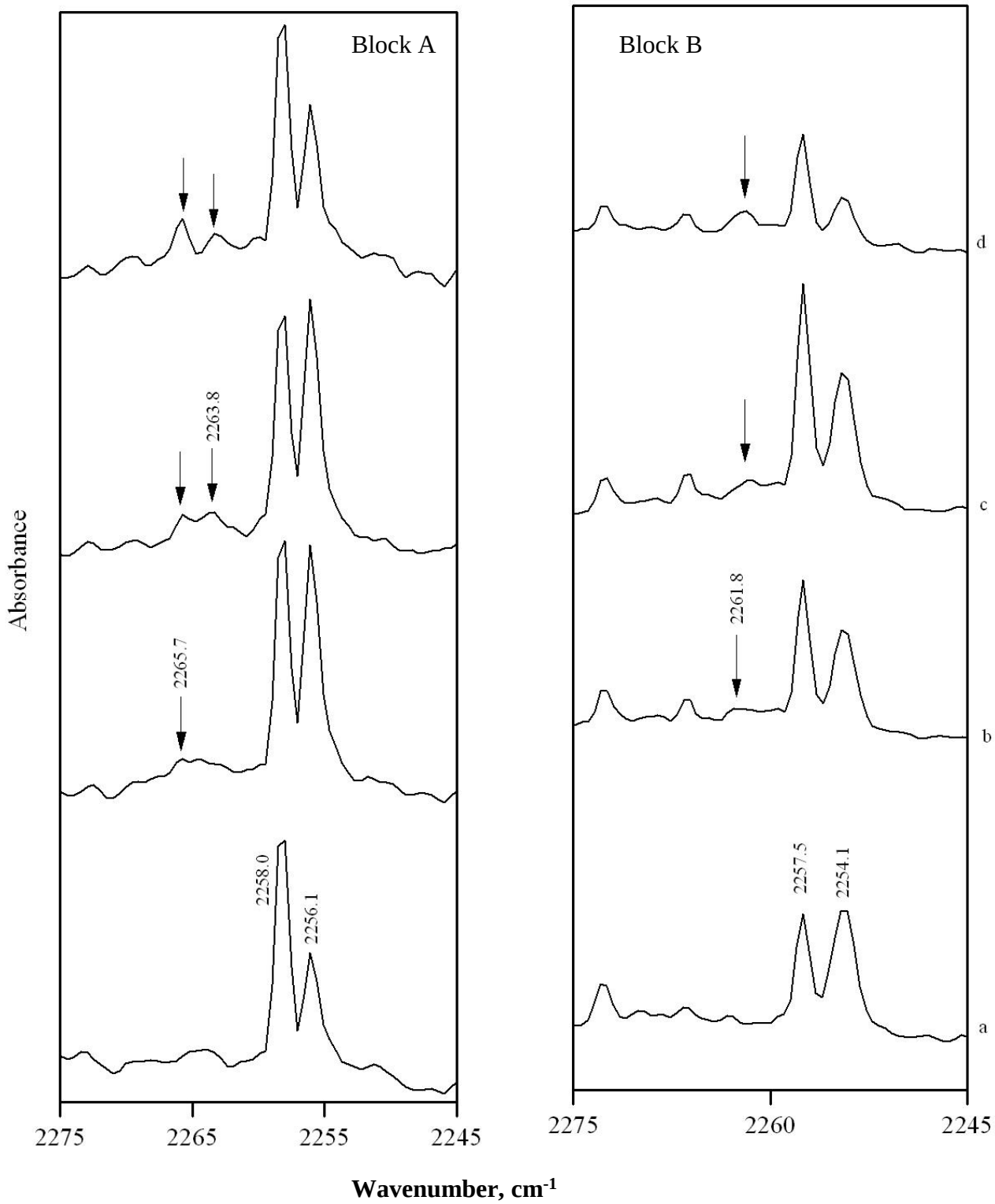

Figure 4.5: Spectra of C_2H_2/CH_3CN complex in Ar (block A) and N_2 (block B) matrixes spanning the region 2275-2245 cm^{-1}. Matrix isolation spectra for various concentrations of $C_2H_2/CH_3CN/Ar$ (a) 0/2.5/1000; (b) 0.1/1.5/1000; (c) 0.2/2.5/1000; (d) 0.1/2.5/1000 and $C_2H_2/CH_3CN/N_2$ (a) 0/2.5/1000; (b) 0.25/1.5/1000; (c) 0.25/2.5/1000; (d) 0.5/1.5/1000. Spectra shown here were recorded after annealing the matrix at 35 K and 30 K.

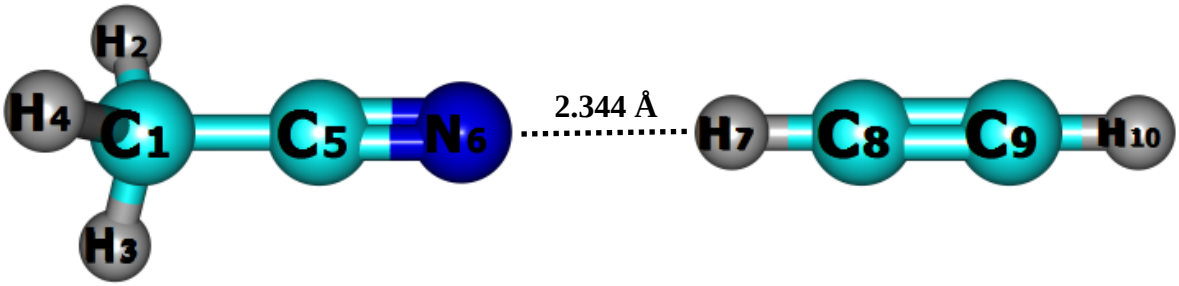

Complex A

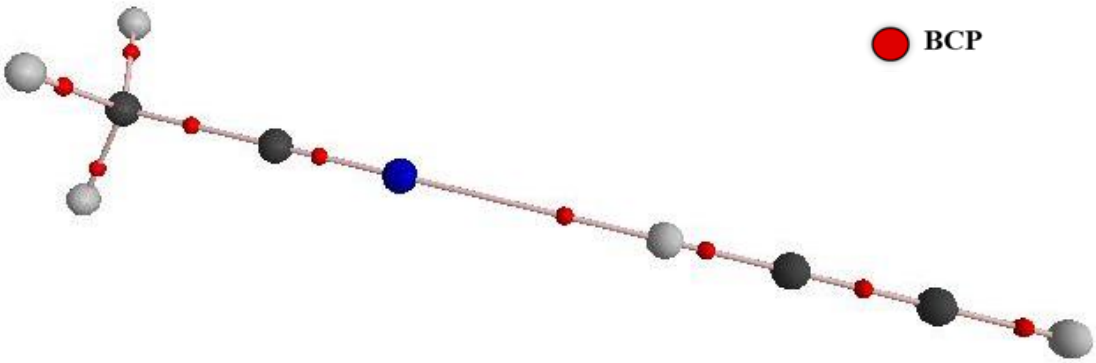

Figure 4.6: Structure of C_2H_2-CH_3CN complex A computed at B3LYP/6-311++G(d,p) level of theory.

product absorption band appeared in the υ_5 stretching region as a doublet in an Ar matrix at 2263.8 and 2265.7 cm^{-1} whereas in N_2 matrix new feature was observed at 2261.8 cm^{-1}.

New features in the υ_4 symmetric CC stretch, υ_7 CH_3 rocking, υ_3 CH_3 deformation, υ_6 asymmetric CH_3 deformation, υ_1 symmetric CH stretching, υ_5 asymmetric CH stretching modes of CH_3CN was not observed in both Ar and N_2 matrixes.

All the features of the product bands appeared only when both the reagents were co-deposited and showed a concentration dependence on the precursors, lending credence to their assignments to the C_2H_2-CH_3CN complexes.

4.2.2 Computations on the 1:1 C_2H_2-CH_3CN complexes

Ab initio computations on the C_2H_2-CH_3CN system at the B3LYP and MP2 level of theory using the 6-311++G(d,p) and aug-cc-pVDZ basis set yielded only one minima corresponding to C-H⋯N complex A. Figure 4.6 shows the structure for the C-H⋯N complex A computed at B3LYP/6-311++G(d,p) level of theory. For the complex A, the bond distance between the hydrogen, H7 of C_2H_2 and N6 of CH_3CN is 2.344 Å. The selected bond distances, bond angles and dihedral angles for these complexes are given in table 4.1 and 4.1a. The stabilization energies for the C_2H_2-CH_3CN complex A with and without ZPE and also with BSSE correction computed at the B3LYPand MP2 methods using 6-311++G(d,p) basis set and B3LYP/aug-cc- pVDZ level of theory are given in table 4.2. A combined correction for ZPE and BSSE was not calculated as it has been shown to underestimate the bonding enthalpy [218]. From the table it is clear that the formation of complex A is indicated to be exothermic by about 2.6 kcal/mol at MP2/6-311++G(d,p) level with ZPE correction. Although there are deviations in the numerical values of energies with the different basis sets, the trends in the energies are found to be the energies are found to be qualitatively similar for the complex A.

Table 4.1: Selected structural parameters[a] for the C_2H_2-CH_3CN complex A calculated at the B3LYP/6-311++G(d,p) level of theory

Parameter	Complex A
C5-N6	1.152 (1.153)[b]
C5-C1	1.456 (1.456)
C1-H3	1.092 (1.092)
N6-H7	2.344
C8-H7	1.069 (1.063)
C8-C9	1.201 (1.199)
H10-C9	1.063 (1.063)
∠N6-C5-C1	180.0(180.0)
∠H7-C8-C9	180.0(180.0)
∠H4-C1-H3	108.8(108.8)
∠H4-C1-C5	110.1
tor∠N6-C5-C1-H4	-84.7
tor∠N6-H7-C8-C9	-49.9

Table 4.1a: Selected structural parameters[a] for the C_2H_2-CH_3CN complex A calculated at the MP2/aug-cc-pVDZ level of theory

Parameter	Complex A
C5-N6	1.184 (1.185)[b]
C5-C1	1.470 (1.471)
C1-H3	1.099 (1.099)
N6-H7	2.252
C8-H7	1.081 (1.075)
C8-C9	1.233 (1.236)
H10-C9	1.075 (1.075)
∠N6-C5-C1	180.0 (180.0)
∠H7-C8-C9	180.0(180.0)
∠H4-C1-H3	109.2 (108.8)
∠H4-C1-C5	109.7
tor∠N6-C5-C1-H4	38.9
tor∠N6-H7-C8-C9	46.2

[a]Bond lengths in Å, angles and torsional angles in °.
[b]The parameters for the monomer are given in brackets.

Table 4.2: Raw[a]/ZPE-corrected/BSSE-corrected stabilization energies for the C_2H_2-CH_3CN complexes A, B, C and D computed at the B3LYP and MP2 using 6-311++G(d,p) and B3LYP/aug-cc-pVDZ levels of theory.

Complexes	Stabilization Energy (ΔE)		
	B3LYP/6-311++G(d,p)	MP2/6-311++G(d,p)	B3LYP/aug-cc-pVDZ
A	-2.7/-2.0/-2.5	-3.3/-2.6/-2.7	-3.1/-2.2/-2.5
B	-7.1/-5.6/-3.5	-[b]	-7.7/-6.14/-3.5
C	-4.3/-3.0/-3.4	-7.5/-6.2/-4.4	-5.0/-3.5/-3.5
D	-3.3/-2.2/-2.3	-5.1/-3.8/-2.5	-3.9/-2.6/-2.3

All energies are in kcal/mol (see text for details).
[a]Raw stabilization energies refer to energies not corrected for either ZPE or BSSE.
[b]Calculation could not be performed.

Table 4.3: Experimental (cm^{-1}), computed unscaled and scaled vibrational wavenumbers (cm^{-1}), scaling factors and mode assignments for the C_2H_2-CH_3CN complexes A, B, C, and D in Ar and N_2 matrixes. Computations were performed at B3LYP/6-311++G(d,p) level of theory.

Computed/ unscaled (υ)	Ar			N_2			Mode assignment
	Computed/ scaled (υ)	Scaling factor	Exp (υ)	Computed/ scaled (υ)	Scaling factor	Exp (υ)	
CH_3CN							
930.0(2)[a]	917.2	0.9856	916.6	917.6	0.9967	917.6	υ_4 sym. CC str. (A_1) mode of CH_3CN
1061.0(2)	1038.2	0.9785	1038.2	1043.3	0.9833	1040.7/ 1045.8	υ_7 CH_3 rock (E) mode of CH_3CN
1411.6(3)	1375.9	0.9747	1375.9	1378.5	0.9766	1378.5	υ_3 sym.CH_3def (A_1) mode of CH_3CN
1474.7(12)	1445.5	0.9802	1445.5	1447.9	0.9818	1446.7/ 1449.1	υ_6 asym. CH_3 def. (E) mode of CH_3CN
2362.9(12)	2258.0	0.9556	2258.0	2257.6	0.9554	2257.6	υ_2 sym. CN str. (A_1) mode of CH_3CN
3045.9(4)	2950.6	0.9687	2950.5	2949.0	0.9682	2949.0	υ_1 sym. CH str. (A_1) mode of CH_3CN
3115.6(1)	3004.4	0.9643	3004.5	3009.3	0.9659	3009.3	υ_5 asym. CH str. (E) mode of CH_3CN
C_2H_2							
3420.6(94)	3288.9	0.9615	3288.9	3282.6	0.9597	3282.6	υ_3 C-H assym. str. mode of C_2H_2
772.7(112)	736.8	0.9535	736.8	744.7	0.9638	742.0 / 747.4	υ_5 C-H bending mode of C_2H_2

Complex A							
3373.3(314)	3243.4	0.9615	3234.9	3237.4	0.9597	3234.3	υ_3 asym. C-H str. mode of C_2H_2
834.8(90)	796.0	0.9535	785.5	804.6	0.9638	785.9	υ_5 C-H bending mode of C_2H_2
2368.8(20)	2263.6	0.9556	2265.7/ 2263.8	2264.1	0.9554	2261.8	υ_2 sym. CN str. mode of CH_3CN
Complex B							
3366.6(319)	3237.0	0.9615	3228.6	3237.0	0.9597	3227.6	υ_3 asym. C-H str. mode of C_2H_2
835.2(82) /838.1(101)	796.4 / 799.1	0.9535	780.6/ 783.0	805.0 / 807.8	0.9638	773.9 / 778.7	υ_5 C-H bending mode of C_2H_2
2361.2(36) / 2357.0(15)	2256.4 / 2252.4	0.9556	-[b]	2255.9/ 2251.9	0.9554	-[b]	υ_2 sym. CN str. mode of CH_3CN
Complex C							
3371.8(227)/3389.9(194)	3242.0/3259.4	0.9615	-[b]	3235.9/3253.3	0.9597	-[b]	υ_3 asym. C-H str. mode of C_2H_2
796.6(47)/807.6(95) 822.9(118)/827.0(127)	759.5/770.1 784.6/788.5	0.9535	-[b]	767.8 / 778.4 793.1 / 797.0	0.9638	-[b]	υ_5 C-H bending mode of C_2H_2
2363.8(20)	2258.9	0.9556	-[b]	2258.4	0.9554	-[b]	υ_2 sym. CN str. mode of CH_3CN
Complex D							
3368.5(391) 3418.1(98)	3238.8 3286.5	0.9615	-[b]	3232.7	0.9597	-[b]	υ_3 asym. C-H str. mode of C_2H_2
773.6(93) / 779.0(126) 838.1(100) / 841.0(83)	737.6 / 742.8 799.1 / 801.9	0.9535	-[b]	745.6 / 750.8 807.8 / 810.6	0.9638	-[b]	υ_5 C-H bending mode of C_2H_2
2363.8(21)	2258.8	0.9556	-[b]	2258.4	0.9554	-[b]	υ_2 sym. CN str. mode of CH_3CN

[a]Computed infrared intensities (KM/mol) are given in parentheses.
[b]Experimental features were not observed.

Table 4.3a: Experimental (cm^{-1}), computed unscaled and scaled vibrational wavenumbers (cm^{-1}), scaling factors and mode assignments for the C_2H_2-CH_3CN complex A in Ar and N_2 matrixes. Computations were performed at MP2/aug-cc-pVDZ level of theory.

Computed/ unscaled (υ)	Ar			N_2			Mode assignment
	Computed scaled	Scaling factor	Exp (υ)	Computed scaled	Scaling factor	Exp (υ)	
CH_3CN							
930.5(1)[a]	916.6	0.9851	916.6	917.6	0.9861	917.6	υ_4 sym. CC str. (A_1) mode of CH_3CN
1048.2(1)	1038.2	0.9904	1038.2	1043.3	0.9953	1040.7/1045.8	υ_7 CH_3 rock (E) mode of CH_3CN
1390.7(1)	1375.9	0.9893	1375.9	1378.5	0.9912	1378.5	υ_3 sym.CH_3def (A_1) mode of CH_3CN
1466.5(10)	1445.5	0.9857	1445.5	1447.9	0.9873	1446.7/1449.1	υ_6 asym.CH_3 def. (E) mode of CH_3CN
2180.2(0)	2258.0	1.0357	2258.0	2257.6	1.0355	2257.6	υ_2 sym. CN str. (A_1) mode of CH_3CN
3088.7(4)	2950.6	0.9553	2950.5	2949.0	0.9548	2949.0	υ_1 sym. CH str. (A_1) mode of CH_3CN
3188.9(1)	3004.4	0.9421	3004.5	3009.3	0.9437	3009.3	υ_5 asym. CH str. (E) mode of CH_3CN
C_2H_2							
3431.8 (93)	3288.9	0.9583	3288.9	3282.6	0.9565	3282.6	υ_3 C-H assym. str. mode of C_2H_2
702.9 (95)	736.8	1.0482	736.8	744.7	1.0594	742.0/ 747.4	υ_5 C-H bending mode of C_2H_2
Complex A							
3382.9(344)	3241.8	0.9583	3234.9	3235.7	0.9565	3234.3	υ_3 asym. C-H str. mode of C_2H_2
802.0 (76)	840.6	1.0482	785.5	849.6	1.0594	785.9	υ_5 C-H bending mode of C_2H_2
2190.3 (.2)	2268.5	1.0357	2265.7 2263.8	2268.1	1.0355	2261.8	υ_2 sym. CN str. mode of CH_3CN

[a]Computed infrared intensities (KM/mol) are given in parentheses.

4.2.3 Vibrational assignments: C_2H_2-CH_3CN complex A

The experimental vibrational wavenumber of the C_2H_2-CH_3CN complex A were compared with the wavenumber calculated using B3LYP/6-311++G(d,p) and MP2/aug-cc-pVDZ level of theory (Table 4.3 and Table 4.3a). The deviation between the experimental and calculated vibrational wavenumbers is attributed to matrix shifts as well as deficiencies of the theoretical model. Scaling factors for each vibrational mode of the C_2H_2 and CH_3CN monomers were calculated to correct these deviations. These scaling factors, by definition, exactly reproduce the experimental values of the monomer. Applying scaling factor to the modes of the complexes allows one to reliably predict the band position of the C_2H_2-CH_3CN complex.

4.2.3.1 υ_3 asymmetric stretch of C_2H_2

As mentioned earlier in Ar matrix, two new features were observed at 3242.1 and 3234.9 cm^{-1} in the as-deposited spectrum and the feature observed at 3234.9 cm^{-1} increased in intensity on annealing whereas the intensity of the feature at 3242.1 cm^{-1} slightly decreases. The experimental shifts of these features from the monomer are 46.8 and 54.0 cm^{-1}, respectively, compare well with the scaled computed value of 3243.4 cm^{-1} for the complex A with a shift of 45.5 cm^{-1}. It should be mentioned that the feature observed at 3242.1 cm^{-1} slightly decreased on annealing and could be attributed to site split feature for the complex A in an Ar matrix. In N_2 matrix, a new feature was observed at 3234.3 cm^{-1}, a red shift of 48.3 cm^{-1}, which increases on annealing and agrees well with the scaled computed shift of 45.2 cm^{-1} for the complex A. The agreement between the experimental and computed vibrational wavenumbers supports the computationally derived C-H⋯N structure of the complex, with C_2H_2 being the proton donor. The assignments for the feature observed at 3228.6 and 3227.6 cm^{-1} in Ar and N_2 matrixes will be discussed in the later section.

4.2.3.2 υ_5 mode of C_2H_2

The υ_5 mode of the C_2H_2 submolecule in the complex A in an Ar and N_2 matrix was computed to occur at 796.0 and 804.6 cm^{-1}, which is a blue shift of 59.2 and 59.9 cm^{-1} from the computed feature for the same mode in free C_2H_2. A feature was experimentally observed in an Ar and N_2 matrix at 780.6 and 773.9 cm^{-1}, which is in close agreement with our computations.

4.2.3.3 υ_2 symmetric CN stretching mode of CH_3CN

This mode of CH_3CN submolecule was observed as a *site-split* doublet feature at 2263.8/2265.7 and 2261.8 cm^{-1}, a blue shift of 5.8/7.7, 4.3 cm^{-1} in an Ar and N_2 matrixes, which compares well with the scaled computed value for the complex A, a blue shift of 5.6 and 6.5 cm^{-1} in Ar and N_2 matrixes, respectively.

4.2.4 Computations on the higher C_2H_2-CH_3CN complexes

To find out the possible sites of attack of the next C_2H_2 or CH_3CN molecule on the C_2H_2-CH_3CN complex *ab initio* computations were carried out for the higher cluster like C_2H_2-$(CH_3CN)_2$ and $(C_2H_2)_2$-CH_3CN. One minimum energy structure C_2H_2-$(CH_3CN)_2$ (complex B) was obtained in the potential energy surface while two minima were found for $(C_2H_2)_2$-CH_3CN (complexes C and D). Figure 4.7 shows the structure of these complexes calculated at B3LYP/6-311++G(d,p) level of theory. The higher complexes B, C and D shown in the figure 4.7 are stabilized by both C-H⋯N and C-H⋯π interactions. Table 4.2 gives the stabilization energies for the higher complexes B, C and D at B3LYP and MP2 levels of theory using 6-311++G(d,p) basis sets and B3LYP/aug-cc-pVDZ level of theory. The ZPE-corrected energy for complex B is exothermic by 5.6 kcal/mol at B3LYP/6-311++G(d,p) level. It is well known that CH_3CN forms dimer in the gas phase and the structure of the dimer is well documented [102].

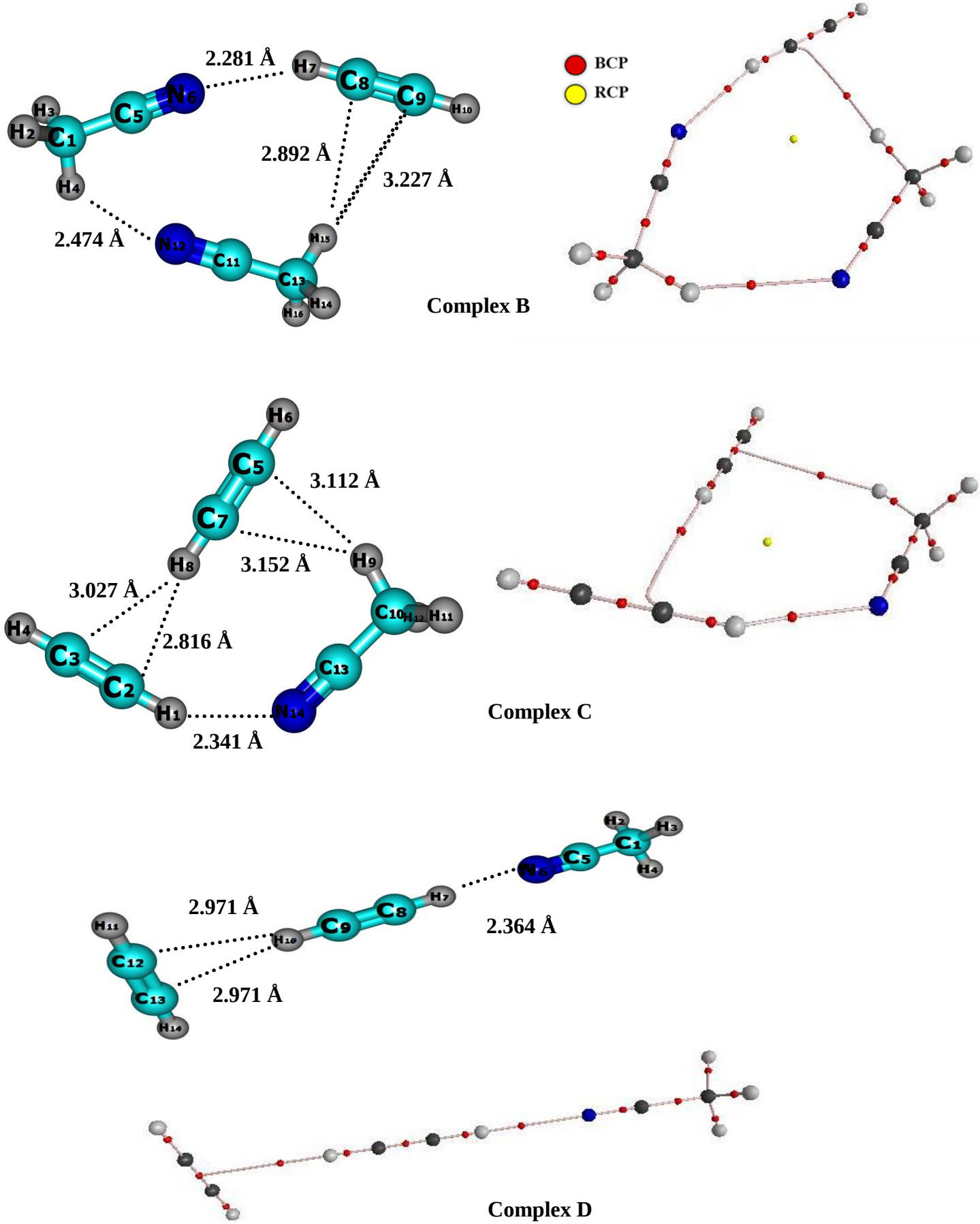

Figure 4.7: Structure of C_2H_2-CH_3CN complexes B, C and D computed at B3LYP/6-311++G(d,p) level of theory.

Table 4.4: Selected Structural parameters[a] for the C_2H_2-CH_3CN complex B, C and D calculated at the B3LYP/6-311++G(d,p) level of theory

Parameter	Complex B	Parameter	Complex C	Parameter	Complex D
C11-N12	1.153	H1-C2	1.069	C5-N6	1.152
N12-H13	2.279	H1-N14	2.340	N6-H7	2.360
N6-H9	2.472	H8-C2	2.815	H10-C12	2.974
H3-C14	2.891	H8-C3	3.017	H10-C13	2.974
H3-C15	3.216	H9-C7	3.147	C1-C5	1.456
∠C11-N12-H13	154.1	H9-C5	3.113	C1-H2	1.092
∠C5-N6-H9	133.9	∠N14-H1-C2	155.3	∠C5-N6-H7	179.9
∠H4-C14-H13	87.5	∠C13-N14-H1	135.0	∠C9-H10-C13	168.4
∠N6-H9-C7	144.1	∠C10-H9-C7	136.6	∠C9-H10-C12	168.3
tor∠C11-N12-H13-C14	-0.19	∠C10-H9-C5	158.7	∠H2-C1-H4	110.1
tor∠C5-N6-H9-C7	-0.01	∠C7-H8-C2	169.9	∠H3-C1-H2	108.8
tor∠C1-H4-C14-H13	-0.76	tor∠C2-H1-N14-C13	-0.08	tor∠H3-C1-C5-N6	4.76
tor∠C1-H4-C14-C15	179.2	tor∠C10-H9-C7-H8	-0.18	tor∠C5-N6-H7-C8	1.97
tor∠C15-C14-H13-N12	0.50	tor∠C7-H8-C2-H1	-0.05	tor∠C9-H10-C12-C13	179.7

[a]Bond lengths in Å, angles and torsional angles in °.

$(CH_3CN)_2$ forms a cyclic dimer with C-H···N interaction between the two CH_3CN molecules [105]. When C_2H_2 interacts with the $(CH_3CN)_2$ (complex B) the hydrogen H15 of CH_3CN interacts with the carbons C8 and C9 of C_2H_2, the bond distances are 2.892 Å and 3.227 Å respectively and the nitrogen N6 of CH_3CN interacts with the hydrogen H7 of C_2H_2, a bond distance of 2.281 Å. Further, there is yet another interaction between the hydrogen H4 and nitrogen N12 between the two acetonitrile, a bond distance of 2.474 Å making a ten member cyclic structure. In complex B, there are two C-H···N interactions and one C-H···π interaction. Due to these interactions, the C-H bond of C_2H_2 submolecule is elongated by 0.0078 Å, which results in a red shift of 54.0 cm^{-1} at B3LYP/6-311++G(d,p) level of theory.

In complex C, the hydrogen H1 of C_2H_2 interacts with N14 of CH_3CN, the hydrogen H9 of CH_3CN interacts with π cloud of C_2H_2 (C5 and C7 carbons) and the hydrogen H8 of C_2H_2 interacts with the π cloud of C_2H_2 (C2 and C3 carbons) giving a nine-member cyclic structure. In complex C, there are two C-H···π interaction and one C-H···N interaction, due to this interaction the C-H bond is lengthened by 0.0056 Å and red shifted by 46.9 and 29.5 cm^{-1} respectively.

Complex D has a linear structure with one C-H···π and C-H···N interaction. The bond distance between the hydrogen H10 and carbons C12 and C13 is 2.971 Å and between the N6 and H7 is 2.364 Å. The C-H bond is red shifted by 50.1 and 2.4 cm^{-1} and the C-H bonds are lengthened by 0.0053 Å and 0.0014 Å respectively. Among the complexes C and D, C is more stable than D since the ZPE corrected energy of complex C is exothermic by about 3.0 kcal/mol at B3LYP/6-311++G(d,p) level of theory relative to complex D. This could be due to the fact that complex C is stabilized by two intermolecular C-H···π interaction and one C-H···N interaction whereas complex D with an open and linear structure, stabilized only by intermolecular C-H···π and C-H···N interactions.

4.2.5 Vibrational assignments: C_2H_2-CH_3CN higher complexes

At higher concentrations of CH_3CN in Ar and N_2 matrixes, new features were observed in the spectra and the intensity of the absorption band increases with the CH_3CN concentration, indicating that more than one molecule of CH_3CN is involved in the complex. In both the matrixes, new absorption peaks were observed at 3228.6 and 3227.6 cm^{-1}, which is assigned to the υ_3 mode of C_2H_2 submolecule in the C_2H_2-$(CH_3CN)_2$ complex B. The experimentally observed red shift of the C-H asymmetric stretching vibration of 60.3 and 55.0 cm^{-1} in Ar and N_2 matrixes, which is in good agreement with the calculated shift of 51.9 cm^{-1} for the complex B computed at B3LYP/6-311++G(d,p) level of theory. The υ_5 bending mode of C_2H_2 submolecule for the complex B was computed to occur at 796.1, 799.4 and 805.0, 807.8 cm^{-1}, in an Ar and N_2 matrixes, respectively. These features compare well with the experimental feature observed at 780.6, 783.0 cm^{-1} in Ar and 773.9 785.9 cm^{-1} in N_2 matrix, respectively. It should be mentioned that the feature observed at 780.6 cm^{-1} in Ar and 773.9 cm^{-1} in N_2 matrix in the υ_5 bending mode of C_2H_2 submolecule is assigned for the complex A that could be assigned for the complex B because the computed frequencies are very close for the complexes A and B and there is some probability that the bending mode of these complexes can get overlapped.

4.2.6 Nature of interaction: AIM calculation

To understand the nature of the interaction in C_2H_2-CH_3CN complexes, AIM theory was used. A (3, -1) bond critical point (BCP) was sought, using the optimized geometry of the C_2H_2-CH_3CN complexes A, B, C and D computed at B3LYP/6-311++G(d, p) level of theory. The locations of the bond critical points are shown in figure 4.6. Table 4.5 gives the properties of BCP for all the complexes computed at B3LYP/6-311++G(d,p) level of theory. At the BCP for all the complexes A, B, C and D, electron density ($\rho(r_c)$), Laplacian of electron density ($\nabla^2\rho(r_c)$) were examined. At the BCP for all the complexes the values of $\rho(r_c)$ are of the order of 10^{-2} a.u. and $\nabla^2\rho(r_c)$ values are positive, as are typical of closed shell interactions.

4.2.7 NBO analysis

Table 4.6 shows the results of NBO analysis of C_2H_2-CH_3CN complexes A, B, C and D computed at B3LYP/6-311++G(d,p) level of theory. From the table it is clear that for the complex A, the dominant part of the electron density transfer (EDT) occurs from the n^1N6 lone pair to anti bonding σ* orbital of the H7-C8 of C_2H_2 submolecule, which is evident from the increase in the electron occupancy of antibonding σ*(H7-C8) orbital of C_2H_2 submolecule (by about ~0.007e) and decrease in the occupancy of donor lone pair on N6 (by about ~0.006e) in complex A relative to the corresponding monomers. The delocalization of the electron density to the antibonding, σ*(H7-C8) orbital of C_2H_2 weakens the C-H bond, resulting in elongation of the C-H bond with a concomitant red shift of its C-H stretching wavenumber. The second order perturbation E_2 energy for the delocalization interaction was found out to be ~3.30 kcal/mol. In complex B, there are two C-H⋯N and one C-H⋯π interactions. The hyperconjugative interaction between the n^1N6 → σ*(H9-C7) and n^1N12 → σ*(H13-C14) are the dominant interactions were found to be ~1.17 and ~3.77 kcal/mol, respectively. Due to the hyperconjugative interaction the electron occupancy in the antibonding orbital of σ*(H9-C7) and σ*(H13-C14) increases making the C-H bond to lengthen and concomitant red shift in the C-H wavenumber was observed. The next dominant interaction in the complex B was found to be the π_1(C14-C15) → σ*(H4-C1) as the E_2 energy for this interaction was calculated to be 0.64 kcal/mol. In addition to the above interactions, complex B is also stabilized by bond pair-acceptor orbital interaction such as σ(C7-H9) → π*(C5-N6), π_2(C5-N6) → σ*(C7-H9), σ(C14-H13) → π_1*(C11-N12) and π_1(C11-N12) → σ*(C14-H13) whose magnitudes are smaller than lone pair-acceptor orbital interactions but still cannot be neglected.

Table 4.5: Properties of intermolecular (3,-1) bond critical point in C_2H_2-CH_3CN complexes A, B, C and D computed at B3LYP/6-311++G(d,p) level of theory.

Complexes		$\rho(r_C)$	$\nabla^2\rho(r_C)$	λ_1	λ_2	λ_3	$\lvert\lambda_1\rvert / \lambda_3$
Complex A	C≡N (AN)···H(Ac)	0.01107	0.08339	-0.01111	-0.01111	0.06117	0.18162
Complex B	C≡N(AN)···H (Ac)	0.01284	0.04552	-0.01337	-0.01330	0.07221	0.18419
	C-H(AN)···N≡C(AN)	0.00968	0.03068	-0.00894	-0.00864	0.04824	0.18532
	C-H(AN)···π (Ac)	0.00492	0.01220	-0.00343	-0.00286	0.01852	0.18520
Complex C	C≡N (AN)···H(Ac)	0.01121	0.03882	-0.01110	-0.01086	0.06078	0.18263
	C-H (AN)···π(Ac)	0.00403	0.00991	-0.00264	-0.00209	0.01464	0.18033
	C-H(Ac)···π (Ac)	0.00528	0.01352	-0.00377	-0.00306	0.02035	0.18526
Complex D	C≡N(AN)···H (Ac)	0.01071	0.03746	-0.01064	-0.01064	0.05874	0.18114
	C-H(Ac)···π (Ac)	0.00460	0.01169	-0.00314	-0.00251	0.01734	0.18108

Table 4.6: Electron occupancies of various natural bonding orbitals (NBOs) of C_2H_2-CH_3CN complexes A, B, C and D computed at B3LYP/6-311++G(d,p) level of theory. The donor-acceptor delocalization interaction and delocalization energies (E_2, kcal/mol) are also shown.

Complexes	NBO	Occupancy	Donor-acceptor delocalization interaction	Second order perturbation (E_2) energy (kcal/mol)
Complex-A	n^1N6	1.96405 (1.96988)[a]	n^1N6 → σ*(H7-C8)	3.30
	σ*(H7-C8)	0.01311 (0.00600)[b]		
Complex-B	n^1N6	1.96738 (1.96988)[a]	n^1N6 → σ*(H9-C7)	1.17
	σ*(H9-C7)	0.01068 (0.00832)[a]	σ(C7-H9) → π*(C5-N6) π_2(C5-N6) → σ*(C7-H9)	0.21 0.24
	σ(C7-H9)	1.96593 (1.97097)[a]		
	π_2*(C5-N6)	0.03998 (0.03563)[a]		
	σ*(C7-H9)	0.01068 (0.00832)[a]		
	n^1N12	1.96188 (1.96988)[a]	n^1N12 → σ*(H13-C14)	3.77
	σ*(H13-C14)	0.01511 (0.00600)[b]		
	π_1(C11-N12)	1.98828 (1.98709)[a]	π_1(C11-N12) → σ*(C14-H13) σ(C14-H13) → π_1*(C11-N12)	0.19 0.12
	σ*(C14-H13)	0.01511 (0.00600)[b]		
	σ(C14-H13)	1.98901 (1.99054)[b]		
	π_1*(C11-N12)	0.04043 (0.03563)[a]		
	π_1(C14-C15)	1.99177(1.99961)[b]	π_1(C14-C15) → σ*(H4-C1)	0.64
	σ*(H4-C1)	0.00933 (0.00832)[a]		
Complex-C	n^1N14	1.96430(1.96988)[a]	n^1N14 → σ*(H1-C2)	2.28
	σ*(H1-C2)	0.01262 (0.00600)[b]		
	π_2(C13-N14)	1.98676 (1.98709)[a]	π_2(C13-N14) → σ*(C1-H2)	0.42
	σ*(H1-C2)	0.01262 (0.00600)[b]		
	σ(H1-C2)	1.98885 (1.99054)[b]		
	π_2* (C13-N14)	0.03887 (0.03563)[a]	σ(C1-H2) → π_2*(C13-N14)	0.23
	π_2(C2-C3)	1.99137 (1.99961)[b]	π(C2-C3)→σ*(H8-C7)	0.98
	σ*(H8-C7)	0.00871 (0.00600)[b]		
	π_1(C5-C7)	1.99712 (1.99961)[b]	π_1(C5-C7) → σ*(H9-C10)	0.33
	σ*(H9-C10)	0.00888 (0.00832)[b]		
Complex-D	n^1N6	1.96441 (1.96988)[a]	n^1N6 → σ*(H7-C8)	3.11
	σ*(H7-C8)	0.01272 (0.00600)[b]		
	π_2(C12-C13)	1.99135 (1.99961)[b]	π_2(C12-C13) →σ*(C9-H10)	0.77
	σ*(C9-H10)	0.00823 (0.00600)[b]		

[a]Occupancy of monomeric CH_3CN is given in parenthesis.
[b]Occupancy of monomeric C_2H_2 is given in parenthesis.

4.3 Interaction of acetonitrile (CH_3CN) with water (H_2O)

Several theoretical groups have performed calculations on the CH_3CN-H_2O system and found CH_3CN and H_2O form linear and cyclic type complexes, there is no clear experimental evidence for the formation of these complexes in the condensed phase [102-110]. In this study, we have used matrix isolation infrared technique and *ab initio* computations to identify the CH_3CN-H_2O complex.

4.3.1 Experimental details

The sample water (H_2O,Milli-Q integral ultrapure,18.2MΩ.cm) and CH_3CN (Merck, HPLC grade 99.8%) were used as such, without further purification. Ar (INOX, 99.9995%) and N_2 (INOX, 99.995%) was used as matrix gas. The H_2O, CH_3CN, N_2 /Ar gas was then deposited separately using triple jet nozzle onto a KBr substrate maintained at 12 K. We used typical matrix-to-sample ratios ranging from 1000:0.5 to 1000:1 for H_2O and 1000:0.5 to 1000:2.5 for CH_3CN. Infrared spectra of matrix isolated samples were recorded using BOMEM MB100 FTIR spectrometer.

Figure 4.8 and 4.9 show the as-deposited (block A) and annealed spectra (block B) of H_2O with and without CH_3CN in N_2 and Ar matrixes. In N_2 matrix, the υ_3 and υ_1 modes of H_2O were observed at 3727.2 cm^{-1} and 3634.6 cm^{-1} respectively. The feature observed at 3715.1 and 3550.2 cm^{-1} correspond to the υ_3 acceptor and υ_1 donor mode of $(H_2O)_2$ in N_2 matrix. In Ar matrix, the υ_3 mode of H_2O was observed at3711.2 cm^{-1}. The feature observed at 3706.9 and 3573.3 cm^{-1} are due to υ_3 donor and υ_1 acceptor of $(H_2O)_2$ in Ar matrix, respectively. These features agree well with the reported literature value [215]. When H_2O and CH_3CN were co-deposited in N_2 and Ar matrix, new feature was observed in the υ_3 and υ_1 mode of H_2O in N_2 and Ar matrix at 3705.5, 3567.1/3564.7 cm^{-1} and 3718.9, 3538.6 cm^{-1} respectively. Furthermore, the intensity of these features increased on annealing the matrix.

Figure 4.10 shows the IR spectra of the υ_2 mode of H_2O in N_2 matrix. Block A and B

correspond to the spectra recorded at 12 K and after annealing the matrix at 30 K. The feature observed at 1597.4 cm^{-1} is due to υ_2 mode of water in N_2 matrix. The features observed at 1618.6 and 1600.8 cm^{-1} are due to υ_2 donor and acceptor modes of $(H_2O)_2$ in N_2 matrix. Co-deposition of H_2O and CH_3CN and subsequent annealing produced a doublet at 1630.2/1632.6 cm^{-1}. In Ar matrix, the υ_2 bending mode of H_2O has multiple features due to the vibration-rotation structure and new features could not be discerned in this region and hence not shown.

Figure 4.11 and 4.12 shows the IR spectra of CN stretching mode of CH_3CN in N_2 and Ar matrix. Figure 4.10a and 4.11a shows the spectra of bare CH_3CN in N_2 and Ar matrixes. The features observed at 2257.5 and 2257.9 cm^{-1} are due to υ_2 CN stretching mode of CH_3CN in N_2 and Ar matrix, whereas the feature observed at 2266.2 cm^{-1} in N_2 matrix is due to CH_3CN monomer trapped in a different site [219]. Features due to CH_3CN dimer in N_2 and Ar matrixes were observed at 2254.6 and 2256.0 cm^{-1}, respectively. When H_2O and CH_3CN were deposited, new feature was observed at 2272.5 cm^{-1} in N_2 and a doublet at 2264.7/2267.6 cm^{-1} in Ar matrix. Experiments were performed where CH_3CN and H_2O alone were deposited separately in the N_2 and Ar matrixes to confirm that all the product features discussed in this work did correspond to the adducts of CH_3CN with H_2O. Unfortunately, in experiments where CH_3CN alone was deposited, H_2O was found to be present as an inevitable impurity (fig. 4.11a and 4.12a). However, the dependence of the intensity of the product features on the H_2O concentration confirmed the participation of both CH_3CN and H_2O in the complex formation. New features could not be observed in the υ_4 CC stretch, υ_7 CH_3 rocking, υ_3 CH_3 deformation, υ_6 anti-symmetric CH_3 deformation, υ_1 symmetric CH stretching, υ_5 anti-symmetric CH stretching modes of CH_3CN in both Ar and N_2 matrixes.

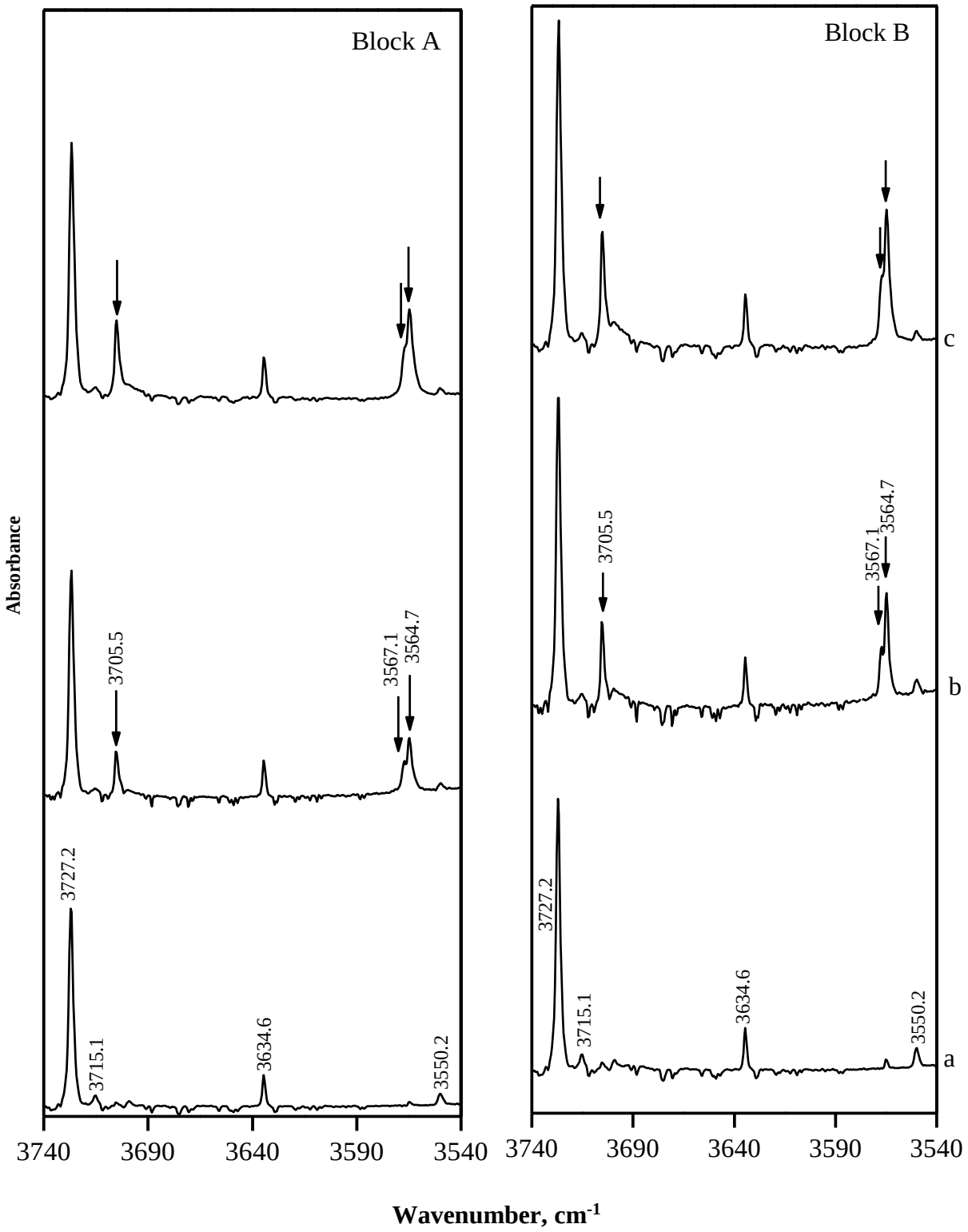

Figure 4.8: Spectra of CH_3CN-H_2O complexes in N_2 matrix in the region 3740-3540 cm^{-1}. Block A shows the as-deposited spectra and block B shows the 30 K annealed spectra. Matrix isolation infrared spectra of various concentrations of $CH_3CN/H_2O/N_2$; a) 0/2/1000; b)1/1/1000; c) 2/1/1000.

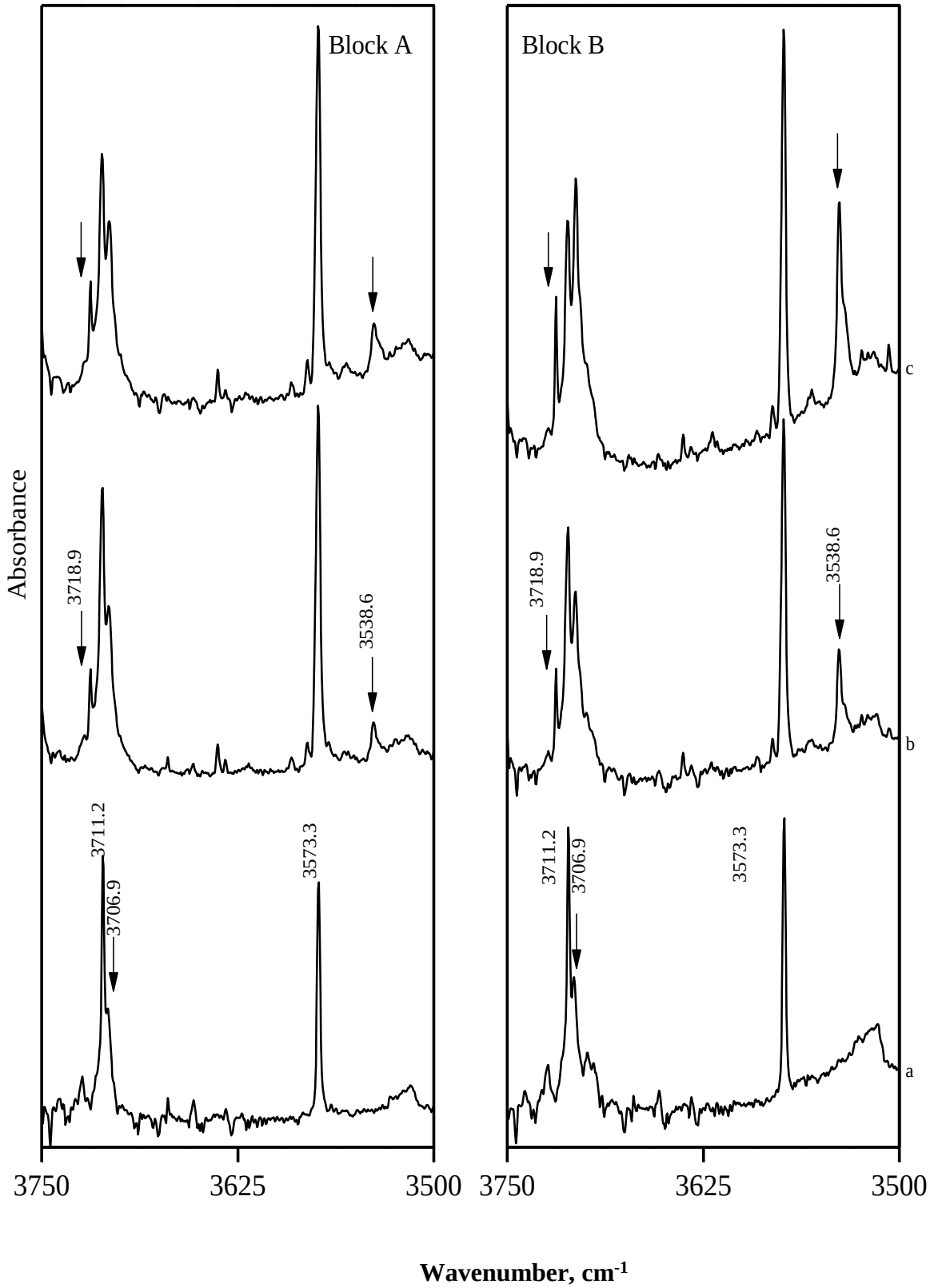

Figure 4.9: Spectra of CH_3CN-H_2O complexes in Ar matrix in the region 3750-3500 cm^{-1}. Block A and block B corresponds to the as-deposited and 35 K spectra. Matrix isolation infrared spectra of various concentrations of CH3CN/H2O/Ar; a) 0/0.5/1000; b) 1.5/0.5/1000; c) 2.5/0.5/1000.

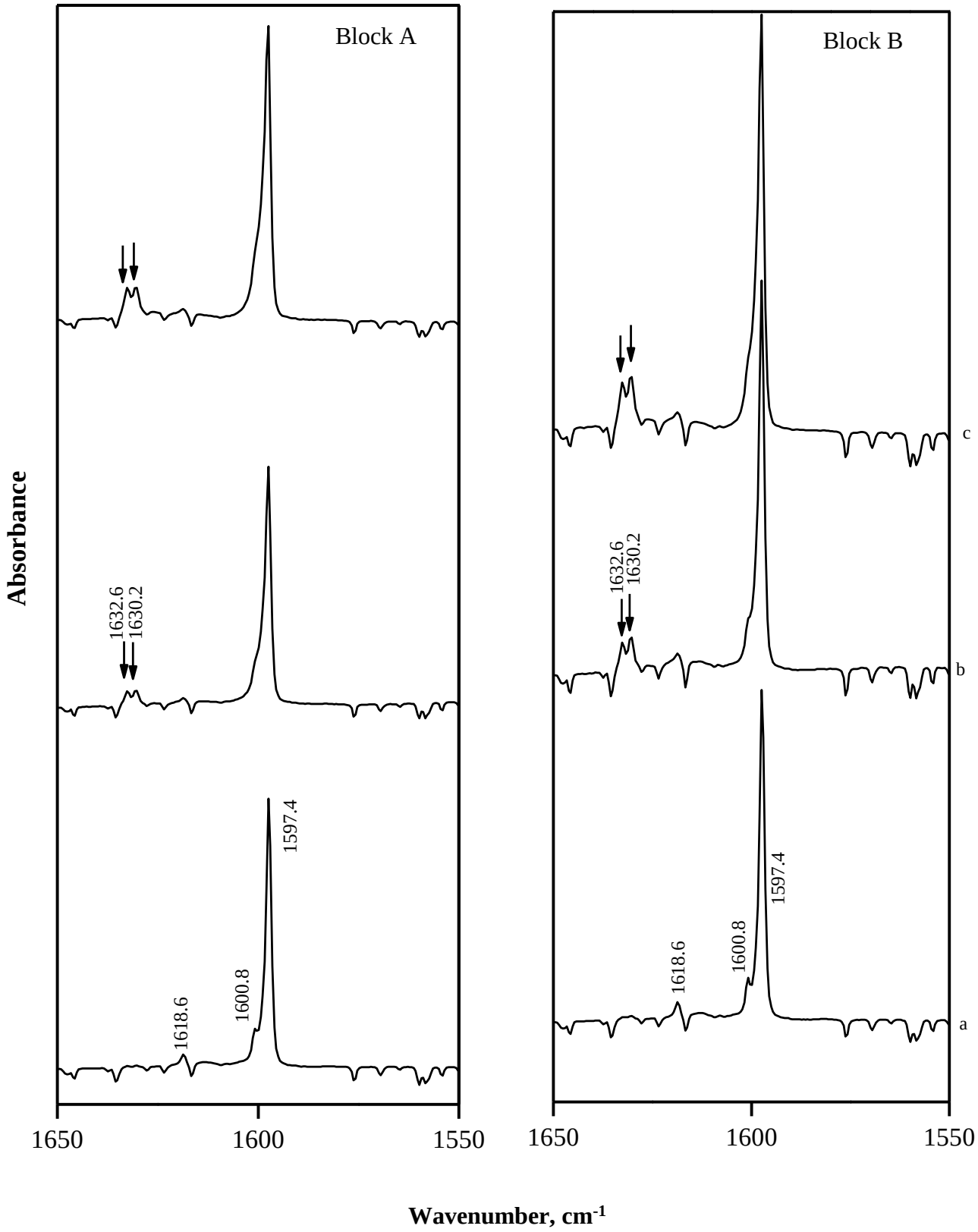

Figure 4.10: Spectra of CH_3CN-H_2O complexes in N_2 matrix in the region 1650-1550 cm^{-1}. Block A shows the as-deposited spectra and block B shows the 30 K annealed spectra. Matrix isolation infrared spectra of various concentrations of $CH_3CN/H_2O/N_2$; a) 0/2/1000; b) 1/1/1000; c) 2/1/1000.

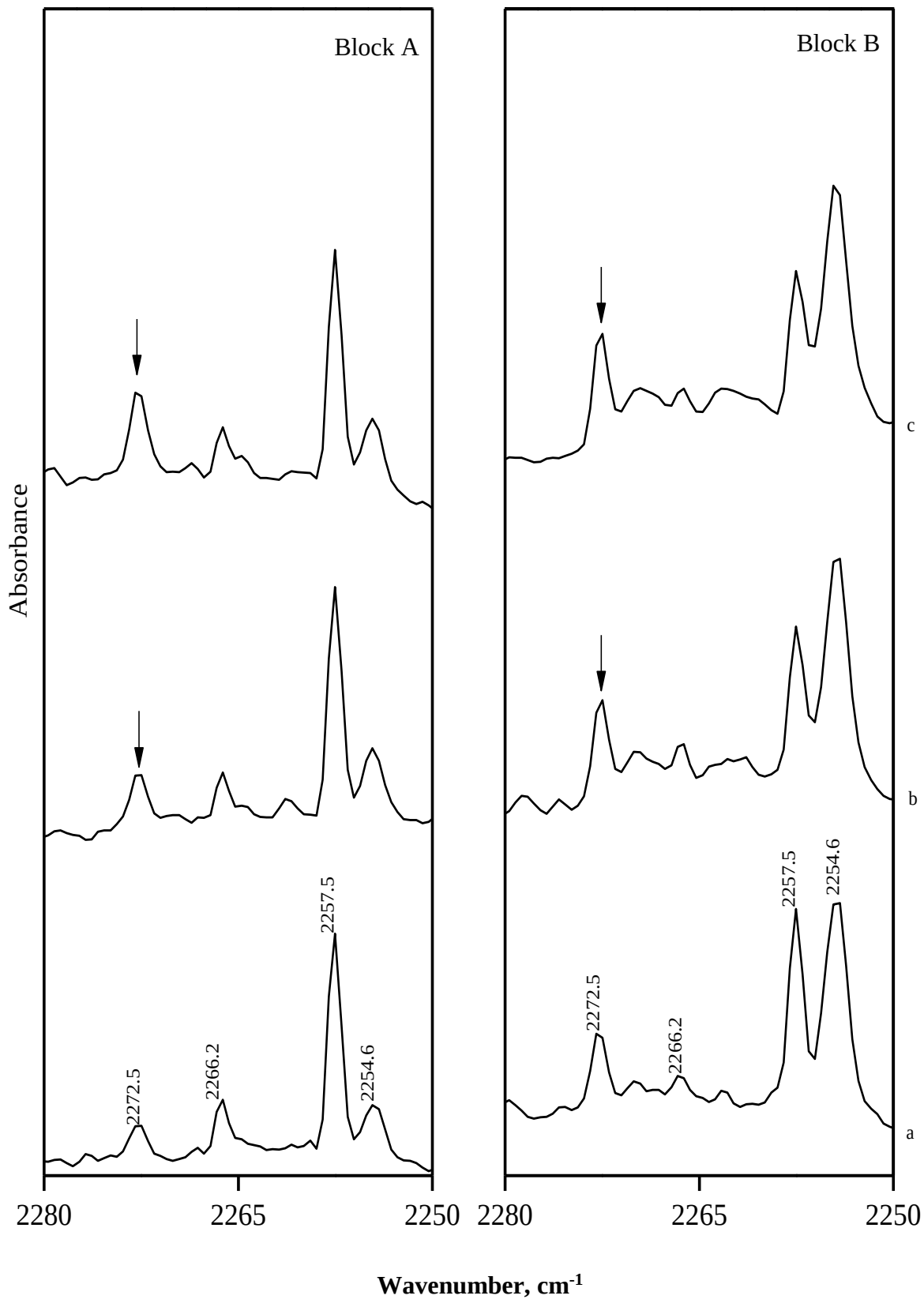

Figure 4.11: Spectra of CH_3CN-H_2O complexes in N_2 matrix in the region 2280-2250 cm^{-1}. Matrix isolation infrared spectra of various concentrations of $CH_3CN/H_2O/N_2$; a) 2.5/0/1000; b) 2.5/0.5/1000; c) 2.5/0.75/1000. Block A shows the as-deposited spectra and block shows the 30 K annealed spectra.

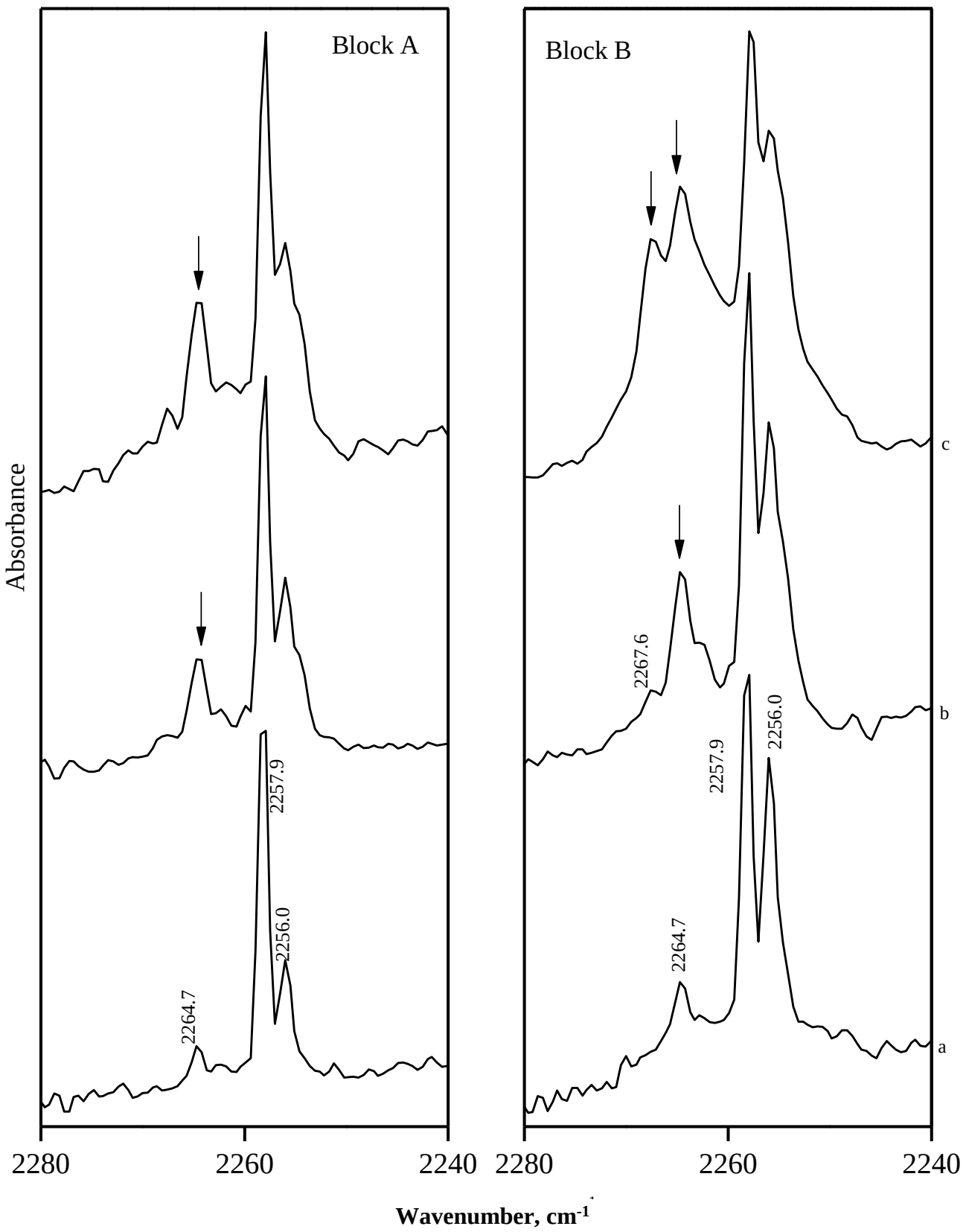

Figure 4.12: Spectra of CH_3CN-H_2O complexes in Ar matrix in the region 2280-2240 cm^{-1}. Matrix isolation infrared spectra of various concentrations of $CH_3CN/H_2O/N_2$; a) 1.5/0/1000; b) 1.5/0.5/1000; c) 1.5/0.75/1000. Block A shows the as-deposited spectra and block B shows the 35 K annealed spectra.

4.3.2 Computational

Figure 4.13 shows the structure of these complexes computed at B3LYP/6-311++G(d,p) level of theory. Table 4.7 shows the selected structural parameters for the complexes A and B computed at this level. For the complex A, the bond distance between N6⋯H8 is 2.081 Å. Due to this hydrogen-bonded interaction, the O-H bond is elongated by 0.006 Å and the C≡N bond distance is decreased by 0.001 Å. For the complex B, the bond distance between the H3⋯O7 is 2.688 Å and there is another interaction between H8⋯N6 and H8⋯C5, the bond distances are 2.475 Å and 2.509 Å, respectively. The O-H and C≡N bond distance in the complex B are elongated by 0.001 Å and 0.006 Å, respectively. Table 4.8 shows the calculated stabilization energies for the complexes A and B computed at B3LYP/6-311++G(d,p) level of theory. As can be seen from the table, the raw stabilization energies of the two complexes are -4.82 and -3.91 kcal/mol, which reduces to -3.43 and -2.67 kcal/mol when zero-point energy corrections are applied. Further, the relative energy difference between the raw energies for the two complexes A and B at B3LYP/6-311++G(d,p) and MP2/aug-cc-pVDZ are -0.91 and -0.12 kcal/mol respectively. It can be seen from the table that at all levels of theory and basis sets used, complex A is more stable than complex B.

4.3.3 Vibrational assignments

The experimental vibrational wavenumbers of the CH_3CN-H_2O complexes A and B were compared with the wavenumber calculated using B3LYP/6-311++G(d,p) level of theory (Table.4.10). Table.4.10 compares the shift between the scaled computed vibrational wavenumbers with experimental wavenumbers in N_2 and Ar matrixes for the complex A.

4.3.3.1 υ_3 and υ_1 modes of H_2O

DFT computations indicated due to the hydrogen bonding in complex A, the υ_3 and υ_1 mode of H_2O are red-shifted by 25.5 and 74.9 cm^{-1} respectively. Experimentally, we

Table 4.7: Selected structural parameters[a] for the CH_3CN-H_2O complex A calculated at B3LYP/6-311++G(d,p) level of theory.

Parameter	Complex A	Parameter	Complex B
C1-H2	1.092 (1.092)[b]	C1-H2	1.092 (1.092)
C1-H3	1.092 (1.092)	C1-H3	1.092 (1.092)
C1-H4	1.092 (1.092)	C1-H4	1.092 (1.092)
C1-C5	1.455 (1.457)	C1-C5	1.455 (1.457)
C5-N6	1.151 (1.153)	C5-N6	1.153 (1.153)
N6-H7	2.080	H2-O7	2.688
C5-H9	4.558	C5-H9	2.509
N6-H9	3.409	N6-H9	2.476
H7-O8	0.968 (0.962)	O7-H8	0.961 (0.962)
O8-H9	0.961 (0.962)	O7-H9	0.965 (0.962)
∠H2-C1-H3	108.9(108.8)	∠H2-C1-H3	109.3(108.8)
∠H2-C1-C5	110.1(110.1)	∠H2-C1-C5	108.7(109.5)
∠C1-C5-N6	179.9 (179.9)	∠C1-C5-N6	178.0 (180.0)
∠C5-N6-H7	168.1	∠C1-H2-O7	120.1
∠N6-H7-O8	178.8	∠C5-N6-H9	82.5
∠H7-O8-H9	104.7(105.1)	tor∠C5-N6-H9-O7	0.0
tor∠N6-H7-O8-H9	5.5	tor∠H4-C1-H2-O7	120.5
tor∠C1-C5-N6-H7	8.5	tor∠O7-H2-C1-C5	0.08

[a]Bond length in Å; bond angle and dihedral angle in °.
[b]Parameters of monomers are given in parentheses.

Table 4.7a: Selected structural parameters[a] for the CH_3CN-H_2O complex A calculated at MP2/aug-cc-pVDZ level of theory.

Parameter	Complex A	Parameter	Complex B
C1-H2	1.099 (1.099)[b]	C1-H2	1.099 (1.099)
C1-H3	1.099 (1.099)	C1-H3	1.099 (1.099)
C1-H4	1.099 (1.099)	C1-H4	1.099 (1.099)
C1-C5	1.470 (1.471)	C1-C5	1.470 (1.471)
C5-N6	1.183 (1.185)	C5-N6	1.186 (1.185)
N6-H7	2.059	H2-O7	2.641
H7-O8	0.972 (0.966)	O7-H8	0.969 (0.966)
O8-H9	0.965 (0.966)	O7-H9	0.965 (0.966)
∠H2-C1-H3	109.2 (108.8)	∠H2-C1-H3	109.7 (108.8)
∠H2-C1-C5	109.7(110.1)	∠H2-C1-C5	109.9 (109.5)
∠C1-C5-N6	179.8 (179.9)	∠C1-C5-N6	177.8 (180.0)
∠C5-N6-H7	169.7	∠C1-H2-O7	119.4
∠N6-H7-O8	176.3	∠C5-N6-H9	81.9
∠H7-O8-H9	103.8(103.8)	tor∠C5-N6-H9-O7	0.0
tor∠N6-H7-O8-H9	-179.7	tor∠H4-C1-H2-O7	120.5
tor∠C1-C5-N6-H7	-0.2	tor∠O7-H2-C1-C5	0.08

[a]Bond length in Å; bond angle and dihedral angle in °.
[b]Parameters of monomers are given in parentheses.

Table 4.8: Raw[a]/ZPE-corrected/BSSE-corrected stabilization energies for the CH_3CN-H_2O complexes A and B computed at B3LYP/6-311++G(d,p) and MP2/aug-cc-pVDZ levels of theory.

Stabilization energy (ΔE)		
Complexes	**B3LYP/6-311++G(d,p)**	**MP2/aug-cc-pVDZ**
A	-4.82/-3.43/-4.50	-5.32/-3.91/-4.45
B	-3.91/-2.67/-3.79	-5.20/-3.81/-4.36

All energies are in kcal/mol (see text for details).
[a]Raw stabilization energies refer to energies not corrected for either ZPE or BSSE.

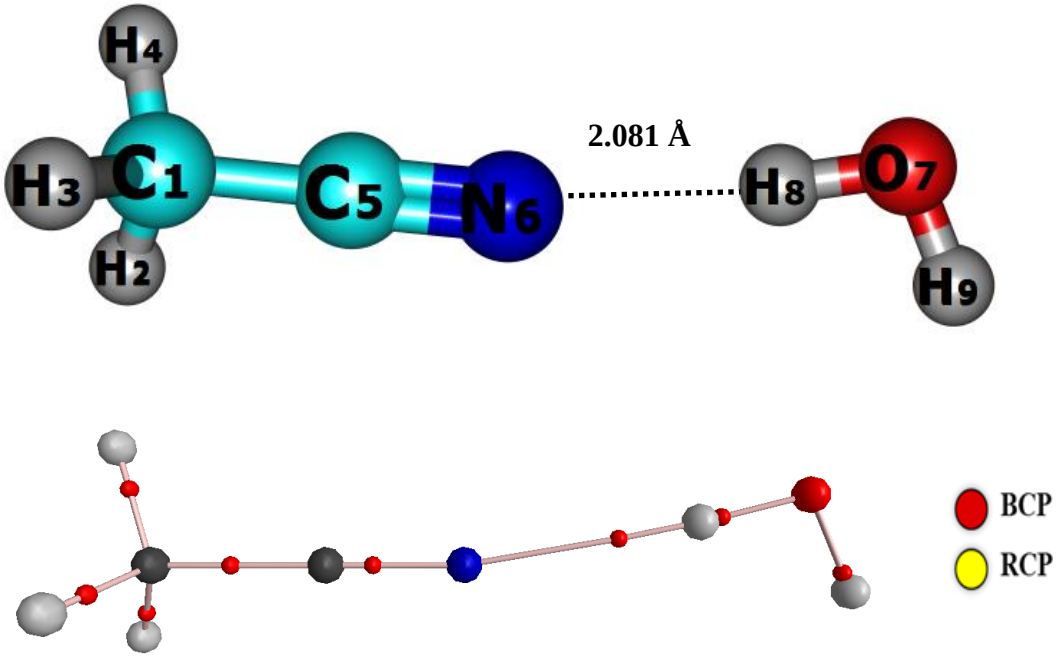

Complex A

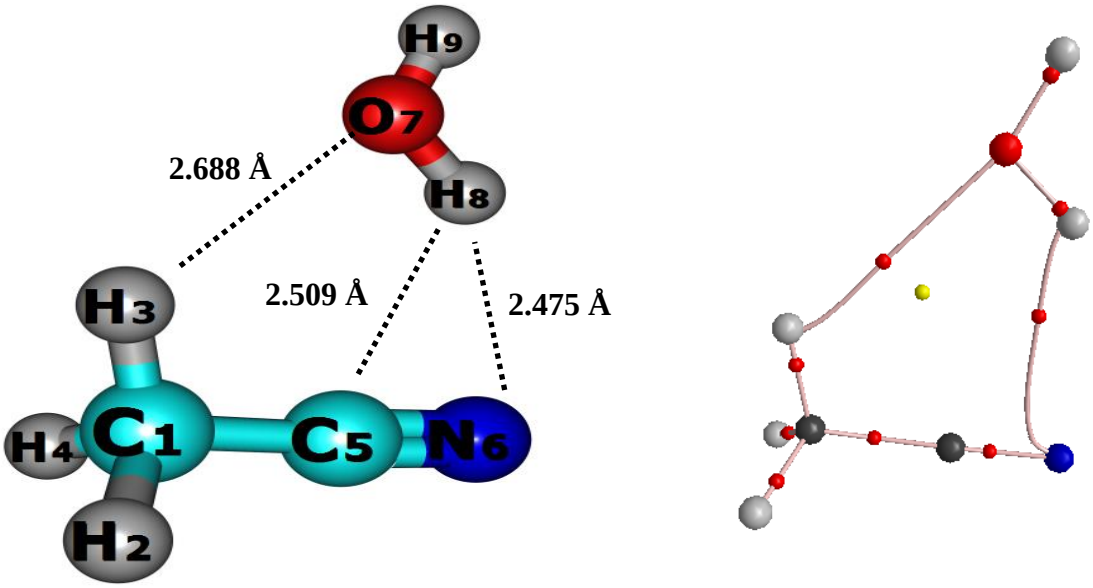

Complex B

Figure 4.13: Structure of the CH_3CN-H_2O complexes A and B optimized at B3LYP/6-311++G(d,p) level of theory.

observed new features at 3705.5 and 3564.7/3567.1 cm^{-1} in N_2 and at 3718.9 and 3538.6 cm^{-1} in Ar matrixes, which amounts to a red shift of 21.7,68.7 cm^{-1} and 14.1, 99.4 cm^{-1}, respectively. The experimental shift compares well with the scaled computed wavenumbers for the complex A. The features observed at 3564.7/3567.1 cm^{-1} in the υ_1 mode of H_2O may be due to the matrix splitting in N_2 matrix for the complex A.

It should be mentioned that for the complex A, computation shows the IR intensity of the υ_1 symmetric stretching mode of H_2O increases by a factor of ~ 40 whereas the same mode in the complex B increases only by a factor of ~3 when compared to the H_2O monomer.

4.3.3.2 υ_2 mode of H_2O

In N_2 matrix, the υ_2 mode for the complex A is observed as a site split feature at 1630.2 and 1632.6 cm^{-1}, a blue shift of 34.0 cm^{-1} from the monomeric H_2O feature. The computations also showed a similar trend, i.e., the computed value for the complex A occurs at 1632.1 cm^{-1}, a blue shift of 28.9 cm^{-1}, which compares well with the experimentally observed feature at 1630.2 cm^{-1}. The complexity in the υ_2 mode of H_2O in Ar matrix due to vibration-rotation congestion did not enable us to clearly discern the new feature for the complex.

4.3.3.3 υ_2 CN stretch of CH_3CN

The computed value in this mode for the complex A occurs at 2373.7 cm^{-1}, a blue shift of 11.5 cm^{-1}. In N_2 matrix, on complex formation new feature was observed at 2272.5 cm^{-1}, and in Ar matrix as a doublet at 2264.7/2267.6 cm^{-1}, with a blue shift 15.0 and 8.3 cm^{-1}, respectively, which agrees well with the computed feature for the complex A. It should be mentioned that computed value for the complex B shows a red shift of 7.2 cm^{-1}.

Experimentally, we could observe only the blue-shifted feature with respect to the CH_3CN monomer, which clearly ascertains the formation of complex A in both the matrixes.

Table 4.9: Computed unscaled and scaled vibrational wavenumbers (cm^{-1}), scaling factors and mode assignments calculated at the B3LYP/6-311++G(d,p) level of theory and comparison with the experimental wavenumbers (cm^{-1}) for the CH_3CN-H_2O complexes A and B in Ar and N_2 matrixes.

Computed/ unscaled (υ)	Ar			N_2			Mode assignment
	Computed/ scaled (υ)	Scaling factor	Exp (υ)	Computed/ scaled (υ)	Scaling factor	Exp (υ)	
CH_3CN							
930.0(2)[a]	917.2	0.9856	916.6	917.6	0.9967	917.6	υ_4 sym. CC str. (A_1)
1061.0(2)	1038.2	0.9785	1038.2	1043.3	0.9833	1040.7 1045.8	υ_7 CH_3 rock (E)
1411.6(3)	1375.9	0.9747	1375.9	1378.5	0.9766	1378.5	υ_3 sym.CH_3def (A_1)
1474.7(12)	1445.5	0.9802	1445.5	1447.9	0.9818	1446.7 1449.1	υ_6 antisym.CH_3 def. (E)
2362.9(12)	2258.0	0.9556	2258.0	2257.5	0.9557	2257.5	υ_2 CN str. (A_1)
3045.9(4)	2950.6	0.9687	2950.5	2949.0	0.9682	2949.0	υ_1 sym. CH str. (A_1)
3115.6(1)	3004.4	0.9643	3004.5	3009.3	0.9659	3009.3	υ_5 antisym. CH str. (E)
H_2O							
3813.5 (9)	3638	0.9540	3638	3634.6	0.9531	3634.6	υ_1 mode of H_2O
1603.2(66)	1589.7	0.9916	1589.7 1608.0 1623.9	1597.4	0.9964	1597.4	υ_2 mode of H_2O
3918.8 (57)	3733.0	0.9526	3776.4 3756.2 3711.2	3727.2	0.9511	3727.2	υ_3 mode of H_2O
Complex A							
2373.7(24)	2268.3	0.9556	2264.7 2267.6	2268.6	0.9557	2272.5	υ_2 C-N stretch
3738.6(368)	3566.6	0.9540	3538.6	3563.3	0.9531	3564.7 3567.1	υ_1 mode of H_2O
1632.1(60)	1618.3	0.9916	-[b]	1626.2	0.9964	1630.2 1632.6	υ_2 mode of H_2O
3893.3(111)	3708.7	0.9526	3718.9	3702.9	0.9511	3705.5	υ_3 mode of H_2O
Complex B							
2355.7(20)	2251.1	0.9556	-[b]	2251.3	0.9557	-[b]	υ_2 C-N stretch
3789.4(32)	3615.1	0.9540	-[b]	3611.7	0.9531	-[b]	υ_1 mode of H_2O
1611.4(97)	1597.9	0.9916	-[b]	1605.6	0.9964	-[b]	υ_2 mode of H_2O
3906.9(90)	3721.4	0.9526	-[b]	3715.9	0.9511	-[b]	υ_3 mode of H_2O

[a]Infrared intensities in kcal/mol are given in parentheses.
[b]Experimental feature not observed.

Table 4.9a: Computed unscaled and scaled vibrational wavenumbers (cm^{-1}), scaling factors and mode assignments calculated at the MP2/aug-cc-pVDZ level of theory and comparison with the experimental wavenumbers (cm^{-1}) for the CH_3CN-H_2O complexes A and B in Ar and N_2 matrixes.

Computed/ unscaled (υ)	Ar			N_2			Mode assignment
	Computed/ scaled (υ)	Scaling factor	Exp (υ)	Computed/ scaled (υ)	Scaling factor	Exp (υ)	
CH_3CN							
930.5(1)[a]	916.6	0.9851	916.6	917.6	0.9855	917.6	υ_4 sym. CC str. (A_1)
1048.2(1)	1038.2	0.9904	1038.2	1043.3	0.9953	1040.7 1045.8	υ_7 CH_3 rock (E)
1390.7(1)	1375.9	0.9893	1375.9	1378.5	0.9912	1378.5	υ_3 sym.CH_3def (A_1)
1466.5(10)	1445.5	0.9857	1445.5	1447.9	0.9873	1446.7 1449.1	υ_6 antisym.CH_3 def. (E)
2180.2(0)	2258.0	1.0350	2258.0	2257.5	1.0354	2257.5	υ_2 CN str. (A_1)
3088.7(4)	2950.6	0.9552	2950.5	2949.0	0.9548	2949.0	υ_1 sym. CH str. (A_1)
3188.9(1)	3004.4	0.9422	3004.5	3009.3	0.9437	3009.3	υ_5 antisym. CH str. (E)
H_2O							
3803.4(4)	3638	0.9565	3638.0	3634.6	0.9556	3634.6	υ_1 mode of H_2O
1622.2(67)	1589.7	0.9799	1589.7	1597.4	0.9847	1597.4	υ_2 mode of H_2O
3937.7(67)	3733.0	0.9590	3776.4 3756.2 3711.2	3727.2	0.9465	3727.2	υ_3 mode of H_2O
Complex A							
2197.5(15)	2274.4	1.035	2264.7 2267.6	2275.3	1.0354	2272.5	υ_2 C-N stretch
3729.6(310)	3567.4	0.9565	3538.6	3564.0	0.9556	3564.7 3567.1	υ_1 mode of H_2O
1646.9 (46)	1613.8	0.9799	-[b]	1621.7	0.9847	1630.2 1632.6	υ_2 mode of H_2O
3905.8(144)	3745.7	0.9590	3718.9	3696.8	0.9465	3705.5	υ_3 mode of H_2O
Complex B							
2178.9 (4)	2255.2	1.0350	-[b]	2256.0	1.0354	-[b]	υ_2 C-N stretch
1627.9(94)	1557.0	0.9565	-[b]	1555.6	0.9556	-[b]	υ_1 mode of H_2O
3773.1(27)	3697.3	0.9799	-[b]	3715.4	0.9847	-[b]	υ_2 mode of H_2O
3917.2(99)	3756.6	0.9590	-[b]	3707.6	0.9465	-[b]	υ_3 mode of H_2O

[a]Infrared intensities in kcal/mol are given in parentheses.
[b]Experimental feature not observed.

Table 4.10: Shift in the computed (unscaled) and experimental vibrational wavenumbers for the CH_3CN-H_2O complex A computed at B3LYP/6-311++G(d,p) level of theory.

Mode	$\Delta\upsilon^a_{cal}$(cm^{-1})	$\Delta\upsilon^a_{exp}$ (cm^{-1})	
		N_2	Ar
υ_2 CN stretching	+11.5	+15.0	+8.3
υ_1 mode of H_2O	-74.9	-68.7	-99.4
υ_2 mode of H_2O	+28.9	+34.0	-[b]
υ_3 mode of H_2O	-25.5	-21.7	-14.1

[a]$(\Delta\upsilon)_{expt/calc} = (\upsilon_{complex}-\upsilon_{monomer})$.

Table 4.11: Influence of dielectric constant on the raw energies of the CH_3CN-H_2O complexes A and B calculated at B3LYP/6-311++G(d,p) level of theory, using the Onsager solvation model.

Complexes	Dipole moment[a]	Stabilization energy (ΔE) (kcal/mol)		
		Gas (0.00)[b]	Nitrogen (2.00)[b]	Argon (1.43)[b]
A	6.20	-4.82	-5.63	-5.24
B	2.26	-3.91	-2.16	-2.95

[a]Dipole moment in Debye.
[b]Dielectric constant of the medium.

4.3.4 Onsager solvation model

In order to understand the effects of the N_2 and Ar matrixes on to the structure and energetics of the CH_3CN-H_2O complexes A and B, the structures of the two complexes were optimized within the Onsager reaction field model. The value of the dielectric constant ε was set equal to 2.00 and 1.43, which were appropriate for the N_2 and Ar matrixes, respectively [220-222]. We performed SCRF single point energy calculation at the B3LYP/6-311++G(d,p) level of theory for the CH_3CN-H_2O complexes A and B. Table 4.8 gives the relative raw energies of the complexes A and B in the N_2 and Ar matrixes computed at B3LYP/6-311++G(d,p) level of theory. As can be seen from the table that the complex A is stabilized by -0.81 (N_2) and -0.42 (Ar) kcal/mol, whereas the complex B is destabilized by 1.75 (N_2) and 1.00 (Ar) kcal/mol. It should be mentioned that the dipole moments of the complexes A and B were found to be 6.20 D and 2.26 D at B3LYP/6-311++G(d,p) level of theory, respectively. To summarize, the Onsager model indicates that the complex A is stabilized more than the complex B, due to the higher dipole moment of the former, when the solvent effects of the N_2 and Ar matrixes were taken into account, which lends support to our assignments of the observed vibrational features in the two matrixes *only* to complex A.

4.3.5 Nature of the interaction: AIM analysis

A (3,-1) bond critical point (BCP) was searched using the optimized geometry of the CH_3CN-H_2O complexes A and B computed at B3LYP/6-311++G(d,p) level of theory. At the BCP for both complexes A and B, electron density $\rho(r_C)$, Laplacian of electron density $\nabla^2\rho(r_C)$ were examined. Table 4.12 gives the properties of the (3,-1) BCP for the complexes A and B. At the BCP for both complexes A and B the values of $\rho(r_c)$ were positive as are typical of closed shell interaction. Further, two (3,-1) BCP's were located for the complex B, one between the hydrogen of CH_3CN and oxygen of H_2O and another between hydrogen of

Table 4.12: Properties of (3,-1) bond critical points in the CH_3CN-H_2O complexes A and B computed at the B3LYP/6-311++G(d,p) level of theory.

(a) Intermolecular bond critical points in CH_3CN-H_2O complexes

Molecule		$\rho(r_C)$	$\nabla^2\rho(r_C)$	λ_1	λ_2	λ_3
Complex A	C≡N(AN)···H-O(H_2O)	0.0187	0.0689	-0.0230	-0.0223	0.1142
Complex B	C-H(AN)···O-H(H_2O)	0.0059	0.0217	-0.0047	-0.0038	0.0302
	O-H(H_2O)···C≡N(AN)	0.0094	0.0339	-0.0079	-0.0043	0.0462

(b) Bond critical point corresponding to the C≡N Bond in CH_3CN, and CH_3CN-H_2O complexes

Molecule	$\rho(r_C)$	$\nabla^2\rho(r_C)$	λ_1	λ_2	λ_3
CH_3CN	0.4802	-0.2628	-1.0285	-1.0285	1.7940
Complex A	0.4799	-0.2517	-1.0356	-1.0340	1.8179
Complex B	0.4802	-0.2980	-1.0403	-1.03295	1.7753

(c) Bond critical point corresponding to the O-H in H_2O and CH_3CN-H_2O complexes

Molecule	$\rho(r_C)$	$\nabla^2\rho(r_C)$	λ_1	λ_2	λ_3
H_2O	0.3664	-2.4926	-1.7763	-1.7321	1.0158
Complex A	0.3572	-2.4938	-1.7806	-1.7405	1.0272
Complex B	0.3617	-2.5038	-1.7836	-1.7415	1.0214

Table 4.13: Electron occupancies of various natural bonding orbitals (NBOs) of CH_3CN-H_2O complexes A and B computed at B3LYP/6-311++G(d,p) level of theory. The donor-acceptor delocalization interaction and delocalization energies (E_2, kcal/mol) are also shown.

Complex	NBO	Occupancy	Donor-acceptor delocalization interaction	Second order Perturbation (E_2) energy (kcal/mol)
A	n^1N6	1.96302 (1.96983)[a]	n^1N6 → σ*(H7-O8)	4.37
	σ*(H7-O8)	0.00971 (0.00002)[b]		
	σ*(C5-N6)	0.01182(0.01089)	σ(H7- O8) → σ*(C5-N6) n^1O8 → σ*(C5-N6)	0.17 0.11
B	π(2)(C5-N6) σ*(O7-H9) σ*(O7-H8)	1.98691(1.98712) (0.00217)(0.00002) (0.00043)(0.00002)	π(2)(C5-N6) →σ*(O7-H9) π(2)(C5-N6) →σ*(O7-H8)	0.52 0.09
	n^2 O7	1.99612(1.99689)	n^2 O7 → σ*(1)(C1-H2)	0.27
			n^2 O7 → σ*(2)(C1-H2)	0.27
			σ(O7- H9) → π*(2)(C5-N6)	0.05

[a]Occupancy of monomeric CH_3CN is given in parentheses.
[b]Occupancy of monomeric C_2H_2 is given in parentheses.

H_2O and nitrogen of CH_3CN, confirming the cyclic nature of the complex. The comparison of the BCPs revealed that the magnitude of electron density $\rho(r_c)$ and Laplacian of electron density ($\nabla^2\rho(r_c)$) as a result of C-H⋯N interaction is higher in complex A than complex B.

BCPs corresponding to the C≡N bonds of CH_3CN and O-H bond of H_2O in the complexes were evaluated to understand the effect of intramolecular interaction on the neighboring bonds in the submolecules. Table 4.12 (b-c) gives the properties for these BCPs. In the same table the values for the monomeric CH_3CN and H_2O are given for comparison. The high positive values of electron density and high negative values of Laplacian, clearly indicates a shared nature of interactions in the neighbouring bonds of the submolecules of the CH_3CN-H_2O complexes.

4.3.6 NBO Analysis

The charge-transfer effect successfully explains the red-shifted hydrogen bonding as a result of delocalization of the nitrogen lone pair. The results of NBO analysis of CH_3CN-H_2O complexes A and B computed at B3LYP/6-311++G(d,p) level of theory are shown in table 4.13 from the table it is clear that due to the hyperconjugative interaction between $n^1N6 \rightarrow \sigma^*(H7\text{-}O8)$ for the complex A, the electron occupancy of antibonding orbital $\sigma^*(H7\text{-}O8)$ of the H_2O submolecule increased by ~0.00969e relative to the H_2O monomer. Similarly, a reduction in electron occupancies by ~0.00679e was noticed for n^1N6 non-bonding orbital for the CH_3CN submolecule in the complex A with respect to the CH_3CN monomer. The second order perturbation energy (E_2) for this interaction is found to be ~4.37 kcal/mol. As can be seen from the Table 4.13 in complex A apart from charge transfer interaction there is *bond pair-acceptor orbital interaction* [$\sigma(H7\text{-}O8) \rightarrow \sigma^*(C5\text{-}N6)$ and $n^1O8 \rightarrow \sigma^*(C5\text{-}N6)$] due to which, the electron occupancy in the antibonding $\sigma^*(C5\text{-}N6)$ increases marginally by 0.0009e, and the corresponding E_2 energy of this interaction was found to be ~ 0.17 and ~0.11 kcal/mol, respectively.

Interestingly, for the complex B, the stabilization does not stem from the

delocalization of nitrogen lone pair to antibonding O7-H9 acceptor orbital as the nitrogen lone pair does not have the linear orientation (~180°) for the facile delocalization. This orientational effect likely precludes the interaction originating from lone pair on nitrogen. Nevertheless, complex B is stabilized due to the delocalization of C≡N π-electrons to the acceptor orbital of H_2O moiety as it is evident from the marginal decrease in the occupancy of π (2) (C5-N6) orbital by 0.00021e with the concomitant increase in the acceptor, σ*(O7-H9) orbital by 0.00215e. The corresponding E_2 energy for this interaction was found to be ~ 0.52 kcal/mol. Being cyclic, complex B also gets extra stabilization due to the n^2O7→σ*(C1-H2) delocalization and the E_2 energy for such delocalization was ~ 0.27 kcal/mol.

4.4 Interaction of benzonitrile (C_6H_5CN) with acetylene (C_2H_2)

Benzonitrile has three electron rich sites, nitrogen, C≡N triple bond and π-cloud of the benzene ring, which can form either a σ or π type hydrogen bond or both. C_2H_2 acts as a proton donor as the hydrogen attached to the 'sp' carbon atom is acidic. Alternatively, C_2H_2 can also play the role of a proton acceptor through its π-cloud. It is interesting to study the interaction between the C_2H_2 and C_6H_5CN to see whether any or all complexes could be trapped and studied in the experiment performed at low temperatures.

4.4.1 Experimental details

C_2H_2 (Commercial Grade, Asiatic Oxygen Limited, India) and benzonitrile, C_6H_5CN (Merck, HPLC grade 99.8%) were used as such, without further purification. However, the samples were subjected to several freeze-pump-thaw cycles before its use. Ultra high pure N_2 (INOX, 99.995%) and Ar (INOX, 99.9995%) was used as matrix gases, in which C_2H_2 gas was premixed to obtain the desired matrix-to-sample ratio. The C_2H_2/matrix gas mixture and C_6H_5CN were then deposited using double jet nozzle onto a KBr substrate. We used typical matrix-to-sample ratios ranging from 1000:0.1 to 1000:0.25 for C_2H_2 and 1000:0.2 to 1000:0.8 for C_6H_5CN. Infrared spectra of matrix isolated samples were recorded using Bruker Vertex 70 FTIR spectrometer.

Figure 4.14 (block A and B) shows the matrix isolated infrared spectra of C-H asymmetric υ_3 stretching mode of C_2H_2 in N_2 and Ar matrixes. The spectra shown in the figure corresponds to the 30 K (N_2) and 35 K (Ar) annealed spectra. The υ_3 mode of C_2H_2 is observed at 3282.8 and 3288.8 cm^{-1} in N_2 (fig. 4.14a block A) and Ar matrix (fig. 4.14a block B), respectively [148]. The features due to C_2H_2 dimer were observed at 3279.5 and 3257.4 cm^{-1} in N_2 and at 3285.6, 3270.2 and 3263.2 cm^{-1} in Ar matrix. A strong absorption peak at 3240.0 cm^{-1} is due to C_2H_2-H_2O complex in Ar matrix [223]. When C_2H_2 and

C_6H_5CN were co-deposited and annealed, a new feature was observed at 3238.8 (fig. 4.13b-c, block A) and 3238.6 cm^{-1} (fig. 4.13b-c, block B) in N_2 and Ar matrixes, respectively.

Figure 4.15 block A and B (2260-2230 cm^{-1}) shows the infrared spectra of υ_2 symmetric CN stretching mode of C_6H_5CN isolated in N_2 and Ar matrixes. The features observed as a site split features at 2242.6, 2238.1, 2235.9 cm^{-1} (fig. 4.15a block A) in N_2 and at 2245.3, 2241.7 and 2237.6 cm^{-1} in Ar matrix (fig. 4.15a block B) are due to υ_2 symmetric CN stretching mode of C_6H_5CN, which agrees well with the reported value [124]. The feature observed at 2251.3 and 2247.9 cm^{-1} in N_2 and Ar matrixes is be due to C_6H_5CN-H_2O complex. When the precursors were co-deposited and annealed new product absorption peaks appeared in the CN stretching region of C_6H_5CN at 2245.8 and 2246.0 cm^{-1}in N_2 and Ar matrixes.

The new features were observed only when both C_2H_2 and C_6H_5CN were co-deposited and gained in intensity as the concentration of either of the precursors was increased indicating that the feature is only due to C_2H_2 and C_6H_5CN complex.

4.4.2 Computational

DFT computations on the 1:1 C_2H_2-C_6H_5CN complex at the B3LYP level of theory using 6-311++G(d,p) and aug-cc-pVDZ basis sets yielded two minima, the global minimum being the C-H⋯N interaction and the local minimum was the C-H⋯π interaction, where C_2H_2 is the proton donor in both the complexes. Figure 4.15 shows the structure of the complexes A and B computed at B3LYP/6-311++G(d,p) level of theory. For the linear complex A, the bond distance between the hydrogen, H1 of C_2H_2 and N13 of C_6H_5CN is 2.345 Å whereas for the C-H⋯π complex B the bond distances between the H1 of C_2H_2 and C11 is 3.118 Å. Table 4.14 gives the selected bond distances, bond angles and dihedral angles for the complexes A and B. Table 4.15 shows the stabilization energies for the 1:1 C_2H_2-C_6H_5CN complexes A and B with and without ZPE and also with BSSE correction

computed at the B3LYP levels using 6-311++G(d,p) and aug-cc-pVDZ basis sets. As can be seen from the table that at different basis sets, complex A is indicated to be more exothermic than complex B.

4.4.3 Vibrational wavenumber

Table 4.16 compares the experimental vibrational wavenumbers of the 1:1 C_2H_2-C_6H_5CN complexes A and B computed at B3LYP/6-311++G(d,p) level of theory

4.4.3.1 υ_3 mode of C_2H_2

DFT computations using 6-311++G(d,p) basis sets indicated that for the complex A (stabilized by C-H⋯N interaction), the computed wavenumber in the υ_3 mode of C_2H_2 submolecule occur at 3373.1 cm^{-1}, a red shift of 44.9 cm^{-1}. Experimentally, a new feature was observed at 3238.8 cm^{-1}, a red shift of 43.8 cm^{-1} from the uncomplexed C_2H_2. The agreement between the experimental and computed vibrational shift clearly supports the formation of the complex with C-H⋯N interaction. The computed wavenumber for the complex B (stabilized by C-H⋯π interaction) occur at 3414.7 cm^{-1}, a small red shift of 3.3 cm^{-1}. Experimentally, we could not discern any new feature for this complex. The shift in the υ_3 mode of C_2H_2 submolecule is a good indicator of the strength of the interaction. In adducts where C_2H_2 is a proton donor, the shift in the υ_3 mode of C_2H_2 submolecule are usually large. For example, the υ_3 mode of C_2H_2 in C_2H_2-C_6H_5OH complex B [146] is shifted by 45.4 cm^{-1}, where C_2H_2 is the proton donor. In adducts where C_2H_2 is the proton acceptor the shift in the υ_3 mode of C_2H_2 submolecule are comparatively smaller.

In C_2H_2-C_6H_5OH complex A, the shift in the υ_3 mode of C_2H_2 submolecule is 8.8 cm^{-1}. The shift in the υ_3 mode of C_2H_2 submolecule also depends on the strength of interaction in the complex. In C_2H_2-CH_3OH [148] and C_2H_2-C_6H_5OH [146], the ZPE corrected stabilization energy for the C-H⋯O υ_3 mode of C_2H_2 submolecule also depends on the strength of interaction in the complex.

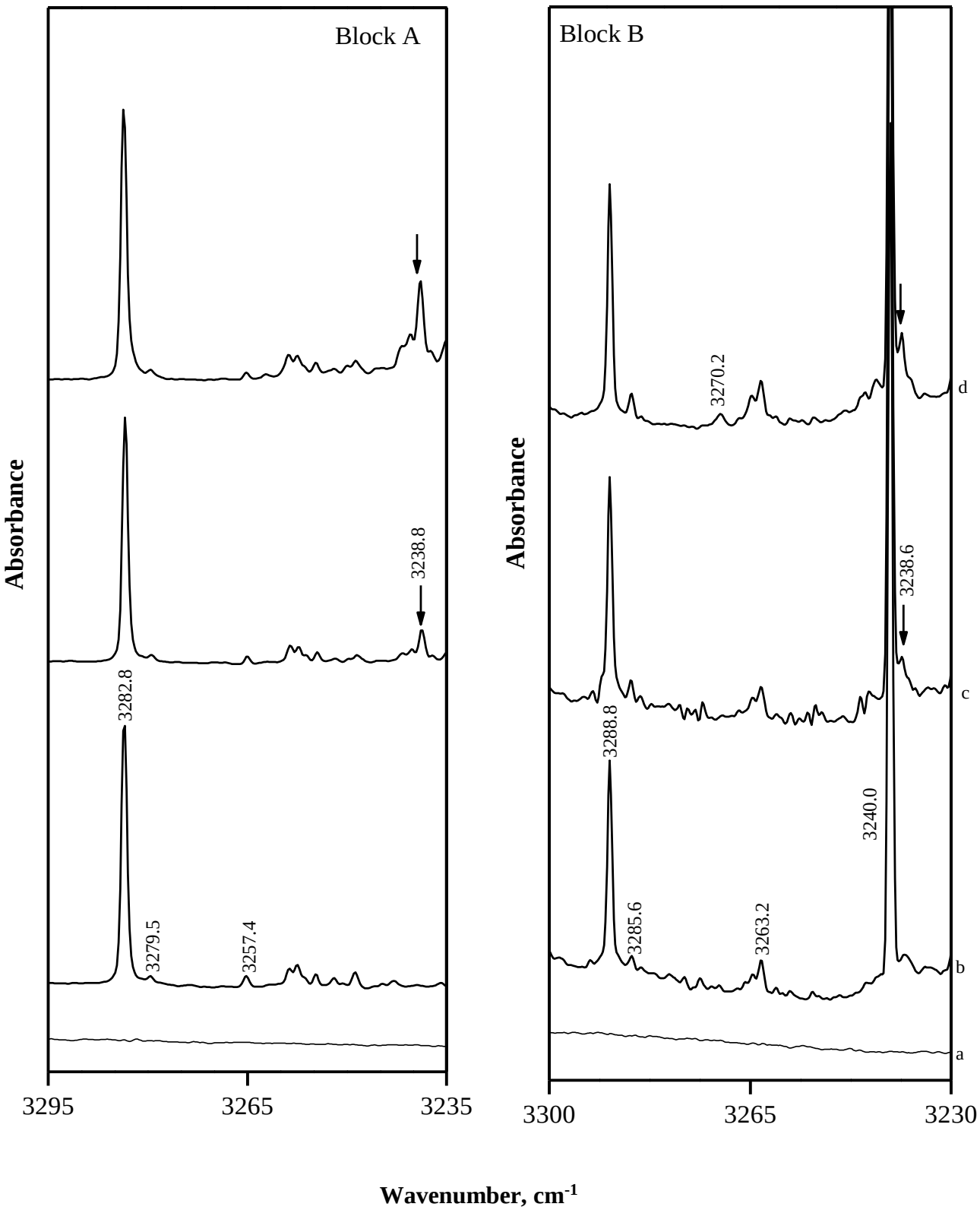

Figure 4.14: Spectra of C_2H_2/C_6H_5CN complex in N_2 (block A, 3295-3235 cm^{-1}) and Ar (block B, 3300-3230 cm^{-1}). Matrix isolation spectra for various concentrations of $C_2H_2/C_6H_5CN/N_2$ (a) 0/0.8/1000; (b) 0.1/0.0/1000; (c) 0.1/0.25/1000; (d) 0.1/0.8/1000 and $C_2H_2/C_6H_5CN/Ar$ (a) 0/0.4/1000; (b) 0.1/0.0/1000; (c) 0.1/0.2/1000;(d) 0.1/0.4/1000. Spectra shown here were recorded after annealing the matrix at 30 K (N_2) and 35 K (Ar).

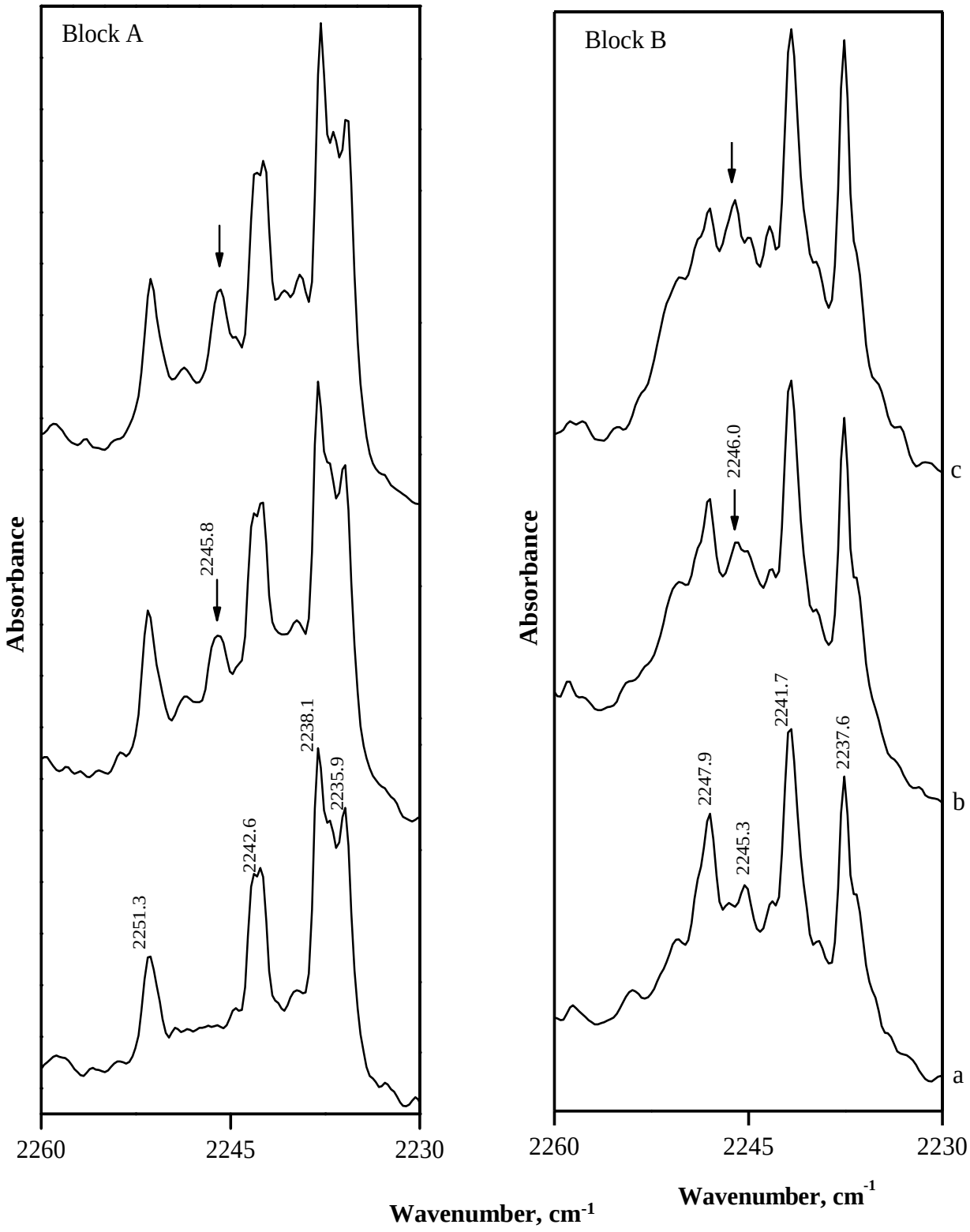

Figure 4.15: Spectra of C_2H_2/ C_6H_5CN complex in N_2 (block A) and Ar (block B) matrixes covering the region 2260-2230 cm^{-1}. Matrix isolation spectra for various concentrations of $C_2H_2/C_6H_5CN/N_2$ (a) 0/0.4/1000; (b) 0.1/0.4/1000; (c) 0.2/0.4/1000 and C_2H_2/C_6H_5CN/Ar (a) 0/0.4/1000; (b) 0.25/0.4/1000; (c) 0.5/0.4/1000. Spectra shown here were recorded after annealing the matrix at 30 K (N_2) and 35 K (Ar).

Table 4.14: Selected structural parameters[a] for the C_2H_2-C_6H_5CN complexes A and B computed at B3LYP/6-311++G(d,p) level of theory.

Parameter	Complex A	Parameter	Complex B
H1-N13	2.345	H1-C11	3.118
C1-H2	1.069 (1.063)[b]	H1-C14	3.341
C2-C3	1.200	H1-C7	3.349
C9-N13	1.155	H1-C10	3.755
C6-C9	1.431	H1-C5	3.762
C5-H8	1.083	H1-C6	3.948
C5-C6	1.402	C2-H1	1.064 (1.063)
∠N13-H1-C2	179.9	C2-C3	1.199 (1.199)
∠C10-C6-C9	119.9	C9-N13	1.156 (1.155)
∠C10-C6-C5	120.2	∠C2-H1-C11	149.1
∠C3-C2-H1-N13	0.0	∠C7-C11-C14	120.1
∠C10-C6-C9-N13	157.1	∠C3-C2-H1-C11	-56.6
Dipole moment[c]	5.7	Dipole moment[c]	4.5

Table 4.14a: Selected structural parameters[a] for the C_2H_2-C_6H_5CN complexes A and B computed at MP2/aug-cc-pVDZ level of theory.

Parameter	Complex A	Parameter	Complex B
H1-N13	2.258	H1-C11	2.642
C1-H2	1.080 (1.075)[b]	H1-C14	2.665
C2-C3	1.233	H1-C7	2.671
C9-N13	1.188	H1-C10	2.719
C6-C9	1.443	H1-C5	2.725
C5-H8	1.093	H1-C6	2.739
C5-C6	1.413	C2-H1	1.076 (1.075)
∠N13-H1-C2	179.9	C2-C3	1.232 (1.232)
∠C10-C6-C9	119.6	C9-N13	1.189 (1.185)
∠C10-C6-C5	120.7	∠C2-H1-C11	164.8
∠C3-C2-H1-N13	-178.1	∠C7-C11-C14	120.0
∠C10-C6-C9-N13	-5.9	∠C3-C2-H1-C11	-173.4
Dipole moment[c]	5.7	Dipole moment[c]	4.5

[a]Bond lengths in Å, bond angles and dihedral angles in °.
[b]Parameters of the monomers are given in brackets.
[c]Dipole moment in Debye.

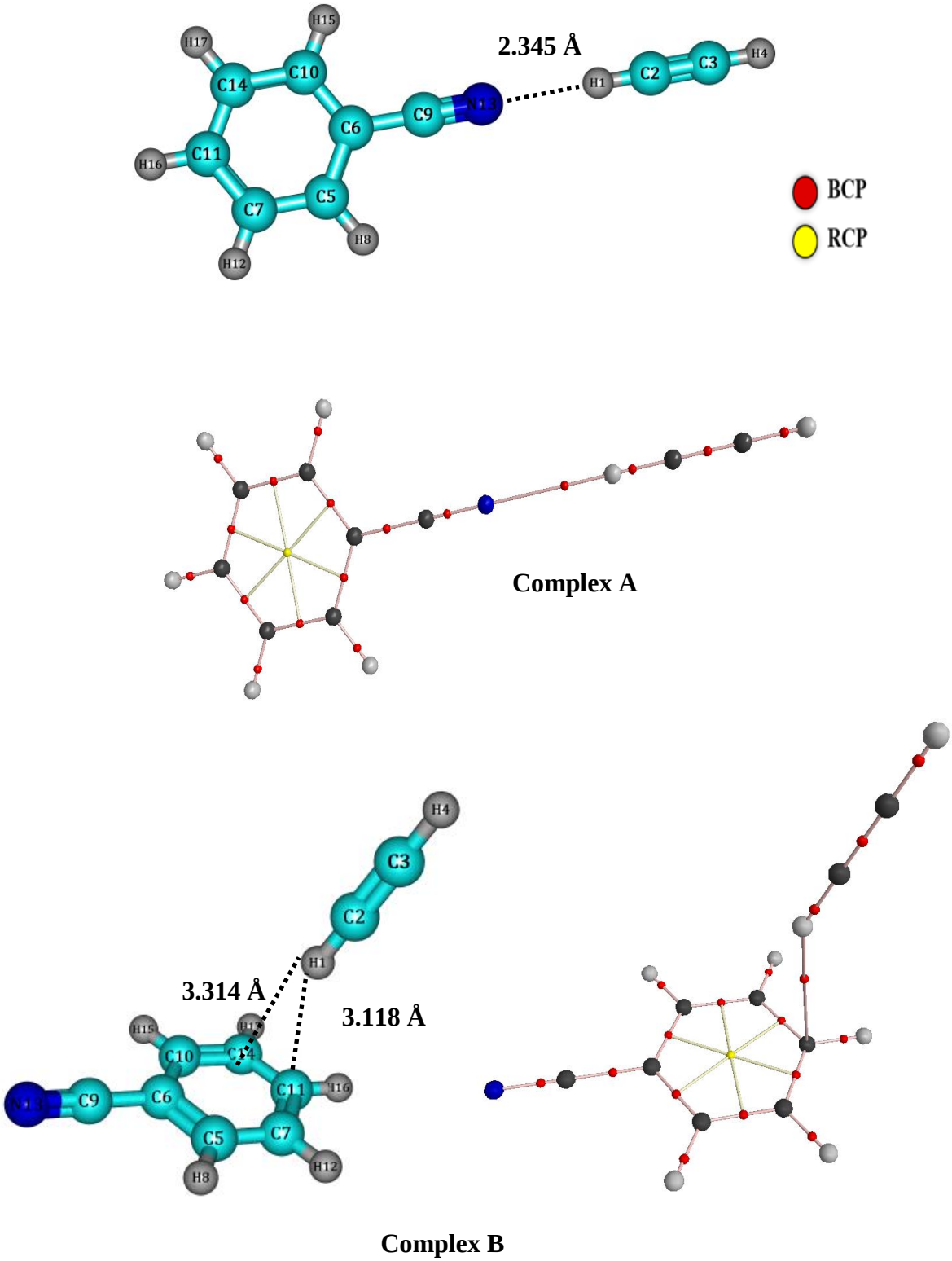

Figure 4.16: Structure of the 1:1 C_2H_2-C_6H_5CN complexes A and B computed at B3LYP/6-311++G(d,p) level of theory. Bond critical point (BCP) and ring critical point (RCP) is also shown in the figure.

Table 4.15: Raw[a]/ZPE-corrected/BSSE-corrected stabilization energies for the C_2H_2-C_6H_5CN complexes A and B computed at the B3LYP and B3LYP+D3 level of theory using the 6-311++G(d,p) and aug-cc-pVDZ basis set.

Level of theory	Stabilization energy (ΔE)	
	Complex A	Complex B
B3LYP/6-311++G(d,p)	-2.7/-2.0/-2.5	-0.4/-0.2/-0.1
B3LYP+D3/6-311++G(d,p)	-3.3/-2.6/-2.5	-2.4/-2.0/0.6
B3LYP/aug-cc-pVDZ	-3.2/-2.3/-2.5	-0.5/-0.3/-0.2
B3LYP+D3/aug-cc-pVDZ	-3.8/-2.9/-2.5	-2.8/-2.2/0.7

All energies are in kcal/mol (see text for details).
[a]Raw stabilization energies refer to energies not corrected for either ZPE or BSSE.

Table 4.16: Comparison of experimental with computed unscaled vibrational wavenumbers for the C_2H_2-C_6H_5CN complexes A and B in N_2 and Ar matrixes. Computations were performed at B3LYP /6-311++G(d,p) level of theory.

Computed		Experimental				Mode assignment
		Ar		N_2		
υ (cm^{-1})	Δυ (cm^{-1})	υ (cm^{-1})	Δυ (cm^{-1})	υ (cm^{-1})	Δυ (cm^{-1})	
Benzonitrile						
2332.9 (37)	-	2241.7	-	2242.6 2238.1 2235.9	-	υ_2 sym. CN str. mode of C_6H_5CN (A_1)
Acetylene						
3418.0 (94)	-	3288.8		3282.8	-	υ_3 C-H assym. str. mode of C_2H_2
773.8 (112)	-	736.8		742.0 747.4	-	υ_5 C-H bending mode of C_2H_2
Complex A						
2336.7 (64)	3.8	2246.0	4.3	2245.8	6.9	υ_2 sym. CN str. mode of C_6H_5CN in complex
3373.1 (386)	-44.9	3238.6	-50.2	3238.8	-44.0	υ_3 asym. C-H str. mode of C_2H_2 in complex A
834.7 (85)	60.9	-[b]	-	-[b]	-	υ_5 C-H bending mode of C_2H_2 in complex A
836.1 (89)	62.3					
Complex B						
2333.7 (35)	0.8	-[b]	-	-[b]	-	υ_2 sym. CN str. mode of C_6H_5CN in complex
3414.7 (145)	-3.3	-[b]	-	-[b]	-	υ_3 asym. C-H str. mode of C_2H_2 in complex A
775.2 (98)	1.4	-[b]	-	-[b]	-	υ_5 C-H bending mode of C_2H_2 in complex A
780.2 (37)	6.4					

[a]Computed infrared intensities (km/mol) are given in parentheses.
[b]Experimental features were not observed.

Table 4.16a: Comparison of experimental with computed unscaled vibrational wavenumbers for the C_2H_2-C_6H_5CN complexes A and B in N_2 and Ar matrixes. Computations were performed at MP2/aug-cc-pVDZ level of theory.

Computed		Experimental				Mode assignment
		Ar		N_2		
υ (cm^{-1})	Δυ (cm^{-1})	υ (cm^{-1})	Δυ (cm^{-1})	υ (cm^{-1})	Δυ (cm^{-1})	
Benzonitrile						
2151.6 (.2)	-	2241.7	-	2242.6 / 2238.1/ 2235.9	-	υ_2 sym. CN str. mode of C_6H_5CN (A_1)
Acetylene						
3431.8 (93)	-	3288.8		3282.8	-	υ_3 C-H assym. str. mode of C_2H_2
702.9 (95)	-	736.8		742.0 / 747.4	-	υ_5 C-H bending mode of C_2H_2
Complex A						
2162.0 (2)	10.4	2246.0	4.3	2245.8	6.9	υ_2 sym. CN str. mode of C_6H_5CN in complex A
3385.2 (415)	-46.6	3238.6	-50.2	3238.8	-44.0	υ_3 asym. C-H str. mode of C_2H_2 in complex A
797.4 (73)	94.5	-[b]	-	-[b]		υ_5 C-H bending mode of C_2H_2 in complex A
798.4 (77)	95.5					
Complex B						
2149.3 (0)	2.3	-[b]	-	-[b]	-	υ_2 sym. CN str. mode of C_6H_5CN in complex A
3427.2 (183)	-4.6	-[b]	-	-[b]	-	υ_3 asym. C-H str. mode of C_2H_2 in complex A
719.5 (57)	16.6	-[b]	-	-[b]	-	υ_5 C-H bending mode of C_2H_2 in complex A
731.8(54)	28.9					

[a]Computed infrared intensities (km/mol) are given in parentheses.

[b]Experimental features were not observed.

In these complexes, the ZPE corrected stabilization energy for the C-H⋯O complex is -2.46 and -1.53 kcal/mol, respectively, where C_2H_2 acts as a proton donor in these complexes. The experimental shift in the υ_3 mode of C_2H_2 submolecule for the C_2H_2-CH_3OH and C_2H_2-C_6H_5OH C-H⋯O complex was found to be 70.2 cm^{-1} and 46.3 cm^{-1}, respectively. In this study, the ZPE corrected stabilization energy for the complex A and complex B is -2.7 and -0.2 kcal/mol respectively and the experimental shift in the υ_3 mode of C_2H_2 submolecule for the complex A is 43.8 cm^{-1}.

4.4.3.2 υ_2 mode of C_6H_5CN

The υ_2 mode of C_6H_5CN submolecule was observed as a site split features at 2242.6, 2238.1 and 2235.9 cm^{-1} in N_2 matrix, which agrees well with the reported literature value. On complex formation, a new feature was observed at 2245.8 cm^{-1}, which amounts to a blue shift of 6.9 cm^{-1} from that of uncomplexed C_6H_5CN. The computed blue shift for the complex A was found to be 3.8 cm^{-1}. The experimental vibrational wavenumber shift is in reasonable agreement with the computed shift for the complex A. For the complex B, the computed shift is 0.8 cm^{-1} from the uncomplexed C_6H_5CN. Experimentally no new feature could be clearly discerned for the complex B.

Experimentally, no new features could be observed in the other modes of C_2H_2 and C_6H_5CN submolecule for the complex A.

4.4.4 Nature of the interaction: AIM analysis

Table 4.17 gives the properties of the intermolecular BCP for the complexes A and B. One BCP was located for complex A, between the hydrogen of C_2H_2 and nitrogen of C_6H_5CN, confirming unambiguously the C-H⋯N interaction in C_2H_2-C_6H_5CN complex A. As can be seen from the table for both the complexes A and B, the values of $\rho(r_c)$ were found to be of the order of 10^{-2} a.u., ($\nabla^2\rho(r_c)$) was positive, and $|\lambda_1|/\lambda_3 < 1$, as are typical of closed shell interaction. Likewise, the comparison of the BCP in the complexes A and B

Table 4.17: Properties of (3,-1) bond intermolecular bond critical points in C_2H_2-C_6H_5CN complexes A and B computed at B3LYP/6-311++G(d,p) level of theory.

Complexes	$\rho(r_C)$	$\nabla^2\rho(r_C)$	λ_1	λ_2	λ_3	$\lvert\lambda_1\rvert / \lambda_3$
A	0.0110	0.0388	-0.0111	-0.0110	0.0609	0.1818
B	0.0031	0.0086	-0.0020	-0.0013	0.0119	0.1709

Table 4.18: Electron occupancies of various natural bonding orbitals (NBOs) of C_2H_2-C_6H_5CN complexes A and B computed at B3LYP/6-311++G(d,p) level of theory. The donor-acceptor delocalization interaction and delocalization energies (E_2, kcal/mol) are also shown.

Complexes	NBO	Occupancy	Donor-acceptor delocalization interaction	Second order Perturbation (E_2) energy (kcal/mol)
A	n^1N13	1.96596 (1.97164)[a]	n^1N13 → σ*(C1-H2)	2.98
	σ*(C1-H2)	0.01285 (0.0060)[b]		
B	σ*(C1-H2) π(2)(C11-C14)	0.00684 (0.0060)[b] 1.64134 (1.65429)[a]	π(2)(C11-C14) →σ*(C1-H2)	0.19

[a]Occupancy of monomeric C_6H_5CN is given in parentheses.
[b]Occupancy of monomeric C_2H_2 is given in parentheses.

revealed that electron density and the Laplacian of the electron density for the BCP formed as a result of C-H···N interaction (complex A) is higher in magnitude than the C-H···π interaction (complex B), clearly indicating that the former complex is stronger than the latter.

BCPs corresponding to the C-H bonds of C_2H_2 and C-N bonds of C_6H_5CN in the complexes were evaluated to understand the effect of intermolecular interaction on the neighboring bonds in the submolecules. Table 4.17 gives the properties of these BCPs. In the same table the value of the monomeric C_2H_2 and C_6H_5CN are given for comparison. In contrast to the BCPs produced due to the hydrogen bonding interaction, the BCPs of the neighboring bonds exhibit strong interactions. The high positive values of electron density and high negative values of Laplacian clearly confirmed the shared nature of the interactions in the neighboring bonds of the submolecules of complexes and the perturbation in the neighboring bonds is relatively low in comparison to the monomers [224,225].

4.4.5 NBO analysis

The results of NBO analysis of C_2H_2-C_6H_5CN complexes A and B computed at B3LYP/6-311++G(d,p) level of theory are given in table 4.18. From the table, it is clear that electron occupancy of antibonding orbital σ^*(C1-H2) of C_2H_2 submolecule in the complex A is increased relative to the C_2H_2 monomer. Similarly, a reduction in electron occupancies is noticed for the n^1N13 nitrogen lone pair for the C_6H_5CN submolecule in the complex A with respect to monomer. It should be noted from the table that the magnitude of electron occupancy of antibonding orbital σ^*(C1-H2) of C_2H_2 submolecule in complex A is more than the complex B, which is reflected by a larger red shift in the former than the latter complex. The E_2 energies for the delocalization were found to be ~ 2.98 and ~0.19 kcal/mol for the complexes A and B, respectively, which supports the above observation.

4.5 Interaction of benzonitrile (C_6H_5CN) with water (H_2O)

Several theoretical groups have performed calculations on the C_6H_5CN-H_2O system and found that the C_6H_5CN and H_2O form isoenergetic cyclic and linear type complexes. Gas phase experiments coupled with fluorescence and IR-UV double resonance technique revealed the formation of the cyclic complex.

The aim of the present work is to study the interaction between C_6H_5CN and H_2O. Matrix isolation experiments have the capability to trap the linear complex (local minimum) and/or both global and local minima, and it is therefore interesting to study the C_6H_5CN-H_2O system under cold isolated condition.

4.5.1 Experimental details

The sample water (H_2O,Milli-Q integral ultrapure,18.2MΩ.cm) and benzonitrile (C_6H_5CN, Alfa Aesar, 99.0%) were used as such, without further purification. Ar (INOX, 99.9995%) and N_2 (INOX, 99.995%) were used as matrix gases. A triple-jet nozzle was used to co-deposit C_6H_5CN, H_2O and N_2 or Ar by streaming them separately onto the cold KBr substrate. A suitable temperature was maintained for H_2O and C_6H_5CN in the bulb to control its concentration in the matrix and deposited through a nozzle. The matrix-to-solute ratio varied between 0.5:0.5:1000 to 1.5:1:1000 for $C_6H_5CN/H_2O/N_2$ or Ar.

Infrared spectra of the matrix isolated samples were recorded using a Bruker Vertex 70 FTIR spectrometer. All the spectra shown in this report were those recorded after annealing the matrix.

Figure 4.17 block A (3740-3560 cm^{-1}) and block B (3800-3550 cm^{-1}) corresponds to the υ_3 antisymmetric, υ_1 symmetric stretching modes of H_2O in N_2 and Ar matrix. Trace ‘a’ shows the annealed spectra of H_2O alone while traces ‘b’ and ‘c’ show the annealed spectra with varying relative concentrations of H_2O and C_6H_5CN. In N_2 matrix, the υ_3 and υ_1 modes of H_2O were observed at 3727.8 and 3635.2 cm^{-1}, and the corresponding υ_3 mode in Ar

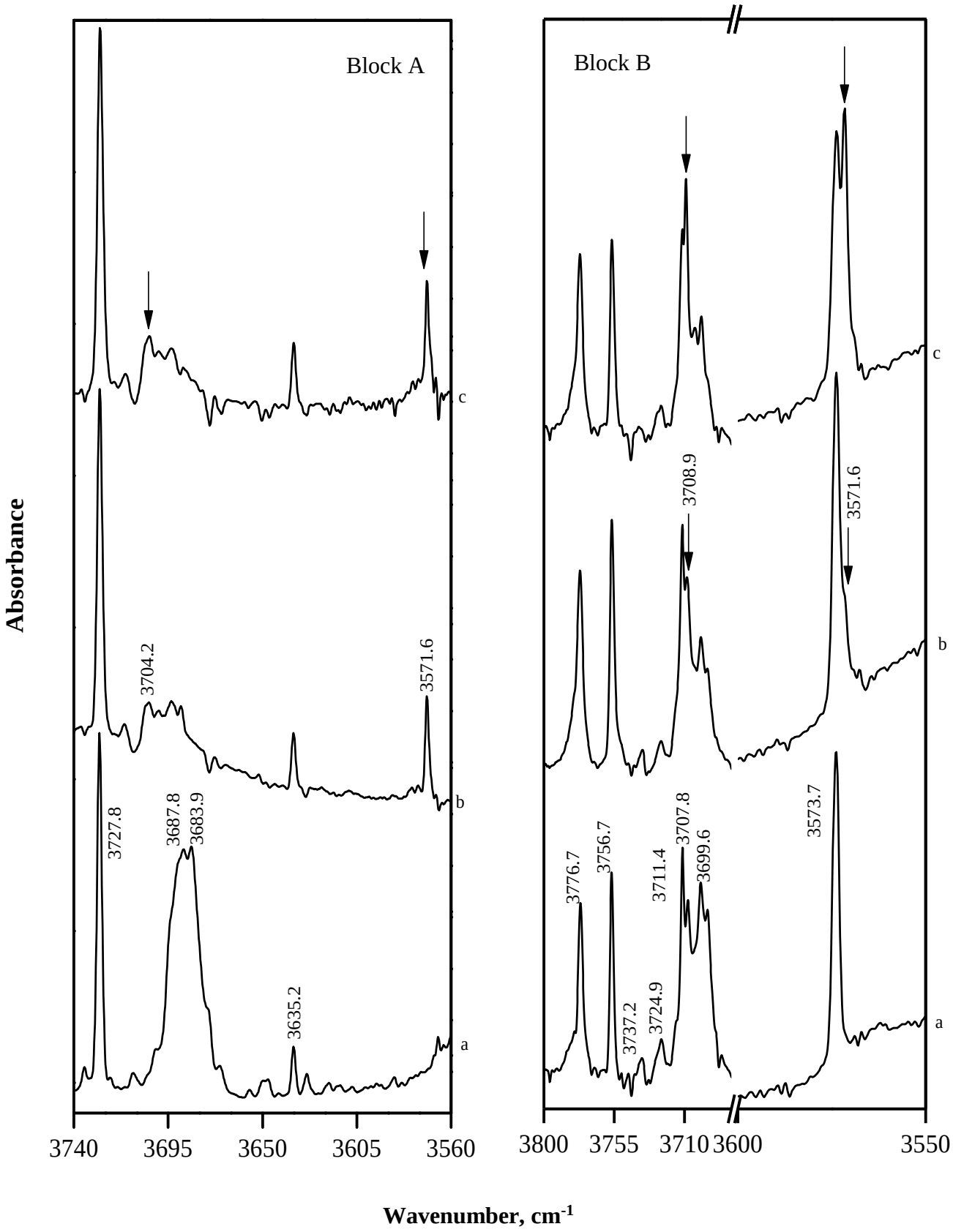

Figure 4.17: Spectra of C_6H_5CN-H_2O complexes: Block A corresponds to the 30 K annealed spectra in N_2 matrix covering the region 3740-3560 and Block B corresponds to the 35 K annealed spectra Ar matrix in the region 3800-3550 cm^{-1}. Matrix isolation infrared spectra of various concentrations of $C_6H_5CN/H_2O/N_2$ (Ar) ; a) 0/0.5/1000; b) 1/0.5/1000; c) 1.5/0.5/1000.

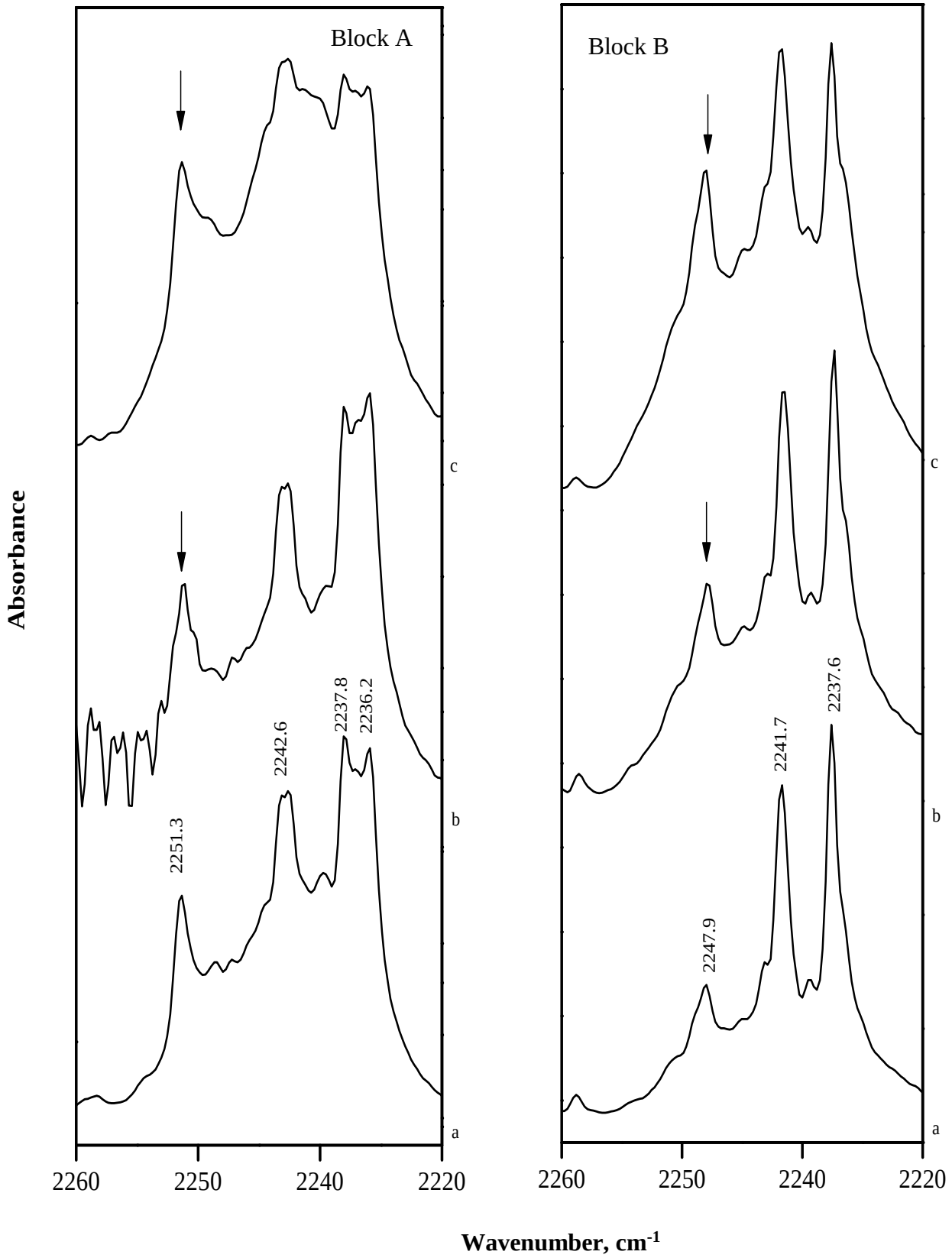

Figure 4.18: Spectra of C_6H_5CN-H_2O complexes: Block A corresponds to the 30 K annealed spectra in N_2 matrix spanning the region 2260-2220 cm^{-1} and Block B corresponds to the 35 K annealed spectra in Ar matrix spanning the region 2260-2220 cm^{-1}. Matrix isolation infrared spectra of various concentrations of $C_6H_5CN/H_2O/N_2$; a) 1.0/0/1000; b) 1.0/0.5/1000; c) 1.0/0.75/1000 and $C_6H_5CN/H_2O/Ar$; a) 1.0/0/1000; b) 1.0/0.5/1000; c) 1.0/0.75/1000.

matrix was observed as three intense features for rotating H_2O monomer at 3776.7($1_{01}\rightarrow 2_{02}$), 3756.7($0_{00}\rightarrow 1_{01}$), and 3711.4 cm^{-1}($1_{01}\rightarrow 0_{00}$), respectively. Broad features observed at 3687.8 and 3683.9 cm^{-1} correspond to the polymeric water in N_2 matrix. In Ar matrix, the feature observed at 3724.9 cm^{-1} is due to proton acceptor band for the of H_2O dimer and the multiplet features observed at 3707.8 and 3669.6 $cm^{-1}$are due to proton donor υ_3 mode of H_2O dimer and multimers. The feature observed at 3573.7 cm^{-1} is due to the proton donor υ_1 mode of H_2O dimer in Ar matrix. All the features observed for monomer and dimer in N_2 and Ar matrixes agree well with the reported literature value [215]. When the concentration of C_6H_5CN is increased in the matrix, new features started appearing at 3704.2, 3571.6 cm^{-1} in N_2 and 3708.5, 3571.6 cm^{-1} in Ar matrixes. All the new features appeared only when both the precursors were deposited and showed concentration dependence, lending credence to their assignments to the C_6H_5CN-H_2O complex.

Figure 4.18, block A and B shows the matrix isolated infrared spectra of υ_2 CN stretching region of C_6H_5CN in N_2 and Ar matrixes. Trace 'a' in the figure shows the C_6H_5CN alone spectra in N_2 and Ar matrixes. The multiple site split features observed at 2242.6, 2237.8 and 2236.2 cm^{-1} and a doublet at 2241.7, 2237.6 cm^{-1} are due to υ_2 CN stretch mode of C_6H_5CN in N_2 and Ar matrixes, respectively [219]. When the concentration of the H_2O was increased (fig. 4.18 traces b and c) the feature observed at 2251.3 cm^{-1} in N_2 and 2247.9 cm^{-1} in Ar matrixes increases in intensity. Since water is an inevitable impurity in the MI experiments, the feature due to C_6H_5CN-H_2O complex was observed even when no H_2O was deliberately added. However, the features assigned to the C_6H_5CN-H_2O complex were found to increase in intensity, when the concentration of either of the two reagents were increased, indicating that the features are due to the complex. The features due to the complex are clearly resolved and shifted from the precursor molecules and are marked with arrows in the figure 4.18. Furthermore, these features were observed even at low

concentrations of C_6H_5CN and H_2O in the matrix, which suggests that these are due to 1:1 complex.

New features could not be observed in the υ_4 symmetric CC stretch, υ_7 CH_3 rocking, υ_3 CH_3 deformation, υ_6 anti-symmetric CH_3 deformation, υ_1 symmetric CH stretching, υ_5 antisymmetric CH stretching modes of C_6H_5CN and υ_2 bending modes of H_2O in both Ar and N_2 matrixes.

4.5.2 Structure and energetics of the C_6H_5CN-H_2O complexes

It can be reiterated that several groups have performed calculations on the C_6H_5CN-H_2O system [154,155,157,159]. DFT computations invariably showed C_6H_5CN and H_2O forms two types of complexes; a linear complex, local minimum, σ-type (complex A) where the nitrogen of C_6H_5CN interacts with the hydrogen of H_2O and a cyclic complex, global minimum, π-type (complex B) where the ortho- hydrogen of C_6H_5CN interacts with oxygen of H_2O and hydrogen of H_2O interacts with the nitrogen of C_6H_5CN. We have carried out the computations at B3LYP and MP2 levels of theory using aug-cc-pVDZ basis sets and found similar structures for the C_6H_5CN-H_2O complexes. Figure 4.19 shows the structures of the C_6H_5CN-H_2O complexes A and B computed at MP2/aug-cc-pVDZ level of theory. Table 4.19 gives the selected structural parameters of the two complexes. For the complex A, the bond distance between the N2 of C_6H_5CN and the H16 of H_2O is 2.066 Å. The bond angle between the N2-H16-O14 is ~177.8° and the dihedral angle between the C1-N2-H16-O4 is ~0.1° making the complex A to be a linear. In complex A, the CN bond gets slightly contracted by 0.002 Å and the O-H bond gets elongated by 0.006 Å. Due to this contraction of the CN bond and elongation of the OH bond, the corresponding vibrational wavenumber is blue- and red-shifted. In complex B, the bond distances between the N2-H16 and H9-O14 are 2.263 Å and 2.378 Å respectively, and the complex is cyclic. Due to this interaction both CN and OH bonds get elongated by 0.001 and 0.003 Å, which induces a red shift of the

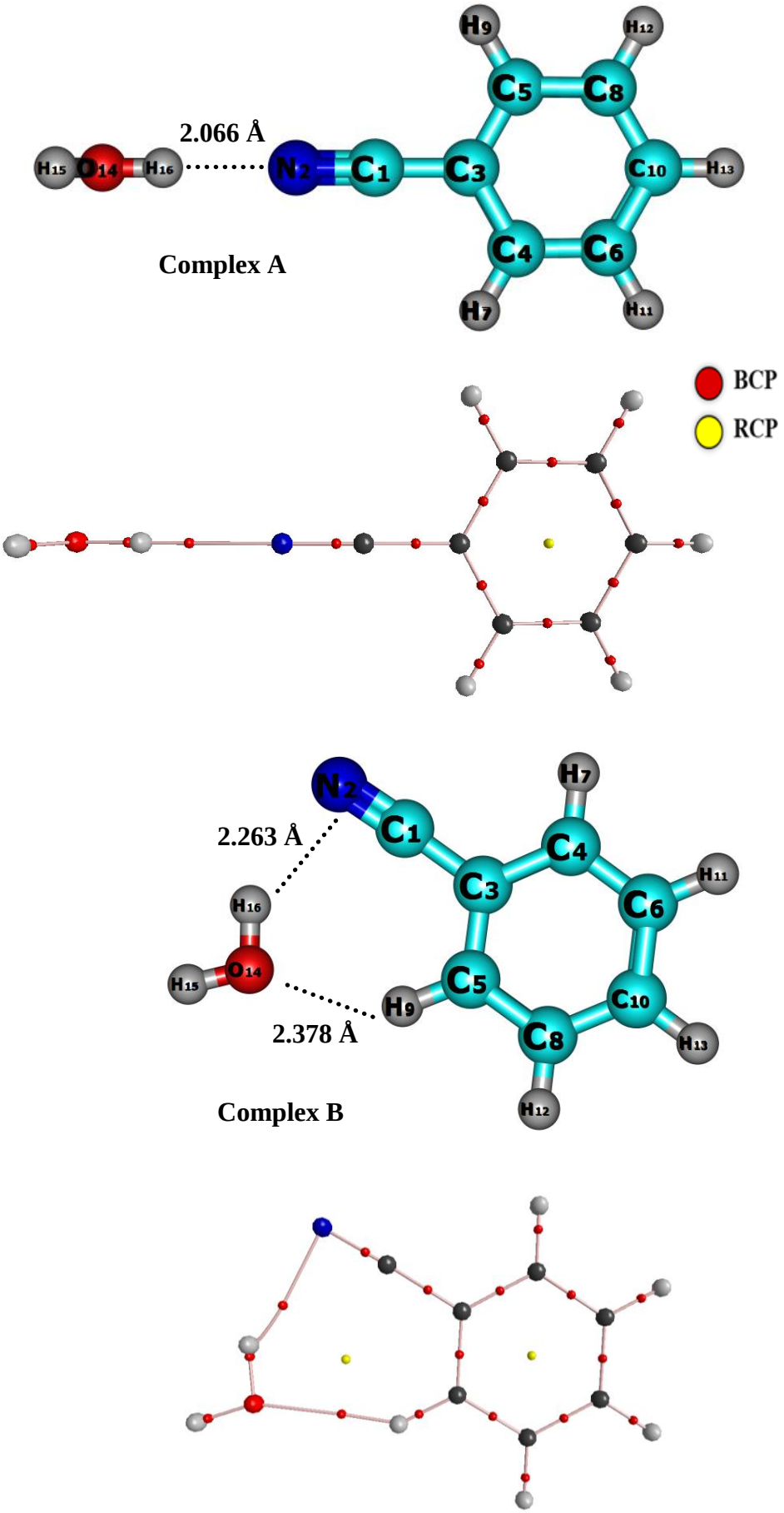

Figure 4.19: Structure of the C_6H_5CN-H_2O complexes A and B optimized at MP2/aug-cc-pVDZ level of theory. Bond critical point (BCP) and ring critical point (RCP) are shown in the figure.

Table 4.19: Selected structural parameters[a] for the C_6H_5CN-H_2O complexes A and B calculated at MP2/aug-cc-pVDZ level of theory.

Parameter	Complex A	Parameter	Complex B
N2-H16	2.066	N2-H16	2.263
C1-N2	1.187 (1.189)[b]	H9-O14	2.378
C1-C3	1.443 (1.444)	C1-N2	1.189(1.189)
C3-C5	1.413 (1.413)	C1-C3	1.443 (1.444)
C5-C8	1.404 (1.404)	C3-C5	1.441 (1.413)
C8-C10	1.408 (1.408)	C5-C8	1.405 (1.404)
C5-H9	1.093(1.093)	C8-C10	1.408 (1.408)
C4-H7	1.093(1.093)	C5-H9	1.094(1.093)
H16-O14	0.971 (0.966)	H16-O14	0.970 (0.966)
∠N2-H16-O14	177.8	∠N2-H16-O14	144.4
∠C1-N2-O16	172.5	∠C5-H9-O14	144.8
∠C3-C1-N2	179.9 (180.00)	∠C3-C1-N2	178.0 (180.00)
∠H16-O14-H15	103.8 (103.9)	∠H16-O14-H15	104.5 (103.9)
tor∠H15-O14-H16-N2	179.8	tor∠H15-O14-H16-N2	179.8
tor∠C1-N2-H16-O14	0.139	tor∠C3-C1-N2-H16	-0.014

[a]Bond length in Å; bond angle and dihedral angle in °.
[b]Numbers in parentheses are those of uncomplexed molecule.

Table 4.20: Raw[a]/ZPE-corrected/BSSE-corrected stabilization energies for the C_6H_5CN-H_2O complexes A and B computed at B3LYP/aug-cc-pVDZ and MP2/aug-cc-pVDZ levels of theory.

Satbilization energy (ΔE)		
Complexes	**B3LYP/aug-cc-pVDZ**	**MP2/aug-cc-pVDZ**
A	-4.63/-3.21/-4.26	-5.35/-3.89/-4.36
B	-4.46/-2.92/-3.96	-6.31/-4.78/-4.97

All energies are in kcal/mol (see text for details).
[a]Raw stabilization energies refer to energies not corrected for either ZPE or BSSE.

corresponding vibrational wavenumber. Table 4.20 gives the stabilization energies of the complexes A and B computed at B3LYP and MP2 levels using aug-cc-pVDZ basis sets. From the table it is evident that at DFT level both complexes A and B are iso-energetic and the ZPE corrected energy difference is -0.29 kcal/mol. Incorporation of the dispersion correction makes the complex B more stable than complex A and the ZPE corrected energy difference between the complex B and A is -0.89 kcal/mol.

4.5.3 Vibrational assignments

Table 4.21 compares the shift in the calculated vibrational wavenumbers of the C_6H_5CN-H_2O complexes A and B computed at MP2/aug-cc-pVDZ level of theory with the experimental shift in Ar and N_2 matrixes.

4.5.3.1 υ_3 and υ_1 modes of H_2O

Co-deposition experiments produced new features in the υ_3 and υ_1 mode of H_2O submolecule at 3704.2 and 3571.6 cm^{-1} in N_2 and 3708.9 and 3571.6 cm^{-1} in Ar matrix, which amounts to a red shift of 23.0,63.0 cm^{-1} and 24.0,66.3 cm^{-1}, respectively from the monomer absorption band. These experimental shifts agree well with the computed shifts of 31.5 and 70.7 cm^{-1} in the υ_3 and υ_1 mode of H_2O submolecule, respectively. This agreement between the experimental and computed shift is a clear evidence of the formation of linear complex in both the matrixes. For the complex B, the computed red shifts in the υ_3 and υ_1 modes of H_2O submolecule are 27.6 and 45.8 cm^{-1}, respectively from the monomer absorption. Experimentally, new feature could not be discerned for this complex. Computations showed that the magnitude of bond length change is slightly higher for complex A (~0.006 Å) than complex B (~0.001 Å) and the corresponding vibrational red shift in the υ_3 and υ_1 mode of H_2O submolecule for the former complex is larger than the latter. Furthermore, the IR intensity of the υ_1 and $\upsilon_3$mode for the linear complex A increases by a factor of ~100 and ~2.6 km/mol, respectively whereas for the complex B, it is only ~ 13

Table 4.21: Comparison of computed wavenumbers with experimental vibrational wavenumbers, shift in the calculated ($\Delta\upsilon_{cal}$), and experimental vibrational wavenumbers ($\Delta\upsilon_{exp}$) in Ar and N_2 matrixes. Computations were performed at MP2/aug-cc-pVDZ level of theory for the C_6H_5CN-H_2O complexes A and B.

Computed/ unscaled υ (cm^{-1})	Ar (cm^{-1})			N_2 (cm^{-1})		Mode Assignment
	$\Delta\upsilon^c_{cal}$	Exp (υ)	$\Delta\upsilon^c_{exp}$	Exp (υ)	$\Delta\upsilon^c_{exp}$	
C_6H_5CN						
2151.6 (0.2) [a]	-	2237.6	-	2236.2	-	υ_2CN str. (A_1) of C_6H_5CN
H_2O						
1622.2 (67)	-	1589.7	-	1597.4	-	υ_2 O-H bending of H_2O
3803.4 (4)	-	3637.9	-	3634.6	-	υ_1O-H sym. str. of H_2O
3937.7 (67)	-	3732.9	-	3727.2	-	υ_3O-H antisym. str. of H_2O
Complex A						
2169.3 (5)	17.7	2247.9	10.3	2251.3	15.1	υ_2CN str. (A_1) of Complex A
1647.2 (47)	25.0	-[b]	-	1618.7	21.3	υ_2 O-H bending of Complex A
3732.7 (398)	-70.7	3571.6	-66.3	3571.6	-63.0	υ_1O-H sym.str. of Complex A
3906.2 (179)	-31.5	3708.9	-24.0	3704.2	-23.0	υ_3 O-H antisym. str, of Complex A
Complex B						
2149.5 (5)	-2.1	-[b]	-	-[b]	-	υ_2CN str. (A_1) of Complex B
1630.6 (80)	8.4	-[b]	-	-[b]	-	υ_2 O-H bending of Complex B
3757.6 (50)	45.8	-[b]	-	-[b]	-	υ_1O-H sym.str. of Complex B
3910.1 (116)	-27.6	-[b]	-	-[b]	-	υ_3 O-H antisym. str, of Complex B

[a]Computed infrared intensities (km/mol) are given in parentheses
[b]Experimental features were not observed.
[c]$\Delta\upsilon = \upsilon_{complex} - \upsilon_{monomer}$

Table 4.22: Influence of dielectric constant on the raw energies of the C_6H_5CN-H_2O complexes A and B computed at MP2/aug-cc-pVDZ level of theory, using the Onsager solvation model.

Complexes	Dipole moment (D)[b]	Relative energies kcal/mol		
		Isolated complex (0.00)[a]	Nitrogen matrix (2.00)[a]	Argon matrix (1.43)[a]
A	6.99	-5.35	-6.02	-5.68
B	3.10	-6.31	-5.27	-5.75

[a]Dipole moment of the matrix.
[b]Unit of dipole moment in Debye.

and ~1.7 km/mol.

4.5.3.2 υ_2 CN stretch of C_6H_5CN

The computed value in this mode for the complex A occurs at 2169.3 cm^{-1}, a blue shift of 17.7 cm^{-1}whereas for the complex B the same mode showed a red shift of 2.1 cm^{-1} from the monomer absorption feature. Experimentally, new feature observed at 2251.3 and 2247.9 cm^{-1} in N_2 and Ar matrixes, respectively, with a blue shift of 15.1 and 10.3 cm^{-1} agrees well with the computed blue shift of 17.7 cm^{-1} for the complex A. The observation of the blue-shifted feature clearly confirms the formation of local minimum linear complex A in N_2 and Ar matrixes. The blue-shifted feature is discerned clearly in both the matrixes even though the IR intensity is increased marginally from 0.2 km/mol in the monomer to 5 km/mol in the C_6H_5CN-H_2O complex A. It could be possible that the matrixes do play a significant role in enhancing the IR intensity and trapping the complex A. Experimentally, the red-shifted feature was not observed in both matrixes for the complex B.

It is evident from the υ_3 and υ_1 modes of H_2O submolecule and υ_2 CN stretch of C_6H_5CN submolecule the local minimum linear complex A is produced and stabilized in Ar and N_2 matrixes. The matrixes play a significant role in stabilizing the complex A rather than complex B. In order to understand the effect of matrixes onto the complexes A and B, computations using Onsager solvation model were performed.

4.5.4 Onsager solvation model

To analyze the influence of surrounding matrix on the C_6H_5CN-H_2O complexes A and B calculations were performed using single point Onsager and isodensity polarized continuum (IPCM) models by incorporating the structure of two complexes in a cavity surrounded by a continuum with constant dielectric properties. To model the effect of the N_2 and Ar matrixes, the appropriate dielectric constants of N_2 (ε = 2.0) and Ar (ε = 1.43) were chosen in the calculation [220-222]. Table 4.22 gives the influence of dielectric constant on

the relative energies of the complexes A and B in the N_2 and Ar matrixes computed at MP2/aug-cc-pVDZ level of theory using Onsager solvation model. Interestingly, when the matrix effect was included, the complex A (linear local minimum) was found to be stabilized further in comparison with complex B (cyclic, global minimum), as this linear complex A was found to have maximum dipole moment among the two complexes. Thus, the computations performed using Onsager and IPCM models clearly preclude the production of the global minimum and supported the formation of only local minimum in the matrixes. It can therefore be concluded that the vibrational features appear in the N_2 and Ar matrixes should correspond exclusively to the wavenumbers of the C_6H_5CN-H_2O complexes A.

4.5.5 Nature of the interaction: AIM analysis

AIM theory was employed to analyze the nature of the interaction in the C_6H_5CN-H_2O complexes. A (3,-1) bond critical point (BCP) was searched using the optimized geometry of the C_6H_5CN-H_2O complexes A and B computed at MP2/aug-cc-pVDZ level of theory. At the BCP for both complexes A and B, electron density ($\rho(r_c)$), Laplacian of electron density ($\nabla^2\rho(r_c)$) were examined. Table 4.23 gives the properties of the intermolecular (3,-1) BCP for the complexes A and B. At the BCP for both complexes A and B the values of $\rho(r_c)$ were found to be of the order of 10^{-2} a.u. and $\nabla^2\rho(r_c)$ were positive, which is typical of closed shell interaction. Figure 4.19 shows the AIM plot of the complexes A and B computed at MP2/aug-cc-pVDZ level of theory. For the linear complex A, one (3,-1) BCP was located between the N_2 of C_6H_5CN and H16 of H_2O whereas for the complex B, two (3,-1) BCP's were located, one between the H9 of C_6H_5CN and O14 of H_2O and another between H16 of H_2O and N_2 of C_6H_5CN, confirming the cyclic nature of the complex. The magnitude of the electron density $\rho(r_c)$ and Laplacian of electron density $\nabla^2\rho(r_c)$ at the BCPs is higher in complex A than complex B.

Table 4.23: Properties of (3,-1) bond critical points in the C_6H_5CN-H_2O complexes A and B computed at the MP2/aug-cc-pVDZ level.

(a) Intermolecular bond critical points in C_6H_5CN-H_2O complexes

Molecule		$\rho(r_C)$	$\nabla^2\rho(r_C)$	λ_1	λ_2	λ_3
Complex A	C≡N(BN)···H-O (H_2O)	0.01924	0.06731	-0.02216	-0.02156	0.11103
Complex B	C-H(BN)···O-H (H_2O)	0.01047	0.04581	-0.01069	-0.00996	0.05577
	O-H(H_2O)···C≡N (BN)	0.01291	0.04199	-0.01214	-0.00966	0.06380

(b) Bond critical point corresponding to the C≡N bond in C_6H_5CN, and C_6H_5CN-H_2O complexes

Molecule	$\rho(r_C)$	$\nabla^2\rho(r_C)$	λ_1	λ_2	λ_3
C_6H_5CN	0.43611	-0.07048	-0.84670	-0.84128	1.61750
Complex A	0.43731	-0.15657	-0.98349	-0.85700	1.68392
Complex B	0.43632	-0.09696	-0.85411	-0.85273	1.60988

(c) Bond critical point corresponding to the O-H in H_2O and C_6H_5CN-H_2O complexes

Molecule	$\rho(r_C)$	$\nabla^2\rho(r_C)$	λ_1	λ_2	λ_3
H_2O	0.35148	-2.03630	-1.80155	-1.76171	1.52695
Complex A	0.34370	-2.08062	-1.80694	-1.76995	1.49624
Complex B	0.34651	-2.05561	-1.80364	-1.76679	1.51483
Complex B	0.35267	-2.02510	-1.80462	-1.76574	1.54527

Table 4.24: Electron occupancies of various natural bonding orbitals (NBOs) of C_6H_5CN-H_2O complexes A, and B computed at MP2/aug-cc-pVDZ basis set. The donor-acceptor delocalization interaction and delocalization energies (E_2, kcal/mol) are also shown.

Complex	NBO	Occupancy	Donor-acceptor delocalization interaction	Second order perturbation (E_2) energy (kcal/mol)
A	n^1N2	1.96980 (1.97603)[a]	n^1N2 → σ*(O14-H16) σ^1(C1-N2) → σ*(O14-H16) σ^1(C1-C3) → σ*(O14-H16)	6.03 0.33 0.08
	σ*(H16-O14)	0.00768 (0.00002)[b]		
	σ^1(C1-N2)	1.99512 (1.99533)[a]		
	π^2(C1-N2)	1.99022 (1.98994)[a]		
	π^3(C1-N2)	1.97608 (1.97416)[a]		
	σ*1(C1-N2)	0.00969 (0.00899)[a]	σ(H14- O16) → σ*(C1-N2) n^1O14 → σ*(C1-N2) n^2O14 → σ*(C1-N2)	0.33 0.08 0.06
	π*2(C1-N2)	0.00872 (0.00803 [a]		
	π*3(C1-N2)	0.06365 (0.05908)[a]		
B	π(2)(C1-N2)	1.98787 (1.98994)[a]	π(2)(C1-N2) →σ*(O14-H15) π(2)(C1-N2) →σ*(O14-H16) σ(C5-H9) →σ*(O14-H15) n^1N2 →σ*(O14-H16)	0.07 1.69 0.06 0.55
	π(3)(C1-N2)	1.97595 (1.97416)[a]		
	σ*(O14-H15)	0.00031 (0.00002)[b]		
	σ*(O14-H16)	0.00414 (0.00002)[b]		
	n^1 O14	1.99627 (1.99748)[b]	n^2 O14 → π*(1)(C1-N2) n^2 O14 → π*(1)(C5-H9) n^2 O14 → π*(1)(C5-H8) σ(O14- H15) → σ*(1)(C5-H9)	0.19 2.61 0.05 0.06
	n^2 O14	1.99390 (1.99591)[b]		

[a]Occupancy of monomeric C_6H_5CN is given in parentheses.
[b]Occupancy of monomeric H_2O is given in parentheses.

Table 4.23 (b-c) gives the properties of the BCPs on the neighbouring bonds corresponding to the C≡N bond of C_6H_5CN and O-H bond of H_2O submolecules in the complexes A and B. In the same table, the values for the monomeric C_6H_5CN and H_2O are also given for comparison. BCP's of the neighbouring bonds show high positive of $\rho(r_c)$ and high negative eigenvalues of $\nabla^2\rho(r_c)$, which is characteristic of shared covalent interaction. It must be noted that BCP at the C≡N bond in the complex A and the monomer revealed that the electron density $\rho(r_c)$ is slightly higher (~10^{-2} a.u.) in the complex A than the monomer, which is responsible for the shortening of the C≡N bond in the complex with the concomitant blue shift. The BCP corresponding to O-H bond showed a decrease in the electron density in the complex (~10^{-3}a.u.), which resulted in the red shift of the stretching vibrational wavenumbers. For the cyclic complex B, the increase in the electron density $\rho(r_c)$ at the C≡N BCP is of the order ~10^{-3} a.u. Further, there is an increase and decrease in the electron density $\rho(r_c)$ at the H⋯O and O⋯H BCP of the order ~10^{-3} a.u., which makes the C≡N and O-H vibrational wavenumber to show a red shift.

4.5.6 NBO Analysis

NBO analysis was carried out to correlate the red-shifted hydrogen bonding with the extent of charge-transfer hyperconjugation interactions. The NBO analysis is a useful tool and provides insight on the nature of the interactions particularly of red-shifted type [65,68,75,76 226-234]. The stabilizing interactions that arise due to the hyperconjugation interaction (n-σ*) in the hydrogen-bonded complexes is responsible for the origin of bond lengthening, which results in red shift of vibrational wavenumber.

In NBO analysis, off-diagonal elements of the Fock matrix in the NBO basis give the measure of delocalization effects. The second-order perturbation energy (E_2) provides an estimate of the strength of these delocalization interactions.

Table 4.24 shows the results of NBO analysis of C_6H_5CN-H_2O complexes A and B

computed at the MP2/aug-cc-pVDZ level of theory. From the table, it is clear that due to the hyperconjugation interaction between $n^1N2 \rightarrow \sigma^*(H16\text{-}O14)$ in complex A, there is an increase in the electron occupancy of antibonding orbital σ*(H16-O14) of the H_2O submolecule realtive to H_2O monomer. Due to this, the OH bond elongates and shows a red-shift. Further, there is a reduction in electron occupancy in the n^1N6 non-bonding orbital of the C_6H_5CN submolecule. The second order perturbation E_2 energy for the delocalization interaction was found to be ~6.03 kcal/mol. Apart from the charge transfer interaction there is also bond pair-acceptor orbital interaction $\sigma(H16\text{-}O14) \rightarrow \sigma^*(C1\text{-}N2)$ and $n^1O14 \rightarrow \sigma^*(C1\text{-}N2)$ due to this the electron occupancy in the antibonding σ*(C1-N2) increases marginally and the E_2 energiesof this interaction was ~ 0.33 and ~0.14 kcal/mol, respectively.

For the cyclic complex B, the dominant hyperconjugative interaction is between the $\pi(2)(C1\text{-}N2) \rightarrow \sigma^*(O14\text{-}H16)$ and $n^2\ O14 \rightarrow \sigma^*(1)(C5\text{-}H9)$. Due to this interaction the electron occupancy in the antibonding σ*(O14-H16) and σ*(C5-H9) increases and the E_2 energies for this interaction is ~ 1.69 and 2.61 kcal/mol respectively.

4.6 Conclusion

Using matrix isolation infrared spectroscopy, the 1:1 complexes of C_2H_2 with CH_3CN and C_6H_5CN linear complex, which is stabilized by C-H⋯N interaction was experimentally identified. The formation of the complex was evidenced from the red shift in the C-H asymmetric stretching region of C_2H_2 and blue shift in the C-N stretching region of CH_3CN and C_6H_5CN submolecules, respectively. The structure of the complexes and the energies were computed at the B3LYP level using 6-311++G(d,p) and MP2/aug-cc-pVDZ basis sets. The experimental observation compared well with the computations performed at the B3LYP/6-311++G(d,p) level of theory.

Computations performed at MP2/aug-cc-pVDZ level of theory on the $CH_3CN\text{-}H_2O$ and $C_6H_5CN\text{-}H_2O$ system yielded two minima; a linear complex A (local) and cyclic

complex B (global). Computations identified a blue shift of ~11.5 cm^{-1} and a red shift of ~6.5 cm^{-1} in the CN stretching mode for the complexes A and B, respectively. Experimentally, a blue shift of ~15.0 and ~8.3 cm^{-1} was observed in N_2 and Ar matrixes, respectively, in the CN stretching mode of CH_3CN, which supports the formation of linear complex A. The Onsager Self Consistent Reaction Field (SCRF) model was used to explain the influence of matrixes on the complexes A and B.

For the red-shifted complexes, AIM analysis showed a decrease in the electron density in the BCP corresponding to C-H of C_2H_2 and O-H of H_2O when compared to the monomer, which resulted in the red shift of the stretching wavenumber.

NBO analysis showed the charge transfer hyperconjugative interaction is dominant in the red-shifted complexes. The second order perturbation E_2 energy for the red shifted complexes is in the order CH_3CN-H_2O > C_6H_5CN-H_2O > CH_3CN-C_2H_2 > C_6H_5CN-C_2H_2.

CHAPTER 5

SUMMARY AND CONCLUSION

The highlight of this thesis is the study of blue-shifted hydrogen-bonded complexes of CHF_3 with HCl, H_2O, C_6H_6 and C_2H_2 and the red-shifted complexes of CH_3CN and C_6H_5CN with H_2O and C_2H_2. The complexes were trapped and studied experimentally using matrix isolation infrared spectroscopy and quantum chemical computations were performed on the systems using B3LYP and MP2 levels of theory with 6-311++G(d,p) and aug-cc-pVDZ basis sets to corroborate with the experimental results. AIM, NBO and EDA analyses were carried out to understand the nature of interaction on the blue- and red-shifted complexes.

In the blue-shifted hydrogen bonds, the complex formation was identified from the perturbations in the C-H stretching, bending, $-CF_3$ deformation and -C-F symmetric stretching modes of CHF_3 submolecule and the corresponding shifts in the stretching and bending modes of HCl, H_2O, C_6H_6 and C_2H_2. In the red-shifted complexes, the complex formation was evidenced from the red shifts in the C-H and O-H stretching and bending modes of C_2H_2 and H_2O submolecules and blue shift in the CN stretching modes of CH_3CN and C_6H_5CN submolecules. Computations yielded optimized structures, energies and vibrational wavenumbers of the complexes. The computed vibrational wavenumbers were used to assign the experimentally observed wavenumbers.

CHF_3 is a simplest prototype molecule to observe the blue-shifted H-bonding, where the hydrogen is attached to a sp3 hybridized carbon. Computations performed at B3LYP and MP2 levels of theory using aug-cc-pVDZ basis sets on 1:1 CHF_3-HCl complex gave two minima, one cyclic and the other acyclic. The cyclic complex is stabilized by the C-H⋯Cl and C-F⋯H interactions, where CHF_3 and HCl both submolecules act as proton donor and

proton acceptor. The second minimum corresponded to an acyclic complex stabilized only by C-F···H interaction, in which the CHF_3 is the proton acceptor. Experimentally, 1:1 CHF_3-HCl cyclic complex in an argon matrix, where a blue shift of 6.7 cm^{-1} in the C-H stretching mode of CHF_3 submolecule was observed. AIM analysis located two intermolecular BCPs for complex A, thereby supporting the cyclic nature of the interaction, and one intermolecular BCP for complex B. NBO analysis showed that the hyperconjugative charge-transfer interaction operate in both complexes. Cumulative effects such as lone pair-acceptor orbital/bond pair-acceptor orbital, remote delocalizations, re-hybridization, and intramolecular hyperconjugation on complex formation are contributing factors for the decrease in the C-H bond length and the observed blue-shift of the C-H stretching wavenumber of CHF_3-HCl complex.

As a result of hydrogen bonding in CHF_3-H_2O complex, *ab initio* computations showed a blue shift in the C-H stretching region of CHF_3 submolecule. Experimentally, a blue shift of 20.3 and 32.3 cm^{-1} in the C-H stretching region of CHF_3 submolecule of the CHF_3-H_2O complex was observed in Ar and Ne matrixes. Computations yielded one minimum, which corresponded to a C-H···O interaction between hydrogen of CHF_3 and oxygen of H_2O. AIM analysis located one intermolecular BCP for the complex.

Blue-shifted hydrogen-bonded complexes of CHF_3 with C_6H_6 and C_2H_2 have been investigated using matrix isolation infrared spectroscopy and *ab initio* computations. For CHF_3-C_6H_6 complex, calculations gave two minima corresponding to a 1:1 hydrogen-bonded complex. The global minimum correlated to a structure, where the interaction is between the hydrogen of CHF_3 and the π-electrons of C_6H_6 and a weak local minimum was stabilized through H···F interaction. For the CHF_3-C_2H_2 complex, computation yielded two minima, corresponding to the cyclic C-H···π complex A (global) and a linear C-H···F (n-σ) complex B (local). For the first time we have reported the formation of C-H···π blue-shifted

hydrogen-bonded complexes between CHF_3 and π electrons of C_6H_6 and C_2H_2 donors. Due to the C-H···π interaction, the C-H stretching mode of CHF_3 submolecule in the CHF_3-C_6H_6 and CHF_3-C_2H_2 complexes was found to be blue-shifted by 32.3 and 7.7 cm^{-1}, respectively. The observed experimental vibrational wavenumber correlates well with the computations performed at the MP2/aug-cc-pVDZ level of theory. NBO analysis revealed the participation of π electrons in forming the CHF_3-C_6H_6 and CHF_3-C_2H_2 complexes and collective delocalization interactions are responsible for the observed blue shift.

Hydrogen bonded complexes of acetylene (C_2H_2) with acetonitrile (CH_3CN) and benzonitrile (C_6H_5CN) have been investigated using matrix isolation infrared spectroscopy and *ab initio* computations. The complexes were trapped in both solid argon and N_2 matrixes. Computations indicated one minimum corresponding to the 1:1 C_2H_2-CH_3CN complex, with C-H···N interaction, where C_2H_2 is the proton donor. For the 1:1 C_2H_2-C_6H_5CN complex computations gave two minima corresponding to the C-H···N (global) and C-H···π interactions (local), where C_2H_2 is the proton donor in both complexes. Experimentally, we observed the 1:1 C_2H_2-CH_3CN and C_2H_2-C_6H_5CN complex in Ar and N_2 matrixes, which was evidenced by the shifts in the vibrational frequencies of the modes involving the C_2H_2, CH_3CN and C_6H_5CN submolecules respectively.

The 1:1 hydrogen bonded complexes of CH_3CN and C_6H_5CN with H_2O was trapped in Ar and N_2 matrixes and studied using infrared technique. *Ab initio* computations showed two types of complexes formed between CH_3CN/C_6H_5CN with H_2O, a linear complex with a C≡N···H interaction between nitrogen of CH_3CN/C_6H_5CN and hydrogen of H_2O and a cyclic complex, in which the interactions are between the hydrogen of CH_3CN/C_6H_5CN with oxygen of H_2O and hydrogen of H_2O with π cloud of -C≡N of CH_3CN/C_6H_5CN. Vibrational wavenumber calculations revealed that both linear and cyclic complexes were minima on the potential energy surface. Stabilization energies computed at MP2/aug-cc-pVDZ level of

theory showed that linear complex A is more stable than cyclic complex B. Computations identified a blue shift of ~11.5/17.7 cm^{-1} and a red shift of ~6.5/2.1 cm^{-1} in the CN stretching mode for the linear and cyclic complexes, respectively. Experimentally, we observed a blue shift of ~15.0/10.3 and ~8.3/15.1 cm^{-1} in N_2 and Ar matrixes, respectively, in the CN stretching mode of CH_3CN, which supports the formation of linear complex. Onsager Self Consistent Reaction Field (SCRF) model was used to explain the influence of matrixes on the linear and cyclic complexes.

The results of above studies in this thesis gave some interesting correlations within the blue- and red-shifted hydrogen bonding complexes, which is presented in the following section. We have tried to obtain correlations between experimental stretching vibrational wavenumber of the proton donor in the complex and computationally derived properties (MP2/aug-cc-pVDZ level of theory) such as BSSE corrected stabilization energies (ΔE_{BSSE}), hydrogen bond distance (R), charge densities (ρ), Laplacian of charge densities ($\nabla^2\rho$) and second order perturbation energy (E_2). These correlations will serve as useful tool to provide a link between computational and experimental quantities.

Table 5.1 shows the shift in the computed and experimental wavenumber, change in the bond length, BSSE corrected stabilization energy, hydrogen bond distance, electron density and Laplacian of electron density at the intramolecular bond critical point, second order perturbation energy of the blue- and red-shifted complexes computed at MP2/aug-cc-pVDZ level of theory.

At the outset, it can be seen that the quantities $(\Delta\upsilon)_{comp}$ and $(\Delta\upsilon)_{exp}$ for the blue- and red-shifted complexes listed in Table 5.1 show a reassuring correlation, as shown in Figure 5.1 block A and B.

In the blue-shifted complexes discussed in this work, CHF_3 has played the role of proton donor. The shifts in the C-H stretching mode of CHF_3 appear to be the indicator of the

role that CHF_3 plays in the complex. From the table 5.1 it is clear that in the blue-shifted complexes of CHF_3 with HCl, C_2H_2, H_2O and C_6H_6, the experimental shift in the C-H stretching vibrational wavenumber of CHF_3 is 6.7, 7.4, 20.3 and 32.3 cm^{-1}, where CHF_3 acts as proton donor. In the red-shifted complexes, the experimental shift in the υ_3 mode of C_2H_2 with CH_3CN and C_6H_5CN are 48.3 and 43.8 cm^{-1}, respectively. In the complexes of CH_3CN and C_6H_5CN with H_2O, the υ_1 mode of H_2O is shifted by 69.9 and 63.0 cm^{-1}, respectively.

We next examine the correlation between the experimental shift in the C-H stretching wavenumber $(\Delta\upsilon)_{exp}$ of CHF_3 and BSSE corrected stabilization energy for the blue-shifted complex, shift in the C-H and O-H stretching wavenumber of C_2H_2 and H_2O for the red-shifted complex, which is shown in figure 5.2 block A and B. The correlation is linear for both blue- and red-shifted complexes. It is clear from the figure for both types of complexes, as the stabilization energy of the complexes increases the corresponding blue or red vibrational wavenumber shift increases. For the blue-shifted complex, the data fits to the linear equation $(\Delta\upsilon)_{exp} = -13.96-11.50\times E_{BSSE}$ with a R^2 value of 0.92 whereas for the red shifted complex, the linear equation is $(\Delta\upsilon)_{exp} = 3.14-14.38\times E_{BSSE}$ with a R^2 value of 0.92. This relation allows, in principle, the estimation of the stabilization energy for a given series of blue- and red-shifted complexes from the experimentally observed vibrational wavenumber shifts.

It is generally observed on complex formation that the C-H bond length decreases compared with the values of the uncomplexed CHF_3 of the blue-shifted complex. For the red-shifted complex, the C-H and O-H bond length increase compared with the value of uncomplexed C_2H_2 and H_2O. The magnitude of change in the bond length for the different complexes depends upon the strength of the hydrogen-bonded interaction. The decrease/increase in the bond length correlates well with the blue/red shift in the experimental wavenumbers respectively. For example in the CHF_3-C_6H_6, CHF_3-C_2H_2

complexes the C-H bond length of CHF_3 decreases to -3.22 and -0.61 mÅ and the corresponding experimental blue shift is 32.3 and 7.4 cm^{-1}. Figure 5.3 block A and B shows the linear correlation between the experimental shift with the change in bond length for the blue- and red-shifted complexes. The fit for the blue- and red-shifted complexes is given by the equation $(\Delta\upsilon)_{exp} = 1.59-9.73\times\Delta r$ with a R^2 value of 0.99 and $(\Delta\upsilon)_{exp} = -154.4-38.5\times\Delta r$ with a R^2 value of 0.95.

The blue- and red-shifted hydrogen bonding studied in this work is supported by AIM analysis that describes the topology of the electron density. The value of electron density and Laplacian of electron density in the range 0.002-0.34 and 0.016-0.139 a.u. [201,202,235], respectively are used as criteria for the formation of hydrogen bond. It is also generally observed that the strong H-bonds are associated with higher electron density at the intermolecular bond critical points. For the blue-shifted complexes, the electron density values calculated at the BCPs follows the order HCl< C_2H_2< C_6H_6< H_2O. A similar trend was observed for the Laplacian of the electron density. For the red-shifted complexes, the magnitude of electron density is higher in complexes of CH_3CN and C_6H_5CN with H_2O when compared to C_2H_2 complexes. The inverse correlation between electron density with H-bond distance for the blue- and red-shifted complexes is shown in figure 5.4 block A and B. A decrease in the bond length corresponds to increase in the electron density, which is expected, since decrease in bond distance results in increased overlap, and hence higher electron density along the bond. The fit for the blue- and red-shifted complexes are given by the equation $\rho = 0.038-0.010\times R$ and $\rho = 0.078-0.029\times R$, respectively with a R^2 value of 0.99.

Figure 5.5 blocks A and B shows a linear relationship between the Laplacian of electron density $\nabla^2\rho$ with second order perturbation energy (E_2) for the blue- and red-shifted complexes. As the E_2 energy increases the $\nabla^2\rho$ value also increases and the fit equation for

the blue- and red-shifted complexes is given by the equation $\nabla^2\rho$ = -1.28-0.005×E_2 with R^2 value 0.93 and $\nabla^2\rho$ = 0.05-0.01×E_2 with R^2 value 0.83, respectively.

Table 5.2 shows the natural atomic charges of different atoms in complex and monomer and the electron occupancies of the antibonding orbital σ*(C-H) of CHF_3 for the blue-shifted complexes. From the table it clear that for the blue-shifted complexes the hydrogen atom participating in the bond becomes more negatively charged and the carbon attached to the hydrogen becomes more positively charged. Furthermore, the charge on the fluorine atoms also increases with respect to monomer. The increase in the charges on the fluorine atom is responsible for the elongation of the C-F bond in the complex, which leads to shortening of the C-H bond and a corresponding blue shift in the C-H stretching vibrational wavenumber of CHF_3 in the complexes. The negative charge on the fluorine atoms increase in the order HCl< H_2O< C_2H_2< C_6H_6, which is consistent with the blue shift observed in these complexes. In the same table, the electron occupancies of the complexes and monomer in the antibonding orbital of the σ*(C-H) of CHF_3 for the blue-shifted complexes are given. It is clear from the table that for the blue-shifted complexes the magnitude of change in the electron occupancies of the antibonding orbital σ*(C-H) of CHF_3 is negligible, which makes the C-H bond to contract and concomitant blue shift in the C-H stretching wavenumber was observed.

It can be surmised that the blue-shifted hydrogen-bonded complexes is mainly stabilized by charge transfer interactions n → σ*(C-H) due to which, the occupancies of the donor orbitals decreased with respect to the monomer, while there is an increase in the occupancy of the acceptor orbital. Interestingly for the fluorine lone pair whose occupancy is more than monomer in the complex leads to increase in the atomic charges on the fluorine atom. Further, the electron occupancies of the antibonding orbital of σ*(C-F) increases, which weakens the C-F bond. All the above factors make the C-F bond to elongate followed

by the geometrical rearrangement of the CHF_3 submolecule that causes a contraction of the C-H bond with the associated blue shift in the vibrational wavenumber. This observation is consistent with the prediction made by van der Veken and Hobza and co-workers [50]. NBO analysis showed that the hyperconjugative charge-transfer interaction operates in the blue-shifted complexes. Cumulative effects such as lone pair-acceptor orbital/bond pair-acceptor orbital, remote delocalizations, re-hybridization and intramolecular hyperconjugation on complex formation are the contributing factors for the decrease in the C-H bond length and the observed blue shift of the C-H stretching wavenumber of the complexes studied in this work. AIM analysis also revealed the accumulation of electron density at the C-H BCP of the blue-shifted complexes than the monomer. This increased electron density should be responsible for the shortening of the C-H bond in the complexes and the associated blue shift in the C-H stretching wavenumber.

5.1 Energy decomposition analysis (EDA)

Energy decomposition analysis was performed to precisely delineate the contribution of different stabilizing and destabilizing components and the role of other dominant interactions, in the blue- and red-shifted complexes.

Table 5.3 shows the contribution of different energy components to the total energy of blue- and red-shifted complexes. Energy decomposition analysis (EDA) was performed at B3LYP-D3/TZ2P level of theory using ADF 2016 package. In case of hydrogen bonded interaction, the stabilization energy has been shown to depend on the attractive electrostatic and the Pauli repulsion term, both of which generally have larger values when compared to the contribution from other components.

As the donor and acceptor atoms come close to each other due to the hydrogen bonding in the blue- and red-shifted complexes, the electrostatic and Pauli repulsion term shows higher values. The equilibrium geometry is defined by the net balance between the

Table 5.1: Comparison of shift in the computed and experimental wavenumber ($\Delta\upsilon$, cm^{-1}), change in bond length (Δr,mÅ), BSSE corrected stabilization energies (kcal/mol), hydrogen bond distance (R(Å)), electron density (ρ(a.u.)) and Laplacian of the electron density ($\nabla^2\rho$ (a.u.)) at the intramolecular bond critical point, second order perturbation energy E_2 (kcal/mol) of the blue- and red-shifted complexes. Computations were performed at MP2/ aug-cc-pVDZ level of theory.

Complexes	$\Delta\upsilon_{cal}$[a]	$\Delta\upsilon_{exp}$[a]	Δr[b]	ΔE_{BSSE}	R	ρ	$\nabla^2\rho$	E_2
Blue-Shifted								
CHF_3-HCl	10.1	6.7	-0.59	-1.74	2.958	0.0062	-1.284	1.35
CHF_3-C_2H_2	16.7	7.4	-0.61	-1.84	2.840	0.0080	-1.292	2.17
CHF_3-H_2O	29.2	20.3	-1.78	-3.31	2.181	0.0149	-1.318	6.93
CHF_3-C_6H_6	52.2	32.3	-3.22	-3.77	2.600	0.0099	-1.304	5.67
Red-Shifted								
C_6H_5CN-C_2H_2	-46.5	-43.8	5.10	-2.99	2.252	0.0140	-0.0106	5.50
CH_3CN-C_2H_2	-48.8	-48.3	5.34	-2.95	2.258	0.0138	-0.0108	5.72
C_6H_5CN-H_2O	-70.7	-63.0	5.60	-4.45	2.059	0.0195	-0.0168	6.03
CH_3CN-H_2O	-73.8	-69.9	5.82	-4.36	2.065	0.0193	-0.0171	6.23

[a] $\Delta\upsilon_{cal/exp} = \upsilon_{complex} - \upsilon_{monomer}$

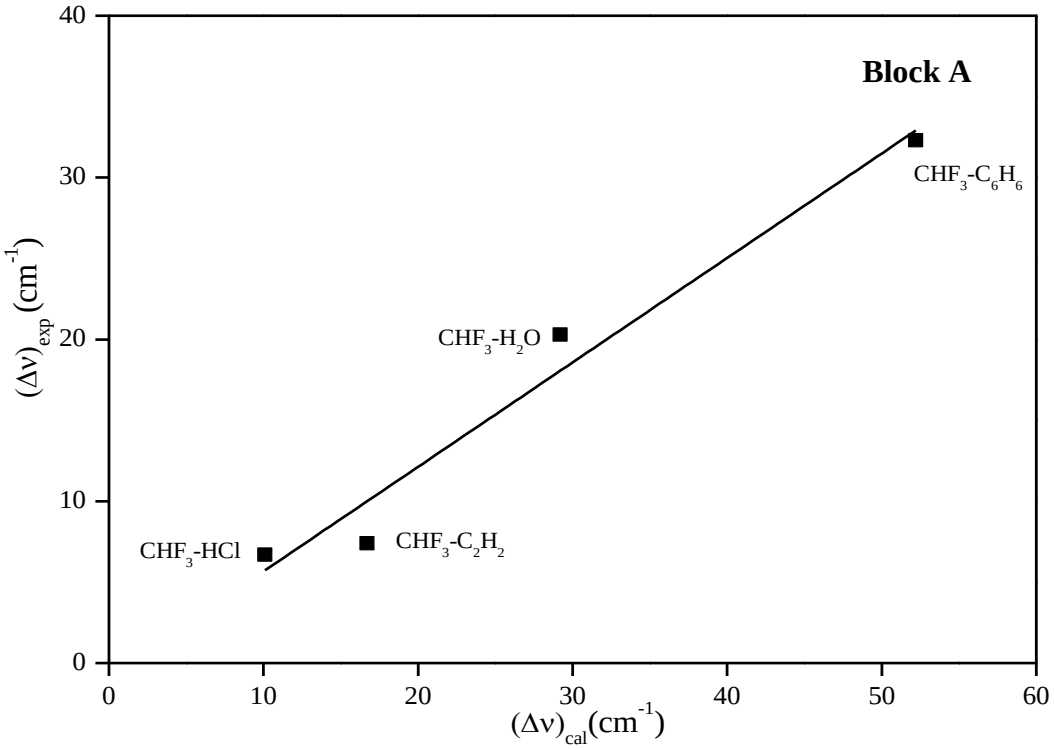

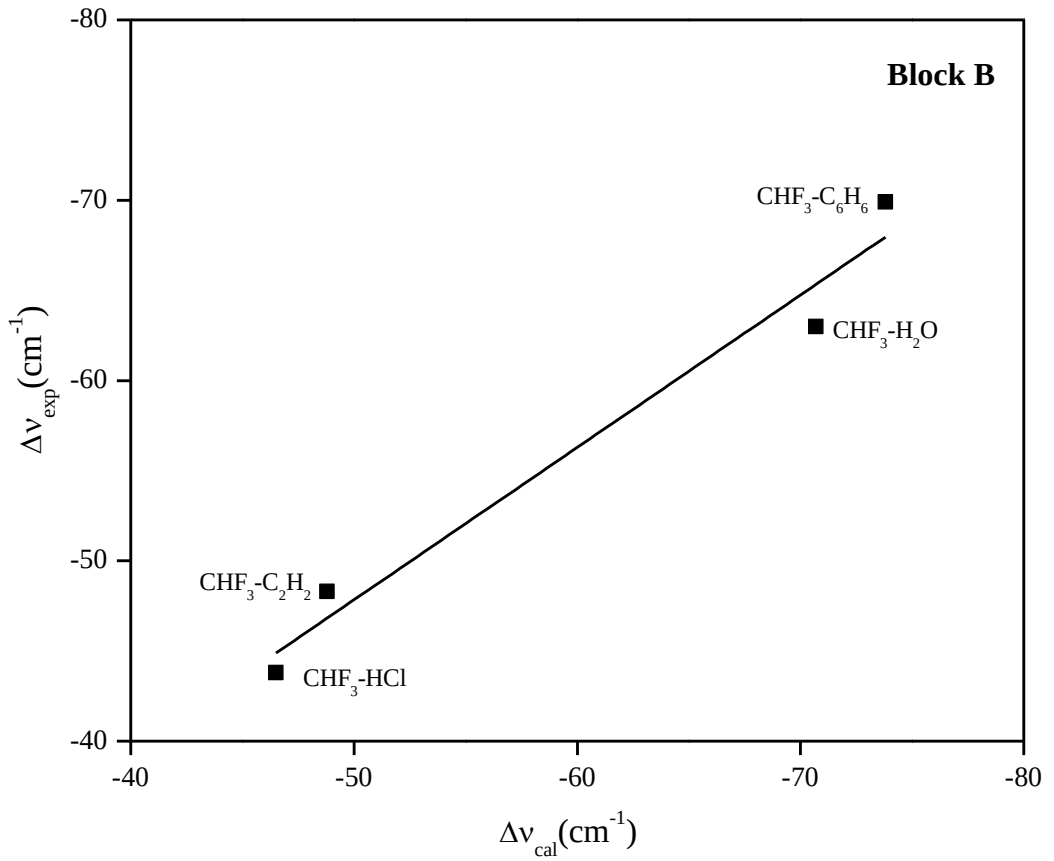

Figure 5.1: Block A and Block B corresponds to the correlation between the shift in the experimental wavenumber ($\Delta\upsilon_{exp}$) with computed vibrational wavenumber ($\Delta\upsilon_{cal}$) of the blue- and red-shifted complexes.

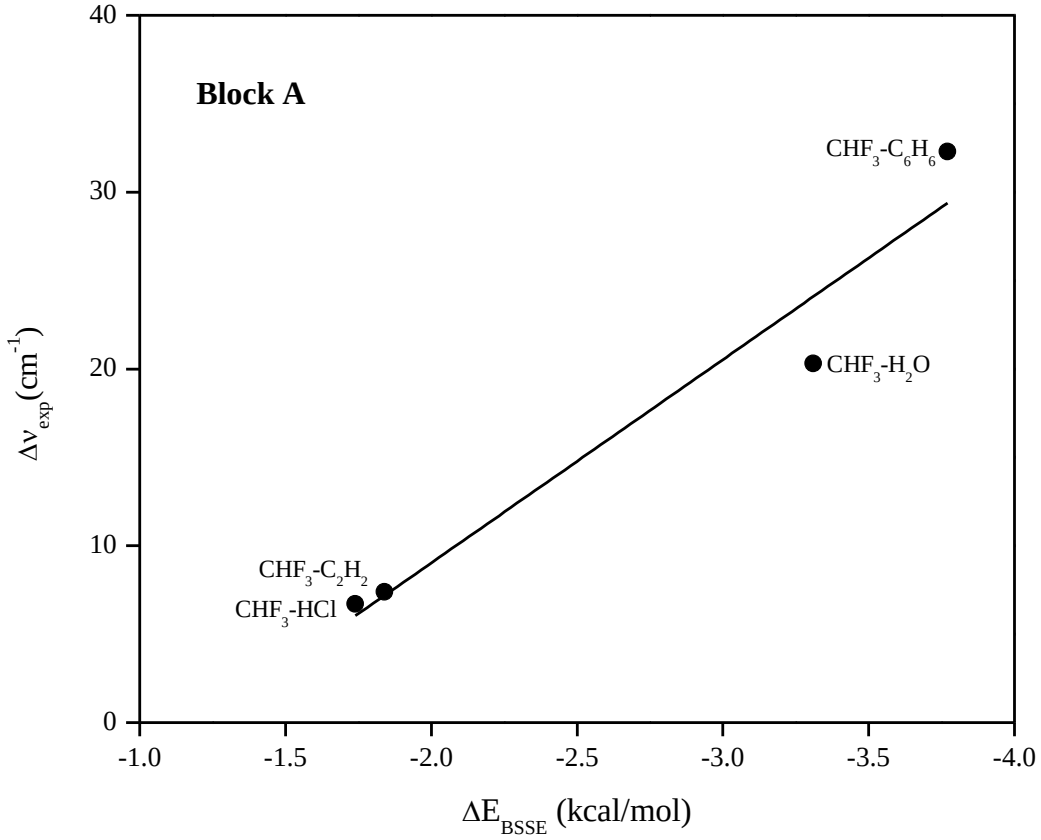

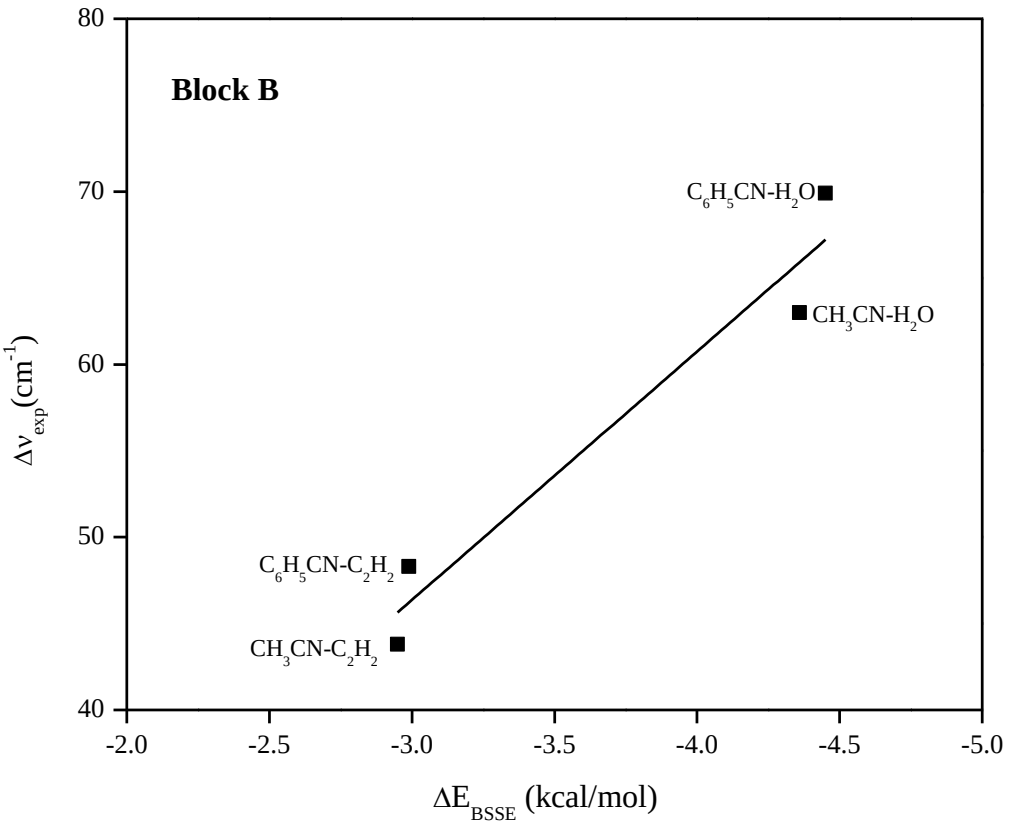

Figure 5.2: Block A and Block B corresponds to the correlation between the shifts in the experimental wavenumber ($\Delta\upsilon_{exp}$) with BSSE corrected stabilization energy (ΔE_{BSSE}) of the blue- and red-shifted complexes.

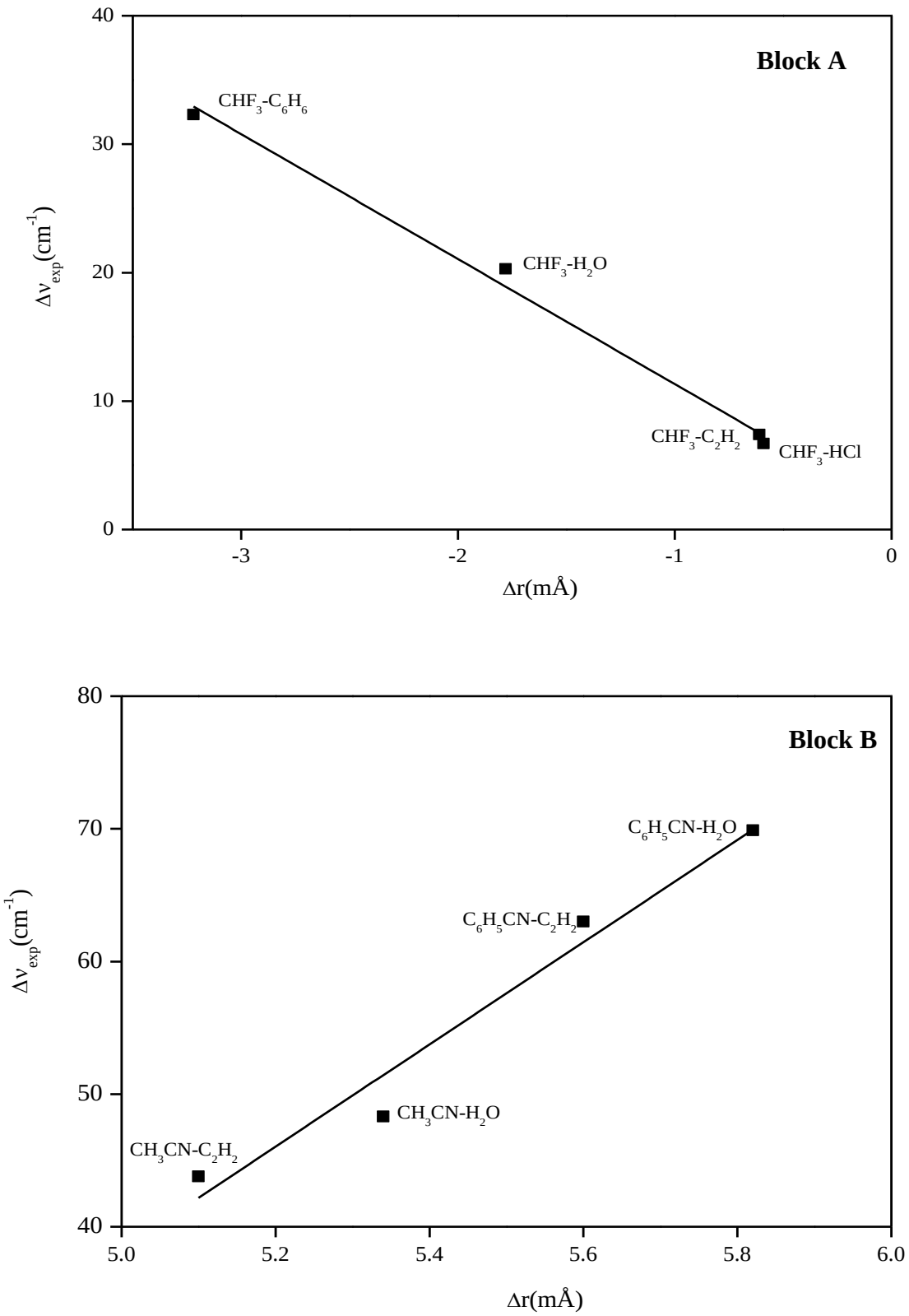

Figure 5.3: Block A and Block B corresponds to the correlation between the shift in the experimental wavenumber ($\Delta\upsilon_{exp}$) with change in the bond length (mΔr) of the blue- and red-shifted complexes.

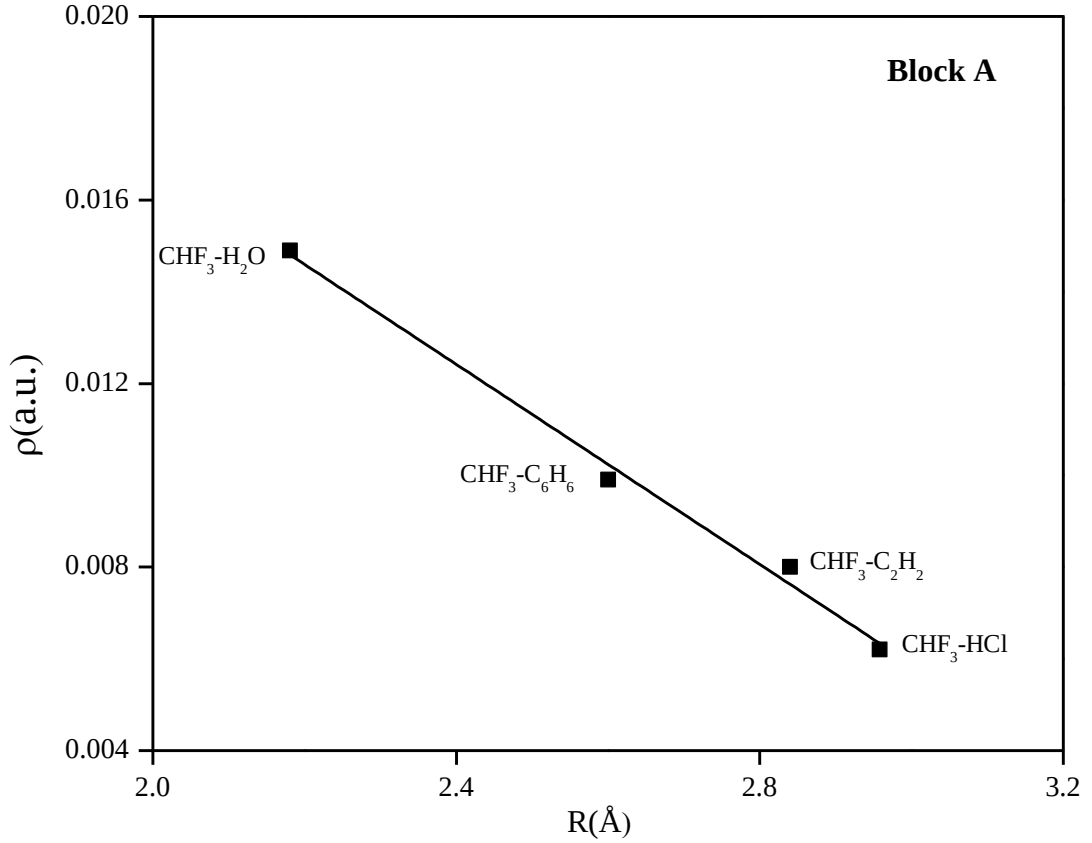

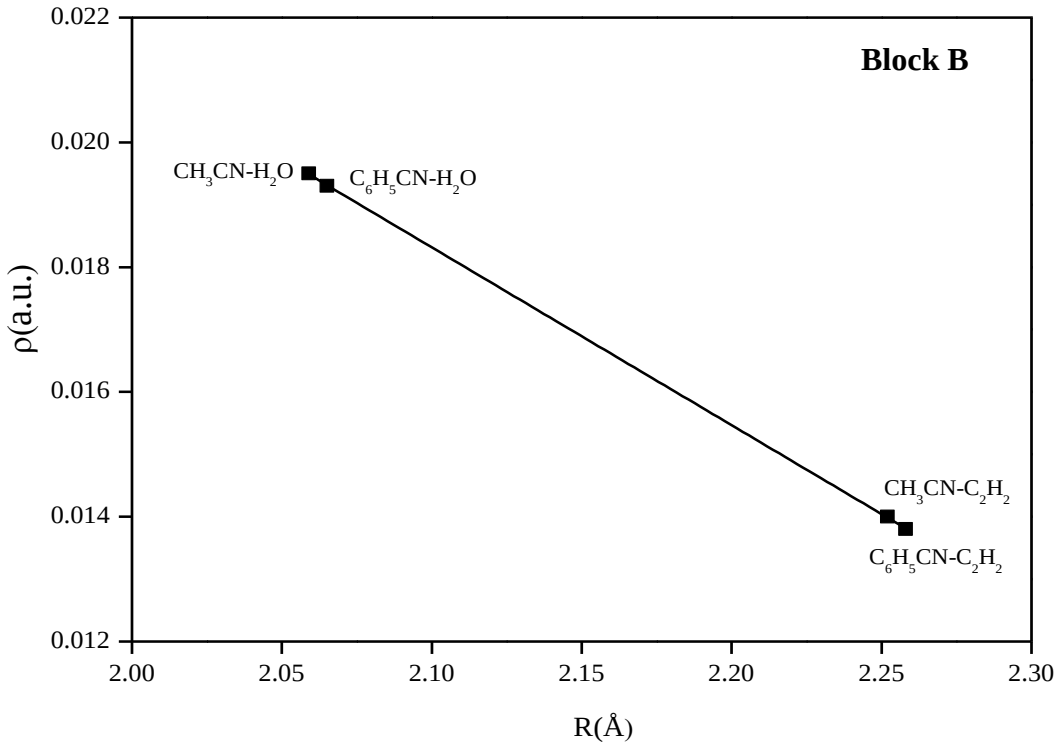

Figure 5.4: Block A and Block B corresponds to the correlation between electron density, ρ(a.u.) at the intermolecular bond critical point and the H-bond distance, R(Å) for the blue- and red-shifted complexes.

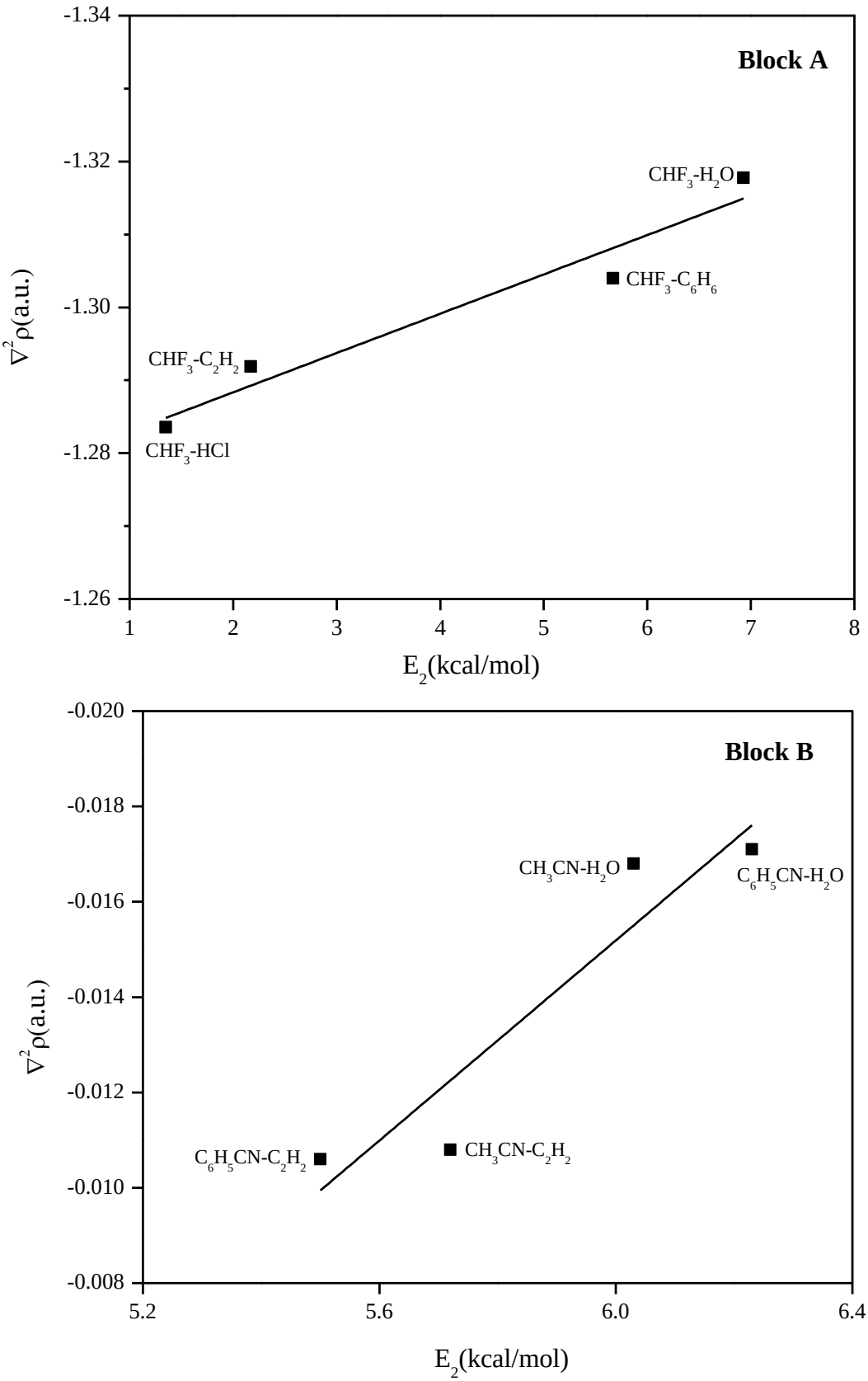

Figure 5.5: Block A and Block B corresponds to the correlation between Laplacian of electron density $\nabla^2\rho$(a.u.) at the intermolecular bond critical point and the H-bond distance R(Å) for the blue- and red-shifted complexes.

Table 5.2: Mulliken atomic charges (e) on the atoms of CHF_3 monomer (within parentheses) and in blue-shifted complexes and the electron occupancy in the antibonding C-H orbital computed at MP2/aug-cc-pVDZ level of theory.

Complexes	CHF_3-HCl	CHF_3-C_2H_2	CHF_3-H_2O	CHF_3-C_6H_6
C1	1.815 (1.757)	1.912 (1.757)	1.937 (1.757)	2.142 (1.757)
H2	-0.199 (-0.164)	-0.238 (-0.164)	-0.270 (-0.164)	-0.211 (-0.164)
F3	-0.524 (-0.531)	-0.549 (-0.531)	-0.555 (-0.531)	-0.613 (-0.531)
F4	-0.574 (-0.531)	-0.549 (-0.531)	-0.557 (-0.531)	-0.614 (-0.531)
F5	-0.524 (-0.531)	-0.575 (-0.531)	-0.557 (-0.531)	-0.613 (-0.531)
σ*(C-H)	0.03765(0.03720)	0.03774 (0.03720)	0.03801(0.03720)	0.03610(0.03720)

Table 5.3: Energy decomposition analysis (kcal/mol) for the blue- and red-shifted complexes computed at B3LYP-D3/TZ2P level of theory.

Complexes	Electrostatic	Dispersion	Orbital (delocalization)	Pauli repulsion	Total energy
Blue-shifted					
CHF_3-HCl	-2.82 (52%)	-1.50 (28%)	-1.10 (20%)	2.96	-2.46
CHF_3-C_2H_2	-2.46 (49%)	-1.39 (28%)	-1.15 (23%)	2.54	-2.60
CHF_3-H_2O	-5.22 (69%)	-0.73 (10%)	-1.58 (21%)	3.61	-3.91
CHF_3-C_6H_6	-4.66 (43%)	-3.32 (31%)	-2.80 (26%)	6.64	-4.13
Red-shifted					
C_2H_2-CH_3CN	-4.42 (63%)	-0.63 (9%)	-1.98 (28%)	3.59	-3.44
C_2H_2-C_6H_5CN	-4.33 (62%)	-0.66 (10%)	-1.95 (28%)	3.47	-3.47
H_2O-CH_3CN	-6.77 (65%)	-0.63 (6%)	-3.09 (29%)	5.36	-5.13
H_2O-C_6H_5CN	-6.57 (64%)	-0.66 (7%)	-2.99 (29%)	5.12	-5.10

electrostatic and the Pauli term contribute to the same order of magnitude with opposite sign and cancelling each other, and the other terms such as orbital delocalization and dispersion term contribute to the stabilization energy. It is clear from the table that the strongest attractive interaction is electrostatic followed by dispersion and orbital interaction for the blue-shifted complex whereas it is electrostatic followed by orbital and dispersion interaction for the red-shifted complexes. The magnitude of electrostatic interaction is higher in the red shifting when compared to blue shifting except for the CHF_3-H_2O complex. The relatively large orbital delocalization energy or polarization in the red shifted complex indicates that there is a significant orbital overlap between the molecules. This could probably be the reason for the larger electrostatic interaction in these complexes. The magnitude of dispersion contribution is significantly higher in the blue-shifted complexes except for CHF_3-H_2O when compared to the red-shifted complexes.

5.2 Scope for future work

The work described in this thesis pertaining to the blue-shifted hydrogen-bonded complexes of CHF_3 with various Lewis bases and red-shifted hydrogen-bonded of H_2O and C_2H_2 with CH_3CN and C_6H_5CN. The work can be further extended to study the blue-shifted halogen bonding in CF_3Br, CF_3I, and $CHBr_3$ with various Lewis bases. Proton shared or proton transfer hydrogen bonding can be studied using the matrix isolation infrared technique.

References

[1] G. R. Desiraju, T. Steiner, The Weak Hydrogen Bond in Structural Chemistry and Biology, Oxford University Press, **1999**.

[2] L. Pauling, R. B. Corey, H. R. Branson, *Proc. Natl. Acad. Sci. U.S.A.* **1951**, 37, 205.

[3] J. D. Watson, F. H. C. Crick, *Nature* **1953**, 171, 737.

[4] G. E. Schulz, R. H. Schirmer, Principles of Protein Structure, Springer Advanced Texts in Chemistry,**1979**.

[5] J. Sponer, J. Leszczynski, P. Hobza, *J. Biomol. Struct. Dyn*. **1996**, 14, 117.

[6] J. Sponer, J. Leszczynski, P. Hobza, *J. Phys. Chem*. **1996**, 100, 1965.

[7] O. Khakshoor, S. E. Wheeler, K. N. Houk, E. T. Kool, *J. Am. Chem. Soc*. **2012**, 134(6), 3154.

[8] E. F. Guerra , F. M. Bickelhaupt, J. G. Snijders, E. J. Baerends, *J. Am. Chem. Soc*. **2000**, 122 (17), 4117.

[9] Y. Mo, *J. Mol. Model*. **2006**, 12(5), 665.

[10] L. Pauling, The Nature of the Chemical Bond, Cornell University Press, Ithaca, NY (**1960**). The first edition was published in **1939**.

[11] G. C. Pimentel, A. L. McClellan. The Hydrogen Bond, W. H. Freeman, San Francisco **1960**.

[12] G. A. Jeffrey, An Introduction to Hydrogen Bonding, Oxford University Press, Oxford **1997**.

[13] G. R. Desiraju, *Acc. Chem. Res*. **2002**, 35, 565.

[14] A. E. Reed, L. A. Curtiss, F. Weinhold, *Chem. Rev*. **1988**, 88, 899.

[15] T. Steiner, *Angew. Chem. Int. Ed*. **2002**, 41, 48.

[16] A. Werner, *Liebigs Ann*. **1902**, 322, 261.

[17] A. Hantzsch, *Chem. Ber*. **1910**, 43, 3049.

[18] T. S. Moore, T. F. Winmill, *J. Chem. Soc*. **1912**, 101, 1635.

[19] P. Pfeiffer, P. Fischer, J. Kuntner, P. Monti, *Z. Pros, Liebigs Ann. Chem*. **1913**, 398, 137.

[20] W. M. Latimer, W. H. Rodebush, *J. Am. Chem. Soc*. **1920**, 42, 1419.

[21] T. Steiner, W. Saenger, *J. Am. Chem. Soc*. **1993**, 115, 4540.

[22] IUPAC Compendium of Chemical Terminology 2nd Edition **1997**.

[23] G. R. Desiraju, *Angew. Chem. Int. Ed*. **2011**, 50, 52.

[24] E. Arunan, G. R. Desiraju, R. A. Klein, J. Sadlej, S. Scheiner, I. Alkorta, D. C. Clary, R. H. Crabtree, J. J. Dannenberg, P. Hobza, H. G. Kjaergaard, A. C. Legon, B. Mennucci, D. J. Nesbitt. *Pure Appl. Chem*. **2011**, 83, 1619.

[25] D. R. Davies, G. H. Cohen, *Proc. Natl. Acad. Sci*. **1996**, 93, 7.

[26] C. B. Aakeröy, A. Rajbanshia, J. Despera, *Chem. Commun*. **2011**, 47, 11411.

[27] R. Horikoshi, C. Nambu, T. Mochida, *New J. Chem*. **2004**, 28, 26.

[28] A. J. Dingley, S. Grzesiek, *J. Am. Chem. Soc*. **1998**, 120, 8293.

[29] A. C. Legon, *Chem. Soc. Rev*. **1993**, 22, 153.

[30] K. Liu, J. D. Cruzan, R. J. Saykally, *Science* **1996**, 271, 929.

[31] K. Liu, M. G. Brown, R. J. Saykally, *J. Phys. Chem. A* **1997**, 101, 8995.

[32] A. S. N. Murthy, C. N. R. Rao, *Appl. Spectrosc. Rev*. **1968**, 2, 69.

[33] S. T. Roberts, K. Ramasesha, A. Tokmakoff, *Acc. Chem. Res.* **2009**, 42, 1239.

[34] V. A. Shubert, C. W. Muller, T. S. Zwier, *J. Phys. Chem. A* **2009**, 113, 8067.

[35] Z. Xue, M. A. Suhm, *J. Chem. Phys*. **2009**, 131, 054301.

[36] H. Biswal, R. R Shirhatti, S. Wategaonkar, *J. Phys. Chem. A* **2009**, 113, 5633.

[37] S. Maiti, G. N. Patwari, *J. Phys. Chem. A* **2009**, 113, 1760.

[38] J. P. Toennies, A. F. Vilesov, *Angew. Chem. Int. Ed.* **2004**, 43, 2622.

[39] A. Engdahl, B. Nelander, P. O. Aastrand, *J. Chem. Phys.* **1993**, 99, 4894.

[40] C. F. Guerra, F. M. Bickelhaupt, J. G. Snijders, E. J. Baerends, *Chem. Eur. J.* **1999**, 5, 3581.

[41] C. F. Guerra, F. M. Bickelhaupt, E. J. Baerends, *Chem. Phys. Chem.* **2004**, 5, 481.

[42] G. T. Trudeau, J. M. Dumas, P. Dupuis, M. Guerin, C. Sandorfy, *Top. Curr. Chem.* **1980**, 93, 91.

[43] M. Budesinsky, P. Fiedler, Z. Arnold, *Synthesis* **1989**, 11, 858.

[44] I. E. Boldeskul, I. F. Tsymbal, E. V. Ryltsev, Z. Latajka, A. J. Barnes, *J. Mol. Struct.* **1997**, 167, 436.

[45] P. Hobza, V. Spirko, H. L. Selzle, E. W. Schlag, *J. Phys. Chem. A* **1998**, 102, 2501.

[46] P. Hobza, Z. Havlas, *Chem. Phys. Lett.* **1999**, 303, 447.

[47] P. Hobza, V. Spirko, Z. Havlas, K. Buchhold, B. Reimann, H. D. Barth, B. Brutschy, *Chem. Phys. Lett.* **1999**, 299, 180.

[48] B. Reimann, K. Buchfold, S. Vaupel, B. Brutschy, Z. Havlas, V. Spirko, P. Hobza, *J. Phys. Chem. A* **2001**, 105, 5560.

[49] B. Reimann, K. Buchfold, S. Vaupel, B. Brutschy, *Z. Phys. Chem.* **2001**, 215, 777.

[50] B. J. van der Veken, W. A. Herrebout, R. Szostak, D. N. Shchepkin, Z. Havlas, P. Hobza, *J. Am. Chem. Soc.* **2001**, 123, 12290.

[51] S. N. Delanoye, W. A. Herrebout, B. J. van der Veken, *J. Am. Chem. Soc.* **2002**, 124, 7490.

[52] S. N. Delanoye, W. A. Herrebout, B. J. van der Veken, *J. Am. Chem. Soc.* **2002**, 124, 11854.

[53] W. A. Herrebout, S. N. Delanoye, B. J. van der Veken, *J. Phys. Chem. A* **2004**, 108, 6059.

[54] W. A. Herrebout, S. N. Delanoye, B. J. van der Veken, *J. Phys. Chem. A* **2005**, 109, 9836.

[55] K. S. Rutkowski, P. Rodziewicz, S. M. Melikova, W. A. Herrebout, B. J. Van der Veken, A. Koll, *Chem. Phys.* **2005**, 313, 225.

[56] W. A. Herrebout, S. N. Delanoye, B. U. W. Maes, B. J. van der Veken, *J. Phys. Chem. A* **2006**, 110, 13759.

[57] B. Michielsen, W. A. Herrebout, B. J. van der Veken, *Chem. Phys. Chem*. **2008**, 9, 1693.

[58] K. S. Rutkowski, S. M. Melikova, P. Rodziewicz, W.A. Herrebout, B. J. van der Veken, A. Koll, *J. Mol. Struct.* **2008**, 880, 64.

[59] J. M. E. Ahokas, K. J. Vaskonen, H. M. Kunttu, *J. Phys. Chem. A* **2006**, 110, 7816.

[60] H. Matsuura, H. Yoshida, M. Hieda, S.Yamanaka, T. Harada, K. Shin-ya, K. Ohno. *J. Am. Chem. Soc*. **2003**, 125, 13910.

[61] N. C. Craig, T. W. Brickey, P. T. Lingenfelter, A. S. Osmani, M. O. Rathore, A. Pearson, *Spectrochim. Acta Part A* **2005**, 61, 1571.

[62] A. Masunov, J. J. Dannenberg, R. H. Contreras, *J. Phys. Chem. A* **2001**, 105, 4737.

[63] K. Hermansson, *J. Phys. Chem. A* **2002**, 106, 4695.

[64] X. Li, L. Liu, H. B. Schlegel, *J. Am. Chem. Soc.* **2002**, 124, 9639.

[65] W. Zierkiewicz, P. Jurecka, P. Hobza, *Chem. Phys. Chem*. **2005**, 6, 609.

[66] L. Pejov, K. Hermansson, *J. Chem. Phys.* **2003**, 119, 313.

[67] P. Hobza, Z. Havlas, *Chem. Rev*. **2000**, 100, 4253.

[68] I. V. Alabugin, M. Manoharan, S. Peabody, F. Weinhold, *J. Am. Chem. Soc*. **2003**, 125, 5973.

[69] E. Cubero, M. Orozco, P. Hobza, F. J. Luque, *J. Phys. Chem. A* **1999**, 103, 6394.

[70] Y. Gu, T. Kar, S. Scheiner, *J. Am. Chem. Soc*. **1999**, 121, 9411.

[71] W. Caminati, S. Melandri, P. Moreschini, P. G. Favero, *Angew. Chem*. **1999**, 111, 3105; *Angew. Chem. Int. Ed.* **1999**, 38, 2924.

[72] R. H. Contreras, J. E. Peralta, C. G. Giribet, M. C. Ruiz de Azua, J. C. Facelli, *Prog. Nucl. Magn. Reson. Spectrosc.* **2000**, 4, 321.

[73] S. A. Melikova, K. S. Ruykowski, P. Rodziewicz, A. Koll, *Chem. Phys. Lett*. **2002**, 352, 301.

[74] W. Quian, S. Krimm, *J. Phys. Chem. A* **2002**, 106, 6628.

[75] W. Zierkiewicz, D. Michalska, Z. Havlas, P. Hobza, *Chem. Phys. Chem*. **2002**, 3, 511.

[76] P. Hobza, Z. Havla, *Theor. Chem. Acc.* **2002**, 108, 325.

[77] J. Joseph, E. D. Jemmis, *J. Am. Chem. Soc.* **2007**, 129, 4620.

[78] S. L. Paulson, A. J. Barnes, *J. Mol. Struct*. **1982**, 80, 151.

[79] Y. Mo, C. Wang, L. Guan, B. Brada, P. C. Hiberty, W. Wu, *Chem. Eur. J.* **2014**, 208, 444.

[80] A. Mukhopadhyay, *Comp. Theor. Chem.* **2016**, 1083, 19.

[81] M. Nishio, M. Hirota, Y. Umezawa, The CH/π Interaction: Evidence, Nature, and Consequences; Wiley-VCH: New York, **1998**.

[82] S. Scheiner, S. J. Grabowski, T. J. Kar, *J. Phys. Chem. A* **2001**, 105, 10607.

[83] B. G. Oliveira, Phys. *Chem. Chem. Phys.* **2013**, 15, 37.

[84] O. Takahashi, Y. Kohno, M. Nishio, *Chem. Rev.* **2010**, 110, 6049.

[85] J. Li, R. Q. Zhang, *Scientific Reports*, **2016**, 6, 22304.

[86] B. Michielsen, J. J. J. Dom, B. J. van der Veken, S. Jacobs, Z. Xue, S. Hesse, H. M. Loritz, M. A. Suhm , W. A. Herrebout, *Phys. Chem. Chem. Phys.* **2010**, 12, 14034.

[87] D. Hauchecorne, N. Nagels, B. J. van der Veken W. A. Herrebout, *Phys. Chem. Chem. Phys.* **2012**, 14, 681.

[88] J. J. J. Dom, B. J. van der Veken, B. Michielsen, S. Jacobs, Z. Xue, S. Hesse, Hans-Martin Loritz, M. A. Suhm , W. A. Herrebout, *Phys. Chem. Chem. Phys*. **2011**, 13, 14142.

[89] P. R. Shirhatti, S. Wategaonkar, *Phys. Chem. Chem. Phys.* **2010**, 12, 6650.

[90] J. C. Lopez, W. Caminati, J. L. Alonso, *Angew. Chem. Int. Ed.* **2005**, 45, 290.

[91] O. D. Tauda, P. Jaque , J. C. Santos, *Phys. Chem. Chem. Phys.* **2011**, 12, 1552.

[92] S. Tsuzuki, K. Honda, T. Uchimaru, M. Mikami, K. Tanabe *J. Phys. Chem.* A **2002**, 106, 4423.

[93] J. Ran, M. W. Wong, *J. Phys. Chem. A* **2006**, 110, 9702.

[94] R. C. Dey, P. Seal, S. Chakrabarti, *J. Phys. Chem. A* **2009**, 113, 10113.

[95] C. D. Keefe, M. Isenor, *J. Phys. Chem. A* **2008**, 112, 3127.

[96] E. D. Jemmis, K. T. Giju, K. Sundararajan, K. Sankaran, V. Vidya, K. S.Viswanathan, J. Leszczynski, *J. Mol. Struct.* **1999**, 510, 59.

[97] K. Sundararajan, N. Ramanathan, K. S. Viswanathan, K. Vidya, E. D. Jemmis, *J. Mol. Struct*. **2013**, 1049, 69.

[98] B. A. Lindquist, K. E. Furse, S. A. Corcelli, *Phys. Chem. Chem. Phys.* **2009**, 11, 8119.

[99] O. W. Kolling, *Anal. Chem.* **1987**, 59 (4), 674.

[100] http://science.gsfc.nasa.gov/691/cosmicice/interstellar.html.

[101] T. B. Freedman, E. R. Nixon, *Spectrochim. Acta* **1972**, 28A, 1375.

[102] H. S. Kim, K. Kim, *Bull. Korean Chem. Soc.* **1992**, 13, 521.

[103] A. Givan, A. Loewenschuss, *J. Mol. Struct.* **1983**, 98, 231.

[104] S. Coussan,Y. Boutelier, J. P. Perchard,V. Brenner, P. Millié, W. Q. Zheng. F. Talbot, *J. Chem. Phys.* **1999**,110, 10046.

[105] E. Kryachko, M. T. Nguyen, *J. Phys. Chem. A* **2002**, 106, 4267.

[106] S. C. White, H. W. Thompson, *Proc. R. Soc. London* **1966**, 291A, 460.

[107] M. S. Sousa Lopes, H. W. Thompson, *Spectrochim. Acta.* **1968**, 24A, 1367.

[108] S. S. Mitra, *J. Chem. Phys.* **1962**, 36, 3286.

[109] A. Allerhand, P. V. R. Schelyer, *J. Am. Chem. Soc.* **1963**, 85, 371.

[110] N. P. Wells, J. A. Phillips, *J. Phys. Chem.* A **2002**,106, 1518.

[111] R. Hattori, E. Suzuki, K. Shimizu, *J. Mol. Struct.* **2005**, 750, 123.

[112] D. S. Ahn, S. Lee, *Bull. Korean. Chem. Soc.* **2003**, 24, 545.

[113] A. Chaudhari, S. Lee, Int. *J. Quantum Chem.* **2005**, 102, 106.

[114] A. K. Lyashchenkoa, V. S. Dunyashev, *Russ. J. Phys. Chem A* **2014**, 88, 271.

[115] J. E. Bertie, Z. Lan, *J. Phys. Chem. B* **1997**,101, 4111.

[116] T. Takamuku, M. Tabata, A. Yamaguchi, J. Nishimoto , M. Kumamoto, H. Wakita, T. Yamaguchi, *J. Phys. Chem. B* **1998**, 102, 8880.

[117] G. M. Chaban, *J. Phys. Chem. A* **2004**, 108, 4551.

[118] R. D. Mountain, *J. Phys. Chem. A* **1999**,103, 10744.

[119] K. S. Rutkowski, S. M. Melikova, J. Janski, A. Koll, *Chem. Phys.* **2010**, 375, 92.

[120] M. Domagała, S. J. Grabowski, *Chem. Phys.* **2009**, 363, 42.

[121] N. Goldberg, S. R. Lubell, B. S. Ault, *J. Mol. Struct*. **2005**, 740, 125.

[122] R. Hattori, E. Suzuki, K. Shimizu, *J. Mol. Struct.* **2005**, 750, 123.

[123] A. B. Baker , C. Samet, J. T. Lyon, L. Andrews, *J. Phys. Chem.* A **2005**, 109, 8280.

[124] M. P. Bernstein, S. A. Sandford, L. J. Allamandola, *APJ*. **1997**, 476, 932.

[125] L. Schriver, A. Schriver, S. Racine, J. P. Perchard, *Chem. Phys*. **1988**, 119, 95.

[126] Y. Gu, T. Kar, S. Scheiner, *J. Mol. Struct.* **2000**, 552, 17.

[127] W. P. Schroeder, K. Chenoweth, C. E. Dykstra, *Chem. Phys. Lett.* **2003**, 373, 8.

[128] E. Sanchez-Garcıa, A. Mardyukov, A. Tekin , R. Crespo-Otero, L. A. Montero, W. Sander, G. Jansen, *Chem. Phys.* **2008**, 343, 168.

[129] E. L. Zins, L. Krim, *Phys. Chem. Chem. Phys.* **2014**, 16, 3388.

[130] A. Chaudhari, S. Lee, *Int. J. Quantum Chem.* **2005**, 102, 106.

[131] E. Rissi, E. E. Fileti, S. Canuto, *Theor. Chem. Acc.* **2003**, 110, 360.

[132] I. Bako, T. Megyes, G. Palinkas, *Chem. Phys.* **2005**, 316, 235.

[133] T. Takamuku, M. Tabata, A. Yamaguchi, J. Nishimoto , M. Kumamoto, H. Wakita, T. Yamaguchi, *J. Phys. Chem. B* **1998**, 102, 8880.

[134] G. M. Chaban, *J. Phys. Chem. A* **2004**, 108, 4551.

[135] A. Banerjee, R. Sharma, U. Banerjee, *Appl. Microbiol. Biotechnol*. **2002**, 60, 33.

[136] F. F. Fleming, L. Yao, P. C. Ravikumar, L. Funk, B. C. Shook, *J. Med. Chem.* **2010**, 53(22), 7902.

[137] T. L. Cairns, J. C. Sauer, W. K. Wilkinson, *J. Am. Chem. Soc.* **1952**, 74(16), 3989.

[138] J. H. S. Green, *Spectrochim. Acta.* **1961**, 17, 607.

[139] J. H. S Green. D. J. Harrison, *Spectrochim. Acta.* **1976**, 32A, 1279.

[140] R. J. Jakobsen, *Spectrochim. Acta.* **1965**, 21, 127.

[141] M. D. Hoops, B. S. Ault, *Chem. Phys.* **2007**, 334, 18.

[142] M. Hartmann, L. Radom, *J. Phys. Chem. A* **2000**, 104, 968.

[143] W. P. Schroeder, K. Chenoweth, C. E. Dykstra, *Chem. Phys. Lett*. **2003**, 373, 8.

[144] K. Sundararajan, K. Sankaran, K. S. Viswanathan, A. D. Kulkarni, S. R. Gadre, *J. Phys. Chem. A* **2002**, 106, 1504.

[145] K. Sundararajan, K. S. Viswanathan, A. D. Kulkarni, S. R. Gadre, *J. Mol. Struct*. **2002**, 613, 209.

[146] K. Sundararajan, N. Ramanathan, *J. Mol. Struct.* **2009**, 920, 369.

[147] K. Sundararajan, K. Sankaran, K. S. Viswanathan, *J. Mol. Struct*. **2004**, 733, 187.

[148] K. Sundararajan, K. S.Viswanthan, *J. Mol. Struct*. **2006**, 798, 109.

[149] T. Kobayashi, K. Honma, O. Kajimoto, S. Tsuchiya, *J. Chem. Phys*. **1987**, 86, 1111.

[150] T. Kobayashi, O. Kajimoto, *J. Chem. Phys.* **1987**, 86, 1118.

[151] V. Storm, D. Consalvo, H. Drei-zler, *Z. Naturforsch*. **1997**, 52A, 293.

[152] V. Storm, H. Dreizler, D. Consalvo, *Chem. Phys*. **1998**, 239, 109.

[153] R. M. Helm, H. P. Vogel, H. J. Neusser, V. Storm, D. Consalvo, H. Z. Dreizler, *Z. Naturforsch.* **1997**, 52, 655.

[154] S. Melandri, D. Consalvo, W. Caminati, P. G. Favero, *J. Chem. Phys.* **1999**, 111, 3874.

[155] S. Ishikawa, T. Ebata, N. Mikami, *J. Chem. Phys*. **1999**, 110, 9504.

[156] R. Yamamoto, T. Ebata, N. Mikami, *Eur. Phys. J.* **2002**, 20, 403.

[157] R. Yamamoto, S. Ishikawa, T. Ebata, N. Mikami, *J. Raman Spectrosc*. **2000**, 31, 295.

[158] R. Yamamoto, T. Ebata, N. Mikami, *J. Chem. Phys*. **2001**, 114, 7866.

[159] E. S. Kryachko, M. T. Nguyen, *J. Chem. Phys.* **2001**, 115, 833.

[160] D. R. Borst, D. W. Pratt, M. Schafer, *Phys. Chem. Chem. Phys*. **2007**, 9, 4563.

[161] E. Whittle, D. A. Dows, G. C. Pimentel, *J. Chem. Phys.* **1954**, 22, 1943.

[162] I. Dunkin, Matrix Isolation Technique: A practical Approach, **1998**.

[163] S. Cradock, A. J. Hinchliffe, Matrix Isolation: A technique for the study of reactive inorganic species, Cambridge University Press, Cambridge, **1975**.

[164] H.E. Hallam (ed.), Vibrational Spectroscopy of Trapped Species, John Wiley & Sons, London, **1973**.

[165] L. Andrews, M. Moskovits (eds.), Chemistry and Physics of Matrix-isolated Species, Elsevier Science, Amsterdam, **1989**.

[166] A. J. Barnes, W. J. Orville-Thomas, A. Muller, R. Gaufres (eds.), Matrix Isolation Spectroscopy, D. Reidel, Dordrecht, **1981.**

[167] T. Momose, M. Miki, M. Uchida, T. Shimizu, I. Yoshizawa, T. Shida, *J. Chem. Phys.* **1995**, 103, 1400.

[168] S. Tam, M. E. Fajardo, *Rev. Sci. Instrum.* **1999**, 70, 1926.

[169] M. E. Fajardo, Chapter 6 matrix isolation spectroscopy, in: L. Khariachtchev (Ed.), Solid Para Hydrogen a Primer in Physics and Chemistry at Low Temperatures, Pan Stanford, Singapore, **2011.**

[170] G. C. Pimentel, S.W. Charles, *Pure Appl. Chem.* **1963**, 7, 111.

[171] A. J. Barnes, *Faraday Discuss. Chem. Soc.* **1988**, 86, 45.

[172] L. Schriver, A. Schriver, J. P. Perchard, *J. Chem. Phys.* **1986**, 84, 5553.

[173] A. J. Barnes , Z. Mielke, *J. Mol. Struct*. **2012**, 1023, 216.

[174] S. D. Buckingham, *Proc. Roy. Soc. (London) A*, **1958**, 248, 169.

[175] F. Jensen, Introduction to Computational Chemistry, John Wiley and Sons, **1999**.

[176] J. B. Foresman, A. Frisch, Exploring Chemistry with Electronic Structure Methods, Second ed., Gaussian, Inc., Pittsburgh, **1996**.

[177] S. Scheiner, Hydrogen Bonding: A Theoretical Perspective, Oxford University Press, New York, **1997**.

[178] M. J. Frisch, G. W. Trucks, H. B. Schlegel, G. E. Scuseria, M. A. Robb, J. R. Cheeseman, G. Scalmani, V. Barone, B. Mennucci, G. A. Petersson, H. Nakatsuji, M. Caricato, X. Li, H. P. Hratchian, A. F. Izmaylov, J. Bloino, G. Zheng, J. L. Sonnenberg, M. Hada, M. Ehara, K. Toyota, R. Fukuda, J. Hasegawa, M. Ishida, T. Nakajima, Y. Honda, O. Kitao, H. Nakai, T. Vreven, J. A. Montgomery, Jr., J. E. Peralta, F. Ogliaro, M. Bearpark, J. J. Heyd, E. Brothers, K. N. Kudin, V. N. Staroverov, R. Kobayashi, J. Normand, K. Raghavachari, A. Rendell, J. C. Burant, S. S. Iyengar, J. Tomasi, M. Cossi, N. Rega, J. M. Millam, M. Klene, J. E. Knox, J. B. Cross, V. Bakken, C. Adamo, J. Jaramillo, R. Gomperts, R. E. Stratmann, O. Yazyev, A. J. Austin, R. Cammi, C. Pomelli, J. W. Ochterski, R. L. Martin, K. Morokuma, V. G. Zakrzewski, G. A. Voth, P. Salvador, J. J. Dannenberg, S. Dapprich, A. D. Daniels, Ö. Farkas, J. B. Foresman, J. V. Ortiz, J. Cioslowski, and D. J. Fox, Gaussian, Inc., Wallingford CT, **2009**.

[179] E. Lewars, Computational Chemistry: Introduction to theory and applications of Molecular and Quantum Mechanics, Kluwer Academic Publishers, Boston, **2003**.

[180] W. J. Hehre, L. Radom, P. V. R. Schleyer J. A. Pople, *ab initio* molecular orbital theory, John Wiley and Sons, New York, **1985**.

[181] T. A. Clark, Hand book of Computational Chemistry: A practical guide to Chemical Structure and Energy Calculations, John Wiley & sons, New York, **1985**.

[182] J. P. Lowe, Quantum Chemistry, Academic Press, New York, **1978**.

[183] E. D. Glendening, J. E. Carpenter, F. Weinhold, NBO version 3.1.

[184] F. Biegle-Koning, R. F. W. Bader, W. H. J. Tang, *Comput. Chem.* 96 (2000) 6796 (AIM **2000**, Version 1).

[185] K. Kitaura, K. Morokuma, *Int. J. Quantum Chem.* **1976**, 10, 325.

[186] G. Te. Velde, F. M. Bickelhaupt, E. J. Baerends, C. F. Guerra, S. J. A. van Gisbergen, J. G. Snijders, T. Ziegler, *J. Comput. Chem.* **2001**, 22, 931.

[187] R. G. Parr, W. Yang, Density-Functional Theory of Atoms and Molecules, International series of monographs on chemistry No.16, 1st ed., R. Breslow, J. B. Goodenough, J. Halpern, J. S. Rowlinson, Eds., Oxford University Press, New York, **1989**.

[188] C. Møller, M. S. Plesset, *Phys. Rev.* **1934**, 46, 618. (b) A. Szabo, N. S. Ostlund, Modern Quantum Chemistry: Introduction to Advanced Electronic Structure Theory, 1st ed. Revised, McGraw-Hill, New York, **1989**.

[189] C. Lee, W. Yang, R. G. Parr, *Phys. Rev. B* **1988**, 37, 785.

[190] K.Schoone, J.Smets, R.Ramaekers, L.Houben, L.Adamowicz, G.Maes, *J. Mol. Struct.* **2003**, 649, 61.

[191] Zhang, Zheng-yu Zhou and Yun Shi; *J. Phys. Chem. A* **2004**, 108, 6735.

[192] F. Bergero, C. S. Alvaro, N. S. Nudelman, S. R.s de Debiaggi, *J. Mol. Struct. (Theochem),* **2009**, 896, 18.

[193] J.P. Merrick, D.Moran, and L. Radom, *J.Phys.Chem A* **2007**,111,11683

[194] S. F. Boys, F. Bernadi, *Mol. Phys*. **1970**, 19, 553.

[195] F. Jensen, *Chem. Phys. Lett.* **1996**, 261, 633.

[196] I. Mayer, P. R. Surján, *Chem. Phys. Lett.* **1992**, 191, 497.

[197] D. W. Schwenke, D. G. Truhlar, *J. Chem. Phys.* **1985**, 82, 2418.

[198] L. Turi, J. J. Dannenberg, *J. Phys. Chem.* **1993**, 97, 2488.

[199] L. Turi, J. J. Dannenberg, *J. Phys. Chem.* **1995**, 99, 639.

[200] N. B. Wong, Y. S. Cheung, D. Y. Wu, Y. Ren, X. Wang, A. M. Tian, W. K. Li, *J. Mol. Struct.* **2000**, 507, 153.

[201] R. F. W. Bader, Atoms in Molecules. A Quantum Theory, Clarendon Press, Oxford, **1994**.

[202] R. F. W. Bader, H. Essen, *J. Chem. Phys.* **1984**, 80, 1943.

[203] R. G. A. Bone, R. F. W. Bader, *J. Phys. Chem.* **1996**, 100, 10892.

[204] F. Weinhold, C. R. Landis, *Chem. Educ. Res. Pract*. **2001**, 2, 91.

[205] P. O. Lowdin, H. Shull, *Phys. Rev.* **1956**, 101, 1730.

[206] P. Su, H. Li, *J. Chem. Phys.* **2009**, 131, 014102.

[207] M. Von Hopffgarten, G. Frenking, *WIREs Comput. Mol. Sci.* **2012**, 2, 43.

[208] M. Mitoraj, A. Michalak,T. Ziegler, *J. Chem. Theory Comput*. **2009**, 5, 962.

[209] S. Grimme, J. Antony, S. Ehrlich and H. Krieg, *J. Chem. Phys*.,**2010**, 132, 154104.

[210] D.P.Chong, E. Van Lenthe, S. Van Gisbergen, E. J .Baerendes, *J.Comput. Chem.* **2004**,25,1030.

[211] D. Maillard, A. Schriver, J. P. Perchard, C. Girardet, *J. Chem. Phys.* **1979**, 71, 505.

[212] P. Ramasami, A. F. Thomas, *J. Mol. Struct.* **2012**, 1023, 163.

[213] C. Peng, H. B. Schlegel, *Israel J. Chem.*, **1993,** 33, 449.

[214] N. Dozova, L. Krim, M. E. Alikhani, N. Lacome, *J. Phys. Chem. A* **2005**, 109, 10273.

[215] R. M. Bentwood, A. J. Barnes, W. J. Orville-Thomas , *J. Mol. Spectrosc*. **1980**, 84, 391.

[216] S. Wojtulewski, S. J. Grabowski, *Chem. Phys.* **2005**, 309, 183.

[217] R. J. Bemish, P. A. Block, L. G, Pederson, W. Yang, R. E. Miller, *J. Chem. Phys.* **1993**, 99 , 8585.

[218] L. Turi, J. Dannenberg, *J. Phys. Chem.* **1993**, 97, 7899.

[219] L. Schriver, A. Schriver, J. P. Perchard. *J. Chem. Soc. Faraday Trans.* **1985**, 81, 1407.

[220] S. Pilla, J. A. Hamida, K. A. Muttalib, N. S. Sullivan. *Phys. Lett. A* **1999**, 256, 75.

[221] M. E. Jacox, *J. Phys. Chem.* Ref. Data, Monogr. **1994**, No. 3.

[222] M. J. T. Jordan, J. E. Del Bene, *J. Am. Chem. Soc.* **2000**, 122, 2101.

[223] A. Engdahl, B. Nelander, *Chem. Phys. Lett.* **1983**, 100, 129.

[224] M. T. Caroll, R. F. W. Bader, *Mol. Phys.* **1988**, 65, 695.

[225] M. T. Caroll, C. Chang, R. F. W. Bader, *Mol. Phys.* **1988**, 63, 387.

[226] F. Weinhold, *J. Mol. Struct. (Theochem)* **1997**, 181, 398.

[227] G. L. Sosa, N. M. Peruchena, R. H. Conteras, E. A. Castro, *J. Mol. Struct. (Theochem)* **2002**, 219, 577.

[228] P. Kolandaivel, V. Nirmala, *J. Mol. Struct***. 2004**, 33, 694.

[229] Y. X. Lu, J. W. Zou, Y. H. Wang, Y. J. Jiang, Q. S. Yu, *J. Phys. Chem. A* **2007**, 111, 10781.

[230] W. Wang, P. Hobza, *J. Phys. Chem. A* **2008**, 112, 4114.

[231] N. J. M. Amezaga, S. C. Pamies, N. M. Peruchena, G. L. Sosa, *J. Phys. Chem. A* **2010**, 114, 552.

[232] W. Wang, *J. Phys. Chem. A* **2011**, 115, 9294.

[233] M. Jablonski, M. Palusiak, *J. Phys. Chem. A* **2012**, 116, 2322.

[234] M. Solimannejad, M. Malekani, *J. Phys. Chem. A* **2013**, 117, 5551.

[235] S. J. Grabowski, *Chem. Phys. Lett*. **2001**, 338, 361.